

A SEARCH FOR NEW PHYSICS IN HIGGS TO
DIPHOTON ASSOCIATED PRODUCTION IN
PROTON-PROTON COLLISIONS AT $\sqrt{s} = 8$ TeV

By

ANTHONY BARKER

A dissertation submitted to the
Graduate School—New Brunswick
Rutgers, The State University of New Jersey
in partial fulfillment of the requirements
for the degree of
Doctor of Philosophy
Graduate Program in Physics and Astronomy
written under the direction of
Yuri Gershtein
and approved by

New Brunswick, New Jersey

January, 2015

ABSTRACT OF THE DISSERTATION

A search for new physics in Higgs to diphoton associated production in Proton-Proton collisions at $\sqrt{s} = 8$ TeV

By ANTHONY BARKER

Dissertation Director:

Yuri Gershtein

Searches for “natural” supersymmetry (SUSY) scenarios are presented in which only neutralinos, charginos, and potentially also the top-quark superpartner (stop) are assumed to be accessible, and which result in multi-boson final states. These efforts rely on a novel and versatile method whereby the narrow $H \rightarrow \gamma\gamma$ resonance is used to identify events with a Higgs boson candidate, and to determine backgrounds. This provides a sufficiently clean search environment to largely overcome the small $H \rightarrow \gamma\gamma$ branching fraction. First, a search is performed for stop pair production resulting in $2b2H$. Events with two photons forming a Higgs boson candidate and at least two b-jets are selected and missing transverse energy is examined. Then, the diphoton components of a comprehensive search for electroweak production of neutralinos and charginos are presented, which may decay to Higgs and Z, bosons and undetected lightest SUSY particles (LSPs). This latter search is then reinterpreted in terms of chargino-neutralino pair production, leading to HW^\pm states with E_T^{miss} . The searches are performed using 19.5 fb^{-1} of proton-proton collisions at $\sqrt{s} = 8$ TeV, recorded in the Compact Muon Solenoid (CMS) detector. No compelling evidence for new physics is found and

95% confidence limits are set.

Acknowledgments

This work represents a long journey for both myself and high energy physics during which a great many people deserve thanks. First I should thank the armies of men and women who have been building the LHC, CMS detector, and surrounding infrastructure, since I was a toddler and got them operational in just time for me to do research. I would like to thank Yuri Gershtein for being my adviser, template, friend and motivator. His guidance, drive, and unwavering support has been vital at every step.

I'd also like to thank my closest collaborators: On the theory side, Scott Thomas and Yevgeny Kats sparked this direction of experimental study and built the theoretical models underpinning it. And thanks again to Scott Thomas, Patrick Zywicki, Yevgeny Kats, Jared Evans, Nathaniel Craig and Michel Park for their work in developing the template S LHA templates and Monte Carlo generation setup. Credit is due to Nathaniel Craig, John Killick, and Jared Evans for developing the Higgs decayer.

Very special thanks and credit are due to David Morse for his work on the diphoton plus lepton channels, as well as Patrick Zywicki and Emmanuel Contreras for tirelessly carrying out the Monte Carlo generation from end to end. Also to David Mason, who managed many of the most daunting computation task and whose council was useful on a daily basis. Kira Burt also deserves mention for her work on optimization studies.

I am very grateful to those agencies and grant writers whose funds supported this work: the DOE, NSF, and Sunil Somalwar. I should thank Yuri Maravin who tolerated my protracted efforts to develop a diphoton fake rate ratio method. As well as Gail Hanson for expediting the stop paper as ARC chair. I would like to express my appreciation to the Rutgers physics department, which has been my home more than any other location.

Special thanks is due to Nima Arkani-Hamed for his inspiration, and to Ilya Weinstein for his friendship and for challenging my ideas. Also, I would like to offer special thanks to the friends who kept me sane on this journey: Tia Miceli, Souvik Das, Anna Krasner, and Cathy Farrow. Finally, I would like to thank my parents Bruce and Valerie Barker for their endless support.

Dedication

*For SUSY, wherever she may be,
and for all the enablers.*



Figure 1: CERN ground breaking, 1954

Table of Contents

| | |
|---|------|
| Abstract | ii |
| Acknowledgments | iv |
| Dedication | vi |
| List of Tables | x |
| List of Figures | xiii |
| 1. Introduction | 1 |
| 2. Theory | 9 |
| 2.1. Brief Overview of the Standard Model Physics | 9 |
| 2.2. SuperSymmetry | 24 |
| 3. The Experimental Apparatus: LHC and CMS | 36 |
| 3.1. Introduction | 36 |
| 3.2. The LHC | 37 |
| 3.3. CMS Detector | 39 |
| 4. Particle Reconstruction | 56 |
| 4.1. Introduction | 56 |
| 4.2. Global Event Description | 57 |
| 4.3. Vertex Identification | 60 |
| 4.4. Electromagnetic Objects | 60 |

| | |
|---|------------|
| 4.5. Hadronic Objects | 68 |
| 4.6. Muons | 75 |
| 5. Signal Simulation | 77 |
| 5.1. introduction | 77 |
| 5.2. Stop Production | 79 |
| 5.3. Higgsino Electroweak Production | 80 |
| 5.4. HW^\pm Production | 81 |
| 6. Background Modeling and the Crane | 83 |
| 6.1. Background Prediction with the Hgg+X Sideband Method | 83 |
| 6.2. Example Background Estimation Calculation | 87 |
| 6.3. The Crane Framework | 91 |
| 6.4. SM Higgs Background | 94 |
| 7. Datasets and Trigger | 97 |
| 7.1. Data Sets | 97 |
| 7.2. Triggers Used | 97 |
| 8. Analysis Design | 99 |
| 8.1. SUSY Partners of the Top Quark (Stops) | 99 |
| 8.2. Higgsino with b-Jets | 114 |
| 8.3. Higgsino with Leptons | 119 |
| 8.4. Higgsino with Electroweak Bosons | 120 |
| 8.5. Systematic Uncertainties | 123 |
| 8.6. Statistical Limit Setting Methods | 123 |
| 9. Results and Limit Setting | 126 |
| 9.1. Stops | 126 |

| | |
|--|------------|
| 9.2. Higgsino $b\bar{b}$ Results | 138 |
| 9.3. Higgsino Leptonic Results | 144 |
| 9.4. Higgsino Electro-Weak Results | 150 |
| 9.5. Higgsino Combination Interpretation | 161 |
| 10. Conclusion | 166 |
| 10.1. Summary | 166 |
| 10.2. Outlook | 167 |
| Bibliography | 169 |
| Appendix A. Non-parametric Multivariate Methods | 173 |
| Appendix B. Anomalies | 176 |

List of Tables

| | |
|---|----|
| 2.1. Properties for fields. | 12 |
| 2.2. W boson major decay modes and branching ratios. The $c+X$ decay channel is contained within the hadronic decay channel. Reprinted from (63). | 15 |
| 2.3. Z boson major decay modes and branching ratios. Reprinted from (63). | 15 |
| 2.4. Selected Higgs branching ratios used. | 18 |
| 2.5. Higgs boson production Feynman diagrams. | 19 |
| 2.6. Higgs boson production cross sections used. | 19 |
| 4.1. Smearing Factor Results | 66 |
| 4.2. From left to right, the previously obtained smearing factors for FullSim (36), the gaussian widths of the fits to FullSim Monte Carlo, the gaussian widths of the fits to FastSim Monte Carlo, and the FastSim smearing factor results derived from these. | 66 |
| 5.1. Higgs boson decay branching ratios used. | 79 |
| 5.2. Number of events generated for simulated stop production. | 80 |
| 5.3. Number of events generated for simulated electroweak HH production for each range of mass points and considered Higgs decay channels. | 80 |
| 5.4. Number of events generated for simulated electroweak HZ production for each range of mass points and considered Higgs decay channels. | 80 |
| 5.5. Number of events generated for simulated electroweak HW production for each range of mass points and considered Higgs decay channels. | 82 |
| 6.1. The SM Higgs production channels, datasets, and cross sections used in this analysis. | 95 |
| 7.1. Datasets used in the analysis | 97 |
| 7.2. Triggers used in the analysis | 98 |

| | |
|---|-----|
| 8.1. Expected Backgrounds using Various Fit Functions | 113 |
| 8.2. Background estimates made using four fit functions for the three b-jet categories and the combined. Aside from the poor 3rd order polynomial fits, the variation from changing fit functions is well described by the uncertainty on the power law fit. Additional systematic uncertainty from the fit shape is negligible. | 113 |
| 8.3. Cutflow for $H(bb)H(\gamma\gamma)$ for $\mu = 130 \text{ GeV}/c^2$. Here the second Higgs is assumed to decay to bb | 118 |
| 8.4. Cutflow for HW^\pm for $\mu = 130 \text{ GeV}/c^2$ | 121 |
| 8.5. Cutflow for HZ for $\mu = 130 \text{ GeV}/c^2$ | 121 |
| 8.6. Sources of systematic uncertainties | 123 |
| 9.1. Expected and observed event counts | 126 |
| 9.2. Observations and Background Estimates | 129 |
| 9.3. Selected Limit Results | 138 |
| 9.4. Expected and observed event counts for the Higgsino two Higgs channel | 140 |
| 9.5. The uncertainties includes the statistical uncertainty and the normalization uncer- tainty from the fit function. | 140 |
| 9.6. Observations and Background Estimates for the two-Higgs channel | 141 |
| 9.7. The uncertainties includes the statistical uncertainty and the normalization uncer- tainty from the fit function. | 141 |
| 9.8. Comparison of the observed data and background estimates for the lepton channels. The electron channel shows an excess with a 1.3% p-value. | 145 |
| 9.9. Signal region counts and background estimates using M_T variable for the di-photon+electron selection, showing also the signal yields for the signal model with $m_{\tilde{\chi}_1^0} = m_{\tilde{\chi}_2^0} =$ $m_{\tilde{\chi}_1^\pm} = 130 \text{ GeV}/c^2$ and $m_{\tilde{\chi}_1^0} = 1 \text{ GeV}/c^2$. The last three columns show the break- down of the uncertainty in the | 145 |

| | |
|---|-----|
| 9.10. Signal region counts and background estimates using M_T variable for the di-photon+muon selection, showing also the the signal yields for the signal model with $m_{\tilde{\chi}_1^0} = m_{\tilde{\chi}_2^0} = m_{\tilde{\chi}_1^\pm} = 130 \text{ GeV}/c^2$ and $m_{\tilde{\chi}_1^0} = 1 \text{ GeV}/c^2$ | 146 |
| 9.11. Expected and observed event counts | 151 |
| 9.12. The uncertainties includes the statistical uncertainty and the normalization uncertainty from the fit function. | 151 |
| 9.13. Observations and Background Estimates for the Electroweak channel | 155 |
| 9.14. The uncertainties includes the statistical uncertainty and the normalization uncertainty from the fit function. | 155 |

List of Figures

| | | |
|------|--|----|
| 1. | CERN ground breaking, 1954 | vi |
| 1.1. | Example diphoton mass spectrum. The upper and lower sidebands are bounded by the red lines. The Higgs mass window (signal region) is bounded by blue lines. An power law fit function which ignores the signal region is shown in green. | 2 |
| 1.2. | A priori expected 95% exclusions in 20 fb^{-1} at 8 TeV for a simplified search for stop quark production in $H \rightarrow \gamma\gamma + 2b$ (Solid black line). The shaded regions are excluded by other searches: the CMS 8 TeV $3b + \text{MET}$ search (diagonal hatching) (5), the CMS 7 TeV multilepton search (horizontal hatching) (24), the CMS 8 TeV same-sign dilepton + $2b$ search (vertical hatching) (45), and the CMS 8 TeV $\gamma\gamma + E_T^{\text{miss}}$ search (solid colored) (44). The dashed line is the expected limit for a $H \rightarrow \gamma\gamma + 1 cPqb$ -jet search. The implemented search significantly improves on this bound. Reprinted from (52). | 4 |
| 1.3. | Mondrian tables for for the decay of two Higgs bosons (top), one Higgs bosons and one Z (bottom left) and two Z bosons (bottom right). The area of each rectangle proportional to the branching fraction. | 7 |
| 1.4. | Diphoton events may fall into one of four categories divided between four analyses. To pass the 2 b-jet requirement, both b-jets must pass CSV-Medium or better. While failing events may have at most two CSV-Loose jets, at most one of which CSV-Medium b-jet. This creates a gap in the b-jet selection that prevents variations in b-jet tagging efficiency from transferring events from one category to another. Events falling into this gap are discarded. | 8 |
| 2.1. | The particles of the standard model. | 10 |

| | | |
|-------|--|----|
| 2.2. | Cross sections and rates of various processes in the CMS. | 22 |
| 2.3. | Feynman diagram of the gluon fusion contributing to Standard Model Diphoton production at leading order (left) and NLO (center and right). Reprinted from (20). . . | 23 |
| 2.4. | Sample Feynman diagrams for the production of $\gamma + \text{jets}$ background. Reprinted from (11). | 24 |
| 2.5. | Two-loop renormalization group evolution of the inverse gauge couplings of the Standard Model (dashed lines) and the MSSM (solid lines). Reprinted from (59). . . . | 26 |
| 2.6. | <i>Top Left:</i> The spectrum of the minimal model under consideration. <i>Top Right:</i> Example Feynman diagram of strong production. <i>Bottom:</i> Example Feynman diagram of electroweak production. The jets or leptons resulting from transitions between Higgsinos are extremely soft in both diagrams due to the near mass degeneracy of the chargino and the neutralino. | 29 |
| 2.7. | Top: Neutralino branching fractions as a function of supersymmetric parameters. Reprinted from (60). Bottom: Contours of Higgsino branching fractions as a function of $\tan\beta$ and the neutralino mass parameter μ in the decoupling limit. This takes $\text{sign}(\mu) < 0$. Higgsinos decay is dominated by decay to Higgs at low $\tan\beta$. Reprinted from (52). | 31 |
| 2.8. | Feynman diagrams of neutralino production processes. | 32 |
| 2.9. | Example Feynman diagrams for production of Higgsinos resulting in 2 Higgs bosons (left), a Higgs and a Z (right), and two Z bosons (bottom). | 33 |
| 2.10. | Feynman Diagrams for the Wino-Bino model. The left most diagram generates the WH signal. | 35 |
| 3.1. | The LHC and its precursor accelerators. Protons begin in Linac2, and proceed through the booster, PS, SPS, and are finally enter into the LHC. | 38 |
| 3.2. | A longitudinal cross section of the CMS detector. A full schematic would mirror this slice both vertically and horizontally. | 41 |

| | | |
|-------|---|----|
| 3.3. | The CMS detector during construction as the tracker (protruding from the center) is being inserted. The Endcap is retracted and out of view. The white dots are reflectors used for alignment. The LHC beam pipe traverses the center of the cylinder, but was not yet installed at the time of this photo. The red and silver outer layers are the iron magnetic-field return yoke (red) and the muon system. Just inside that the solenoid is clearly visible. The HCAL and ECAL are also visible in the indentation. | 42 |
| 3.4. | A transverse cross section of the CMS detector | 43 |
| 3.5. | CMS luminosity history | 45 |
| 3.6. | Distribution of pileup events in CMS proton collision events. | 46 |
| 3.7. | A r-z view of the CMS tracker, detailing its sub-systems. The short line segments indicate layers of CCD detectors. The sub-detectors are the Tracker Inner Barrel (TIB), Tracker Outer Barrel (TOB), Tracker Endcaps (TEC), Tracker Inner Disk (TID), and Pixel Detector. (23) | 48 |
| 3.8. | The CMS tracker outer barrel durring construction. | 48 |
| 3.9. | Tracks and vertices reconstructed by the CMS tracking system in an example high pileup event. Charged hadrons are shown as green tracks, and reconstructed vertices are shown as yellow dots. The event has one electron (blue blue), and one muons (red track). | 49 |
| 3.10. | The radiation thickness of the tracking system as a function of pseudorapidity η . (23) | 50 |
| 3.11. | A cut-away view of the CMS ECAL. In green and purple are the barrel crystals. In grey are the endcap crystals. | 52 |
| 3.12. | Schematic of the one fourth of the HCAL in the r-z plane detailing the tower segmentation. Reprinted from (23). | 53 |
| 4.1. | Fits of photon resolution in FastSim and FullSim Monte Carlo simulation for eight photon categories. The inner cone is fit with a Gaussian. | 67 |
| 4.2. | Comparison of E_T^{miss} distributions using jet energy corrections, and with the energy corrections shifted up and down by 1σ for mass point $M_{\tilde{\chi}_1^0} = 150 \text{ GeV}/c^2$ | 70 |

| | | |
|------|--|-----|
| 4.3. | Comparison of E_T^{miss} distributions using b-tag scale factors, and with the scale factors shifted up and down by 1σ for mass point $M_{\text{stop}} = 210 \text{ GeV}/c^2$, $M_{\tilde{\chi}_1^0} = 150 \text{ GeV}/c^2$. | 75 |
| 5.1. | Cross section times $\text{Br}(\text{H} \rightarrow \gamma\gamma)$ as a function of stop and Higgsino masses for the generated MC points on linear and log scales. These use the “official” NLO cross stop pair production cross sections(32) and branching ratios(30). | 79 |
| 5.2. | Cross section x $br[H \rightarrow \gamma\gamma]$ for the generated MC points for Higgsino pair production on linear and log scales. These use the “official” NLO production cross sections (32) and branching ratios (30). | 81 |
| 6.1. | The logo of the Crane analysis framework. | 91 |
| 6.2. | Expected standard model Higgs boson background contribution to the two-Higgs channel from FullSim Monte Carlo in combined gluon-gluon fusion, vector boson fusion, and vector boson + Higgs boson production channels. top-top-Higgs is negligible compared to these three production channels. In total, the standard model Higgs production is a negligible background for this channel. | 95 |
| 6.3. | Expected standard model Higgs boson background contribution to the electroweak channel from FullSim Monte Carlo in combined gluon-gluon fusion, vector boson fusion, vector boson + Higgs boson production, and top-top-Higgs production channels. In total, the standard model Higgs production is a negligible background for this study. | 96 |
| 7.1. | Turn-on curves for the leading and sub-leading photon candidates. | 98 |
| 8.1. | Maximum of the absolute values of the two photon’s pseudo-rapidities (color points) from expected signal normalized to the integrated luminosity on linear and log scales. The shaded rectangles show the background estimate from the sidebands. For events below 1.4442, both photons are restricted to the barrel. Requiring this dramatically reduces background. | 100 |
| 8.2. | E_T^{miss} of expected signal (color points) normalized to the integrated luminosity. The shaded rectangles show the background estimate from the sidebands. | 101 |

| | | |
|------|---|-----|
| 8.3. | MHT of expected signal (color points) normalized to the integrated luminosity. MHT is the transverse momentum the vector sum of all jets with $p_T > 30$ GeV/ c . The shaded rectangles show the background estimate from the sidebands. | 102 |
| 8.4. | Transverse momentum of the diphoton system for expected signal (color points) normalized to the integrated luminosity. The shaded rectangles show the background estimate from the sidebands. Both photons satisfy the photon definition described in Section 4.4. | 103 |
| 8.5. | H_T of expected signal (color points) normalized to the integrated luminosity. H_T is the scalar sum of of the p_T of all jets with $p_T > 30$ GeV/ c . The shaded rectangles show the background estimate from the sidebands. | 104 |
| 8.6. | Scalar sum of transverse momenta of all b-jets passing the CSV-Loose working point, for expected signal (color points) normalized to the integrated luminosity and the data driven background estimates. The shaded rectangles show the background estimate from the sidebands and the red rectangles are the combined data driven background estimate. | 105 |
| 8.7. | S_T for expected signal (color points) normalized to the integrated luminosity. S_T is the scalar sum of the p_T of all the jets in the event with $p_T > 30$ GeV/ c , photons passing the loose photon definition, and E_T^{miss} . The shaded rectangles show the background estimate from the sidebands. | 106 |
| 8.8. | Transverse momentum of all jets with $p_T > 30$ GeV/ c for expected signal (color points) normalized to the integrated luminosity and the data driven background estimates. The shaded rectangles show the background estimate from each sideband and the red rectangles are the combined data driven background. | 107 |
| 8.9. | Number of jets for expected signal (color points) normalized to the integrated luminosity. The shaded rectangles show the background estimate from the sidebands. . . | 108 |

| | |
|--|-----|
| 8.10. Two-body invariant mass of the leading two b-jets for Monte Carlo signal points and background estimates. In the case of four b-jets in the final state there is a six fold combinatoric background hiding the Higgs resonance, resulting in a broad peak. But in cases where the mass difference between the stop and Higgsino is small the leading two b-jets are more likely to be from the Higgs and the Higgs resonance is more pronounced. The vertical gray lines show the boundaries of the 95-155 GeV/ c^2 M_{bb} window. | 110 |
| 8.11. Comparison of E_T^{miss} distributions for each of the cut categories for background and Monte Carlo signal. Upper left: the 2 b-jets categories with M_{bb} on the Higgs mass. Upper Right: the 2 b-jets categories with M_{bb} off the Higgs mass. Lower left: the 3 or more b-jets categories. | 111 |
| 8.12. Monte Carlo efficiency maps for each of the cut categories. Upper left: the 2 b-jets categories with M_{bb} on the Higgs mass. Upper Right: the 2 b-jets categories with M_{bb} off the Higgs mass. Lower left: the 3 or more b-jets categories. Lower right: the sum of the three categories. In each case both photons be in the barrel with a diphoton mass on the Higgs mass. | 112 |
| 8.13. A comparison of the fits using different fit functions. First row: The 2 b-jet category with M_{bb} on M_H . Second row: The 2 b-jet category with M_{bb} off of M_H . Third row: The 3 b-jet category. Fourth row: The combination of the three categories. The different columns correspond to different fit functions used. First Columns: two parameter power law fit. Second Columns: an exponential fit Third Columns: A second order polynomial fit. Fourth Columns: A third order polynomial fit. | 114 |
| 8.14. Expected standard model Higgs boson background contribution to the two-Higgs channel from FullSim Monte Carlo in combined gluon-gluon fusion, vector boson fusion, and vector boson + Higgs boson production channels. top-top-Higgs is negligible compared to these three production channels. In total, the standard model Higgs production is a negligible background for this channel. | 117 |

| | |
|---|-----|
| 8.15. Expected standard model Higgs boson background contribution to the electroweak channel from FullSim Monte Carlo in combined gluon-gluon fusion, vector boson fusion, vector boson + Higgs boson production, and top-top-Higgs production channels. In total, the standard model Higgs production is a negligible background for this study. | 118 |
| 8.16. E_T^{miss} Distributions for ZH (Left side) and WH (Right side) signals compared to the background. | 121 |
| 8.17. Above: M_{jj} distribution for $mu = 130$ ZH production. Below: M_{jj} distribution for $mu = 130$ WH production. The green lines indicate the boundaries of the dijet mass window used. The peaks of both the ZH and WH signal fit comfortably within the window. The last bins include the overflow. | 122 |
| 9.1. Diphoton mass distribution for events with two or more b-jets; detailing the fit to the background (green line) using the Higgs boson mass sidebands. The red lines bound the upper and lower side bands while the blue lines bound the signal region. | 127 |
| 9.2. Diphoton mass distributions with background fits. From left to right: diphoton mass with exactly two b-jets whose dijet mass is on the Higgs boson mass, exactly two b-jets whose mass is off the Higgs mass, and three or more b-jets. | 127 |
| 9.3. Above: E_T^{miss} distributions for diphoton events with two or more b-jets, comparing data, expected background and expected signal (color points) normalized to the integrated luminosity. The shaded rectangles show the background estimate from the sidebands. The last bin includes the overflow. Below: A version of the same histogram using the absolute number of events per bin rather than events per 10 GeV. This shows the behavior at high E_T^{miss} more clearly. | 128 |

- 9.4. E_T^{miss} distributions for the data, background, and selected Monte Carlo points, used for limit setting when subdividing into three categories. Top Row: Besides requiring that the diphoton mass is on the Higgs mass we require (a) three or more b-jets, (b) exactly two b-jets whose dijet mass is on the Higgs boson mass, and (c) exactly two b-jets whose mass is off the Higgs mass. The last bins include the overflow. The E_T^{miss} distribution for the sum of these three channels is shown in Figure 9.3. Bottom Row: The same plots as above with absolute bin content rather than normalized bin content. This makes the behavior more clear at high E_T^{miss} 129
- 9.5. H_T for the data, background, and selected Monte Carlo points. H_T is the scalar sum of the p_T of all the jets in the event with $p_T > 30$ GeV/c. Upper left: the 2 b-jets categories with M_{bb} on the Higgs mass. Upper Right: the 2 b-jets categories with M_{bb} off the Higgs mass. Lower left: the 3 or more b-jets categories. Lower right: the sum of the three categories. In each case the two barrel photons are required with diphoton mass on the Higgs mass. The shaded rectangles show the background estimate from the sidebands. The last bin includes the overflow. 130
- 9.6. MHT for the data, background, and selected Monte Carlo points. MHT is the transverse vector sum of all the jets in the event with $p_T > 30$ GeV/c. Upper left: the 2 b-jets categories with M_{bb} on the Higgs mass. Upper Right: the 2 b-jets categories with M_{bb} off the Higgs mass. Lower left: the 3 or more b-jets categories. Lower right: the sum of the three categories. In each case the two barrel photons are required with diphoton mass on the Higgs mass. The last bin includes the overflow. 131

- 9.7. S_T for the data, background, and selected Monte Carlo points. S_T is the scalar sum of the p_T of all the jets in the event with $p_T > 30$ GeV/ c , photons passing the loose photon definition, and E_T^{miss} . Upper left: the 2 b-jets categories with M_{bb} on the Higgs mass. Upper Right: the 2 b-jets categories with M_{bb} off the Higgs mass. Lower left: the 3 or more b-jets categories. Lower right: the sum of the three categories. In each case the two barrel photons are required with diphoton mass on the Higgs mass. The shaded rectangles show the background estimate from the sidebands, and the colored points are the expected contributions from selected signal points, normalized to the integrated luminosity. The last bin includes the overflow. 132
- 9.8. B_T for the data, background, and selected Monte Carlo points. B_T is the scalar sum of the p_T of all the b-jets in the event with $p_T > 30$ GeV/ c . Upper left: the 2 b-jets categories with M_{bb} on the Higgs mass. Upper Right: the 2 b-jets categories with M_{bb} off the Higgs mass. Lower left: the 3 or more b-jets categories. Lower right: the sum of the three categories. In each case the two barrel photons are required with diphoton mass on the Higgs mass. The shaded rectangles show the background estimate from the sidebands, and the colored points are the expected contributions from selected signal points, normalized to the integrated luminosity. The last bin includes the overflow. 133
- 9.9. Diphoton p_T for the two photons whose mass is on the Higgs mass, for the data, background, and selected Monte Carlo points. Upper left: the 2 b-jets categories with M_{bb} on the Higgs mass. Upper Right: the 2 b-jets categories with M_{bb} off the Higgs mass. Lower left: the 3 or more b-jets categories. Lower right: the sum of the three categories. In each case the two barrel photons are required with diphoton mass on the Higgs mass. The shaded rectangles show the background estimate from the sidebands, and the colored points are the expected contributions from selected signal points, normalized to the integrated luminosity. The last bin includes the overflow. . . 134

| | |
|--|-----|
| 9.10. Distributions of the number of jets with $p_T > 30$ GeV/ c for the data, background, and selected Monte Carlo points. Upper left: the 2 b-jets categories with M_{bb} on the Higgs mass. Upper Right: the 2 b-jets categories with M_{bb} off the Higgs mass. Lower left: the 3 or more b-jets categories. Lower right: the sum of the three categories. In each case the two barrel photons are required with diphoton mass on the Higgs mass. The shaded rectangles show the background estimate from the sidebands, and the colored points are the expected contributions from selected signal points, normalized to the integrated luminosity. The last bin includes events with more than 8 jets. . . . | 135 |
| 9.11. Jet p_T for distributions for the data, background, and selected Monte Carlo points. Upper left: the 2 b-jets categories with M_{bb} on the Higgs mass. Upper Right: the 2 b-jets categories with M_{bb} off the Higgs mass. Lower left: the 3 or more b-jets categories. Lower right: the sum of the three categories. In each case the two barrel photons are required with diphoton mass on the Higgs mass. The shaded rectangles show the background estimate from the sidebands, and the colored points are the expected contributions from selected signal points, normalized to the integrated luminosity. The last bin includes the overflow. | 136 |
| 9.12. Limits on SUSY production cross sections for different stop and Higgsino masses using b-jet categories. The regions to the left of the contours are expected (red) and observed (black) to be excluded with 95% confidence. Black dashed curves reflect the theoretical uncertainty on cross section. Red dotted curves correspond to one standard deviation in expected sensitivity. | 137 |
| 9.13. Limit on the stop pair production cross section without using categorization. | 138 |
| 9.14. Diphoton mass spectrum for the Higgsino two Higgs channel. | 139 |

| | |
|---|-----|
| 9.15. Higgs S_T distributions for the data, background, and selected Monte Carlo points, used for limit setting for the two Higgs channel. The last bins include the overflow. The background estimate uncertainty (black hatching) includes the statistical uncertainty and the normalization uncertainty from the fit function which is the same for all the bins. | 140 |
| 9.16. Higgs S_T distributions for the data, background, and selected Monte Carlo points when the b-tag requirements of the 2H channel are relaxed. This shows the natural shape of the Higgs S_T background before the effects of low statistics seen in Figure9.15 become dominant. | 141 |
| 9.17. $p_T^{\gamma\gamma}$ (left) and p_T^{bb} (right) for the 2H channel. The red indicates the range of background estimates. Signal accumulates at high values in both distributions. | 142 |
| 9.18. Reconstructed Higgs masses decaying through $H(\gamma\gamma) + H$ in the 2H channel. The left column shows the $mu = 130 \text{ GeV}/c^2$ mass point and the right column shows the $mu = 250 \text{ GeV}/c^2$ mass point. The top row shows M_{bb} vs. $M_{\gamma\gamma}$. The middle row shows projections onto $M_{\gamma\gamma}$. And the bottom row shows projections onto M_{bb} | 143 |
| 9.19. Left: Cross section limits for pure HH production and the theory cross section. Right: The corresponding r-values for the limits. | 144 |
| 9.20. The results from fitting a power law in the electron + $h \rightarrow \gamma\gamma$ diphoton invariant mass distribution (left) and same for muons + $h \rightarrow \gamma\gamma$ (right). Also overlaid is the signal yield from addition of all the HH SMS scans with $m_{\tilde{\chi}_1^0} = 130 \text{ GeV}/c^2$, $m_{LSP} = 1 \text{ GeV}/c^2$ | 145 |
| 9.21. The M_T distribution for the muon + Higgs selection. In grey is the sideband estimated non Higgs background, with the statistical and systematic errors from the full background estimate in the red hatching. The SM Higgs background contribution is shown with gray-blue fill. All SM Higgs samples have $m_h = 126 \text{ GeV}/c^2$, and all SMS lines represent the $m_{\tilde{\chi}_2^0} = m_{\tilde{\chi}_1^\pm} = 130 \text{ GeV}/c^2$, $m_{\tilde{\chi}_2^\pm} = 1 \text{ GeV}/c^2$ point. | 146 |

| | | |
|-------|--|-----|
| 9.22. | The M_T distribution for the electron + Higgs selection. In tan is the sideband estimated non Higgs background, with the statistical and systematic errors from the full background estimate in the red hatching. The SM Higgs background contribution is shown with gray-blue fill. All SM Higgs samples have $m_h = 126 \text{ GeV}/c^2$, and all SMS lines represent the $m_{\tilde{\chi}_2^0} = m_{\tilde{\chi}_1^\pm} = 130 \text{ GeV}/c^2$, $m_{\tilde{\chi}_1^0} = 1 \text{ GeV}/c^2$ point. | 147 |
| 9.23. | E_T^{miss} distributions for the muon channel (left) and electron channel (right). | 148 |
| 9.24. | r-value limits for the di-photon+electron alone (left) and di-photon+muon alone (right) selections for the HH signal model. Shown are the observed limit (black), expected limit (black dashed), $\pm 1\sigma$ expected limits (green), and $\pm 2\sigma$ expected limits (yellow). | 149 |
| 9.25. | r-value limits for the di-photon+electron alone (left) and di-photon+muon alone (right) selections for the HZ signal model. Shown are the observed limit (black), expected limit (black dashed), $\pm 1\sigma$ expected limits (green), and $\pm 2\sigma$ expected limits (yellow). | 150 |
| 9.26. | Diphoton mass spectrum for the electroweak channel. Here the signal has been scaled up by a factor of 30 to make it visible. | 152 |
| 9.27. | Signal and background prediction for the electroweak channel. The last bin includes the overflow. The background estimate (red) uncertainty includes the statistical uncertainty and the normalization uncertainty from the fit function which is the same for all the bins. | 153 |
| 9.28. | Data, background and expected signal comparison for the electroweak channel. Left: E_T^{miss} distributions for the data, data driven background, and selected HW^\pm Monte Carlo points, used for limit setting for the two Higgs channel. Right: The same, but instead using HZ Monte Carlo. Bottom: the expected SM Higgs background contribution. The last bins include the overflow. The background estimate (red) uncertainty includes the statistical uncertainty and the normalization uncertainty from the fit function which is the same for all the bins. | 154 |

| | | |
|-------|---|-----|
| 9.29. | $p_T^{\gamma\gamma} + p_T^{jj}$ in the electroweak channel for HZ (right) and HW^\pm (left). This is the quantity in the electroweak channel most comparable to Higgs S_T in the 2H channel. | |
| | p_T^{jj} is the p_T of the leading pair of dijets. | 155 |
| 9.30. | $p_T^{\gamma\gamma}$ (left column) and p_T (right column) of the leading pair of jets for the ZH channel. | |
| | The bottom row shows logarithmic versions of the plots in the top row. | 156 |
| 9.31. | $p_T^{\gamma\gamma}$ (left column) and p_T (right column) of the leading pair of jets for the WH channel. | |
| | The bottom row shows logarithmic versions of the plots in the top row. | 157 |
| 9.32. | Reconstructed boson masses decaying through $H(\gamma\gamma) + Z$ in the electroweak channel. | |
| | The left column shows the $mu = 130$ GeV/ c^2 mass point and the right column shows the $mu = 250$ GeV/ c^2 mass point. The top row shows M_{jj} vs. $M_{\gamma\gamma}$. M_{jj} is plotted for all pairs of jets passing our jet selection and $H(b\bar{b})$ veto. The middle row shows projections onto $M_{\gamma\gamma}$. And the bottom row shows projections onto M_{jj} | 158 |
| 9.33. | Reconstructed boson masses decaying through $H(\gamma\gamma) + W^\pm$ in the electroweak channel. | |
| | The left column shows the $mu = 130$ GeV/ c^2 mass point and the right column shows the $mu = 250$ GeV/ c^2 mass point. The top row shows M_{jj} vs. $M_{\gamma\gamma}$. M_{jj} is plotted for all pairs of jets passing our jet selection and $H(b\bar{b})$ veto. The middle row shows projections onto $M_{\gamma\gamma}$. And the bottom row shows projections onto M_{jj} | 159 |
| 9.34. | Left: Cross section limits for pure HZ production and the theory cross section. Right: The corresponding r-values for the limits. | 160 |
| 9.35. | Left: Cross section limits for pure HW^\pm production and the theory cross section. Right: The corresponding r-values for the limits (see (10)). | 160 |
| 9.36. | Combined Higgsino limit, employing information from the $2\gamma 2b$, $2\gamma + \ell$, Multi-lepton, $4b$, $2b 2\ell$, and $2j 2\ell$ analyses. On the vertical axis is the branching ratio of Higgsino to Higgs bosons, as opposed to decays to Z bosons. | 163 |
| 9.37. | Left: the combined limit plot from Figure 9.36 with salient features of the limit labeled by their primary influence. Right: 1D slices of the limit plot for the 100%, 50%, and 0% Higgs branching fractions. | 164 |

9.38. One dimensional slices of the limit from Figure 9.36 overlaid with the limits from individual contributing analyses. These are the same three plots as on the right side of Figure 9.37. Top: 100% Higgs branching fraction (pure HH), Middle: 50%, Bottom: 0% Higgs branching fraction (pure ZZ). $2\gamma + X$ analyses contribute significantly at low Higgsino mass and high branching fraction. The electroweak channel is included in $\gamma\gamma + b\bar{b}$ 165

Chapter 1

Introduction

Supersymmetry (SUSY) is perhaps the foremost and best motivated mechanism for extending the standard model of particle physics to explain dark matter and the low mass of the Higgs boson. So far, all attempts to find supersymmetry have failed. Stringent bounds have been placed on susy parameters, largely from searches involving large amounts of missing transverse energy (E_T^{miss}). However, models of SUSY remain that can be considered “natural”, that is, their parameters do not require fine tuning. These require a fairly light super partner to the top quark (stops) and a compressed spectrum of Higgsino-like neutralinos and charginos a little above the Higgs mass, along with a very light LSP (Goldstino). These models frequently produce two electroweak bosons in the final state, including a broad space of parameters in which two Higgs bosons are produced. The proximity of the Higgsino compressed spectrum to the Higgs mass results in relatively little E_T^{miss} , which allows this class of models to escape previous SUSY searches. The recent discovery of a Higgs boson at $125 \text{ GeV}/c^2$ enables these models to be directly searched for.

In addition, observation of a Higgs boson produced in association with other particles would also be of great interest. The standard model Higgs boson is normally singly produced. It may also be produced in association with two top quarks or a vector boson, but the cross section is too small to observe with current data. Evidence of a pairs of Higgs boson, anomalously large $t\bar{t}H$ or VH , or other associated Higgs production would be clear evidence for physics beyond the standard model.

The $H \rightarrow \gamma\gamma$ decay channel provides a special environment in which to study associated Higgs production. Signal sharply peaks in the diphoton mass spectrum. Searches look for excesses of other particles and kinematic features on the $H \rightarrow \gamma\gamma$ resonance that do not appear in off-resonance events. This yields a clean environment with low and well understood backgrounds, and sufficient

sensitivity to largely overcome the low $H \rightarrow \gamma\gamma$ branching fraction.

Discovering the Higgs boson and determining its mass were critical to allowing line of investigation. I began investigating associated Higgs in the diphoton channel only three weeks after the Higgs boson was discovered.

For a search, first events with two photons and other particles of interest are selected. A diphoton mass spectrum is made with these events, and the spectrum divided into three regions: a Higgs mass window and two side bands (See Figure 1.1).

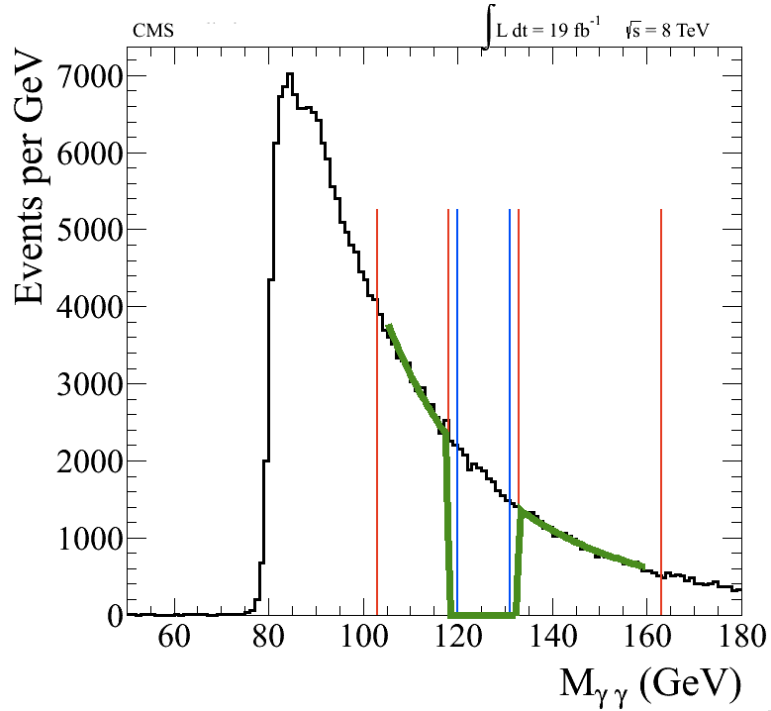


Figure 1.1: Example diphoton mass spectrum. The upper and lower sidebands are bounded by the red lines. The Higgs mass window (signal region) is bounded by blue lines. An power law fit function which ignores the signal region is shown in green.

The shapes of any kinematic distribution of interest (other than $M_{\gamma\gamma}$ can then be taken from events in the two sidebands. The normalization is then taken from a functional fit to the diphoton mass spectrum is fit to a function with the fitter ignoring the Higgs mass window. A simple power law $N = A * M_{\gamma\gamma}^b$ is typically a good choice for the fit function and is motivated by the composition of the continuous background.

The first search approached is a search for stop pair production. Stops are strongly produced,

resulting in relatively large cross sections. (Cross sections up to 19 pb were considered). We assume that these decay by way of a b-quark (or a top which then decays to a b) to particles in the Higgsino compressed spectrum. Particles in the compressed spectrum then promptly decay to each other through a very off-shell W. The W produces very soft particles which do not pass object selection requirements. The neutralinos and charginos are assumed to be in the Higgsino limit and decay predominantly to Higgs bosons. Higgsinos will also be pair produced under this model. In either case, two Higgs bosons are produced in the final state. And two additional b-jets may emerge from stop decays. Figure 2.6 shows Feynman diagrams for these processes.

In the stop search, one Higgs boson is required to decay to two photons. The other Higgs may decay to $b\bar{b}$, so there may be a b-jet resonance as well. Up to four b-jets may be produced, but in the case of four $cPqbs$ at least one will probably be missed by the b-tagging algorithm. The search is divided into three channels:

- $H(\gamma\gamma)$ with 3 or more b-jets.
- $H(\gamma\gamma)$ with exactly 2 b-jets consistent with a second Higgs decay.
- $H(\gamma\gamma)$ with exactly 2 b-jets not consistent with a second Higgs decay.

The first (3b) channel targets the case where two Higgs are produced from stop production, one decays to $\gamma\gamma$ and the other decays to $b\bar{b}$, and there are extra b-jets from the stop decays. The second channel (resonant 2b) targets the case where two Higgs are produced, either from stop decay with both b-jets from stops mis-tagged as light flavor jets, or from Higgsino decay where there are no extra b-jets. And the third channel (non-resonant 2b) targets the cases where either stops decay and the second Higgs does not decay to $b\bar{b}$, or where the resonant $b\bar{b}$ is mis-measured and appears off-resonance, or where stops decay and one or both bs from a Higgs are mis-tagged as light flavor. These channels are not very tuned to the kinematics of stop production and can be reapplied to any new physics signal producing a Higgs boson and multiple b-jets.

After these channels are selected, E_T^{miss} is examined as a discriminating variable. Signal accumulates at modestly large E_T^{miss} (~ 100 GeV), although still low enough to evade other large E_T^{miss}

searches.

Theoretical expected limits were made for this general type of search before experimental work began. Figure 1.2 shows these expected limits along with the existing limits from previous searches. The results of the search presented here (Figure 9.12) significantly improve upon this expected limit.

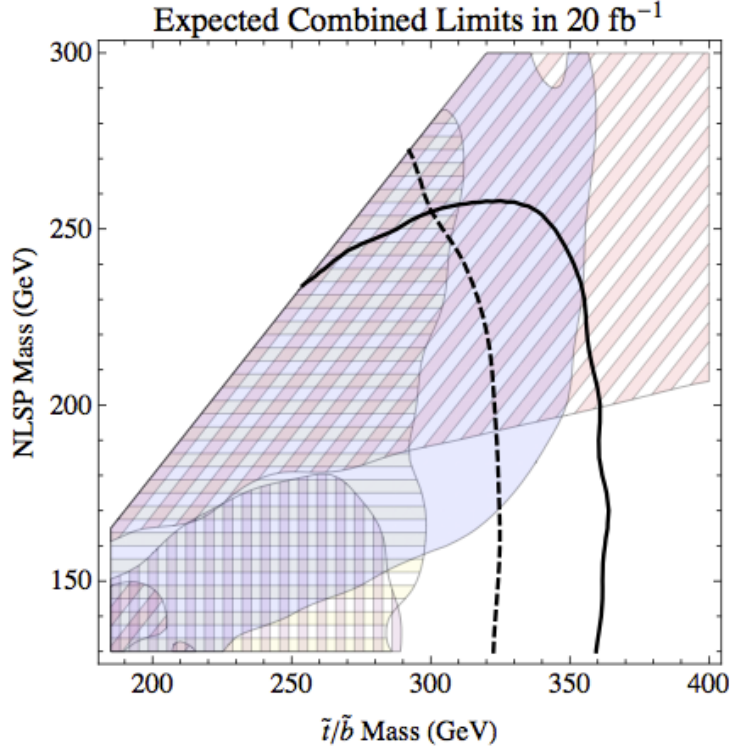


Figure 1.2: A priori expected 95% exclusions in 20 fb^{-1} at 8 TeV for a simplified search for stop quark production in $H \rightarrow \gamma\gamma + 2b$ (Solid black line). The shaded regions are excluded by other searches: the CMS 8 TeV $3b + \text{MET}$ search (diagonal hatching) (5), the CMS 7 TeV multilepton search (horizontal hatching) (24), the CMS 8 TeV same-sign dilepton + $2b$ search (vertical hatching) (45), and the CMS 8 TeV $\gamma\gamma + E_T^{\text{miss}}$ search (solid colored) (44). The dashed line is the expected limit for a $H \rightarrow \gamma\gamma + 1 cPqb\text{-jet}$ search. The implemented search significantly improves on this bound. Reprinted from (52).

A simpler model is that where stops are at inaccessible masses but light Higgsino-like neutralinos and charginos are still produced. This process can produce similar signals to the stop production and is a necessary secondary process in stop production under this model.

The search for Higgsinos relaxes the assumption that Higgsinos decay entirely to $H\tilde{G}$ is relaxed to consider decay to both $H\tilde{G}$ and $Z\tilde{G}$. For simplicity, this is implemented as separate searches for pure $\tilde{\chi}_1^0\tilde{\chi}_1^0 \rightarrow HH$, $\tilde{\chi}_1^0\tilde{\chi}_1^0 \rightarrow ZH$, and $\tilde{\chi}_1^0\tilde{\chi}_1^0 \rightarrow ZZ$. Figure 2.9 shows Feynman diagrams for these

processes. At the end, these results from each of these options will be combined to set a limit in terms of both the $\tilde{\chi}_1^0$ mass and its branching ratio.

However, electroweak production cross of Higgsinos is at best an order of magnitude smaller than optimistic strong production scenarios. This motivates a more comprehensive search strategy.

Both H and Z have multiple decay channels, making this a very complex and multifaceted search. The results of several different CMS analyses are combined in order to span the various final states of a Higgsino signal and in this way maximize sensitivity. To illustrate the complexity of this combined search, the Mondrian tables in Figure 1.3 shows the decay channels of HH, ZH, and ZZ decays with area roughly proportional the branching fraction. Note that the branching fractions of the $H \rightarrow \gamma\gamma$ decay and $ZZ \rightarrow leptons$ are exaggerated to make them legible. The various colors represent different new physics searches within the CMS collaboration that are sensitive to that decay channel and whose results are combined together in reference (54). The yellow and pink are the photon channels described in this work. In most cases the white space in these diagrams is overwhelmed by hadronic background events.

This work presents the components of the combined Higgsino search that involve $H \rightarrow \gamma\gamma$. These channels are meant to be taken in combination with searches in other decay channels other channels and are not particularly sensitive on their own. There are four tightly interlocking diphoton channels

- A 2b-jet channel that is a strict subset of the resonant 2b channel in the stop search
- A $H \rightarrow \gamma\gamma + \text{electron}$ channel
- A $H \rightarrow \gamma\gamma + \text{muon}$ channel
- An electroweak channel which searches for $H \rightarrow \gamma\gamma$ and a W or Z decaying hadronically.

The flow chart in Figure 1.4 shows the division between these channels. The $H \rightarrow \gamma\gamma + \text{electron}$ and $H \rightarrow \gamma\gamma + \text{muon}$ channels together are called the lepton channels. And the 2b and electroweak channels together are called the hadronic channels.

I analyzed the 2b and electroweak channels and my close collaborator David Morse analyzed the lepton channels. The all selection criteria and methods were carefully synchronized between the

lepton and hadronic channels. I present David's work on the lepton channels along side my work on the hadronic because the searches are so tightly interlocking and use identical methods.

As shown on the Mondrian plots (Fig 1.3), there are several other analyses produced by other CMS analyses in fairly close collaboration. I greatly doubt I could even name all the people I have to thank for this work. I will not describe these analyses here. Reference (54) describes them and the process of combining. Section 9.5 discusses the results of combining the photon channels with these other analyses. The plots in section 9.5 are the work of Patrick Zywicki.

The Higgsino electroweak channels are also reinterpreted in terms of a completely different model where the neutralino is wino-like. Then one neutralino is produced together with a chargino resulting in one W and one Higgs boson in the final state. This is the WH final state. The photon component of the WH search is combined with other analyses for a combined search, discussed in (3; 10).

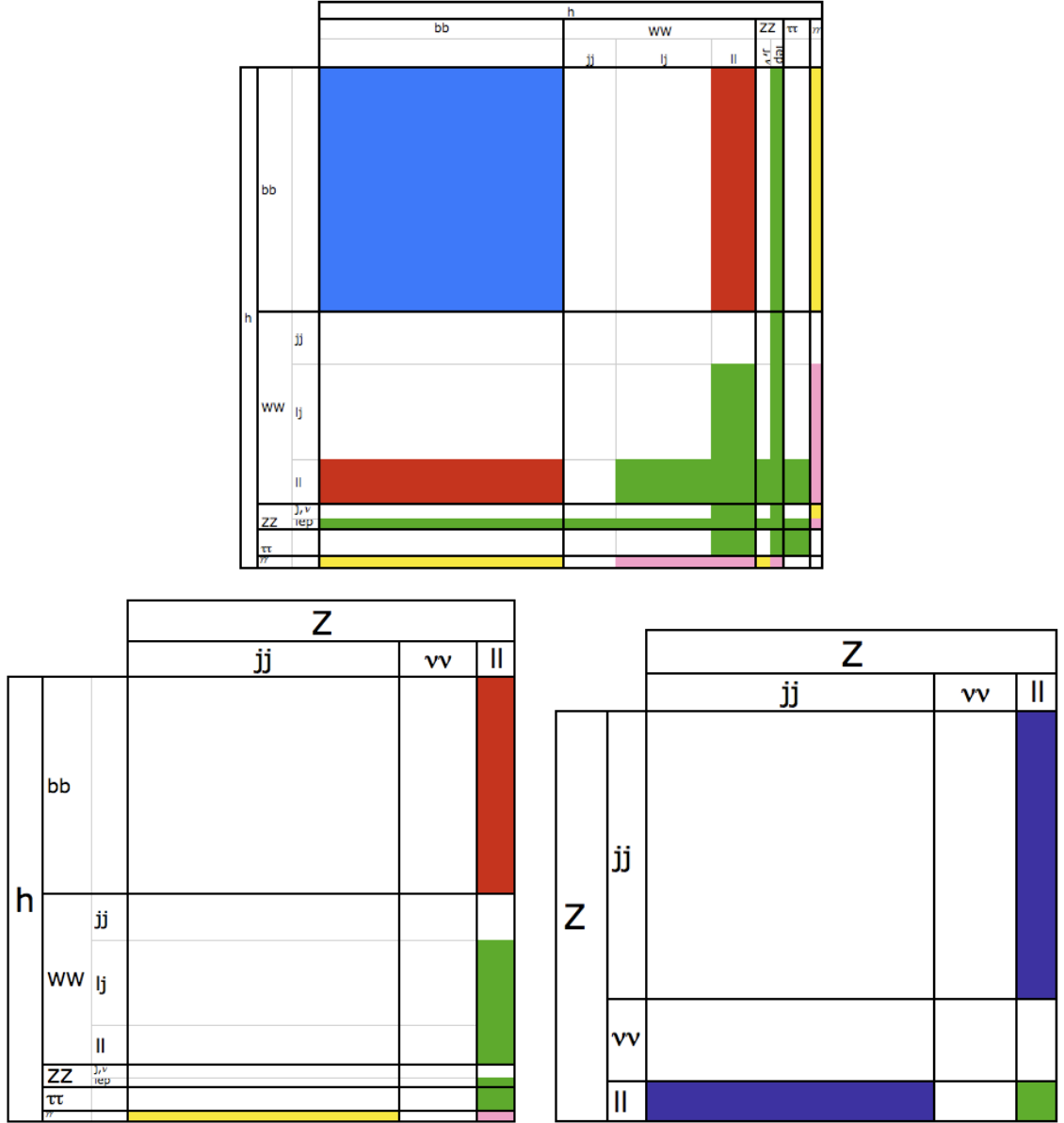


Figure 1.3: Mondrian tables for the decay of two Higgs bosons (top), one Higgs boson and one Z (bottom left) and two Z bosons (bottom right). The area of each rectangle is proportional to the branching fraction.

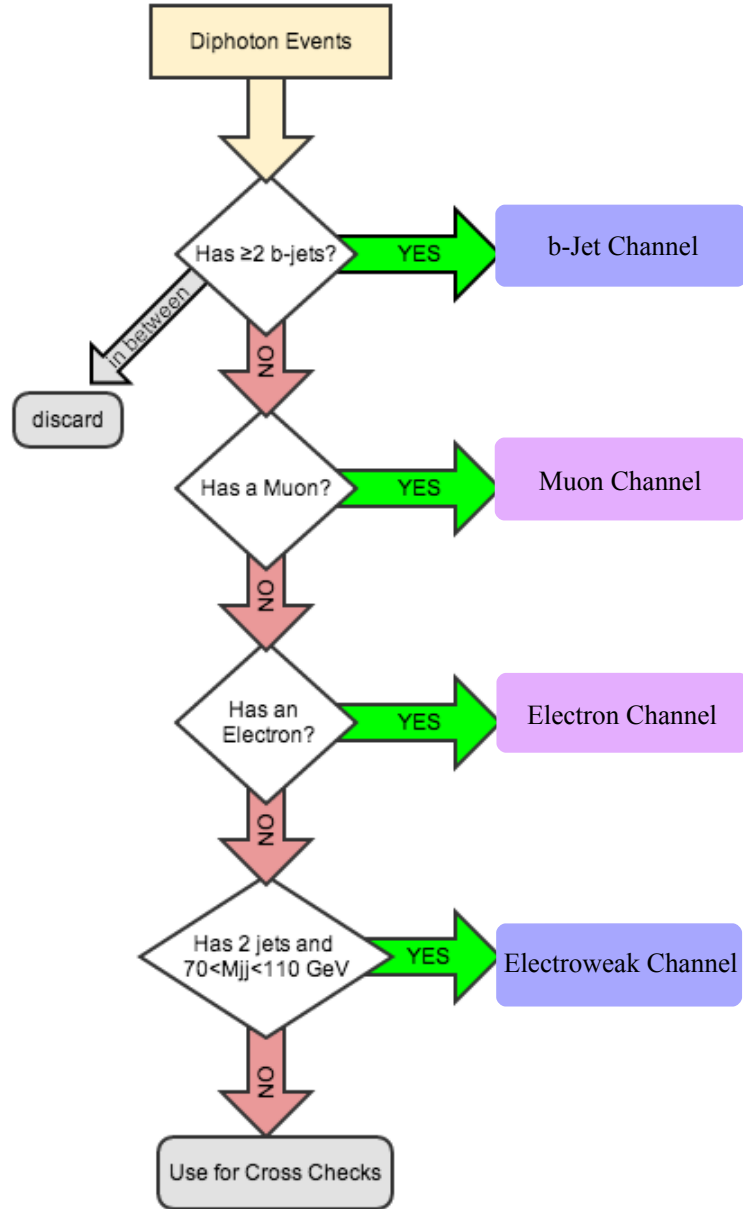


Figure 1.4: Diphoton events may fall into one of four categories divided between four analyses. To pass the 2 b-jet requirement, both b-jets must pass CSV-Medium or better. While failing events may have at most two CSV-Loose jets, at most one of which CSV-Medium b-jet. This creates a gap in the b-jet selection that prevents variations in b-jet tagging efficiency from transferring events from one category to another. Events falling into this gap are discarded.

Chapter 2

Theory

2.1 Brief Overview of the Standard Model Physics

2.1.1 The Standard Model

The Standard Model of particle physics accommodates all phenomenon all particles and forces directly observed to date, with the notable exception of neutrino masses.

Matter particles are described as spin- $\frac{1}{2}$ Dirac fermions which obey Fermi-Dirac statistics. For each of these there is an additional anti-particle. Matter particles are organized into three generations and four families shown in Figure 2.1. Higher generations correspond to increasing mass, at least among the quarks and charged leptons. There are six “flavors” of quarks arranged in three generations. Also, there are six leptons; three charged leptons and three neutrinos. Quarks and leptons interact with each other through the gauge fields associated with gauge bosons.

Centrally, the three gauge fields obey the symmetry:

$$SU(3)_{QCD} \times SU(2)_L \times U(1)_Y$$

In segments, these are the strong nuclear force ($SU(3)_{QCD}$) and the electroweak forces which emerge from the breaking of $SU(2)_L \times U(1)_Y$. The strong nuclear force is mediated by eight gluons. After electroweak symmetry breaking, these appear as three massive bosons: the W^\pm and Z , as well as a massless photon. The photon retains a $U(1)$ symmetry.

| Three Generations of Matter (Fermions) | | | | |
|---|---|---|--|---|
| | I | II | III | |
| mass→ | 2.4 MeV | 1.27 GeV | 171.2 GeV | 0 |
| charge→ | $\frac{2}{3}$ | $\frac{2}{3}$ | $\frac{2}{3}$ | 0 |
| spin→ | $\frac{1}{2}$ | $\frac{1}{2}$ | $\frac{1}{2}$ | 1 |
| name→ | u up | c charm | t top | γ photon |
| Quarks | 4.8 MeV $-\frac{1}{3}$ $\frac{1}{2}$ d down | 104 MeV $-\frac{1}{3}$ $\frac{1}{2}$ s strange | 4.2 GeV $-\frac{1}{3}$ $\frac{1}{2}$ b bottom | 0 0 1 g gluon |
| | <2.2 eV 0 $\frac{1}{2}$ ν_e electron neutrino | <0.17 MeV 0 $\frac{1}{2}$ ν_μ muon neutrino | <15.5 MeV 0 $\frac{1}{2}$ ν_τ tau neutrino | 91.2 GeV 0 1 Z⁰ weak force |
| | 0.511 MeV -1 $\frac{1}{2}$ e electron | 105.7 MeV -1 $\frac{1}{2}$ μ muon | 1.777 GeV -1 $\frac{1}{2}$ τ tau | 80.4 GeV ± 1 1 W[±] weak force |
| Leptons | | | | Bosons (Forces) |

Figure 2.1: The particles of the standard model.

2.1.2 Standard Model Lagrangian

$$\begin{aligned}
\mathcal{L} = & -\frac{1}{4}B_{\mu\nu}B^{\mu\nu} - \frac{1}{8}\text{Tr}(\mathbf{W}_{\mu\nu}\mathbf{W}^{\mu\nu}) - \frac{1}{2}\text{Tr}(\mathbf{G}_{\mu\nu}\mathbf{G}^{\mu\nu}) \\
& + \begin{pmatrix} \nu_L^\dagger & e_L^\dagger \end{pmatrix} \sigma_\mu i D_\mu \begin{pmatrix} \nu_L \\ e_L \end{pmatrix} + e_R^\dagger \sigma^\mu i D_\mu e_R + \nu_R^\dagger \sigma^\mu i D_\mu \nu_R \\
& + \begin{pmatrix} u_L^\dagger & d_L^\dagger \end{pmatrix} \sigma_\mu i D_\mu \begin{pmatrix} u_L \\ d_L \end{pmatrix} + u_R^\dagger \sigma^\mu i D_\mu u_R + d_R^\dagger \sigma^\mu i D_\mu d_R + (h.c.) \\
& - \frac{\sqrt{2}}{v} \left[\begin{pmatrix} \nu_L^\dagger & e_L^\dagger \end{pmatrix} \phi Y^e e_R + \begin{pmatrix} -e_L^\dagger & \nu_L^\dagger \end{pmatrix} \phi Y^\nu \nu_R + (h.c.) \right] \\
& - \frac{\sqrt{2}}{v} \left[\begin{pmatrix} u_L^\dagger & d_L^\dagger \end{pmatrix} \phi Y^d d_R + \begin{pmatrix} -d_L^\dagger & u_L^\dagger \end{pmatrix} \phi Y^u u_R + (h.c.) \right] \\
& + (D_\mu \phi)^\dagger D_\mu \phi - m_h^2 [\phi^\dagger \phi - v^2/2]^2 / 2v^2
\end{aligned}$$

The first line holds the gauge terms. The next two lines hold the lepton and quark dynamical terms respectively. Lines 4 and 5 hold the lepton and quark Yukawa mass terms. Then the last line holds the higgs dynamical and mass terms. h.c. indicates the Hermitian conjugate of the preceding term (46). ϕ is the higgs field doublet. v is the Higgs field's vacuum expectation value, $v = 246 \text{ GeV}$ (63). Each of e , ν , u , d represent a trio of fields with implicit generation indices that contract with the Y mass matrices, as well as implicit 2-component indices that contract with the Pauli- σ matrices. The quarks also have an implicit 3-component index that contracts with \mathbf{G}_μ .

$D_\mu = \partial + ig_1(\frac{1}{2}Y_w)B_\mu + ig_2T_w\mathbf{W}_\mu + ig_3(3B)G_\mu$ where Y_w , T_w , and B are the weak hypercharge, weak isospin, and baryon number for each particle, which are listed in Table 2.1.

T_{3w} is the third component of isospin, which serves to distinguish the two fields in weak doublets. Q is the electrical charge; $Q = \frac{1}{2}Y_w + T_{w3}$.

Table 2.1: Properties for fields.

| | $\frac{1}{2}Y_w$ | T_w | T_{w3} | Q | $3B$ |
|---------|------------------|---------------|------------------|----------------|------|
| ν_L | $-\frac{1}{2}$ | $\frac{1}{2}$ | $\frac{1}{2}$ | 0 | 0 |
| e_L | $-\frac{1}{2}$ | $\frac{1}{2}$ | $-\frac{1}{2}$ | -1 | 0 |
| ν_R | 0 | 0 | 0 | 0 | 0 |
| e_R | -1 | 0 | 0 | -1 | 0 |
| u_L | $\frac{1}{6}$ | $\frac{1}{2}$ | $\frac{1}{2}$ | $\frac{2}{3}$ | 1 |
| d_L | $\frac{1}{6}$ | $\frac{1}{2}$ | $-\frac{1}{2}$ | $-\frac{1}{3}$ | 1 |
| u_R | $\frac{2}{3}$ | 0 | 0 | $\frac{2}{3}$ | 1 |
| d_R | $-\frac{1}{3}$ | 0 | 0 | $-\frac{1}{3}$ | 1 |
| ϕ | $\frac{1}{2}$ | $\frac{1}{2}$ | $\pm\frac{1}{2}$ | 0 | 0 |

The field tensors in the gauge terms are related to the gauge boson vector potentials by:

$$B_{\mu\nu} = \partial_\mu B_\nu - \partial_\nu B_\mu$$

$$\mathbf{W}_{\mu\nu} = \partial_\mu \mathbf{W}_\nu - \partial_\nu \mathbf{W}_\mu + i\frac{1}{2}g_2(\mathbf{W}_\mu \mathbf{W}_\nu - \mathbf{W}_\nu \mathbf{W}_\mu)$$

$$\mathbf{G}_{\mu\nu} = \partial_\mu \mathbf{G}_\nu - \partial_\nu \mathbf{G}_\mu + i\frac{1}{2}g_2(\mathbf{G}_\mu \mathbf{G}_\nu - \mathbf{G}_\nu \mathbf{G}_\mu)$$

The gauge boson vector field \mathbf{W}_μ , and \mathbf{G}_μ are 2x2 and 3x3 respectively traceless Hermitian matrices, while B_μ are scalar (46).

\mathbf{W}_μ is a 2x2 component matrix with $W_{11\mu} = -W_{22\mu}$ and $W_{12\mu} = -W_{21\mu}^*$.

2.1.3 CKM Matrix

Quark masses and mixings arise from the Yukawa interactions with the Higgs field (46).

$$\mathcal{L}_Y = -\frac{\sqrt{2}}{g} \left[\begin{pmatrix} u_{Li}^\dagger & d_{Li}^\dagger \end{pmatrix} \phi Y_{ij}^d d_{Rj} + \begin{pmatrix} -d_{Li}^\dagger & u_{Li}^\dagger \end{pmatrix} \phi^* Y_{ij}^u u_{Rj} \right] + h.c.$$

where i,j label the three generations. u_{Li} and d_{Li} are the wave functions of the left handed up and down type quarks of the i^{th} generation in the weak-eigenstate basis, together making a doublet. u_{Ri} and d_{Ri} are the corresponding quark singlets. ϕ is the higgs field. Y^u and Y^d are two 3x3 complex matrices that can be diagonalized using four unitary matrices $U_R^u, U_L^u, U_R^d, U_L^d$:

$$Y^u = U_L^{u\dagger} M^u U_R^u, \quad Y^d = U_L^{d\dagger} M^d U_R^d$$

where the M matrices are diagonal and contain the quark masses (63).

$$M^u = \begin{pmatrix} m_u & 0 & 0 \\ 0 & m_c & 0 \\ 0 & 0 & m_t \end{pmatrix}, M^d = \begin{pmatrix} m_d & 0 & 0 \\ 0 & m_s & 0 \\ 0 & 0 & m_b \end{pmatrix}$$

Observed fermions with definite masses (mass eigenstates) are linear combinations of the weak eigenstates that participate in weak interactions in the Lagrangian. The U matrices perform the linear transformation between weak eigenstates (u, d) and mass eigenstates (u', d')(63).

$$u_i'^L = U_{Lij}^u u_j^L,$$

$$u_i'^R = U_{Rij}^u u_j^R,$$

$$d_i'^L = U_{Lij}^d d_j^L,$$

$$d_i'^R = U_{Rij}^d d_j^R.$$

When the Lagrangian is written in the mass eigenbasis (in terms of physical particles u' and d'), all the Us vanish except (63)

$$\begin{pmatrix} u_L'^\dagger & c_L'^\dagger & t_L'^\dagger \end{pmatrix} \gamma^\mu W_\mu^+ V_{CKM} \begin{pmatrix} d_L' \\ s_L' \\ b_L' \end{pmatrix} + h.c.$$

Here u and d now indicate the specific fields for the left handed up and down quarks, not the trio of up or down type quarks. $V_{CKM} = U_L^u U_L^{d\dagger}$ is the 3x3 Cabibbo-Kobayashi-Maskawa (CKM) matrix. The CKM can be interpreted as rotation quark mass eigenstates (primed) into weak eigenstates (unprimed)

$$\begin{pmatrix} d \\ s \\ b \end{pmatrix} = \begin{pmatrix} V_{ud} & V_{us} & V_{ub} \\ V_{cd} & V_{cs} & V_{cb} \\ V_{td} & V_{ts} & V_{tb} \end{pmatrix} \begin{pmatrix} d' \\ s' \\ b' \end{pmatrix}$$

A similar expression can be written in terms of the up-type quarks and the CKM matrix. Exactly the same structure exists for leptons, with a different analogue of the CKM matrix called the PMNS matrix.

There's a constraint of weak universality which requires that each row and column of the CKM matrix must sum to 1. The CKM matrix has four free parameters which are fundamental parameters

of the standard model. The four parameters can be expressed as three Euler angles and one CP-violating phase, or equivalently as four Wolfenstein parameters.

$$V_{CKM} = \begin{pmatrix} 1 - \lambda^2/2 & \lambda & A\lambda^3(\rho - i\eta) \\ -\lambda & 1 - \lambda^2/2 & A\lambda^2 \\ A\lambda^3(\rho - i\eta) & -A\lambda^2 & 1 \end{pmatrix} + O(\lambda^4)$$

where:

$$\lambda = 0.2257^{+0.0009}_{-0.0010}, A = 0.814^{+0.021}_{-0.022}, \rho = 0.135^{+0.031}_{-0.016}, \text{ and } \eta = 0.349^{+0.015}_{-0.017} \quad (63).$$

$$|V_{cb}| = (41.1 \pm 1.3) \times 10^{-3} \quad (63)$$

The CKM matrix is nearly diagonal, which is largely responsible for the long lifetime of b-hadrons. b-quarks are only able to decay by way of a W boson, but couple most strongly to the top quark. Decay through a top quark is kinematically forbidden due to the large mass of the top quark. b-hadron lifetimes are approximately proportional to $|V_{cb}|^{-2}$, so the small value of $|V_{cb}|$ contributes to the long lifetime of b-hadrons and the resulting tendency for b-hadrons to produce displaced vertices. Displaced vertices are a key factor in identifying b-jets.

2.1.4 Electroweak Bosons

The four electroweak bosons are the W^\pm , Z, and γ . There are many fascinating details of how the electroweak symmetry $SU(2)_L \times U(1)_Y$ breaks through the Higgs mechanism into three massive bosons and one massless $U(1)$ photon. But for the purposes of this discussion we only need to know the masses and decay behavior of the electroweak bosons. It may be worth mentioning that the weak force breaks parity and interacts with left and right chirality fermions differently. As a result, fermions come in left-handed doublets and right-handed singlet states with no right handed neutrinos.

The electroweak boson fields are composed of \mathbf{W} and B :

$$\begin{pmatrix} A_\mu \\ Z_\mu \end{pmatrix} = \begin{pmatrix} \sin \theta_w & \cos \theta_w \\ \cos \theta_w & -\sin \theta_w \end{pmatrix} \begin{pmatrix} W_{11\mu} \\ B_\mu \end{pmatrix}$$

$$W_\mu^+ = W_\mu^{-*} = W_{12\mu}/\sqrt{2}$$

θ_w is the Weinberg angle, defined as $\cos \theta_w = \frac{m_W}{m_Z}$. It relates the electroweak coupling constants

$g_1 = q_e / \cos \theta_w$, $g_2 = q_e / \sin \theta_w$ with $q_e = \sqrt{4\pi\alpha\hbar c}$ being the elementary electric charge.

Then the electroweak gauge terms can be rewritten:

$$-\frac{1}{4}B_{\mu\nu}B^{\mu\nu} - \frac{1}{8}\text{Tr}(\mathbf{W}_{\mu\nu}\mathbf{W}^{\mu\nu}) = -\frac{1}{4}A_{\mu\nu}A^{\mu\nu} - \frac{1}{4}Z_{\mu\nu}Z^{\mu\nu} - \frac{1}{2}W_{\mu\nu}^-W^{+\mu\nu} + \dots$$

W boson mass $80.385 \pm 0.015 \text{ GeV}/c^2$, with a decay width of $2.085 \pm 0.042 \text{ GeV}/c^2$ (63). The main decay modes of the W boson are shown in Table 2.2. Z boson mass $91.1876 \pm 0.0021 \text{ GeV}/c^2$, with a decay width of $2.4952 \pm 0.0023 \text{ GeV}/c^2$ (63). The main decay modes of the Z boson are shown in Table 2.3.

Table 2.2: W boson major decay modes and branching ratios. The c+X decay channel is contained within the hadronic decay channel. Reprinted from (63).

| Decay Channel | Branching Ratio (%) |
|---------------------------------|---------------------|
| $W \rightarrow e\nu$ | 10.71 ± 0.16 |
| $W \rightarrow \mu\nu$ | 10.63 ± 0.15 |
| $W \rightarrow \tau\nu$ | 11.38 ± 0.21 |
| $W \rightarrow \text{hadronic}$ | 67.41 ± 0.27 |
| $W \rightarrow c+X$ | 33.3 ± 2.6 |

Table 2.3: Z boson major decay modes and branching ratios. Reprinted from (63).

| Decay Channel | Branching Ratio |
|---------------------------------|-------------------|
| $Z \rightarrow e^+e^-$ | 3.363 ± 0.004 |
| $Z \rightarrow \mu^+\mu^-$ | 3.366 ± 0.007 |
| $Z \rightarrow \tau^+\tau^-$ | 3.370 ± 0.008 |
| $Z \rightarrow \nu\nu$ | 20.00 ± 0.06 |
| $Z \rightarrow \text{hadronic}$ | 69.91 ± 0.06 |

The photon is a stable massless spin-1 boson which obeys a $U(1)$ symmetry and conveys electromagnetism.

2.1.5 Quarks and Leptons

Quarks and leptons are the matter fermions of the standard model. They can be expressed as chiral doublets such as $(e_L \ e_R)$ or as weak doublets and singlets as in $(\nu_L \ e_L)$, e_R , ν_R . Table 2.1 lists their properties.

Leptons do not interact through the strong nuclear force, which makes them relatively rare

objects in collider physics.

The electron (e) is stable while the muon (μ) is sufficiently long-lived ($t_{\frac{1}{2}} = 2.2 \mu s$) to be effectively stable on the distance scales of collider physics. Electrons and muons differ in their mass but otherwise share the same quantum numbers. Their difference in mass is sufficient to produce a strong difference in their ability to penetrate matter. The tau (τ) decays promptly to either semi-leptonically or fully hadronically. This makes the tau more difficult to identify and use in new physics searches.

The neutrinos are nearly massless and interact only through the weak nuclear force. They are fantastically difficult to observe since they are able to pass through vast amounts of material without interacting. Typically neutrinos escape the detector and their presence can only be inferred from missing transverse energy.

Quarks interact via the strong nuclear force, and may also interact through electromagnetism and through the weak nuclear force. Quarks are never found individually due to color confinement. They are always bound into hadrons with two or three valence quarks. The exception is the top quark which is so short-lived that it does not have time to hadronize. Instead it promptly decays to a W and b-quark.

Quarks radiating from an energetic interaction cannot remain as free particles and spontaneously dress themselves with other quarks. This turns the an energetic lone quark into a spray of hadrons called a hadronic jet or just a jet.

The decay patterns of bottom and charm quarks produce somewhat distinctive patterns in hadronic jet substructure that can be identified. Bottom quarks spawn b-jets, which have several distinctive features that aid in identification: First, b-hadrons tend to have relatively long lifetimes (1.5 ps) which tend to produce displaced secondary vertices, which can be seen in detectors. b-hadrons also have a relatively hard fragmentation function, meaning that the b-hadrons containing the original b-quark tends to receive a large fraction of the energy of that b-quark (6) (observed as the total jet energy). Also, b-jets may contain soft leptons.

2.1.6 Higgs Boson and Higgs Physics

The Higgs boson (H) was the last piece of the standard model to be discovered. Its discovery in 2012 was central to allowing this work to take place and opened associated Higgs production as a novel direction of study. The Higgs is a fundamental scalar particle with zero spin and even parity. The Higgs field takes a non-zero vacuum expectation, pervading all space and endowing mass to all other massive fundamental particles through its interactions. The theory underlying the standard model Higgs boson has only one free parameter: the mass of the Higgs boson. It is not yet known whether the Higgs boson discovered in 2012 is precisely the standard model Higgs boson, but all observations thus far are consistent with it being the standard model Higgs boson. Currently the best estimates of the Higgs boson mass are:

- CMS Result: $125.03^{+0.26}_{-0.27} \text{ (stat)}^{+0.13}_{-0.15} \text{ (syst)} \text{ GeV}/c^2$
- ATLAS result: $125.36 \pm 0.37 \text{ (stat)} \pm 0.18 \text{ (syst)} \text{ GeV}/c^2$

At the time this work was done the best estimate of the Higgs boson mass was a little less precise. As a result, the Higgs cross sections and branching ratios used will differ slightly (around 1%) from the most up to date values. These differences are accounted for and described in Section 8.5.

The Higgs mechanism allows the W and Z bosons to have mass; massive gauge fields are not possible without a Higgs mechanisms. The Lagrangian for a massive gauge field without a Higgs mechanism is:

$$\mathcal{L} = -\frac{1}{4}F_{\mu\nu}F^{\mu\nu} + \frac{1}{2}m^2A_\mu A^\mu$$

Applying the gauge transform

$$A_\mu(x, t) \rightarrow A'_\mu(x, t) + \epsilon\partial_\mu\theta$$

produced

$$\mathcal{L} = -\frac{1}{4}F'_{\mu\nu}F'^{\mu\nu} + \frac{1}{2}m^2(A'_\mu + \epsilon\partial_\mu\theta)^2$$

If instead, the Lagrangian includes a Higgs mechanism with the form:

$$\mathcal{L} = -\frac{1}{4}F_{\mu\nu}F^{\mu\nu} + \frac{1}{2}m^2A_\mu A^\mu + \frac{1}{2}(\partial_\mu\phi)^2 - mA_\mu\partial^\mu\phi = -\frac{1}{4}F_{\mu\nu}F^{\mu\nu} + \frac{1}{2}m^2(A_\mu - \frac{1}{m}\partial^\mu\phi)^2$$

And then transform both A_μ and $\phi \rightarrow \phi' + \epsilon m\theta$, the transformed Lagrangian remains invariant.

$$\mathcal{L} - \frac{1}{4}F'_{\mu\nu}F'^{\mu\nu} + \frac{1}{2}m^2(A'_\mu - \frac{1}{m}\partial^\mu\phi')^2$$

The Higgs can decay into a broad variety of particles. Selected branching ratios that were used in this analysis are listed in Table 2.4. The most frequent decay channels of the Higgs, such as $H \rightarrow b\bar{b}$, are also the hardest to see without greatly reducing the hadronic background noise processes. While the Higgs is more easily seen in rare decay channels $H \rightarrow \gamma\gamma$ and $H \rightarrow ZZ \rightarrow 4$ leptons. All the analyses in this work require two photons consistent with a Higgs decay by requiring a diphoton mass near $125 \text{ GeV}/c^2$. This suffers the tiny $H \rightarrow \gamma\gamma$ branching ratio but greatly reduces the background. Higgs signal lies in a narrow window of diphoton masses. This Higgs natural width is extremely narrow, only a few MeV. Currently this is too narrow to be measured but for our purposes the exact width does not matter; it's effectively zero. The width of a Higgs peak in the diphoton channel will be due virtually entirely to the precision with which photons can be reconstructed. The amount of background then depends strongly on how well the diphoton mass can be reconstructed, stemming from the photon energy resolution and good vertex identification.

A second Higgs boson in the event will most likely decay to $b\bar{b}$. This decay would be far easier to see than in single Higgs production due to the reduced background that the $H \rightarrow \gamma\gamma$ cut produces.

There are four standard model Higgs boson production processes of importance which are shown in Table 2.5 along with their cross sections in Table 2.6. By far the most important is gluon fusion. As a result, the standard model Higgs tends to be singly produced and thus makes the standard model Higgs a negligible background to most associated Higgs production searches.

Table 2.4: Selected Higgs branching ratios used.

| Decay Channel | Branching Ratio |
|--------------------------------|-----------------|
| $H \rightarrow b\bar{b}$ | 0.561 |
| $H \rightarrow W^+W^-$ | 0.231 |
| $H \rightarrow ZZ$ | 0.0289 |
| $H \rightarrow \tau\bar{\tau}$ | 0.0615 |
| $H \rightarrow \gamma\gamma$ | 0.00229 |

Table 2.5: Higgs boson production Feynman diagrams.

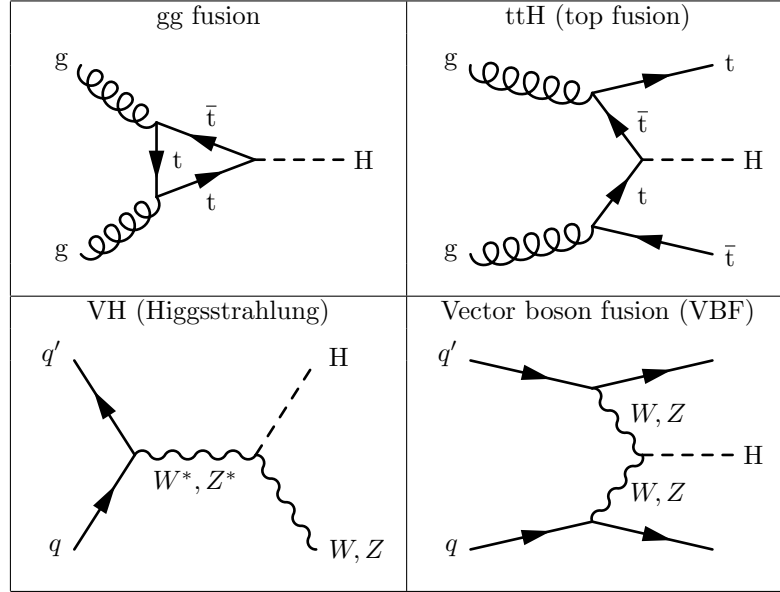


Table 2.6: Higgs boson production cross sections used.

| Higgs Production Channel | Cross section (pb) |
|---------------------------|--------------------|
| Gluon-gluon fusion | 19.56 |
| Vector boson fusion (VBF) | 1.559 |
| VH | 1.11 |
| ttH | 0.127 |

2.1.7 Proton-Proton Collisions at the LHC

When colliding beams of protons, the most likely outcome by far is that the protons miss each other completely. So instead of colliding protons one at a time, bunches of 10^{11} protons are aimed at each other. The likelihood of a collision goes as the square of the number of protons per bunch. Organizing protons into bunches also allows the records of proton collisions to be neatly organized into 25 ns time slices during which two bunches of protons crossed. Next, protons are most likely to have a glancing blow; elastically repelling each other slightly and vanishing down the beam pipe without a trace. The next most likely outcome is that the one of protons disintegrate as they interact and diffract through each other. Again, the remnants vanish down the beam pipe. So far, all of these interactions are invisible to the detector. The first most common interaction that the detector

encounters is scattering of soft partons.

Most people have heard that a proton consists of three quarks: two up quarks and a down quark, however protons are properly described in terms of their parton distribution functions. Three valence quarks are likely to carry a significant fraction of the proton's energy and give the proton most of its properties. But there are also a huge number of other quarks and gluons carrying a smaller fraction of the proton's energy. When colliding protons with other objects it is highly unlikely to hit one of the valence quarks, or even a parton carrying more than a few percent of the proton's energy. The likelihood of hitting a parton becomes increasingly likely with decreasing momentum fraction. Proton-proton collisions with a 8 TeV center of mass energy are highly unlikely to have partons collide with anything near 8 TeV. Instead this is a collision between constituents of the surrounding cloud of parton. Most of the partons with a momentum fraction below about 10% are gluons. So the LHC is primarily a gluon collider. In the mix there are also some anti-quarks.

Consequently, the vast majority of parton collisions between protons are between partons with really puny momentum fractions. These mostly produce very forward or very low energy hadronic showers (jets). Time slices where only this kind of fluff is produced are excluded from consideration by the CMS L1 hardware trigger. Only events with a hard interaction are ever considered, and even the vast majority of these are discarded as boring proton splatter.

The expectation value for number of inelastic proton interactions per bunch crossing is greater than one; the average is typically more like 20 and often up to 40. So when there finally is an interesting hard interaction there will also be several other very soft interactions throwing low energy hadronic fluff at the detector. These parasitic soft interactions are known as “pileup” interactions and the number of them per bunch crossing is also typically called “pileup” or “pileup number”.

While the complex substructure of the proton may seem to generate nothing but noise and headaches it also is the feature that makes proton collision a useful tool for exploration. Colliding protons at a particular energy effectively collides partons (mostly gluons) over a wide range of lower energies. The energy of the beam need not be scanned like in a lepton collider. Instead, the same experiment under the same conditions is repeated a large number of times to reveal rare phenomenon.

In addition, the diverse environment of the proton allows a broad variety of phenomenon to emerge that may or may not be allowed in collisions of two fermions. Gluon-gluon, gluon-quark, quark-quark, and quark-antiquark may all take place, with quarks taking a variety of flavors. These interactions may be accompanied by initial state and final state radiation of gluons jets or photons.

On the bright side, everything that can happen does happen if its cross section isn't too tiny. So most forms of new particles in this energy regime should be produced. On the down side, completely boring hadronic processes are dominant and sufficiently abundant to allow parton showers to fake most signals. New physics signals can only come in the form of a statistical excess above the hadronic background noise.

The hierarchy of physics processes generate at the LHC is shown in Figure 2.2. Detectable processes of interest with available luminosity may be up to 13 orders of magnitude less common than inelastic scatterings.

As an example, the Higgs boson decays two b quarks just over half the time, resulting in two b-jets. But pairs of b quarks from QCD interactions are also generated by proton collisions about 7 and a half orders of magnitude more often. The same goes for most of the Higgs bosons decay channels. This is why the Higgs was first discovered through its decay to diphoton, to which it decays 0.23% of the time, and to $2Z$ bosons which then decay to four leptons, which occurs 0.20% of the time. The hadronic background swamps the most likely production channels leaving only a couple clean but rare decay channels.

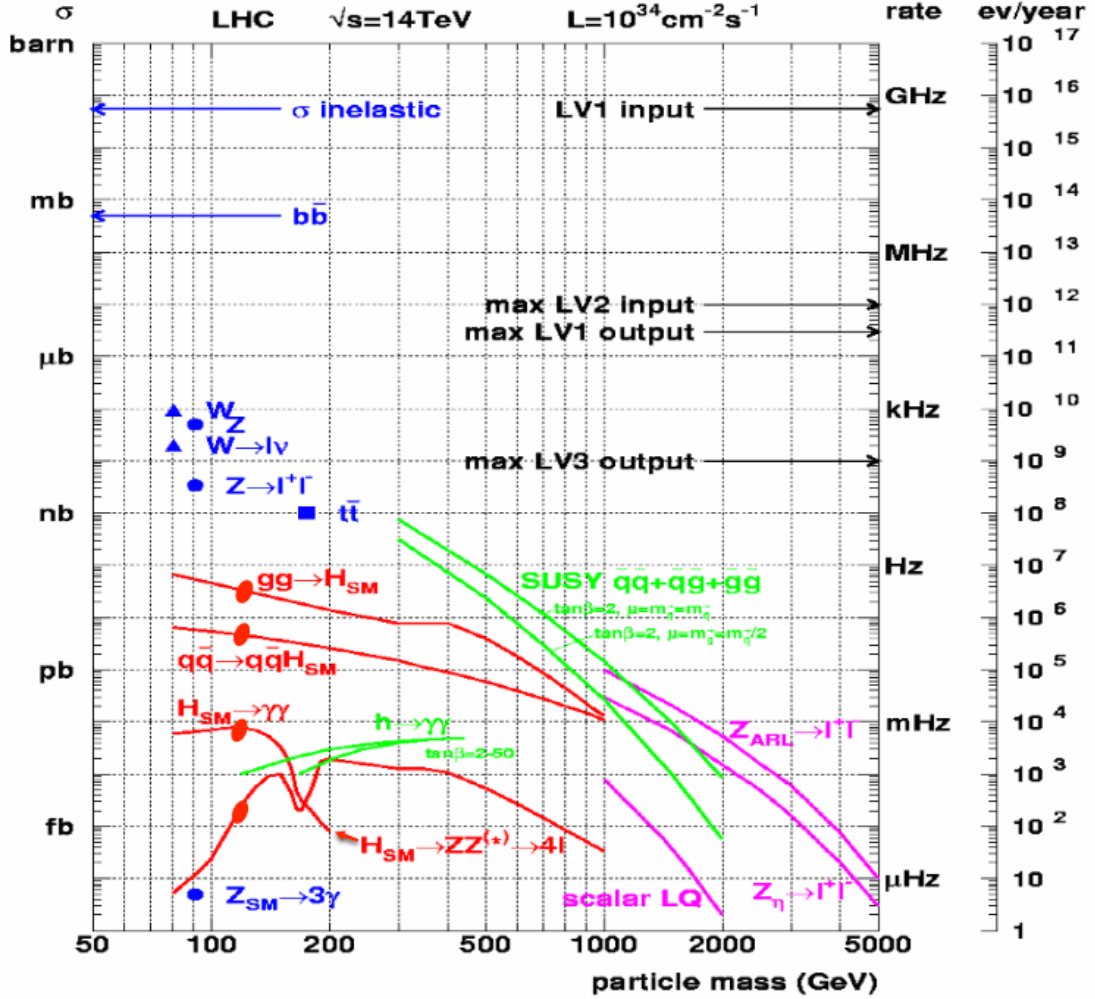


Figure 2.2: Cross sections and rates of various processes in the CMS.

2.1.8 Background Processes to Diphoton

The background to associated Higgs production comes in two important categories: continuous background and resonant background. The most obvious resonant background is standard model $H \rightarrow \gamma\gamma$, which produces a diphoton resonance in the search window. The Higgs cross section times branching ratio is already quite small. When additional rare objects are required the contribution from standard model Higgs production becomes completely negligible.

In addition, electrons from Z decays with both electrons faking photons will show up in the diphoton spectrum. This constrains the range the use diphoton mass side bands to use only $M_{\gamma\gamma}$ above the Z resonance.

The continuous background has an irreducible component from standard model diphoton production, as well as reducible components from $\gamma + \text{Jet}$ and QCD with jets faking photons. For our uses, the composition of the continuous background completely does not matter, but to satiate natural curiosity I'll briefly discuss it.

For standard model diphoton production, the lowest order production process is quark antiquark annihilation to two photons. However, the largest contribution is gluon fusion to diphotons(20). Even though this is higher order, it is compensated by the large fraction of gluons in the proton distribution function for small momentum fractions. The Feynman diagrams for gluon fusion are shown in Figure 2.3.

The irreducible component has a cross section of 210 fb/GeV at 14 TeV (20) and $M_{\gamma\gamma} \approx 125 \text{ GeV}/c^2$. This corresponds to about 60 fb/GeV at 8 TeV. Considering the diphoton efficiency seen in this analysis (0.47), we can expect the irreducible diphoton background to contribute about 25% of the background when no other objects are required.

In addition, we can expect significant contributions from $\gamma + \text{jet}$ with the jet faking a photon. Sample Feynman diagrams for this are shown in Figure 2.4. The cross section for gamma+jet is quite large: roughly $2 \times 10^5 \text{ fb/GeV}$ of p_T^γ around $p_T^\gamma = M_H/2$ (11). Even after the relatively small photon fake rate, this makes up a significant proportion to the continuous background.

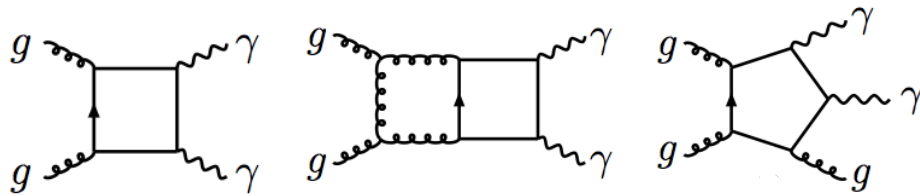


Figure 2.3: Feynman diagram of the gluon fusion contributing to Standard Model Diphoton production at leading order (left) and NLO (center and right). Reprinted from (20).

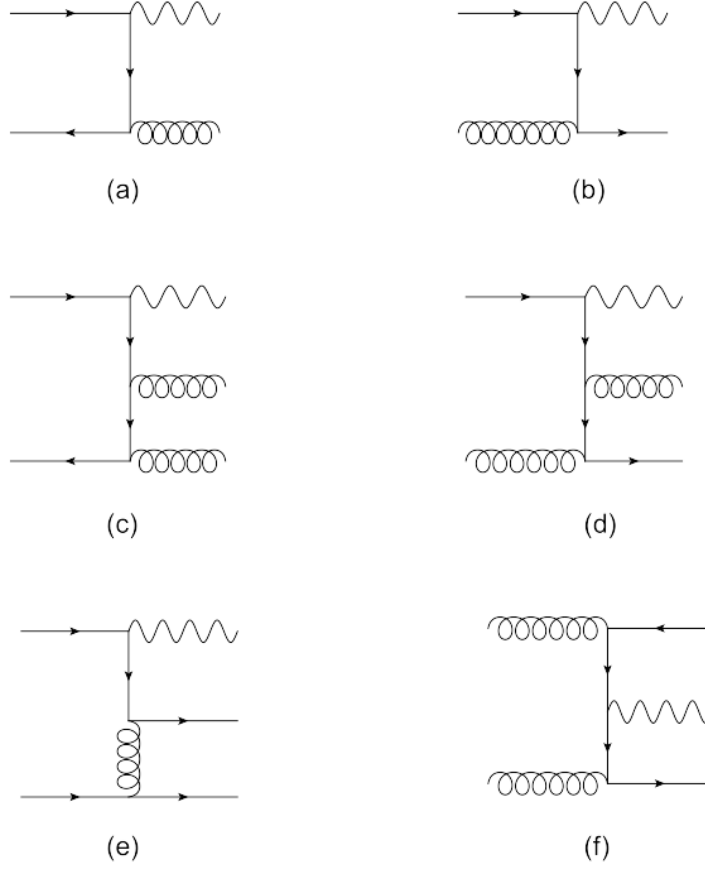


Figure 2.4: Sample Feynman diagrams for the production of $\gamma + \text{jets}$ background. Reprinted from (11).

2.2 SuperSymmetry

2.2.1 Introduction to Supersymmetry

Supersymmetry is perhaps the most promising and well motivated extension to the standard model. Countless papers on supersymmetry have been written, as well as many excellent introductions such as that by S.P. Martin (59). Here I will give a brief review of the relevant aspects of supersymmetry.

Supersymmetry is at heart a symmetry between bosons and fermions where for every fermion has a corresponding supersymmetric boson and vice versa. Specifically, the supersymmetric operator Q which acts on both fermion and boson states:

$$Q|Boson\rangle = |Fermion\rangle$$

$$Q|Fermion\rangle = |Boson\rangle$$

This immediately predicts a duplication of the complete spectrum of standard model particles. Clearly, this symmetry must be broken in such a way that these extra particles are too heavy to have been detected yet. The symmetry corresponds to an extra conserved quantum number called R-parity.

Where B is the baryon number, L is the lepton number, and s is the spin quantum number. All the particles and antiparticles of the standard model have $R=1$, including the standard model Higgs boson. R-parity may or may not be conserved. However if it is effectively conserved for the lightest super-partner, the LSP, then LSPs would be stable. This provides a natural dark matter candidate. Cosmological models indicate that the amount of dark matter observed in the universe could be produced by a new stable particle generated in the big bang, which decoupled from other standard model particles at about a TeV.

Higgs physics also demands some mechanisms for protecting the Higgs mass from large loop-order corrections due to any higher energy particles. Otherwise one would expect the mass of the Higgs, and consequently the mass of all other particles, to be on the order of the Planck scale. A Higgs at 125 GeV requires that new physics appear at about 1 TeV to prevent extreme and unnatural fine tuning. This coincidence of scales is known as the “WIMP miracle”, WIMP standing for weakly interacting massive particle. Supersymmetry (SUSY) has long offered an elegant solution to this hierarchy problem. Each supersymmetric particles cancel the loop order effects of standard model particles. This may indicate that either the LSP has a mass in the vicinity of 1 TeV, or producing it requires interactions on the scale of 1 TeV. Of all the standard model particles, the stop quark gives the largest loop order corrections to the Higgs. Subsequently, light super-partners to the top quarks (stops) are particularly well motivated. The simplest SUSY models have become increasingly more constrained, there remain very large yet un-probed areas of SUSY parameter space that can still be “natural”, i.e. have a fairly small amount of fine tuning.

Supersymmetry is also motivated by its ability to unify the gauge forces’ coupling constants at high energies. Supersymmetry alters the running of standard model coupling constants such that have a point-like intersection at high energies, shown in Figure 2.5.

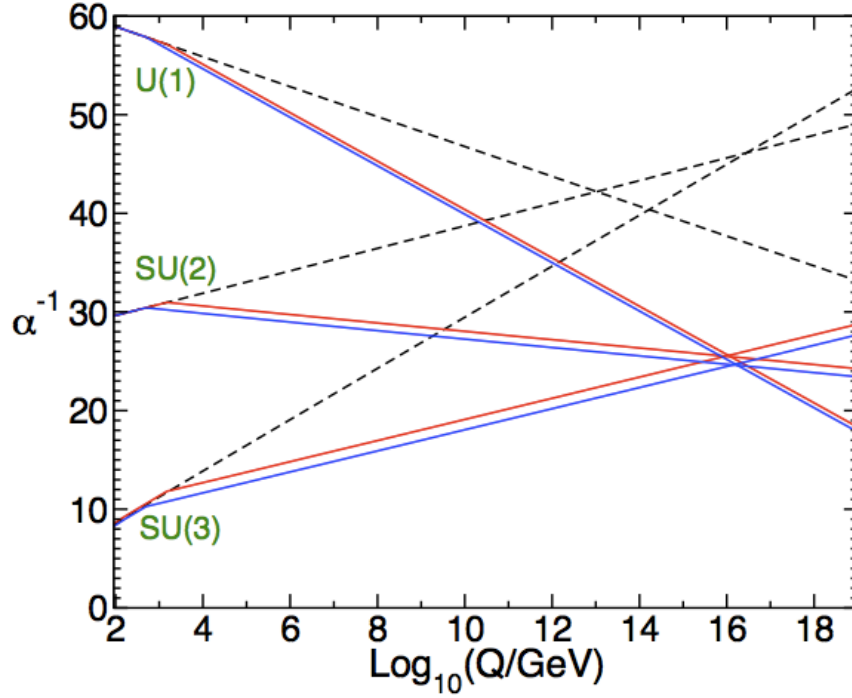


Figure 2.5: Two-loop renormalization group evolution of the inverse gauge couplings of the Standard Model (dashed lines) and the MSSM (solid lines). Reprinted from (59).

2.2.2 Natural SUSY in GMSB

The simplest version of supersymmetry is a model called the minimal supersymmetric standard model (MSSM). One of the most critical aspects of a theory of supersymmetry is the mechanisms and energy scale that breaks supersymmetry. Gauge mediated symmetry breaking (GMSB) is a constrained class of theories within the MSSM.

Light super-partners to the top quark (stop) are an essential requirement for a natural SUSY theory (see, i.g. (13; 64)) since heavy stops give large corrections to the Higgs mass which would have to be fine-tuned away, producing tension with naturalness. In particular, natural SUSY can occur in a spectrum where only the third generation squarks are light (\sim a few hundred GeV) and other squarks are much heavier. This is the so-called “natural” spectrum. Squarks and gluinos have the largest cross sections in hadron colliders among SUSY particles due to their color charge. This makes squark production an attractive means for discovering SUSY, however, such models must evade the stringent experimental bounds imposed on squark and gluino models.

A spin-1/2 Goldstino (\tilde{G}_{frac12}) emerges in the MSSM when SUSY is spontaneously broken by a global symmetry. If the messenger interaction coupling SM super-partners to the SUSY breaking sector are stronger than gravity, then the Goldstino is the LSP (52). If supersymmetry is instead a local symmetry, then SUSY incorporates gravity resulting in a class of theories called supergravity (SUGRA). In which case the goldstino becomes a component of a spin 3/2 superpartner of the graviton (gravitino: \tilde{G}). (63)

GMSB expects four neutralinos and four charginos, of which only two neutralinos $\tilde{\chi}_1^0, \tilde{\chi}_2^0$ and two charginos $\tilde{\chi}_1^\pm$ are used here for model building. Their masses take the arrangement:

$$M(\tilde{\chi}_2^0) > M(\tilde{\chi}_1^\pm) > M(\tilde{\chi}_1^0) \gg M(\tilde{G})$$

The neutralinos and charginos masses are squeezed together with regular intervals in a compressed spectrum with a splitting of a few GeV. Together they are called the co-NLSP (next to lightest super partner). Just as the W, Z, and photon emerge from a mixing of the unbroken electroweak fields, their super-partners may also be a mixture of the pure fields. Depending on the mixing, the co-NLSPs may be a mixture of Higgsino, wino, and Bino. The mixture that these take on controls their decay modes and branching ratios. For information on the neutralino and chargino mixing matrices, see reference (63) section I.4.1 of the Supersymmetry Theory review.

When R-parity is conserved and the scale of supersymmetry breaking to be below $\sim 10^3$ TeV, the NLSP can decay to its standard model partner and \tilde{G} (52). The Higgsino can decay primarily to a Higgs boson since they are super partners. In addition, Higgsino decays to Z bosons are allowed because the longitudinal component of the Z boson mixes with the Goldstone modes of the Higgs field (60). In the limit of pure Higgsino, $\tilde{\chi}_1^0$ can decays predominantly to Higgs. Pair production then has a di-Higgs plus E_T^{miss} signature.

From these considerations comes a the “natural” SUSY spectrum (see Figure 2.6 top left) with a massless Goldstino LSP, a compressed spectrum of neutralinos and charginos a little above the Higgs mass, and a light stop quark (a few hundred GeV). The mass splitting in the compressed spectrum is a few GeV. All other super particles are in the decoupled limit at higher energies. In particular, we assume that the sbottom particle is out of reach and decoupled.

An important consequence of this spectrum is a suppression of E_T^{miss} signatures, allowing this model to evade existing large E_T^{miss} searches. This allows for a large stop cross section that would otherwise have been missed.

2.2.3 Phenomenology of Stop Production

The essential requirement of “natural” SUSY is that the masses of the super-partners of the top quark and the Higgs bosons, the top squark and the Higgsinos, be light (see, e.g. (13; 64)). The first model considered is a complete GMSB model for top squark and Higgsino production with a minimal number of accessible SUSY partners to satisfy the naturalness requirements (9; 48; 52; 60). Here stops and Higgsinos are the only light super-partners. In this case, the lightest chargino and neutralino are almost mass-degenerate and arranged in a compressed spectrum. The accessible SUSY mass spectrum is shown in Figure 2.6. The main stop decay is to a b quark and a chargino, which in turn decay into very soft particles and neutralino. If kinematically allowed, the stop may instead decay to a neutralino and a top quark, which in turn decays to a b quark and W boson.

$$\tilde{t}_R \rightarrow b\tilde{\chi}_1^+ \text{ or } \tilde{t}_R \rightarrow t\tilde{\chi}_i^0, \quad (2.1)$$

where $i = 1, 2$.

The subsequently decays into a very off-shell W^+ (Z) boson and a $\tilde{\chi}_1^0$. The $\tilde{\chi}_1^+$ ($\tilde{\chi}_2^0$) subsequently decays amidst the compressed spectrum through a very off-shell W^+ (Z) boson into very soft particles and the lightest neutralino ($\tilde{\chi}_1^0$) in the compressed spectrum. $\tilde{\chi}_1^0$ then decays into a gravitino and either a Z, or Higgs boson.

$$\tilde{\chi}_1^0 \rightarrow H\tilde{G} \text{ or } \tilde{\chi}_1^0 \rightarrow Z\tilde{G}, \quad (2.2)$$

where \tilde{G} is the gravitino. The branching fractions depend on SUSY parameters, but for a significant portion of the parameter space, for example for low values of $\tan\beta$, the ratio of the up-type to down-type Higgs vacuum expectation values, and negative values of the super-symmetric Higgs mass term μ , neutralino decays into Higgs bosons dominate (61). For alternative regions in $\tan\beta$

and μ , $\tilde{\chi}_1^0 \rightarrow \gamma \tilde{G}$ may occur, but we will not consider this case. The Higgsino decay behavior as a function of SUSY parameters is shown in Figure 2.7.

All SUSY particles except the stable \tilde{G} are assumed to decay promptly.

In this model, strong production of stops is necessarily accompanied by electroweak production of Higgsinos pairs. Higgsino pair production is described further in the next section.

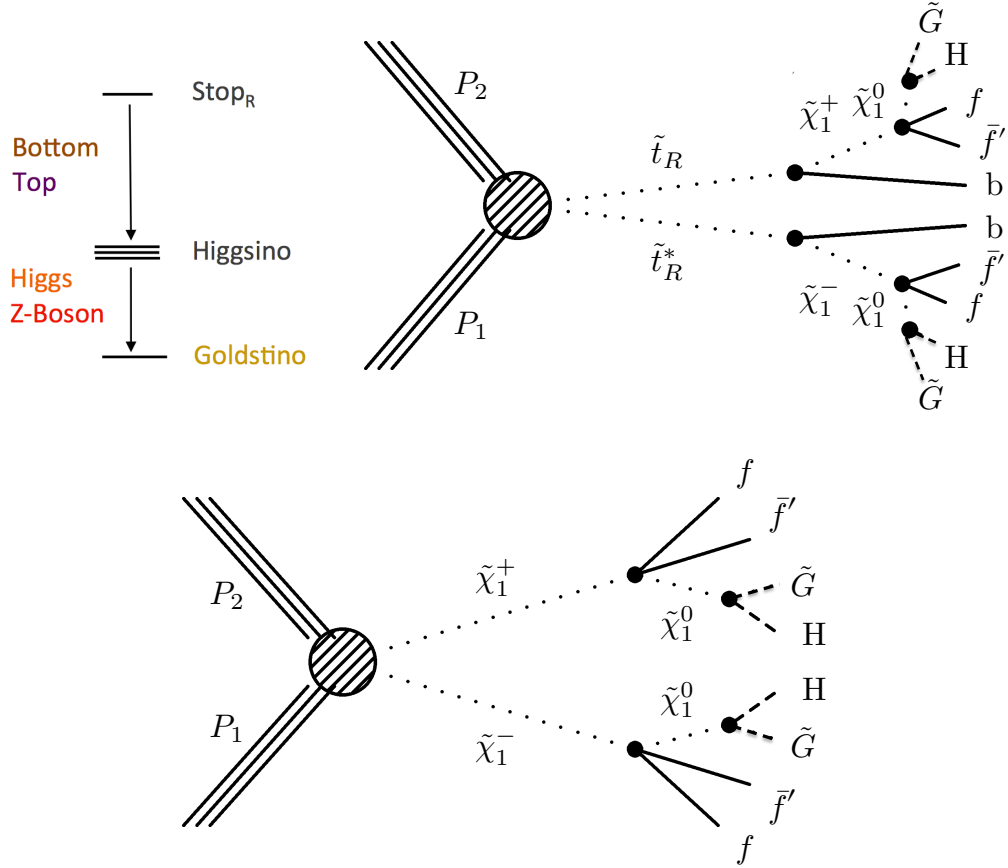


Figure 2.6: *Top Left:* The spectrum of the minimal model under consideration. *Top Right:* Example Feynman diagram of strong production. *Bottom:* Example Feynman diagram of electroweak production. The jets or leptons resulting from transitions between Higgsinos are extremely soft in both diagrams due to the near mass degeneracy of the chargino and the neutralino.

The final state of interest is, therefore, has two Higgs bosons, some missing energy from the gravitinos escaping the detection, and, in case of strong production, two bottom (or top, if kinematically allowed) quarks from stop decays, as shown in Fig. 2.6.

The background is dominated by QCD production of $\gamma\gamma b\bar{b}$ events and $\gamma b\bar{b} + j$ events with the

jet being misidentified as a photon.

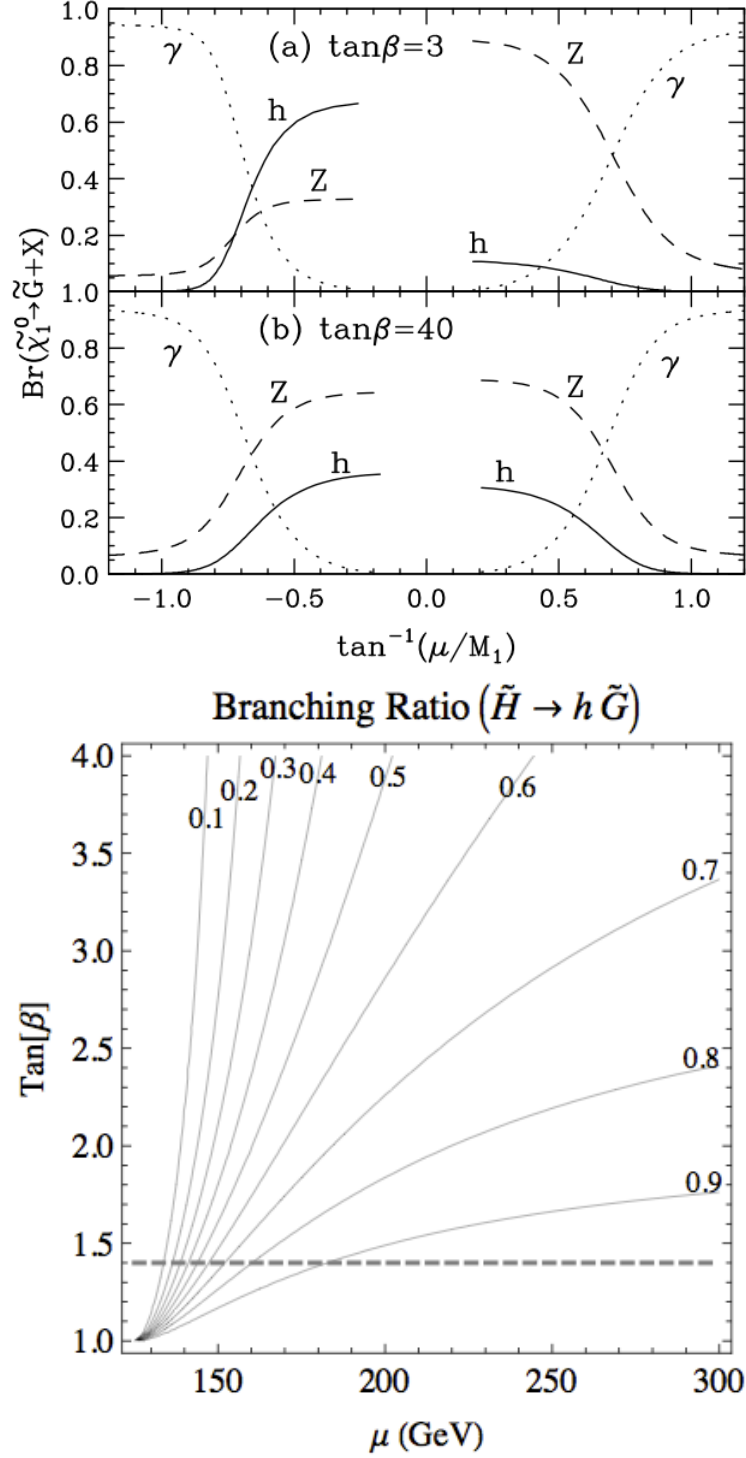


Figure 2.7: Top: Neutralino branching fractions as a function of supersymmetric parameters. Reprinted from (60). Bottom: Contours of Higgsino branching fractions as a function of $\tan\beta$ and the neutralino mass parameter μ in the decoupling limit. This takes $\text{sign}(\mu) < 0$. Higgsinos decay is dominated by decay to Higgs at low $\tan\beta$. Reprinted from (52).

2.2.4 Phenomenology of Higgsino Production

The natural SUSY model described in the previous section is reworked to only include electroweak Higgsino production and the Higgsino is allowed to decay as $\tilde{\chi}_1^0 \rightarrow H\tilde{G}$ or $\tilde{\chi}_1^0 \rightarrow Z\tilde{G}$. This makes for a very simple model in which the mass of the Higgsino and its branching fraction are the only free parameters. Due to the compressed spectrum, several production processes shown in Figure 2.8 give the same final state. The cross sections for these individual processes are added up to give the total Higgsino cross section. The Feynman diagram at the bottom of Figure 2.6 is meant to contain these individual processes. The jets and leptons produced by compressed the spectrum cascades are too soft to observe experimentally.

Higgsino production can produces three signatures: HH, HZ, and ZZ. These are shown in Figure 2.9. HZ cannot occur without the other two, but it is useful to imagine pure HZ production when constructing a search.

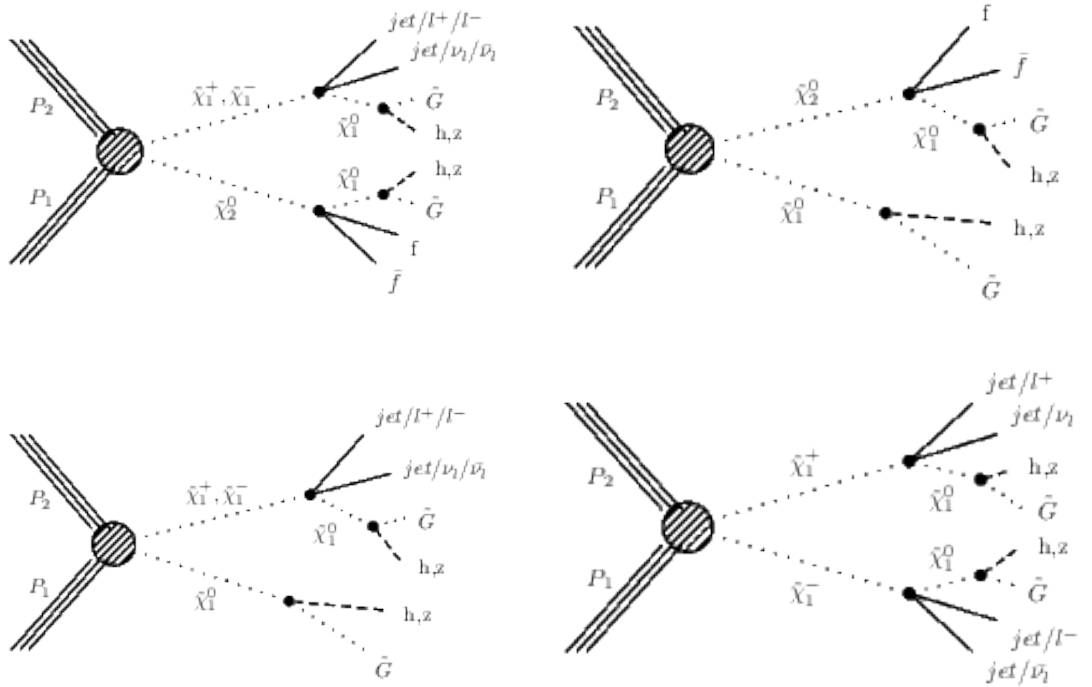


Figure 2.8: Feynman diagrams of neutralino production processes.

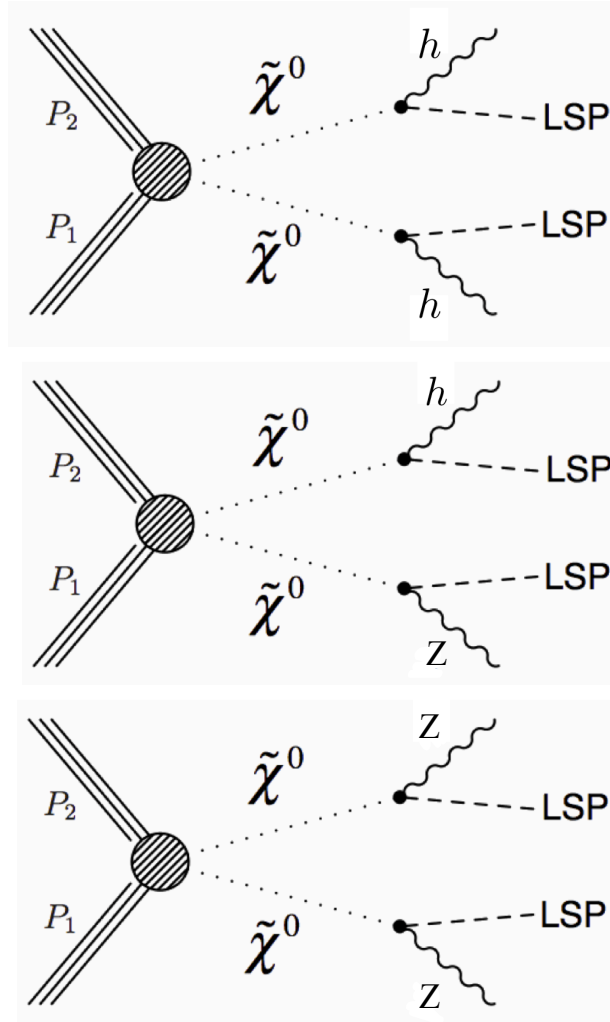


Figure 2.9: Example Feynman diagrams for production of Higgsinos resulting in 2 Higgs bosons (left), a Higgs and a Z (right), and two Z bosons (bottom).

2.2.5 Phenomenology of HW^\pm

The Wino-Bino model uses a significantly different spectrum than the previous stop-Higgsino spectrum. Here, the LSP $\tilde{\chi}_1^0$ is the superpartner of the B gauge boson (the Bino). The Bino is massive, stable, and weakly interacting, and a suitable dark matter candidate. As before, there are mass degenerate $\tilde{\chi}_2^0\tilde{\chi}_1^\pm$. The charginos $\tilde{\chi}_1^\pm$ can be mixtures of Higgsino and wino (18), but are taken to be in the wino limit. The wino decay to an on-shell W boson and $\tilde{\chi}_1^0$. The neutralinos are mixtures of neutral wino, bino(18), and Higgsino. $\tilde{\chi}_2^0$ may decay to either Z or to Higgs bosons (3), but the case where it decays entirely to Higgs bosons is of particular interest.

Charginos and neutralinos can be produced electroweakly in R-parity conserving pairs. These processes are shown in Figure 2.10. Both $\tilde{\chi}_2^0\tilde{\chi}_2^0$ and $\tilde{\chi}_2^0\tilde{\chi}_1^\pm$ should occur. $\tilde{\chi}_2^0\tilde{\chi}_2^0$ is extremely similar to the Higgsino search. When the $\tilde{\chi}_2^0$ decays to Z a $WZ + E_T^{\text{miss}}$ signal is produced which can enter into existing tri-lepton searches. The case where $\tilde{\chi}_2^0$ decays to a Higgs boson is more unique and motivates some search effort.

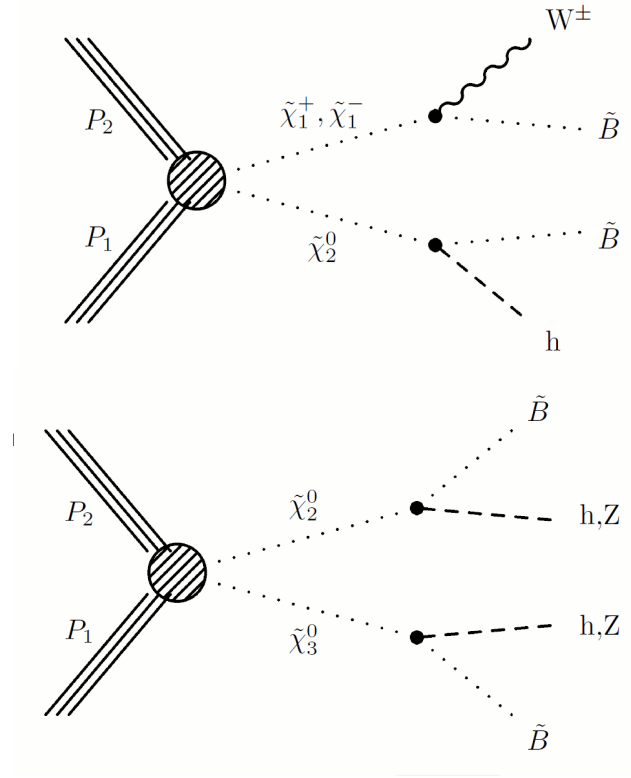


Figure 2.10: Feynman Diagrams for the Wino-Bino model. The left most diagram generates the WH signal.

2.2.6 Signatures Pursued

Three signal models will be pursued are:

- Strong pair production of stops combined with electroweak pair production of Higgsinos in the compressed spectrum assuming the Higgsinos decay entirely to Higgs bosons. The stops are assumed to decay through a b-quark.
- Pure electroweak production of Higgsinos-like neutralinos in the compressed spectrum with the Higgsino allowed to decay to \tilde{G} and either a Higgs boson or a Z boson. This produces
- Electroweak production of WH from the Wino-Bino model.

Chapter 3

The Experimental Apparatus: LHC and CMS

3.1 Introduction

High energy proton collisions are a general probe of physics at short distance scales. The Heisenberg uncertainty principle necessitates high energies in order to probe short distance scales. The parton distribution function of protons allows a mono-energetic beam of protons to produce parton collisions with a broad spectrum of energies lower than the collision energy. With each proton-proton collision event, new particles may be produced and new phenomena explored from the energy of these collisions, including the production of super symmetric particles. By sorting through the results of multiple collisions, most types of standard model physics can be explored and new physics may be found. New physics processes tend to be far less probable than standard model processes, so this process must be repeated a large number of times to produce sufficient numbers of low probability events to permit statistical searches.

Exploring high energy physics with proton collisions requires two basic components: A proton accelerator and collider to produce proton collisions at a single high energy with high luminosity. Preferably the highest energies and luminosity technologically achievable. And a detector to record and reconstruct particles produced by proton collisions. Our tools for this task are the LHC accelerator and the CMS detector. The LHC (Large Hadron Collider) is a circular proton accelerator and collider, the last stage in a series of proton accelerators. The CMS (Compact Muon Solenoid) detector is a large, general purpose particle detector on the LHC ring which records the results of collisions produced by the LHC.

Collision data is digitized and parsed into individual events of interest which are stored in a

database-like structure. Experimentation becomes the task of mining the resulting data for traces of new physics.

3.2 The LHC

The Large Hadron Collider (LHC) is a 23 km circumference modern marvel whose immense complexities are largely irrelevant and far beyond the scope of this thesis. For our purposes, the LHC can be treated as a black box that generates beams of colliding protons and only concern ourselves with the beam conditions it produces at the point inside the CMS detector where the beams collide (the Interaction Point). However there may be some benefit to a brief overview to orient the readers new to the subject. The LHC and its precursor accelerator are located at the CERN laboratory outside of Geneva Switzerland. The LHC is the last and largest stage of a series of accelerators shown in Figure 3.1. Protons are injected into the LHC from the SPS (Super Proton Synchrotron) and accelerated up to the highest energies ever achieved thus far, 4 TeV per beam. The protons are steered into a circle by a magnetic field, focused, and accelerated. Once accelerated, proton beams can then be held in circulation and collided for the better part of a day. The beams are made to collide in four large detectors located on the ring, particularly two general purpose detectors called CMS and ATLAS. CMS and ATLAS compliment each other and serve to provide independent confirmation of physics results.

Our objectives are to obtain high energy and high luminosity. The energy is limited by the size of LHC ring, and the maximum magnetic field which is considered safe in its superconducting magnets, according to the cyclotron equation:

$$E = qcBR_{ring}$$

The magnets are 3.8 Tesla, and the ring's radius is 4 km, corresponding to a an energy of 4 TeV per beam, which was the energy in data used, resulting in a collision center-of-mass energy (\sqrt{s}) of 8 TeV.

Integrated luminosity (L_{int}) is a measure of how much opportunity proton are given to interact. Each physics process in a proton collision has a cross section σ , which in effect is the likelihood

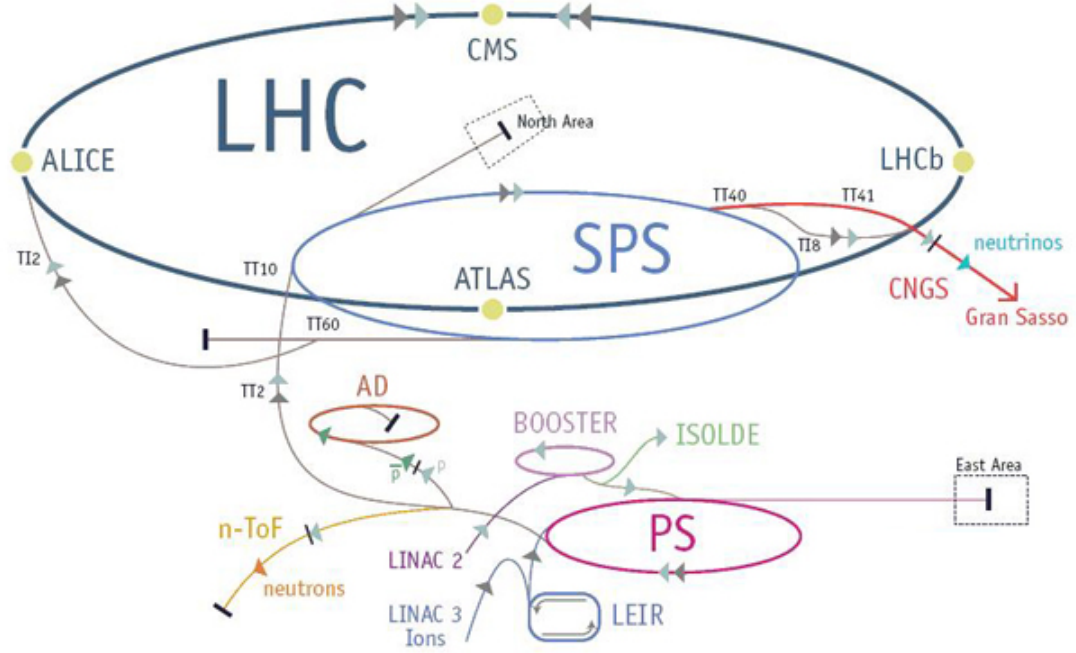


Figure 3.1: The LHC and its precursor accelerators. Protons begin in Linac2, and proceed through the booster, PS, SPS, and are finally enter into the LHC.

that that process will take place. The expected number of occurrences of that process (N) then are determined by $N = \sigma L_{int}$. The integrated luminosity is the integral of the instantaneous luminosity over the time for which the beams are made to collide. $L_{int} = \int L_{inst} dt$. The instantaneous luminosity (L_{inst}) is a measure of the intensity of the proton beams at any given moment and is determined by the machine parameters. Instantaneous luminosity depends strongly on the machine conditions and varied greatly over the course of data collection. The relationship between the machine parameters and the instantaneous luminosity will be discussed further in Section 3.3.3. The LHC beam is pulsed, each pulse of protons is called a “bunch” of protons. For the data used each proton beam had bunches cross every 50 ns (20 MHz). While each bunch circulates the ring at 11 kHz. The exact conditions of the beam varied over the course of the experiment, particularly the number of bunches in the beam. Bunches are roughly the dimensions of a human hair at the interaction point, roughly 10cm long and about $18 \mu m$ across.

Since there are a large number of protons per bunch, more than one proton pair may interact

during a given bunch crossing. This introduces a degree of complexity and even confusion when analyzing collision data. The number of visible interactions per bunch crossing is called the pile-up number. And more generally this effect is referred to as pile-up. Sorting out pile-up requires a high performance detector with a high granularity time projection chamber and a high granularity calorimeter.

3.3 CMS Detector

3.3.1 Introduction

The CMS detector is a large, general purpose particle detector. It is built around a collision point of the LHC beam line, and rests underground, 100m under the village of Cessy France. It is used to identify and reconstruct particles emerging from high energy proton collisions.

The CMS detector consists of several major sub-systems: the tracking system, the electromagnetic calorimeter (ECAL), the Hadronic calorimeter (HCAL), the muon system, and a large superconducting solenoid. The arrangement of these sub-detectors is shown in Figure 3.4. The ECAL, HCAL, tracker, and muon systems are shaped like a cylindrical can, while the solenoid is an open cylinder. Generally the ends of the can are called the endcaps and the cylindrical part is called the barrel. Figure 3.3 shows an illustrative photograph of the CMS detector during construction.

The detector is built around a large 3.8T superconducting solenoid. The main purpose of the magnet is to bend charged particles in the tracker, yet circumscribes calorimeters as well to allow the calorimeters a relatively unobstructed view of the interaction point. The solenoid Outside the solenoid is a large (roughly five stories tall) magnetic field return yoke. The muon system is built in the gaps between layers of the yoke. As muons traverse the muon system they are bent by the returning magnetic field.

The CMS detector is able to measure five types of particles directly: muons, electrons, photons, and charged and neutral hadrons. Other particles are inferred from the behavior of these directly measurable particles. In particular hadrons typically come clustered in sprays of hadrons called jets.

Different flavors of the original parton that generates a jet can be inferred probabilistically from a jet's substructure.

In addition, to these types of particles, non-interacting particles may be detected from missing transverse energy (E_T^{miss}). Measuring E_T^{miss} requires the transverse vector sum of all particles emerging from the primary vertex must be computed. Good E_T^{miss} resolution relies on hermetic coverage around the interaction point as well as good energy resolution on all particles measured and high granularity.

Figure 3.2 shows the basic detection scheme for various types of particles. Charged particles leave a curved track through the tracker. The curved track is used to measure their momentum. Electrons will leave a track and stop in the ECAL, where their deposited energy is measured. High energy photons ideally traverse the tracker without interacting and deposit all their energy in the ECAL in the same manor as electrons. Charged hadrons leave their track in the tracker and pass through the ECAL to stop in the HCAL. Plastic scintillator alone would not stop these hadrons, so scintillator is interleaved with brass absorber in the HCAL. Some energy is left in the ECAL, but most of it is left in the HCAL absorbers. The scintillators sample the amount of energy traversing each layer of absorber. Neutral hadrons do not leave a track and deposit all their energy in the HCAL just as charged hadrons do. Muons escape the detector entirely, but leave a long track from the tracker through the muon system.

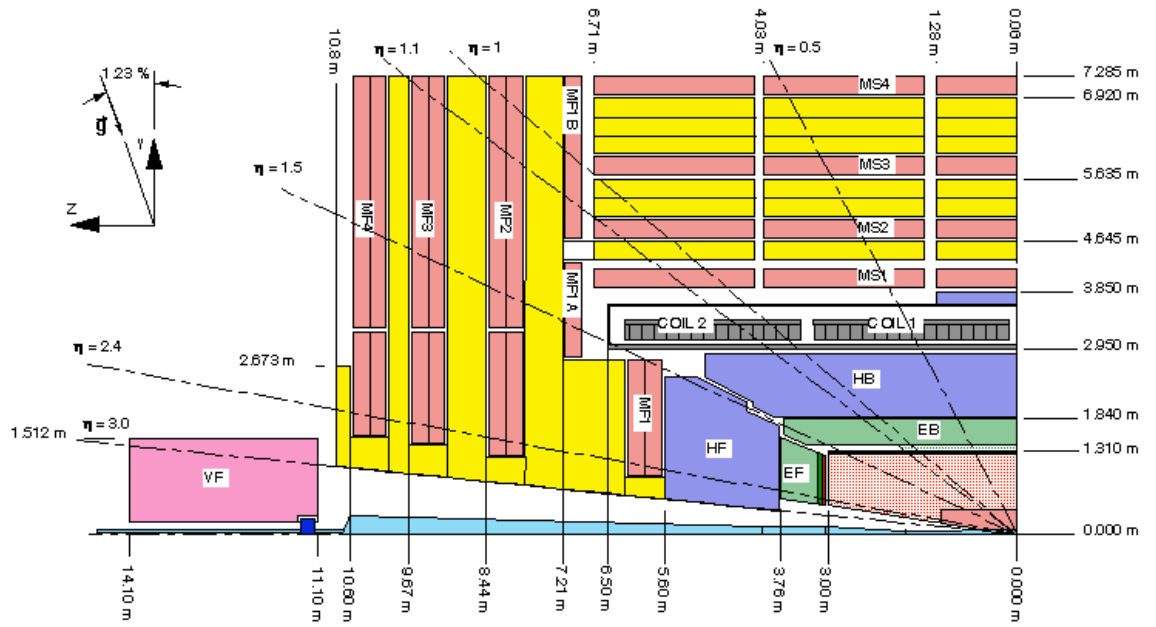


Figure 3.2: A longitudinal cross section of the CMS detector. A full schematic would mirror this slice both vertically and horizontally.

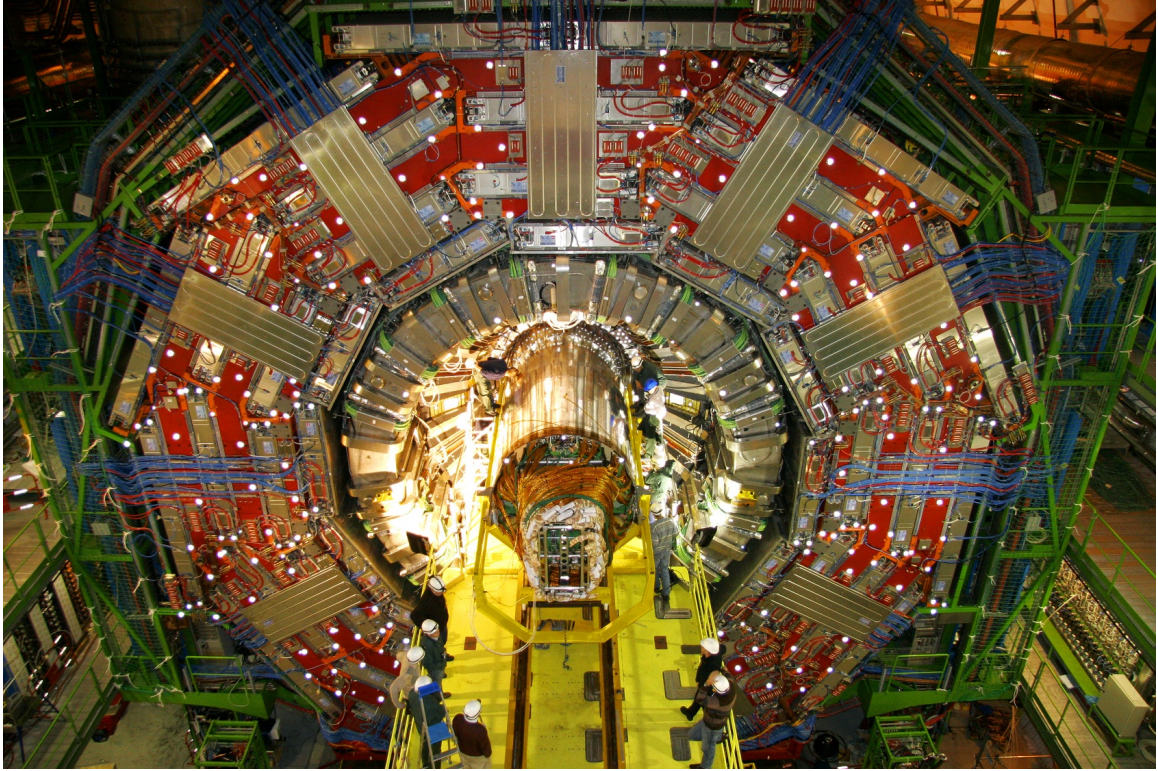


Figure 3.3: The CMS detector during construction as the tracker (protruding from the center) is being inserted. The Endcap is retracted and out of view. The white dots are reflectors used for alignment. The LHC beam pipe traverses the center of the cylinder, but was not yet installed at the time of this photo. The red and silver outer layers are the iron magnetic-field return yoke (red) and the muon system. Just inside that the solenoid is clearly visible. The HCAL and ECAL are also visible in the indentation.

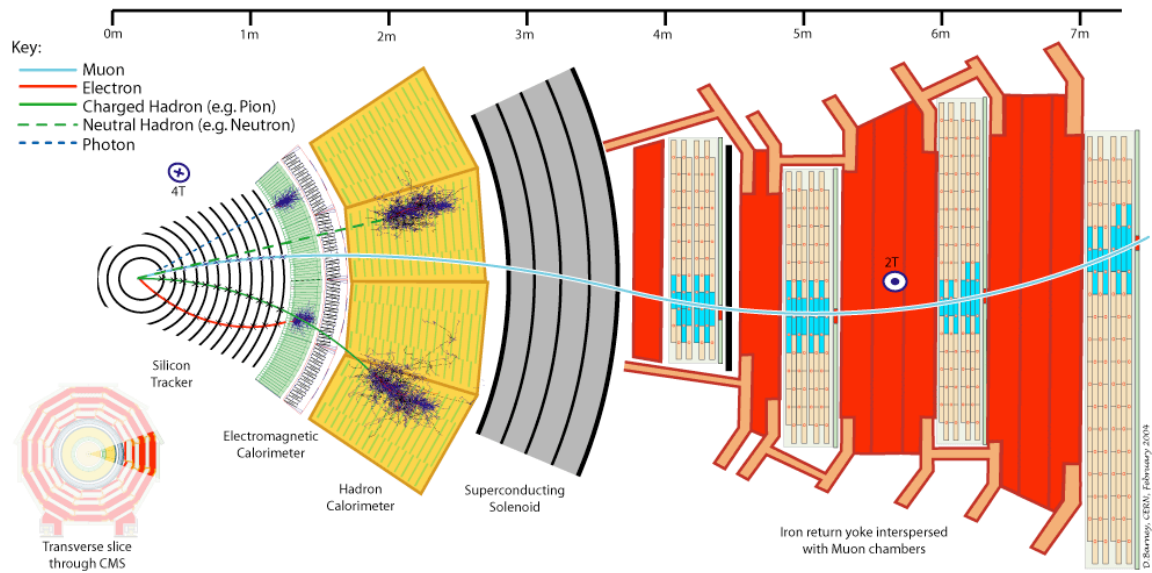


Figure 3.4: A transverse cross section of the CMS detector

3.3.2 Coordinate System

The direction of particles are expressed in terms of η and ϕ , where η is the particle's pseudo-rapidity and ϕ is the azimuthal angle as seen in spherical coordinates where the beam line as the polar axis. The polar axis will hence forth be refereed to as the Z-axis. (X and Y coordinates are virtually never used.)

For those most comfortable with spherical coordinates, η is merely a transform of the polar angle θ : $\eta = -\ln(\tan(\frac{\theta}{2}))$. Pseudorapidity is $-\infty$ and ∞ along the beam line (at the polls), and 0 in the center of the detector (at the equator for polar coordinates). Pseudorapidity of particles is akin to their rapidity (y_z), and, in the ultra-relativistic limit, pseudorapidity and rapidity are identical.

$$\eta = \tanh^{-1}(\frac{p_z}{p})$$

$$y_z = \tanh^{-1}(\frac{p_z}{E})$$

Both protons and the center of mass frame of the collision tend to be virtually at rest in the transverse plane. However the center of mass frames of the collisions tend to have large z-boosts. The location of a particle in the detector is a good indication of the z-boost, which is parameterized in terms of η .

The vicinity of particle is often specified in terms of a radius ΔR around that particle in (η, ϕ) space.

$$\Delta R = \sqrt{\Delta\phi^2 + \Delta\eta^2}$$

3.3.3 Luminosity and monitoring

The integrated luminosity for our data was 19.7 fb^{-1} .

Instantaneous luminosity due the the LHC beam is given by:

$$L_{inst} = \frac{n_{ppb}^2 n_{bpb} f}{4\pi\sigma_x\sigma_y} F$$

Where: n_{ppb} is the number of protons per bunch n_{bpb} is the number of bunches per beam f is the frequency at which the beams circulate around the collider σ_x, σ_y are the x and y widths of the beam at the interaction point, about $18 \mu m$. F is a correction term of order 1 which accounts for geometric and other factors.

During 2012 data taking, instantaneous luminosity reached as high as $7 \times 10^{33} \text{ cm}^{-2}\text{s}^{-1}$ and the trigger menu was designed to accommodate up to $8 \times 10^{33} \text{ cm}^{-2}\text{s}^{-1}$. The history of data collection is summarized in Figure 3.5. Data taking took place in a high pileup environment. Figure 3.6 shows the distribution of pileup interactions during data taking. The on average 21 pileup interactions occurred during every event.

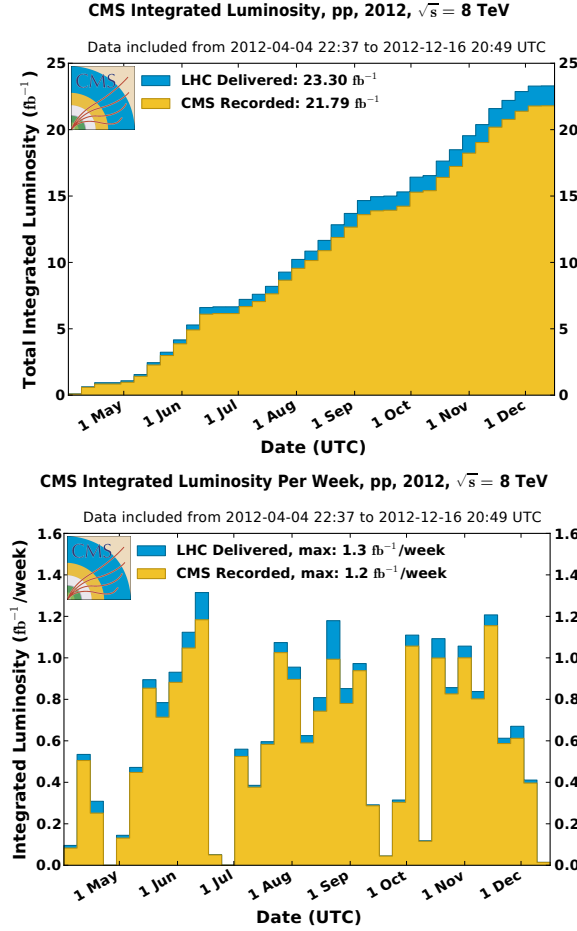


Figure 3.5: CMS luminosity history

A 4.4% uncertainty is applied to the integrated luminosity (33). In the next run, luminosity measurements will be aided by a dedicated luminosity monitor called the Pixel Luminosity Telescope (PLT), which I worked on.

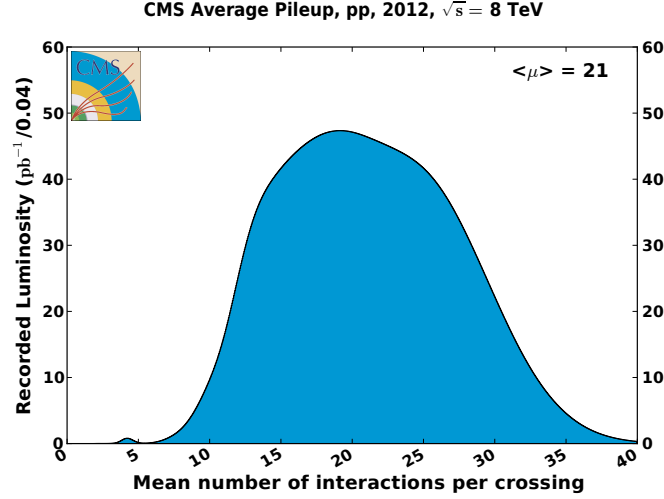


Figure 3.6: Distribution of pileup events in CMS proton collision events.

3.3.4 Superconducting Magnet

The CMS detector's design centers on its superconducting electromagnet, which produces a uniform 3.8 T magnetic field parallel to the beam line over the tracking volume. The solenoid is very large, measuring 12.5 m long with a 6.3 m bore diameter when cold. The large bore allows it to circumscribe the tracking system, EM Calorimeter, and Hadronic calorimeter. This allows radiation to reach the calorimeters with no opportunity for scatter off the solenoid's great mass ($3.9 \chi_0$ radiation thickness). The solenoid is surrounded by a 10,000 ton iron flux return yoke which reduces the amount of energy stored in the magnet and houses the muon detectors.

The magnetic field created by the solenoid serves two functions: first, to azimuthally bend the paths of energetic charged particles, and second, to sweep low energy charged particles into the endcaps, thus reducing the background noise in the barrel. Charged particles in the tracking volume are bent in helical paths around the field lines of radius $r = p/qB$. This allows the tracking system to make a momentum measurement with precision proportional to the magnetic field and the azimuthal granularity of the tracking system. Energetic muons will penetrate the solenoid and experience the irregular return field. Subsequently, muons traverse s-shaped paths through the detector. The muon system uses muons' curved tracks to measure their momentum independent of the tracking system's

measurements.

The solenoid uses superconducting NiTi windings, carrying 19kA, and cooled to the boiling point of helium (4.2K).

The strong magnetic field allows the tracker to make high precision measurements of charged particle momenta. It also aids in distinguishing electrons from charged hadrons.

3.3.5 Tracker and Pixel Detector

As particles emerge from the interaction point through the beam pipe, they first encounter the Pixel detector, followed by the rest of the tracker. These are arrays of silicon CCDs arranged in nested layers. They allow the paths of charged particles to be measured precisely as they emerge from the interaction point.

The tracker and pixel detector have the following functions:

- Identify primary, secondary, and pileup vertices.
- Measure the momentum of charged particles
- Mitigate pileup by identifying charged particles originating from pile-up vertices.
- Linking charged particles to calorimeter deposits and muon tracks
- Associating Bremsstrahlung photons with an electrons.

The general layout of the tracker and pixel detector is shown in Figure 3.7. The tracker extends from a radius 20cm to 120 cm. The pixel detector extends from a radius of 4.4cm to 10.2cm (23). In total, the tracking system has 200 m² of active area of silicon (23). Figure 3.8 shows a section of the CMS tracker during construction.

CCD pixels in the tracker and pixel detector are 100 μ m x 150 μ m across. Charge is distributed over several pixels due to the Lorentz force, allowing position measurements in both r- ϕ and z with resolution of about 15 μ m (23). Charged particles pass through multiple layers of the tracking system while curving in the magnetic field, leaving multiple position measurements. This allows a

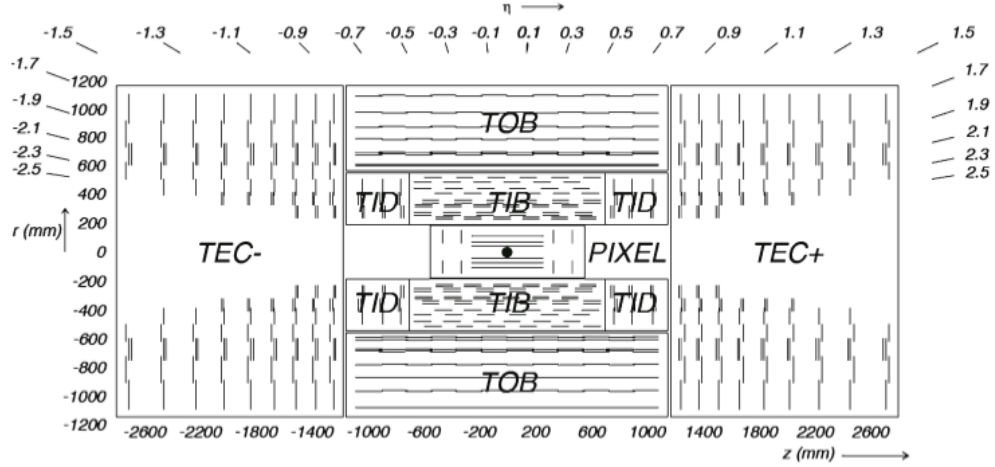


Figure 3.7: A r - z view of the CMS tracker, detailing its sub-systems. The short line segments indicate layers of CCD detectors. The sub-detectors are the Tracker Inner Barrel (TIB), Tracker Outer Barrel (TOB), Tracker Endcaps (TEC), Tracker Inner Disk (TID), and Pixel Detector. (23)

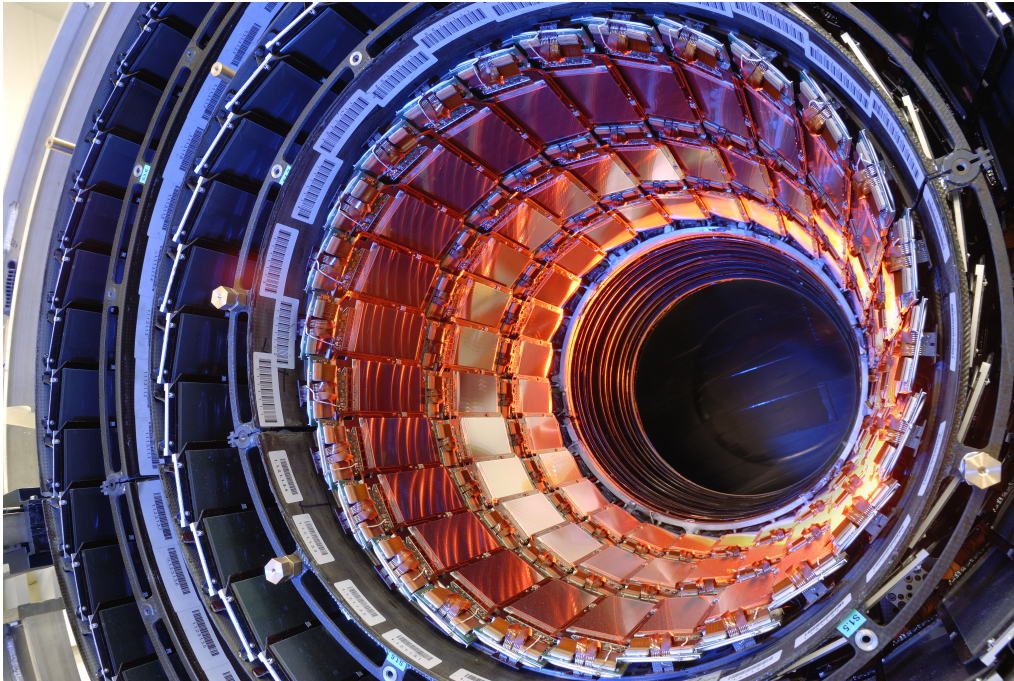


Figure 3.8: The CMS tracker outer barrel during construction.

high precision momentum measurement to be made of the charged particle. The pixel detector plays a central role in identifying primary vertices. Fine resolution is also required to disentangle tracks emerging from each of up to 50 pileup vertices. An example of charged particle tracks and vertices reconstructed by the tracking system in a high pileup environment is shown in Figure 3.9.

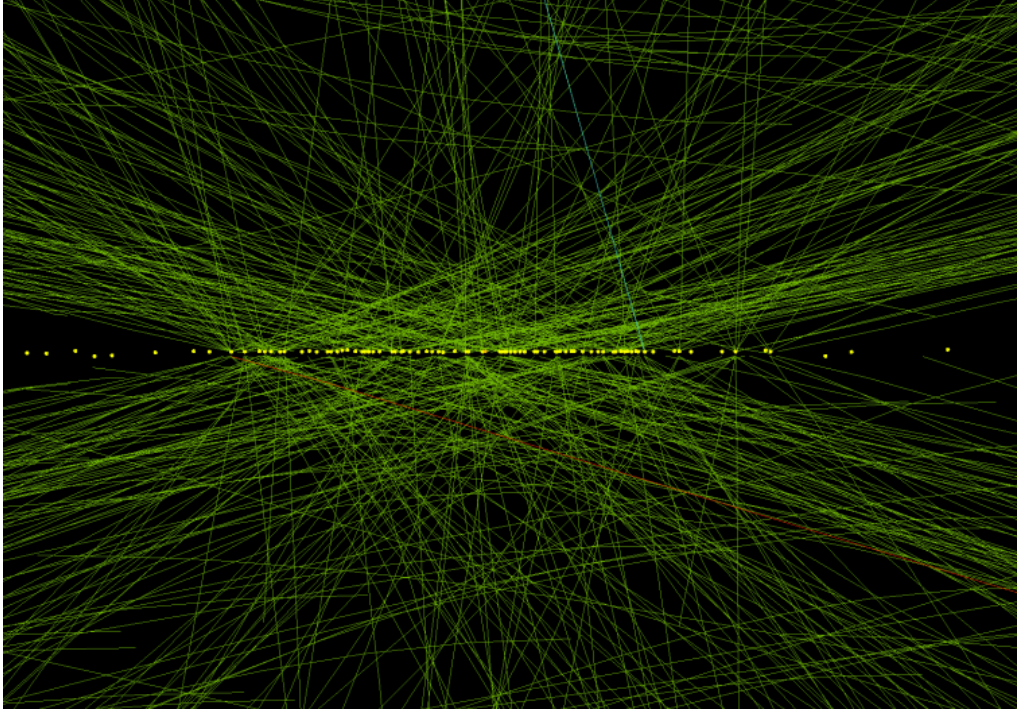


Figure 3.9: Tracks and vertices reconstructed by the CMS tracking system in an example high pileup event. Charged hadrons are shown as green tracks, and reconstructed vertices are shown as yellow dots. The event has one electron (blue blue), and one muons (red track).

The tracking system needs to be as transparent to radiation as possible to prevent premature interactions of particles of interest and the detector. This is particularly the case for photons which have the highest energy resolution when they reach the ECAL in tact. Complicating this is the need to cool the silicon tracking system (using liquid perfluorohexane). The radiation thickness of the tracking system is shown in Figure 3.10. It is clear in figure that photons passing through the barrel with low pseudorapidity will have the best energy resolution.

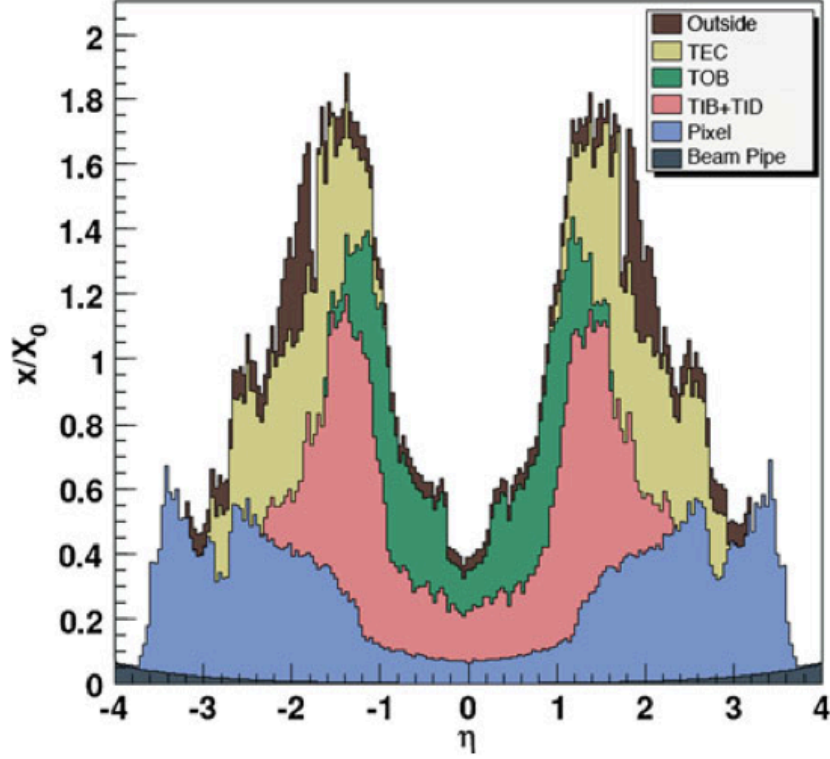


Figure 3.10: The radiation thickness of the tracking system as a function of pseudorapidity η . (23)

3.3.6 Electromagnetic Calorimeter

The CMS electromagnetic calorimeter (ECAL) is a high granularity calorimeter composed of transparent lead-tungstate (PbWO_4) crystals. Photons and electrons deposits nearly all their energy within the ECAL, producing a good energy measurement as well as a fine position measurement. As the name suggests, the ECAL is made to monitor particles with electromagnetic interactions, particularly electrons and photons. Like other detectors, the ECAL is cylindrical, with a barrel section and two circular endcaps, as shown in Figure 3.11. It has nearly hermetic coverage up to a pseudorapidity of $|\eta| < 3$.

ECAL Crystals are arranged in a rectangular array. In the barrel, the rows of the array are aligned with the z -direction and the columns are aligned with the azimuthal direction. In the endcap, the crystals arrays are flat grids. Crystals are oriented more or less towards the interaction point, although not precisely at the interaction point. They are tilted slightly away from the interaction

point to prevent radiation from being lost in the gaps between crystals. This has the added benefit of encouraging photons to share their energy between at least two crystals, which helps distinguish them from single crystal noise events called spikes. Crystals can largely be thought of as pixels arranged on a cylinder.

The crystals convert energy from electromagnetic radiation passing through them into blue-green light, which is then amplified and serves to measure the energy deposited. Light deposited in the crystals is measured using avalanche photo diodes for barrel crystals, and using vacuum phototriodes in endcap crystals. Crystal faces are square, $22 \times 22 \text{ mm}^2$ in the barrel and $28.6 \times 28.6 \text{ mm}^2$ in the endcaps. The crystals in the barrel have a radiation thickness of $25.8 \chi_0$ and in the endcaps they have a radiation thickness of $24.7 \chi_0$. The ECAL barrel as a whole has a radius of 1.29m.

The ECAL serves four functions within the CMS detector:

- Identify and measure photons.
- Catch Bremsstrahlung photons emitted by electrons
- Assist with energy measurement of electrons when needed.
- Separate neutral and charged particles and detect neutral particles overlaid on a charged particle deposit.

Typically the tracker will give a better momentum measurement of charged particles than can be gained by either the ECAL or the hadronic calorimeter. However, the ECAL is the primary tool for detecting and reconstructing Photons. This makes the ECAL of central interest for this analysis.

As the ECAL crystals are irradiated over the lifetime of the detector, they slowly lose transparency. This necessitates frequent calibration of the ECAL. Both a laser system and radioactive sources are used to calibrate the ECAL. The laser system operates during the beam gap, shining a calibration signal at a few crystals at a time. The laser system can then fully calibrate the ECAL every few days.

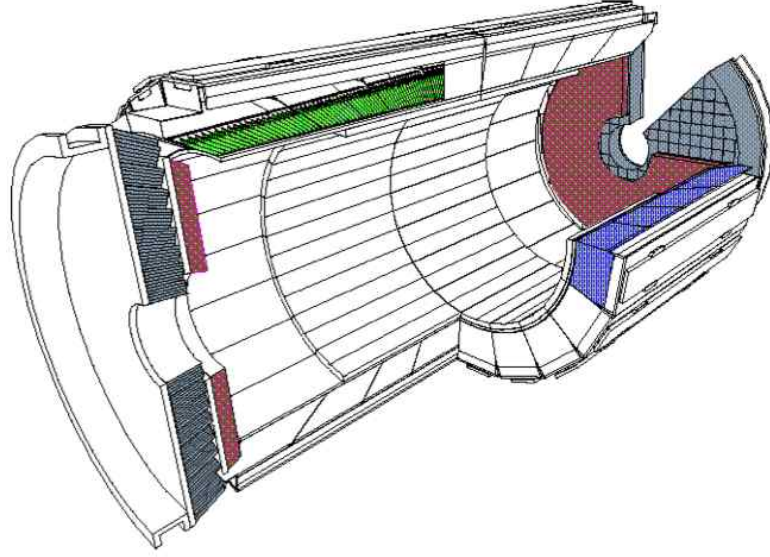


Figure 3.11: A cut-away view of the CMS ECAL. In green and purple are the barrel crystals. In grey are the endcap crystals.

3.3.7 Hadronic Calorimeter

The hadronic calorimeter (HCAL) measures the energy and location of hadrons and its use is analogous to the ECAL for hadrons. It is a sampling calorimeter, interleaving layers of plastic scintillator and metallic absorber. A diagram of the HCAL is shown in Figure 3.12. Like the electromagnetic calorimeter, it is arranged primarily into a barrel section (HB) and two endcap sections (HE). These are stationed just outside of the electromagnetic calorimeters, and in the case of the HB, between the ECAL and the superconducting solenoid. There is an additional pair of detectors (HF) at high rapidity ($5.2 < |\eta| < 3$) with a nearly unobstructed view of the beam spot.

The Hadron Barrel (HB) thickness varies between 5.39 and 10.3 interaction lengths, with the thinnest part in the center and the thinnest part at $\eta = 0$. The barrel is supplemented with an additional layer of hadronic calorimetry outside the solenoid (the HO), using the solenoid as a thick absorber. This serves as a tail catcher for hadronic energy, extending the effective thickness of the calorimeter to 11.8 interaction lengths. The HCAL endcap simply lies between the electromagnetic calorimeter and the endcap muon system. The HF has a nearly unobstructed view of the interaction point and lies alone in its eta region. See Figure 3.2 for a pictorial view.

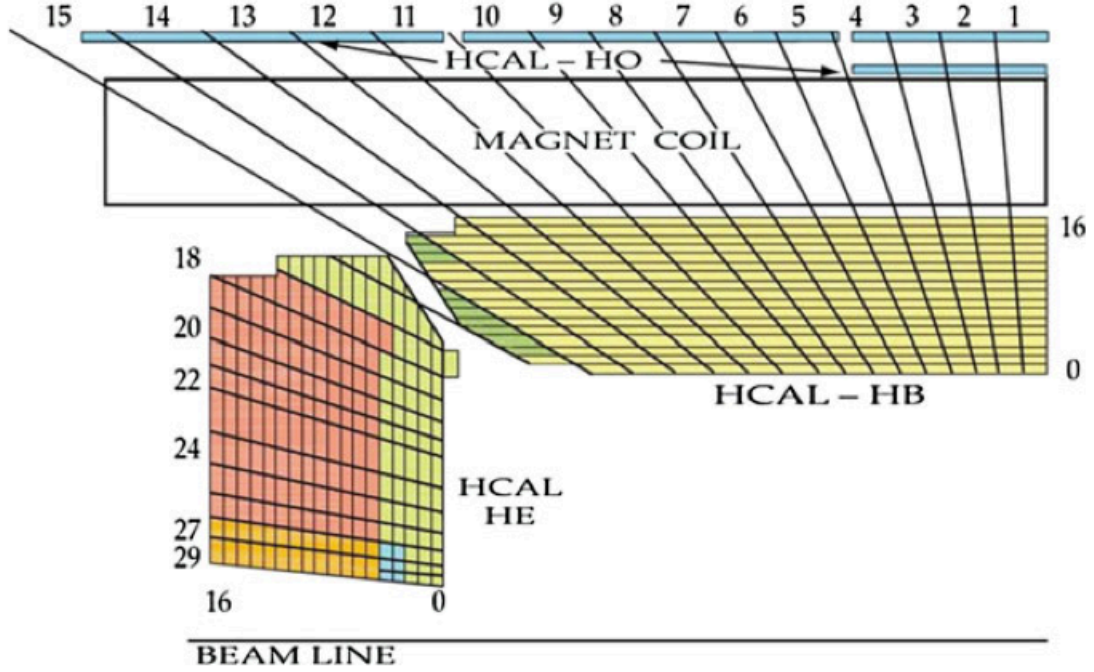


Figure 3.12: Schematic of the one fourth of the HCAL in the r - z plane detailing the tower segmentation. Reprinted from (23).

The HB covers $|\eta| < 1.3$ while the endcap covers most of $1.3 < |\eta| < 3$. The various sections of the HCAL provide nearly hermetic coverage over the full solid angle around the interaction point. Hermetic coverage aids in improving E_T^{miss} resolution.

The HCAL barrel and endcap have a granularity of $(\Delta\eta, \Delta\phi) = (0.087, 0.087)$. Plate scintillators in each layer are arranged radially into towers called “Calo. Tower”. The tiles are readout optically using wavelength-shifting fibers leading to hybrid photodetectors. The first layer of scintillator (layer 0) comes before any absorber material and has a separate readout to allow measurement of hadronic showers before they interact with any absorber material.

The forward hadron (HF) calorimeters consist of two sets of optic fibers set in absorber. One set is set back from the leading surface of the detector by 22 cm, enabling the HF to distinguish between hadronic and electromagnetic energy deposits. It serves as a luminosity monitor and helps improve E_T^{miss} resolution, but is not used for jets used in this analysis. It provides a bunch-by-bunch luminosity estimation once every second. Luminosity is measured using two rings of fibers in the

HF and exploits a linear relationship between the average p_T per tower and the luminosity.

3.3.8 Muon System

Three types of gas-based muon detectors are used in the CMS muon system. Drift tubes (DT), Resistive Plate Chambers (RPC), and Cathode Strip Chambers (CSC).

Drift Tubes are used in the barrel up to $|\eta| < 1.2$, where the magnetic field is uniform. They provide a good timing measurement and have a low neutron background. There are eight layers of drift tubes nestled inside the iron magnetic field return yoke; 4 layers are used for (η, ϕ) position measurement and 4 more layers are used for z measurements. The drift tubes are filled with a mixture of Argon and CO_2 . Charged particles liberated by a passing muon migrate through the gas under the influence of an electric field until they are collected.

Cathode Strip Chambers are used in the endcap, which must contend with a high and variable magnetic field as well as a high neutron-induced background. CSC cover a pseudorapidity range from $0.9 < |\eta| < 2.4$. CSCs are pie-wedge shaped wire chambers that radiate around the endcap.

Resistive Plate Chambers have a very fast response time, 1ns timing resolution, and are highly segmented. (Due to their fast response time, RPC are used for triggering on muons in other analyses.) There are six layers of RPCs in the barrel, as well as three layers in the endcaps. RPCs consist of a layer of gas between two insulating plates in an electric field. Charge gathers on the surface of the insulating plates where it is detected through a capacitive pickup.

3.3.9 Trigger System

The CMS detector processes an event every 50ns during collisions and every event that is saved consumes about 1MB of memory. If some of the data were not discarded, 1 petabyte per minute would have to be saved, which is far beyond the capabilities of the collaboration's (or anyone's?) data processing info structure. This enormous data rate compensates for the very high rate of low energy QCD events that take place. During collisions, data is collected and temporarily stored while an automated decision is made for each event of whether to bother storing the data from that event.

These decisions are made in two stages by the trigger system.

First, a hardware trigger called the “Level 1 trigger” or “L1 trigger” applies simple and very loose selection criterion. The name is somewhat disruptive since there are dozens of L1 triggers, each applying a different selection. The L1 trigger restricts the stream of events from 20MHz to about 10kHz.

Then a slower, software based set of triggers called the “High Level Trigger” or “HLT” are employed. Events that survive to be examined by the HLT have their data fully read out from the detector. Object reconstruction is performed so that the HLT has access to physics objects that consider data from every part of the detector. The HLT is able to make far more complex decisions than are possible at L1. Several hundred high level triggers are implemented at any one time in order to service all the various physics analyses in the collaboration, as well as all the analyses that are considered to be likely in the future. The net output event rate from the HLT is about 300Hz, which is slow enough to store permanently.

Some high level triggers are “prescaled”, meaning they have a loose selection and then only admit a random sampling of the events that pass their selection criterion. This restricts what would otherwise be a flood of events. No prescaled triggers are used in this analysis.

The output of related high level triggers is organized into data sets according to the type of object involved. Therefore, to study photons, do not need to reexamine all the data CMS has ever recorded (several petabytes per year). One need only look in the section of the data that passed certain high level triggers and which accordingly was bundled into the “photon dataset”.

Chapter 4

Particle Reconstruction

4.1 Introduction

The raw data collected by the CMS detector is little more than a list of ADC counts from each sub-detector. This information must be interpreted into a description of the event in terms of particles with four vectors.

First the ADC counts must be translated into calibrated energy deposits. Then calorimeter clustering algorithms transforms the raster image of energy deposits and transforms it into a list of energy clusters and superclusters. The particle flow (PF) algorithm then takes data from all the sub-detectors and constructs a description of the event in terms of particles and four vectors. The result is the so-called “global event description” (GED); global in the sense that it incorporates information from each of the sub-detectors. (See section 4.2 for more details on the PF algorithm.) The list of particles produced by the particle flow algorithm are the building blocks of objects used for analysis, but themselves are too primitive. In the case of photons and electrons, they need considerable filtration to yield a set of high quality objects. In the case of jets further amalgamation is required to turn a spray of PF particles into a jet. Still further processing is required to identify jets that likely originated from b-quarks.

Nature never gives us direct access to the particles in the detector. In the context experimental data, the term “particle” usually means a data object that includes a four vector and other properties, as well as a hypothesis as to what produced it. The same physical particle and its energy deposits can be represented multiple times by different collections of reconstructed particles.

For instance, objects that are called “PF photons” are really PF clusters in the ECAL with no

associated track and little overlapping hadronic energy. However a “SUSY photon” may incorporate several PF photons and often only a fraction of the energy deposits of some PF photons. Further, there’s no guarantee that what is called a photon is the product of a photon at all, and less still that it originated from a photon from the hard interaction. Most photons result from boosted neutral pions decaying to two nearly collinear photons. An energy cluster may be counted both as a photon and as an electron, necessitating a specific requirement that electrons are well separated from photons.

The resolution, efficiency, and fake rate of reconstructed particles depends strongly on how they were constructed and what filtration procedures they were subjected to. Most of this chapter is devoted to defining what qualities are required of the objects used for analysis.

4.2 Global Event Description

The global event description (GED) is a preliminary identification and reconstruction of all particles in the CMS detector during a particular bunch crossing, and is the product of the particle flow (PF) algorithm. Particle flow must link information from the various sub-detectors in an optimized way (14). When it is complete, the event is described in terms of reconstructed particles called “PF candidates” or “PF particles” (I will use these interchangeably). PF candidates come in a few varieties:

- PF Muons
- PF Charged Hadrons
- PF Electrons
- PF photons
- PF Neutral Hadrons

In addition, there is PF E_T^{miss} : the missing transverse energy when considering all particles from the primary vertex.

Particle Flow is able to identify charged particles originating from pile-up interactions and remove those particles from the event description. This makes the global event description relatively insensitive to pileup.

The process begins with tracking and clustering algorithms. The Particle Flow has its own clustering algorithm described further in Section 4.4. Tracking starts with a Kalman filter(53) based tracking. This produces preliminary tracker tracks (that is, tracks limited to the CMS tracker). Also, the muon system is evaluated to produce muon tracks—tracks limited to the muon system.

In the tracker, tracks are build through an iterative track finding algorithm. In the first iteration, the most stringent requirements are placed on track quality. The tracker hits from these tracks are then removed from consideration and the track finding is repeated with less stringent criteria. In the first three iterations tracks are required to emerge from the vicinity of the beam spot. The 4th and 5th iterations allow tracks from secondary vertices up to 50 cm away from the beam spot. Tracks can be found with as little as three hits and 0.15 GeV. The iterative procedure helps prevent fake tracks by reducing the combinatorics of later steps (2).

The first step of particle flow is to try and link tracker tracks to muon tracks. They are linked if a χ^2 fit between them is low enough. Tracks linked between the tracker and the muon system are called “global muons”. Each global muon becomes a particle flow muon if its tracker p_T agrees with the global p_T within 3 standard deviations. Muon tracks and any calorimeter deposits intersected by their track are removed from further consideration (2). If a muon intersects a higher energy calorimeter cluster, only a fraction of the cluster is associated with the muon. The remainder of the cluster may later become a photon or neutral hadron.

As tracking commences, tracks (which are now all tracker tracks) are subjected to a pre- identification step that tries to link them to calorimeter clusters. Tracks are linked to clusters if extrapolated position of the track hits the cluster; that is, the position falls within the bounds of the cluster or up to one cell in any direction. Synchrotron photons are linked to an electron if tangent lines from the electron track project to a photon cluster. Tracks are only linked to one calorimeter cluster; the closest one. However, a cluster can be linked to several tracks. This is particularly useful when

a hadron fragments late. With multiple clusters linked to a track, the list of clusters is sorted by distance from the track, and then the closest clusters are linked until the track's momentum is accounted for. If the track's energy is still 3 standard deviations above what the calorimeter can account for, a relaxed search for muons and fake tracks (2).

Tracks linked to EM clusters with little hadronic energy are pre-identified as electrons. These then have their tracks re-fit using a Gaussian Sum Filter (GSF) tracking procedure (7). The electron's low mass gives electron tracks a different shape than those of heavier particles, which is accounted for by the GSF tracking algorithm to yield higher track quality and a better momentum resolution. Electrons are identified first and their track hits are removed before further evaluating tracks. This helps prevent losing part of an ill-fit electron track which may confuse further tracking (2).

Clusters are also linked with other clusters in radially-adjacent detectors. They are linked if the cluster's center in the higher granularity detector is within the envelope of the cluster in the lower resolution detector. The ECAL can link with the HCAL, and the ECAL has greater resolution. And in the endcap, the preshower can link with the ECAL and the preshower has greater resolution (2).

Tracks give a much more precise momentum measurement than calorimeter measurements and are the preferred means of measuring charged particle energies. The relative momentum uncertainty of a track depends on track quality. If the relative momentum uncertainty is too high, the track will either be rejected as a fake or the momentum measurement from the calorimeters will be used instead (2).

Once PF muons and PF electrons are identified and removed from consideration, the remaining tracks and linked clusters are considered PF hadrons. If the track momentum is significantly less than the energy seen in the calorimeters, it is assumed that there is some overlapping neutral particle (2).

The remaining clusters with no linked tracks are identified as either PF photons or PF neutral hadrons, depending on how much hadronic energy is associated with them. PF photons are given preference over PF neutral hadrons since a significant fraction of jet energy is deposited as photons

and neutral hadrons deposit very little energy in the ECAL (2).

PF photons are not used for photon candidates in associated Higgs production. Instead a SUSY photons are used as defined in Section 4.4.3, however, PF particles are used in defining the isolation of SUSY photons. Isolation is a measure of how much particle activity is in the neighborhood of the photon from the same primary vertex. Good photons are expected to be well isolated, that is, to have very little activity in their vicinity (2).

4.3 Vertex Identification

One of the challenges in particle reconstruction is vertex identification, particularly in the high pile-up environment of CMS. In order to accurately reconstruct the 4-vector of photons, the photon's place of origin is needed in addition to its signature in the ECAL. Vertices are identified by looking for a point where charged particle tracks coincide.

The pile up environment presents an additional challenge. As can be seen in Figure 3.6, there are typically 10 to 35 separate proton collisions and corresponding vertices every time two bunches of protons cross. The high resolution CMS pixel detector is well equipped to identify all these vertices. Typically no more than one of these vertices will be an interaction of so it can be assumed that all energetic of interest come from a single “primary vertex”. The primary vertex is chosen to be the vertex with the most charged particle transverse energy emerging from it.

Unfortunately it is impossible to positively identify which vertex the photons came from. This assumption is not guaranteed to be correct but serves as an adequate approximation.

4.4 Electromagnetic Objects

4.4.1 ECAL Clustering

The ECAL barrel and endcap are arranged in grids of crystals, which can be regarded much like pixels. In the ECAL, these are arranged in cylinder with the crystal coordinate axes coincident with the ϕ and z directions. The task of clustering is the process of turning an raster image of ECAL

crystal (pixels) into a set of sensible objects by collecting crystals into sets of crystals called clusters.

There are three clustering algorithms used in the ECAL. The barrel uses the “Hybrid superclustering algorithm” (31). The endcap uses the multi5x5 clustering algorithm (31). The hybrid algorithm was used for constructing photons in this analysis and be the primary focus here. The multi5x5 was used for building electrons in the endcap. In addition a particle flow clustering algorithm is used to cluster photons used for isolation (PF photon isolation).

The Hybrid Clustering Algorithm (31):

Each clustering algorithm starts by restricting its consideration to crystals reporting energy above the noise threshold. (The noise thresholds for ECAL crystals is two standard deviations above the electronics noise: 80 MeV in the barrel and up to 300 MeV in the endcaps.) This population of crystals make up “ECAL hits”. The algorithm then identifies a seed crystals, for which it uses the highest energy crystal among the ECAL hits that has not yet been clustered and has at least $E_{thres} = 0.1 \text{ GeV}$ of transverse energy.

The seed and all the ECAL hits within a 1x5 crystal “domino” around the seed crystal are then included in a new cluster. Dominos 1x5 crystals wide in ϕ and η respectively. Next, the algorithm takes a step in ϕ and considers including this adjacent domino in the cluster. The domino is included if its transverse energy is $> E_{thres} = 0.100 \text{ GeV}$. The algorithm stops including dominos either when it encounters a domino under E_{thres} or after 17 dominos. Then it clusters dominos on the other side of the seed crystal in the same way. This cluster is then complete and the algorithm moves on to the next most energetic seed crystal for clustering. All clusters now appear as rectangles 5 crystals wide in η and between 1 and 35 crystals wide in ϕ . EM object hits in the ECAL are naturally wider in ϕ than in η due to charged particles bending in the magnetic field.

Once clusters are formed, the hybrid algorithm builds super clusters. It begins by selecting a seed cluster, which must have at least 1 GeV of transverse energy. The super-cluster consists of ECAL hits within the 35x5 crystal box centered on the seed crystals, which are members of clusters, but not members of other super clusters. Often the boundaries of this box will divide up clusters.

The Multi5x5 Clustering Algorithm (31):

Clustering in the Multi5x5 has the same process for ECAL hits and seeds as the hybrid algorithm. But rather than dynamically including dominos, the multi5x5 algorithm defines the cluster as all ECAL hits within the 5x5 array of crystals surrounding the cluster seed.

Then it builds superclusters. Superclusters are seeded by ECAL clusters with at least 1 GeV of transverse energy. Clusters whose seeds lie within $|\Delta\phi| < 0.3$ and $|\Delta\eta| < 0.07$ of the supercluster seed crystal are included in the supercluster.

The Particle Flow Clustering Algorithm:

The particle flow clustering algorithm is a recursive nearest neighbor algorithm that clusters every ECAL hit over 0.08 GeV in a contiguous region around the seed crystal. This prevents selection areas from only including segments of a cluster. Clustered crystals must share one side with a crystal already clustered. Seed crystals have a 0.23 GeV transverse energy threshold and must also be the highest energy crystal in its 3x3 neighborhood. Unlike the other two clustering algorithms, the particle flow clustering does not involve superclustering.

4.4.2 Photon Variables

Several variables are defined to aid in identifying high purity photons in CMS.

First, EM objects are expected to deposit nearly all of their energy in the ECAL and not penetrate into the HCAL. While hadronic showers typically leave some energy in the ECAL but deposit most of their in the HCAL. This motivates the variable H/E. H/E (pronounced “H over E”) loosely speaking is the ratio of hadronic to electromagnetic energy in the object. More specifically, H is the energy in the HCAL Calo. tower behind the ECAL seed crystal, and E is the ECAL supercluster energy. Real electromagnetic objects to have a very low H/E.

Photons and electrons are clustered in the same way, but are treated differently there after. The foremost difference between the signatures of photons and electrons in the detector is the electron’s charged track. Electrons may appear similar to photons by traveling a short distance before interacting with the material in the tracker, dumping their energy into a Bremsstrahlung photon. Photons are required to have a “Pixel seed veto” or similar mechanism for rejecting electrons

faking photons. A pixel seed is a track reaching the lower pixel detector with a direction and energy compatible with the photon candidate's super cluster. A pixel seed veto rejects photon candidates that have such a track.

Unconverted photons typically leave most of their energy within a one crystal radius of the seed. This is not the case for converted photons – that is, photons that interact with the material in the tracker and transfer their energy to an electron from the tracker. In that case, the electron will emit synchrotron radiation as it curves in the magnetic field. The energy of the original photon is then deposited in a train of clusters with about the same η but spread in ϕ . The clustering algorithm does it's best to sum these together and reconstruct the energy of the original photon but the energy resolution is not as high as with unconverted photons. The variable R9 gives an indication of whether or not a photon converted, which intern influences the energy resolution of that photon. It is defined as:

$$R9 = \frac{E_{3x3}}{E_{supercluster}}$$

Since real EM objects should be compact in η their width in η is a useful quantity for differentiating real EM objects from hadronic fakes. $\sigma_{i\eta i\eta}^2$ is just such a measure of its width. It is closely related to the standard deviation of the supercluster in η expressed in pixel coordinates.

$$\sigma_{i\eta i\eta}^2 = \frac{\sum_i^{5x5} w_i (i\eta_i - i\eta_{seed})^2}{\sum_i^{5x5} w_i}$$

where

$$w_i = \max(0, 4.7 + \ln\left(\frac{E_i}{E_{5x5}}\right))$$

Spike Cleaning:

Not all compact energy deposits in the ECAL are real photons. Collisions fill CMS with neutrons which can interact with the ECAL readout machinery to produce single crystal “spikes” that look similar to high energy photons. Real photons in contrast deposit some of their energy into adjacent crystals. Spikes therefore can be eliminated by removing superclusters with zero width. There are several layers of spike removal (or “spike cleaning”), in particular, cuts are made on two quantities related to $\sigma_{i\eta i\eta}^2$:

$$\sigma_{i\phi i\phi}^2 = \frac{\sum_i^{5x5} w_i (i\phi_i - i\phi_{seed})^2}{\sum_i^{5x5} w_i}$$

$$\sigma_{\eta i \phi}^2 = \frac{\sum_i^{5x5} w_i (i\eta_i - i\eta_{seed}) * (i\phi_i - i\phi_{seed})}{\sum_i^{5x5} w_i}$$

4.4.3 Photons

Figure 8.1 shows the rapidity distributions of the photons from SUSY cascades and the background. Since the background is significantly higher in electromagnetic calorimeter (ECAL) endcap, only the photons in the ECAL barrel ($|\eta| < 1.4442$) are used. The photons have transverse energy thresholds of 40 GeV for the leading photon and 25 GeV for the trailing photon.

Photon energy calibration is discussed in reference (25).

The CMS SUSY Loose photon definition (38)(34) is used. The selection requires:

- pixel veto
- $\sigma_{i\eta i\eta}$ less than 0.012
- H/E less than 0.05
- ρ -corrected PF charged hadron isolation less than 2.6
- ρ -corrected PF neutral hadron isolation less than $3.5 + 0.04 \cdot p_T^\gamma$
- ρ -corrected PF neutral hadron isolation less than $1.3 + 0.005 \cdot p_T^\gamma$

Additional spike cleaning is applied through the following cuts:

- $\sigma_{i\eta i\eta}$ greater than 0.001
- $\sigma_{i\phi i\phi}$ greater than 0.001

The background rate in $H \rightarrow \gamma\gamma$ associated production is directly proportional to the width of the Higgs mass window. Maximizing the photon energy and mass resolution as much as possible is therefore strongly motivated. For this reason, photon energy is corrected using MVA regression (36), the same as was used in the $h \rightarrow \gamma\gamma$ analysis.

4.4.4 Electrons

Two electron definitions are used in these analyses. The first is used by the lepton analysis to identify good electrons. This follows a standard definition set by the CMS Egamma POG, called the electron loose cut-based working point (38).

The second is a looser definition used for vetoing electrons, called the electron veto cut-based working point (38). In addition to the standard selection, electrons must satisfy the following analysis specific requirements:

- They must have a transverse energy threshold $E_T > 15 \text{ GeV}$
- They are required to lie within the bounds of the tracker $|\eta_\ell| < 2.4$ and not land in the gap between barrel and endcap.
- Electrons must be well separated from the photons, with $\Delta R(\gamma, \ell) > 0.3$ for both photons.

4.4.5 Monte Carlo Photon Energy Smearing

In order to make the energy resolution of photons used in the Monte Carlo more closely resemble those in the data, the energy of the Monte Carlo photons is smeared. This is done by scaling the photon energy by a random gaussian.

$$E_{FastSimSmeared} = E_{FastSim} * Gauss\left(1, \left(\frac{\sigma_E}{E}\right)_{FastSim\ smearing}\right)$$

Where σ_E/E here is the expected difference in energy resolution between the Monte Carlo photons and real photons in CMS. This has been studied for FullSim photons and FullSim smearing factors have been developed (36), so we merely need to convert the existing FullSim smearing factors to FastSim.

The existing smearing factors for FullSim are essentially:

$$\left(\frac{\sigma_E}{E}\right)_{AN-13-008\ smearing}^2 = \sqrt{\left(\frac{\sigma_E}{E}\right)_{Data}^2 - \left(\frac{\sigma_E}{E}\right)_{FullSim}^2}$$

Then the FastSim smearing factors are:

$$\left(\frac{\sigma_E}{E}\right)_{\text{FastSim smearing}}^2 = \sqrt{\left(\sqrt{\left(\frac{\sigma_E}{E}\right)_{\text{Data}}^2 - \left(\frac{\sigma_E}{E}\right)_{\text{FullSim}}^2}\right)^2 + \left(\frac{\sigma_E}{E}\right)_{\text{FullSim Fit}}^2 - \left(\frac{\sigma_E}{E}\right)_{\text{FastSim Fit}}^2}$$

Simplifying that slightly, we get the applied formula for obtaining FastSim smearing factors:

$$\left(\frac{\sigma_E}{E}\right)_{\text{FastSim smearing}}^2 = \sqrt{\left(\frac{\sigma_E}{E}\right)_{\text{AN-13-008 smearing}}^2 + \left(\frac{\sigma_E}{E}\right)_{\text{FullSim Fit}}^2 - \left(\frac{\sigma_E}{E}\right)_{\text{FastSim Fit}}^2}$$

$\left(\frac{\sigma_E}{E}\right)_{\text{FastSim Fit}}^2$ and $\left(\frac{\sigma_E}{E}\right)_{\text{FullSim Fit}}^2$ are obtained by fitting photon energy resolution distributions for FastSim and FullSim respectively. These fits are seen in Figure 4.1. The fits and smearing factors are made for eight categories: four $|\eta|$ regions and low and high R9. The resulting smearing factors are listed in Table 4.1.

Table 4.1: Smearing Factor Results

| Categories | AN-13-008 Smearing Fac- tors (%) | SUSY FullSim Fit (%) | SUSY FastSim Fit% | FastSim Smear- ing (%) |
|--------------------------------|--|-------------------------|----------------------|---------------------------|
| EB, $ \eta < 1$, $R9 > 0.94$ | 1.13 | 0.74 | 0.99 | 0.92 |
| EB, $ \eta < 1$, $R9 < 0.94$ | 1.09 | 1.02 | 1.11 | 1.00 |
| EB, $ \eta > 1$, $R9 > 0.94$ | 1.71 | 0.83 | 0.98 | 1.63 |
| EB, $ \eta > 1$, $R9 < 0.94$ | 2.03 | 1.26 | 1.63 | 1.75 |
| EB, $ \eta < 2$, $R9 > 0.94$ | 3.09 | 1.41 | 1.64 | 2.98 |
| EB, $ \eta < 2$, $R9 < 0.94$ | 2.78 | 2.71 | 2.47 | 3.00 |
| EB, $ \eta > 2$, $R9 > 0.94$ | 3.72 | 1.27 | 1.81 | 3.49 |
| EB, $ \eta > 2$, $R9 < 0.94$ | 3.75 | 1.77 | 3.34 | 2.45 |

Table 4.2: From left to right, the previously obtained smearing factors for FullSim (36), the gaussian widths of the fits to FullSim Monte Carlo, the gaussian widths of the fits to FastSim Monte Carlo, and the FastSim smearing factor results derived from these.

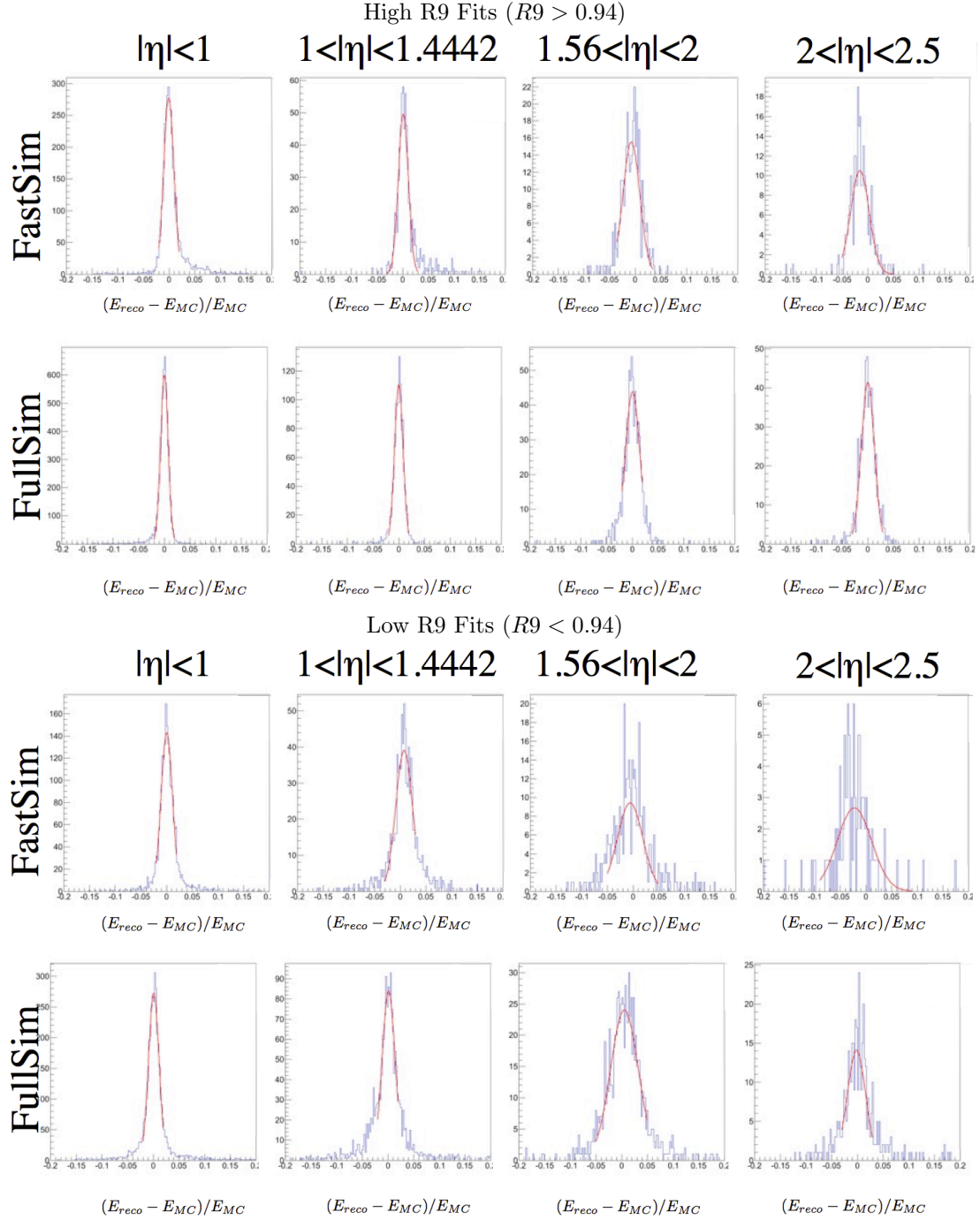


Figure 4.1: Fits of photon resolution in FastSim and FullSim Monte Carlo simulation for eight photon categories. The inner cone is fit with a Gaussian.

4.5 Hadronic Objects

4.5.1 Jets

Type L1FastL2L3 corrected (40) particle flow AK5 jets and E_T^{miss} are used. Jets are required to have E_T greater than 30 GeV. (The rest of this section explains the first sentence for the sake of those not in CMS.)

Unlike photons and electrons, which arrive in the calorimeter as fairly compact objects, partons emerge from a hard interaction as a spray of hadrons. To reconstruct the original four-vector of parton from the hard interaction, the elements of this spray must be identified as fragments of one object and their energies summed up. This results in a composite object called a jet.

First, individual particles are identified from clusters of hadronic energy and tracks using the particle flow algorithm described in Section 4.2. This forms a list of PF (particle flow) candidates with known four-vectors. From this list PF candidates are clustered into jets using the AK5 jet clustering algorithm; that is, the Anti- K_T algorithm with clustering radius $R = 0.5$.

In the Anti- K_T algorithm, for every PF candidate we define $d_i = P_i^k$, where i indicates the i^{th} PF candidate. And for every pair of PF candidate we define:

$$d_{ij} = \min(P_{ti}^k, P_{tj}^k) \left(\frac{\Delta R_{i,j}^2}{R^2} \right)$$

A list of d_i 's and d_{ij} 's is then sorted and the minimum element found. If the minimum element is a d_i , that object is called a jet. d_i is then removed from the list, as is d_{ij} for every j . If the minimum element was instead a d_{ij} , the objects i and j are merged into one four-vector k . The set is then remade using k rather than i and j . This procedure is then iterated until there are no more d 's on the list. Then all PF candidates have been clustered into jets.

The Anti- K_T algorithm uses $k = -2$. This distinguishes it from the K_T algorithm which uses $k = 2$ and the Cambridge-Aachen algorithm which uses $k = 0$. In the literature, p_T is often called k_T , hence the name.

The Anti- K_T algorithm begins with the hardest constituents and clusters gathers softer constituents into it. It typically gathers objects within a simple cone or radius R around the seed. But

if two cones intersect it finds an equitable partition between the two.

L1FastL2L3 jet corrections are a series of jet energy corrections that correct for spurious energy from pile-up interactions thrown into the jet’s catchment. They takes into account the η position of the jet, the jet’s catchment area, the jet’s transverse energy, and the expected PU energy per unit area from in-time and out-of-time pileup given the average amount of hadronic activity in that event. For further details, see (65).

4.5.2 Monte Carlo Jet Energy Scale Uncertainty

A 2% uncertainty in the jet energy scale (JES) is used to account for differences in how jet energy is estimated between data and Monte Carlo.

$$P_{scaled}^{\mu} = P_o^{\mu}(1 \pm 0.02)$$

The shift in energy is then propagated to a corresponding shift in E_T^{miss} .

The jet energy scale can sculpt other kinematic variables, particularly the search variables. Therefore, each Monte Carlo is processed first without a JEC scale factor, then once with a +2% scale factor and once with a −2% scale factor. The same is done for B-tagging efficiency, for a total of 5 analyzer passes per Monte Carlo point. This gives us a set of three histograms for a search variable: a central value and two more showing the effects of the JES uncertainty. An example of this can be seen in Figure 4.2. The limit setting machinery described in Section 8.6 uses this information as a shape uncertainty to properly account for the JES in the limits.

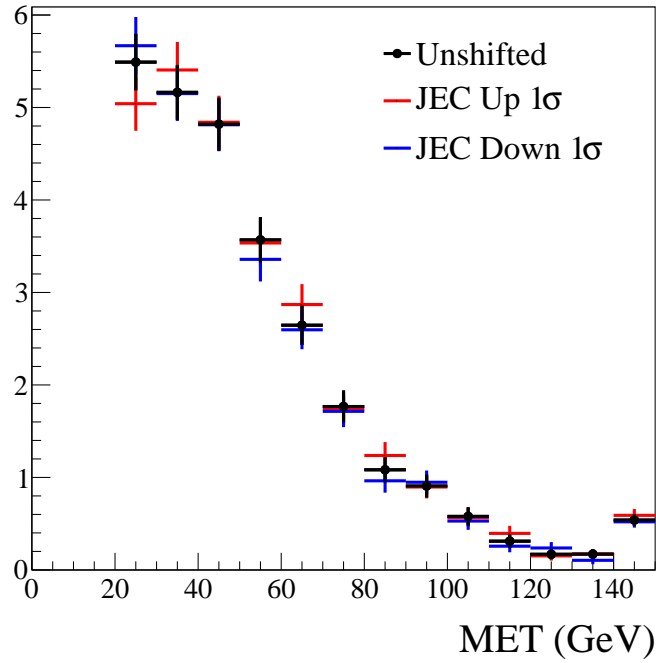


Figure 4.2: Comparison of E_T^{miss} distributions using jet energy corrections, and with the energy corrections shifted up and down by 1σ for mass point $M_{\tilde{\chi}_1^0} = 150 \text{ GeV}/c^2$.

4.5.3 b-Tagging with the CSV Algorithm

The Combined Secondary Vertex (CSV) algorithm is used for b-jet identification. This is a multivariate algorithm that takes into account various observables about the jet. It takes advantage of the tendency of b-hadrons to have relatively long lifetimes (1.5 ps) which tend to produce displaced secondary vertices a small but macroscopic distance away from the primary vertex (PV). The separation between the primary and secondary vertex (SV) can often be resolved using high resolution tracking systems such as the one in CMS. The CSV algorithm also takes advantage of the relatively hard fragmentation function of b-hadrons. The algorithm particularly has to differentiate b-jets from c-jets and from K_s decays, which may also have secondary vertices.

The CSV algorithm starts by searching through the tracks in a jet in search of secondary vertices and tracks that are not consistent with the primary vertex. Reco vertices are allowed to have a transverse distance from the PV between 1 and 25mm. The reconstructed vertex must also be at least $3\sigma_{LT}$ away from the PV in the transverse plane, where σ_{LT} is the uncertainty in the PV's

transverse location. Jets immediately fall into one of three categories:

- Category 1, “Reco Vertex”: One or more suitable secondary vertices were found from the jets tracks.
- Category 2, “Pseudo Vertex”: No good secondary vertices were found but at least two of the jet’s tracks have large impact parameters from the primary vertex. (That is, tracks with a signed transverse impact parameter significance > 2).
- Category 3 “No Vertex”: All other jets.

Different sets of variables are considered for depending on the jet’s category and jet observables are strongly correlated with which category.

For events in category 1, the CSV algorithm considers the following variables:

- The distance between the PV and SV divided by its uncertainty.
- The maximum track impact parameter significance among valid tracks coming off the SV.
- The invariant mass of the vector sum of all charged particles from the SV.
- The number of charged particles from the SV.
- The total energy of charged particles from the SV divided by the total energy of the jet.
- $\Delta\eta$ between each charged particle from the SV and the jet.

Charged particles are considered if their mass is less than $6.5 \text{ GeV}/c^2$ and they pass a charm-hadron mass threshold. Charged particles are also not considered if there is a track of opposite charge, which together have an invariant mass within $30 \text{ MeV}/c^2$ of the K_s^0 mass. The first two items address the tendency of b-hadrons to have displaced vertices. The rest address the hard fragmentation function of b-hadrons and its tendency to fragment into a larger number of charged particles.

For category 2, the same parameters are used except the first item since there is now no identified SV. Also, the set of high impact parameter tracks are used instead of the set of tracks or particles coming off of a SV.

For category 3 the same parameters are used as in category 2, except now all charged hadrons from the PV are used.

A likelihood function is then defined as:

$$f^{b,c,q} = p^{b,c,q}(\alpha) \prod_i f_{\alpha}^{b,c,q}(x_i)$$

where α is the category ($\alpha = 1, 2, 3$). x_i are the observed variables, q stands for u,d, and s-quarks as well as gluon jets. $p^{b,c,q}(\alpha)$ are the probability of a b,c, or q jet being in category α . $f_{\alpha}^{b,c,q}(x_i)$ are the probability densities for observables given each type of jet and jet category. And the CSV discriminant (d) is then defined as:

$$d = p_{bkg}(c) \frac{f^b}{f^b + f^c} + p_{bkg}(q) \frac{f^b}{f^b + f^q}$$

where $p_{bkg}(c)$ and $p_{bkg}(q)$ are the probabilities of charm and light flavored jets under the background b-jet free distribution. ($p_{bkg}(c) + p_{bkg}(q) = 1$).

Out of this relatively complex algorithm emerges a single variable discriminant d on the range 0-1. This is what is normally referred to as a jet's CSV. Higher values of d correspond to a higher confidence that a jet is a b-jets. For greater simplicity, b-jet are characterized by one of three working point thresholds.

- The CSV Loose working point (CSVL): has $CSV > 0.244$ and has a nominal 10% light flavor fake rate. Its 80-85% efficient for b-jets depending on the p_T of the jet.
- The CSV Medium working point (CSVM): has $CSV > 0.679$ and has a nominal 1% light flavor fake rate. It's about 70% efficient for b-jets.
- The CSV Tight working point (CSVT): has $CSV > 0.898$ and has a nominal 0.1% light flavor

fake rate. It's about 50% efficient for b-jets.

Both CSV MEDIUM and CSV LOOSE b-jet identification working points (27; 29) are used in this analysis. b-jets must pass the jet selection specified in the previous section, and so also have p_T threshold of 30 GeV/ c .

In particular, an asymmetric b-tag requirement is used where two or three CSV LOOSE b-jets are required, one of which must also pass CSV MEDIUM.

For the 2H channel it is required that the event have exactly two CSV MEDIUM b-jets. For the electroweak channel, the 2H channel is excluded by requiring at most one CSV MEDIUM b-jet and at most one additional CSV LOOSE b-jet. This introduces a gap in CSV that prevents Monte Carlo events from migrating between channels due to small changes in data/MC efficiency scale factors.

Data/MC scale factors are provided by the BID group (28). The scale of the uncertainty in E_T^{miss} introduced by the b-jet scale factors is shown in Figure 4.3.

4.5.4 Monte Carlo b-Tag Efficiency Scale Factors

To make the Monte Carlo correctly model b-tag efficiency, a series of data/MC scale factors are used. These are ratios of the probability that jets in data will pass selection to the probability that simulated jets in Monte Carlo will pass the same selection. Monte Carlo events are then weighted by these scale factors.

The data/MC scale factors and efficiencies are provided by the CMS BID group (28). If there was only a single jet in the event these could be implemented directly, but in the analyses described here there are multiple b-jets with mixed b-tag requirements, and possibly several other light flavored jets. To accommodate this a bit of work needs to be done. A weighted average of scale factors must then be constructed. The average is over every possible combinations of CSV working points that would have allowed the event to pass selection. The weights for the average are the probabilities of each combination.

First a list is made of jets and for each jet assign both a scale factor and a passing efficiency for each CSV working point (including failing all working points). Selecting the correct efficiencies and

scale factors requires MC truth information. For true b-jets, the efficiencies and scale factors are functions of the CSV working point and the jet Pt alone. For light flavor jets, the miss-tag rates and depend only on the CSV working point and the jet Pt, but the scale factors depend on these and on the jet's η .

Next, hypothetical jets are considered with the same efficiencies and scale factors. Then compute the probabilities for this set of hypothetical jets falls into each combination of CSV working points. The contributions from one combination of scale factors, weighted by this probability, is the product of scale factors of the individual jets. This may be more clear in equation form:

$$P_{Data} = \sum_{c \in C} \delta(c \text{ passes selection}) * \prod_{j \in jets} P(CSV(\text{jet } j) = c(j) | p_T, b \text{ truth}) * SF(c(j), p_T, b \text{ truth}, \eta)$$

$$P_{MC} = \sum_{c \in C} \delta(c \text{ passes selection}) * \prod_{j \in jets} P(CSV(\text{jet } j) = c(j) | p_T, b \text{ truth})$$

In the end, events are weighted by:

$$\text{Event Weight} = \frac{P_{Data}}{P_{MC}}$$

Here C is the set of all combinations CSV working points passed by the jets, and c is one particular combination. The delta function selects only combinations that pass the jet and CSV selection. The product is for the j^{th} jet among the jets in the event. $P(CSV(\text{jet } j) = c(j))$ is the probability P of the jet being reconstructed with the particular CSV working point specified by the combination c. It is derived from the b-tag efficiencies assigned to the observed jets, which in turn are functions of the CSV working point, p_T , and the Monte Carlo truth of whether the jet is a b-jet (“b-truth”). The scale factors (SF) are similarly functions of the CSV working point of this jet ($c(j)$), and so on. P_{MC} is effectively a normalization factor for P_{Data} .

Naturally, there are uncertainties on the b-tag scale factors which must be accounted for. Like the jet energy scale uncertainty described in Section 4.5.2, this requires completely reprocessing each Monte Carlo mass point with the scale factors shifted up and down. This gives us a set of three histograms for a search variable: a central value and two more showing the effects of the b-tag

efficiency uncertainty. An example of this can be seen in Figure 4.3. The limit setting machinery described in Section 8.6 uses this information as a shape uncertainty to properly account for the b-tag efficiency uncertainty in the limits.

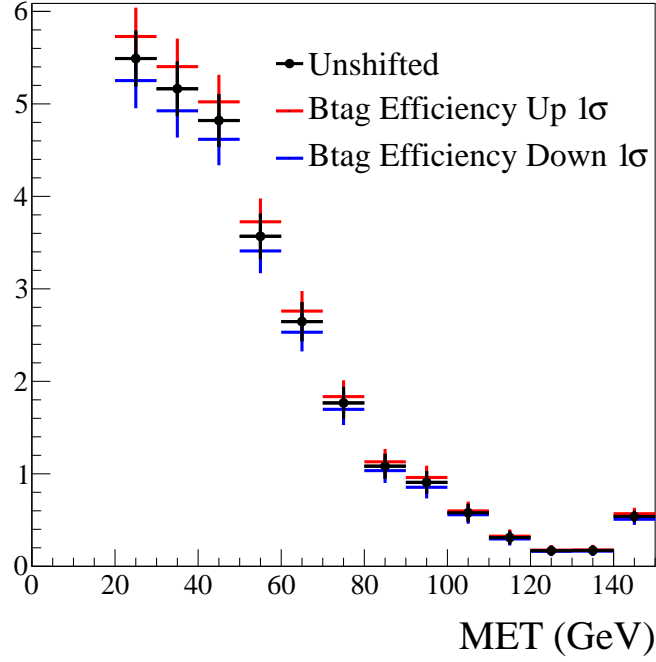


Figure 4.3: Comparison of E_T^{miss} distributions using b-tag scale factors, and with the scale factors shifted up and down by 1σ for mass point $M_{\text{stop}} = 210 \text{ GeV}/c^2$, $M_{\tilde{\chi}_1^0} = 150 \text{ GeV}/c^2$.

4.6 Muons

For muons, the POG Tight muon definition is used (41); the selection requires:

- $p_T > 15 \text{ GeV}/c$
- $|\eta| < 2.4$
- The candidate is reconstructed as a Global Muon,
- Particle-Flow muon id,
- χ^2/ndof of the global-muon track fit < 10 ,

- At least one muon chamber hit included in the global-muon track fit,
- Muon segments in at least two muon stations,
- Its tracker-muon track has transverse impact parameter $d_{xy} < 2$ mm w.r.t. the primary vertex,
- The longitudinal distance of the tracker-muon track with respect to the primary vertex is $d_z < 5$ mm,
- Number of pixel hits > 0
- Cut on number of tracker layers with hits > 5
- Particle Flow based pile up corrected combined isolation (with $\Delta R < 0.4$ cone) < 0.12 .

Here the pile up corrected ($\Delta\beta$) combined isolation is defined as:

$$[I_{ch}^{NoPU} + \max(0, I_{nh} + I_{\gamma} - 0.5 * I_{ch}^{PU})]/p_T$$

Where I_{ch}^{NoPU} is the charged hadron isolation ($dR < 0.4$ cone), I_{nh} is the neutral hadron isolation, I_{γ} is the photon isolation. I_{ch}^{PU} is the p_T sum of the charged particles in the ($dR < 0.4$ cone) cone that do not originate from the primary vertex.

Chapter 5

Signal Simulation

5.1 introduction

Two underlying models are considered: stop-Higgsino models and wino-like Higgsino models. Both assume a compressed spectrum of charginos and neutralinos. Between these, four types of simplified models are simulated:

- Strong production: both stops and Higgsinos are produced. The stops decay to Higgsino by a b-jet and a Higgsino, and the Higgsinos decay entirely to Higgs bosons and goldstinos. This contains Electroweak to HH production. (Recall Figure 2.6.)
- Electroweak production to HH: only Higgsinos are produced which decay entirely to Higgs bosons and goldstinos. (Recall Figure 2.9.)
- Electroweak production to HZ: only Higgsinos are produced. Exactly one Higgsino decays to a Higgs boson and goldstinos while the other decays to a Z boson and goldstino. This is non-physical but is a useful simplified model.
- Electroweak production of HW^\pm . (Recall Figure 2.10 left.)

An additional Electroweak to ZZ channel was simulated for use by other related analyses that enter into the final Higgsino combination in Section 9.5.

Strong production uses two parameters: the mass of the stop and the mass of the Higgsino. Electroweak production has only one parameter: the mass of the neutral Higgsino. The splitting in the compressed spectrum $m_{\tilde{\chi}_2^0} - m_{\tilde{\chi}_1^\pm}$ and $m_{\tilde{\chi}_1^\pm} - m_{\tilde{\chi}_1^0}$ are set to 5 GeV/ c^2 , with the mass ordering $M_{\tilde{\chi}_2^0} > M_{\tilde{\chi}_1^\pm} > M_{\tilde{\chi}_1^0}$. All other super-partners are decoupled and have masses of 4 TeV, except

the gluino (5.05 TeV), H_{heavy} , A , and H^\pm (2 TeV). The goldstino (\tilde{G}) is assumed to be very light, effectively massless with a mass parameter set to 1 GeV/ c^2 . In simulation, the Higgs boson is taken to have a mass of 126 GeV/ c^2 . All Higgs final states are decayed democratically. It is assumed that $\tan \beta = 30$.

The case of Higgsinos decaying entirely to Higgs bosons is the case over a large swath of SUSY parameter space, particularly low $\tan \beta$. However this is not the only case of interest for electroweak production. Sensitivity to any possible branching fraction between Higgs and Z is desired. The case of HZ where exactly one Higgsino decaying to a Higgs and the other only decays to Z is non-physical, but it is a useful simplified model and will play a central role in setting limits as a function of a sliding branching fraction.

Within electroweak Higgsino production, all the particles in the compressed spectrum ($\tilde{\chi}_1^\pm, \tilde{\chi}_2^0, \tilde{\chi}_1^0$) are produced, but $\tilde{\chi}_1^\pm$ and $\tilde{\chi}_2^0$ promptly decay to $\tilde{\chi}_1^0$ and very soft fermions. The relevant pair production processes are: $\tilde{\chi}_1^0 \tilde{\chi}_2^0$, $\tilde{\chi}_1^\pm \tilde{\chi}_1^0$, $\tilde{\chi}_1^\pm \tilde{\chi}_2^0$ ($= \tilde{\chi}_1^\pm \tilde{\chi}_1^0$), and $\tilde{\chi}_1^+ \tilde{\chi}_1^-$. $\tilde{\chi}_1^0 \tilde{\chi}_1^0$ and $\tilde{\chi}_2^0 \tilde{\chi}_2^0$ production have zero cross section.

For those familiar with and interested in simulation machinery, the following steps are common between all aspects of the simulation. Template SLHA files were produced using SUSPECT and their cross sections validated using PROSPINO2. From these, the hard process was simulated in MADGRAPH 5 v.1.5.4 (8). Then the susy particles were decayed using a plugin to MADGRAPH called “SUSY BRIDGE”. Then a script called Exclusive Higgs Decayer (EHD), developed by Rutgers theorists (47), was used to decay the Higgs bosons. The EHD decays the Higgs to chosen decay products oriented in a random direction in the Higgs rest frame. In the process, all spin correlation information of the Higgs bosons are lost. Only the following Higgs decay channels are simulated: $b\bar{b}$, WW^* , ZZ^* , $\tau\tau$, $\gamma\gamma$. This results in Les Houches Event (LHE) format files, one for every mass point and combination of Higgs boson decays.

The assumed Higgs branching ratios are listed in Table 5.1.

Table 5.1: Higgs boson decay branching ratios used.

| Higgs Decay Channel | Branching fraction |
|------------------------------|--------------------|
| $H \rightarrow b\bar{b}$ | 0.561 |
| $H \rightarrow WW$ | 0.231 |
| $H \rightarrow ZZ$ | 0.0289 |
| $H \rightarrow \tau\tau$ | 0.0615 |
| $H \rightarrow \gamma\gamma$ | 0.00229 |

5.2 Stop Production

For the stop analysis, the LHE files are hadronized using PYTHIA 6.4.22 (66) and the CMS detector was simulated using FastSim (1; 35) in CMSSW_5.3.3 to build AODSIMS, which are then ntuplized them using the CMS SUSY ntuplizer. The “official” next-to-leading order (NLO) cross sections, shown in Figure 5.1, are calculated using PROSPINO (15–17; 19; 32; 56; 57).

The signal is simulated for a grid of Higgsino and stop masses. The stop mass ranges from 200-500 GeV in 25 and 50 GeV intervals depending on the region of sensitivity. Higgsino masses were considered in the range of 150-350 in 25 GeV steps.

Different number of Monte Carlo events were generated for each Higgs decay channel considered, shown in Table 5.2. Holding the Higgs decay channel constant, the number of events generated was the same for each mass point. Since the $H \rightarrow b\bar{b}$ decay was the primary interest it received the greatest statistics.

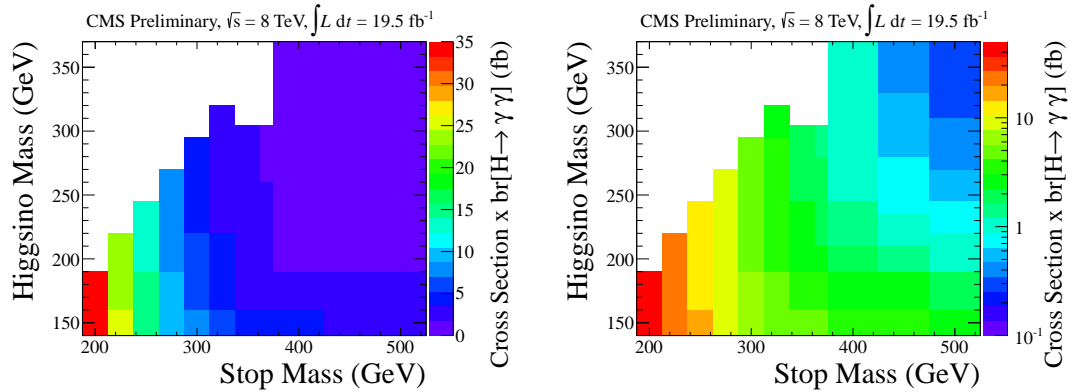


Figure 5.1: Cross section times $\text{Br}(H \rightarrow \gamma\gamma)$ as a function of stop and Higgsino masses for the generated MC points on linear and log scales. These use the “official” NLO cross stop pair production cross sections(32) and branching ratios(30).

Table 5.2: Number of events generated for simulated stop production.

| $H(\gamma\gamma)H(b\bar{b})$ | $H(\gamma\gamma)H(WW)$ | $H(\gamma\gamma)H(ZZ)$ | $H(\gamma\gamma)H(\tau\tau)$ |
|------------------------------|------------------------|------------------------|------------------------------|
| 6000 | 3000 | 300 | 600 |

5.3 Higgsino Electroweak Production

For the Electrohiggs analyses, PYTHIA cards and hadrnoizer files were turned over to CMS Data Ops., who then produced the official AODSIMS. Again, the AODSIMS were ntuplized using the CMS SUSY ntuplizer.

Cross sections are calculated at NLO-NLL for $\sqrt{s} = 8$ TeV using the RESUMMINO code from B. Fuks et al. with CTEQ6.6 PDFs (50; 51). The cross sections include the relevant pair production processes: $\tilde{\chi}_1^0 \tilde{\chi}_2^0$, $\tilde{\chi}_1^\pm \tilde{\chi}_1^0$, $\tilde{\chi}_1^\pm \tilde{\chi}_2^0$ ($= \tilde{\chi}_1^\pm \tilde{\chi}_1^0$), $\tilde{\chi}_1^+ \tilde{\chi}_1^-$.

Higgsinos are simulated for a series of masses: 130 GeV/ c^2 and 150-500 GeV/ c^2 in 25 GeV/ c^2 steps. The cross sections for the simulated points are shown in figure 5.2. The number of Monte Carlo events generated for HH are shown in Table 5.3. The number of events generated for HZ are shown in Table 5.4.

Table 5.3: Number of events generated for simulated electroweak HH production for each range of mass points and considered Higgs decay channels.

| Chargino Mass | $H(\gamma\gamma)H(b\bar{b})$ | $H(\gamma\gamma)H(WW)$ | $H(\gamma\gamma)H(ZZ)$ | $H(\gamma\gamma)H(\tau\tau)$ |
|---------------|------------------------------|------------------------|------------------------|------------------------------|
| 130 | 60,000 | 60,000 | 60,000 | 60,000 |
| 150-500 | 30,000 | 30,000 | 30,000 | 30,000 |

Table 5.4: Number of events generated for simulated electroweak HZ production for each range of mass points and considered Higgs decay channels.

| Chargino Mass | $H(\gamma\gamma)Z$ |
|---------------|--------------------|
| 130 | 120,000 |
| 150,175 | 60,000 |
| 200,225 | 16,000 |
| 250-500 | 30,000 |

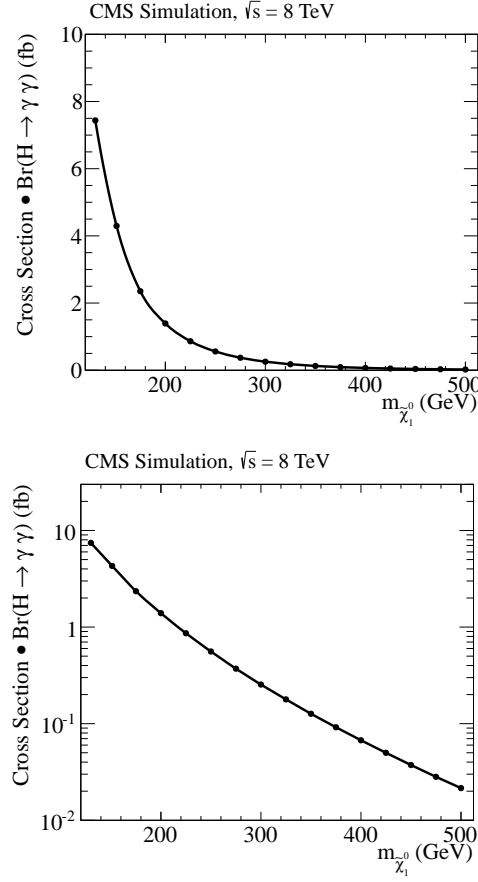


Figure 5.2: Cross section \times $br[H \rightarrow \gamma\gamma]$ for the generated MC points for Higgsino pair production on linear and log scales. These use the “official” NLO production cross sections (32) and branching ratios (30).

5.4 HW^\pm Production

For the wino-like case, the $\tilde{\chi}_2^0 \tilde{\chi}_1^\pm$ production process, seen in Figure 2.10 left, is pursued. Wino mass are considered in the range 130,150-500 in 25 GeV steps. Again, the neutralinos and charginos ($\tilde{\chi}_2^0, \tilde{\chi}_1^\pm, \tilde{\chi}_1^0$) are mass degenerate. The $\tilde{\chi}_1^\pm$ are decayed exclusively to on-shell W’s. Just as before the $\tilde{\chi}_1^0$ decays exclusively to the Higgs to $\gamma\gamma$. (Other analyses in the Higgsino combination use other Higgs decay channels.)

Table 5.5: Number of events generated for simulated electroweak HW production for each range of mass points and considered Higgs decay channels.

| Chargino Mass | $H(\gamma\gamma)W$ |
|---------------|--------------------|
| 130 | 120,000 |
| 150,175 | 60,000 |
| 200,225 | 30,000 |
| 250-400 | 30,000 |
| 425-500 | 60,000 |

Chapter 6

Background Modeling and the Crane

6.1 Background Prediction with the Hgg+X Sideband Method

Standard model background, aside from S.M. Higgs Boson production, are estimates are obtained using the mass side bands of the $M_{\gamma\gamma}$ distribution. The contribution from standard model Higgs boson production is either negligible or estimated using Monte Carlo simulations. The mass side band background method makes the $H \rightarrow \gamma\gamma$ channel trivial to calibrate, which is one of the main attractions of this channel. The $H \rightarrow \gamma\gamma$ decay puts a narrow peak on a simple falling non-Higgs standard model background in the $M_{\gamma\gamma}$ distribution. The narrow resonance guarantees that almost all signal will fall within a narrow window in the $M_{\gamma\gamma}$ distribution centered on the Higgs mass. Events falling outside this window are virtually all from the standard model background. Selecting events in this window greatly reduces the background, which largely compensating for the tiny $H \rightarrow \gamma\gamma$ branching fraction. Selecting events with $M_{\gamma\gamma}$ adjacent to this window provides a pure background population whose kinematics are very similar to the kinematics of the background in the window.

In sketch: for any kinematic variable besides $M_{\gamma\gamma}$, events in the sidebands are used to describe the shape of that kinematic variable's distribution and use the fit to determine the integral of the distribution (its normalization). Then the smoothly falling (non-Higgs) background in the $M_{\gamma\gamma}$ distribution is be fit in order to predict the total background expected in the window. This fit must exclude events in the window from consideration to prevent a signal contributing to the background estimate. This creates a general purpose background method for probing events with a Higgs boson.

Once again, to determine the background to some sensitive variable for a given event selection,

a diphoton mass distribution is made for that selection. Events are categorized based on where they fall on the $M_{\gamma\gamma}$ distribution, producing three populations of events: a signal region in the Higgs window, an upper side band, and a lower side band, as shown in Figure 1.1. The upper mass sideband and the lower mass sideband are defined so that events from these sidebands will be representative of the standard model background in the Higgs window. The sidebands must avoid the Z mass on the low end, and extend to a reasonable upper diphoton mass. In this analysis the lower side band ranges from 103 to 118 GeV/c^2 and the upper side band ranges from 133 to 163 GeV/c^2 .

A fit to the diphoton mass distribution is made, in order to determine the integral of the background in the Higgs mass window. An extended Higgs mass window (118-133 GeV/c^2) is excluded from the fitter's consideration in order to avoid calibrating out any potential signal. Events from either side band are used to produce two distributions of the sensitive variable, which are then normalized to the expected values in the Higgs mass window using the integral of the fit function in the mass window. The non-Higgs standard model background is bracketed by these two estimates, regardless of any correlations between the diphoton mass and the sensitive variable. These two background estimates distributions are averaged to produce a the main standard model background estimate distribution. In order to account for any correlations between the sensitive variable and $M_{\gamma\gamma}$, the difference between them is added in quadrature, bin-by-bin. The bin-by-bin uncertainty then represents both the statistical uncertainty and uncertainty of bracketing the background between the side bands. The details of how the uncertainty in the background estimate is computed are explained in the next section (6.2).

For this analysis, the signal region was taken to be $M_{\gamma\gamma}$ between 120 GeV/c^2 and 131 GeV/c^2 . At time of this study, the best estimate of the Higgs boson mass was between 125 and 126 GeV/c^2 , so 125.5 GeV/c^2 was taken as the best-guess. This range was conceived as a 11 GeV/c^2 wide window centered on the Higgs boson mass to ensure at least 80% of signal events. Monte Carlo simulations of the CMS photon resolution suggested a 5 to 7 GeV/c^2 window would have been optimal, reducing the background by 36% to 54%, but it was not clear that the simulated photon resolution adequately

described the detector's resolution. The width of this window is controlled by the amount of energy mis-measurement that is typical in the CMS detector. The amount of background scales approximately in direct proportion to the width of the window, so in an ideal detector this window would be on the order of the Higgs natural width ($\sim 4 \text{ MeV}/c^2$ (67)) with ultra-low background noise. It should be immediately apparent that improvements in photon resolution, and even improvements on the uncertainty in the typical photon mis-measurement, present significant opportunities to improve these results.

The lower side band was taken to be $M_{\gamma\gamma}$ between $103 \text{ GeV}/c^2$ to $118 \text{ GeV}/c^2$ and the upper side band was taken to be $133 \text{ GeV}/c^2$ to $163 \text{ GeV}/c^2$. $2 \text{ GeV}/c^2$ buffer regions lie between the signal region and the two side bands to let the tails of a signal distribution die out and not contaminate the side bands. The widths of the side bands were chosen to create politically-appealing round numbers, 15 and 30 GeV/c^2 for the lower and upper side bands respectively, which also satisfy certain physics requirements. The low-mass end of the lower side band ($103 \text{ GeV}/c^2$) is limited by the location and width of the Z boson resonance. If the lower edge of the lower sidebands was any lower, $Z \rightarrow ee$ events with both electrons faking photons would be introduced into the sideband, introducing kinematic behavior dissimilar from the background in the Higgs window and inflating the systematic uncertainty. The high-mass edge of the upper side band ($163 \text{ GeV}/c^2$) is far less constrained. The upper side band should be as wide as possible for statistical power but must be cutoff at a reasonable value so events in the sideband have kinematics similar to the background in the signal window. The width of the upper side band, therefore, is a tradeoff between statistical uncertainty and systematic uncertainty.

The range of the fit curve was chosen to be the same as the range of the side bands. This was not necessary, since the range of the fit mathematically disjoint from the size of the side bands, however, this choice is physically reasonable and saves readers from some confusion.

A power law of the form $A * M_{\gamma\gamma}^{-b}$ is used to describe the diphoton mass distribution. This is a physically sensible choice since the background is dominated by QCD events faking photons. The fits for the two-Higgs channel and the electroweak channel are shown in in Figures 9.14 and 9.26.

The uncertainty in background estimate from the choice of fit function is negligible compared to the statistical uncertainty in the fit, particularly in low-statistics cases such as the two-Higgs channel.

$$N[\text{events}/\text{GeV}/c^2] = 3.36 * M_{\gamma\gamma}^{-0.55}$$

the integral over the Higgs mass window gives a standard model background estimate of 2.5 ± 1.3 events (53% uncertainty). For the electroweak channel the fit function is

$$N[\text{events}/\text{GeV}/c^2] = 1.9 * 10^8 * M_{\gamma\gamma}^{-3.1}$$

the integral over the Higgs mass window gives a standard model background estimate of 633 ± 13 events (2% uncertainty).

This method does not capture the effects of standard model Higgs boson production, which produces signal events exclusively in the signal window. Fortunately, the standard model Higgs is usually singly produced, and either very small or entirely negligible for searches for Higgs in association with other objects. Monte Carlo simulations, described in Chapter 5, are relied upon to describe the standard model Higgs contribution, and likewise rely on theoretical predictions of the Higgs production cross section for normalization. Currently these Higgs production cross sections come with large uncertainties since experimental measurements have only shown the Higgs resonance to be coarsely standard-model like. For our purposes, these uncertainties are negligible.

6.1.1 Comments on 2D Fitting as an Alternative Background Method

One of the difficulties with the diphoton sideband background method is that the difference in the sidebands is taken as a systemic uncertainty, even though for low statistics the difference may be statistically driven. A suggested method for eliminating this inflation of uncertainty is to use a 2D fit of M_{gg} and the sensitive variable. This has the difficulty of introducing an additional systematic uncertainty from assuming a parametrized form of each 2D space considered. This method was considered and it was concluded that it would not deliver significant improvements while greatly complicating the analysis.

6.2 Example Background Estimation Calculation

To demonstrate the background calculation in detail, let's consider one bin and see how the background estimate and its uncertainties are determined. Let's take for example the first bin ($E_T^{\text{miss}} = 0\text{-}20$ GeV) of the category with 2 b-jets whose di-b-jet mass is on the Higgs mass. The background estimates we conclude are the left plot in Figure 9.4. And in Table 9.2 we see the total background estimate is 5.0 ± 1.6 events. For this category, the upper sideband contained 13 events and the lower sideband contained 28 events in total. Of those, 6 events from the upper sideband and 13 events from the lower sideband fall in this E_T^{miss} bin.

We assume gaussian statistics, so that the uncertainty in these numbers is simply their square roots. We then fit the diphoton mass distribution with a power law to obtain the background integral in the tag region. The fit uses a two-parameter power-law log likelihood fit. The uncertainty of the integral is calculated from the uncertainties of the fit parameters and the fit's covariance matrix. The fit is the center plot in Figure 9.2. The fit value obtained is 10.8 ± 2.1 . We now scale the sidebands to the integral of the background in the tag region.

$$Bkg_L = bin_L * \frac{\int_{Tag} Fit}{\Sigma_{LSB} M_{gg}} = 13 * \frac{10.8}{28} = 5.02$$

$$Bkg_U = bin_U * \frac{\int_{Tag} Fit}{\Sigma_{USB} M_{gg}} = 6 * \frac{10.8}{13} = 4.99$$

where Bkg_L and Bkg_U are the background estimates from the lower and upper sidebands respectively. bin_L and bin_U are the contents of the E_T^{miss} 0-20 GeV Bin for this channel for the lower and upper sidebands respectively. $\int_{Tag} Fit$ is the integral from the fit which estimates the total (for all E_T^{miss} bins) background in the tag region. $\Sigma_{LSB} M_{gg}$ and $\Sigma_{USB} M_{gg}$ are the total number of events in the lower and upper sidebands respectively.

bin_L is contained within $\Sigma_{USB} M_{gg}$, and likewise for bin_U , so to prevent double counting when handling the uncertainty calculations $\Sigma_{USB} M_{gg}$ must be separated into statistically independent

quantities.

$$Bkg_L = \frac{bin_L}{bin_L + (\Sigma_{LSB}M_{gg} - bin_L)} \int_{Tag} Fit$$

$$Bkg_U = \frac{bin_U}{bin_U + (\Sigma_{USB}M_{gg} - bin_U)} \int_{Tag} Fit$$

Here it is useful to consider the following lemma:

Lemma: If A and B are statistically independent with $\sigma_A = \sqrt{A}$ and $\sigma_B = \sqrt{B}$, and $C = \frac{A}{A+B}$,

then

$$\left(\frac{\sigma_C}{C}\right)^2 = \frac{1}{A} - \frac{1}{A+B} \quad (6.1)$$

Proof: Let $D = B/A$ then

$$C = \frac{1}{1+D}$$

$$\left(\frac{\sigma_D}{D}\right)^2 = \left(\frac{\sigma_A}{A}\right)^2 + \left(\frac{\sigma_B}{B}\right)^2 = \frac{1}{A} + \frac{1}{B} = \frac{A+B}{AB}$$

$$\begin{aligned} \left(\frac{\sigma_C}{C}\right)^2 &= \left(\frac{\sigma_{(1+D)}}{1+D}\right)^2 = \left(\frac{\sigma_D}{1+D}\right)^2 \\ &= \frac{D^2}{(1+D)^2} \frac{A+B}{AB} = \frac{B^2}{(A+B)^2} \frac{A+B}{AB} \\ &= \frac{B}{A(A+B)} = \frac{(B+A) - A}{A(A+B)} = \frac{1}{A} - \frac{1}{A+B} \end{aligned}$$

Using this we obtain the following expressions for the uncertainties:

$$\left(\frac{\sigma_{Bkg_L}}{Bkg_L}\right)^2 = \frac{1}{bin_L} - \frac{1}{\Sigma_{LSB}M_{gg}} + \left(\frac{\sigma_{integ.}}{\int_{Tag} Fit}\right)^2$$

$$\left(\frac{\sigma_{Bkg_U}}{Bkg_U}\right)^2 = \frac{1}{bin_U} - \frac{1}{\Sigma_{USB}M_{gg}} + \left(\frac{\sigma_{integ.}}{\int_{Tag} Fit}\right)^2$$

$$\sigma_{Bkg_L} = Bkg_L * \sqrt{\frac{1}{bin_L} - \frac{1}{\sum_{LSB} M_{gg}} + \left(\frac{\sigma_{integ.}}{\int_{Tag} Fit} \right)^2} = 5.02 * \sqrt{\frac{1}{13} - \frac{1}{28} + \left(\frac{2.1}{10.8} \right)^2} = 1.41$$

$$\sigma_{Bkg_U} = Bkg_U * \sqrt{\frac{1}{bin_U} - \frac{1}{\sum_{USB} M_{gg}} + \left(\frac{\sigma_{integ.}}{\int_{Tag} Fit} \right)^2} = 4.99 * \sqrt{\frac{1}{6} - \frac{1}{13} + \left(\frac{2.1}{10.8} \right)^2} = 1.78$$

Now we take the average of these two background estimates.

$$Bkg_{avg} = \frac{Bkg_U + Bkg_L}{2} = \frac{4.99 + 5.02}{2} = 5.01$$

The integral of the fit and its uncertainty appear in both Bkg_U and Bkg_L , so to compute the uncertainty in the background without double counting we must factor out the integral of the fit.

$$Bkg_{avg} = \frac{1}{2}(Bkg_L + Bkg_U) = \frac{1}{2} \left(\frac{bin_L}{\sum_{LSB} M_{gg}} + \frac{bin_U}{\sum_{USB} M_{gg}} \right) \int_{Tag} Fit$$

It's useful to re-express this with a change of variables:

$$U \equiv \frac{bin_U}{\sum_{USB} M_{gg}} = \frac{6}{13} = 0.4615$$

$$L \equiv \frac{bin_L}{\sum_{LSB} M_{gg}} = \frac{13}{28} = 0.4642$$

$$Bkg_{avg} = \frac{1}{2}(U + L) \int_{Tag} Fit$$

so that $Bkg_L \equiv L * \int_{Tag} Fit$ and $Bkg_U \equiv U * \int_{Tag} Fit$. Again, the numerator and denominator are correlated so we partition the denominator into statistically independent quantities as was done above.

$$\left(\frac{\sigma_L}{L} \right)^2 = \frac{1}{bin_L} - \frac{1}{\sum_{LSB} M_{gg}}$$

$$\left(\frac{\sigma_U}{U} \right)^2 = \frac{1}{bin_U} - \frac{1}{\sum_{USB} M_{gg}}$$

$$\sigma_L = L \sqrt{\frac{1}{bin_L} - \frac{1}{\sum_{LSB} M_{gg}}} = \frac{13}{28} \sqrt{\frac{1}{13} - \frac{1}{28}} = 0.0945$$

$$\sigma_U = U \sqrt{\frac{1}{bin_U} - \frac{1}{\sum_{USB} M_{gg}}} = \frac{6}{13} \sqrt{\frac{1}{6} - \frac{1}{13}} = 0.1383$$

The average has uncertainty

$$\left(\frac{\sigma_{Bkg_{avg}}}{Bkg_{avg}} \right)^2 = \frac{\sigma_U^2 + \sigma_L^2}{(U + L)^2} + \left(\frac{\sigma_{integ.}}{\int_{Tag} Fit} \right)^2$$

$$\begin{aligned} \sigma_{Bkg_{avg}} &= Bkg_{avg} \sqrt{\frac{\sigma_U^2 + \sigma_L^2}{(U + L)^2} + \left(\frac{\sigma_{integ.}}{\int_{Tag} Fit} \right)^2} \\ &= \frac{1}{2} \sqrt{\left((\sigma_U^2 + \sigma_L^2) \sigma_{integ.} + (U + L)^2 \int_{Tag} Fit \right)} \\ &= \frac{1}{2} \sqrt{((0.1383^2 + 0.0945^2) 2.1 + (0.4615 + 0.4642)^2 10.8)} \\ &= 1.33 \end{aligned}$$

But the two predict sidebands predict different background estimates so we incorporate half the difference between the two estimates as a systematic uncertainty to get our final background estimate σ_{Bkg} .

$$\sigma_{Bkg} = \sqrt{\sigma_{Bkg_{avg}}^2 + diff.^2} = \sqrt{1.33^2 + \left(\frac{|5.02 - 4.99|}{2} \right)^2} = 1.33$$

Which is exactly what appears in Table 9.2.

All bins of the histogram use the same estimate for the integral of the background in the signal region, so the bin should not be treated as statistically independent. Therefore for setting limits, the limit setter is provided with a modified version of the histograms seen in Figure 9.4 that have the uncertainty from the limit set to zero. The uncertainty from the limit is reintroduced as an overall uncertainty in the normalization of the background. This procedure changes our limit results by less than 1%.

6.3 The Crane Framework



Figure 6.1: The logo of the Crane analysis framework.

The Crane analysis framework is a software system which implements the Higgs to diphoton side band background method and accompanying analysis, and takes advantage of the generality of the side band method to mass produce associated Higgs production analyses. Centrally, it performs a side-band analysis on a grid of channels and kinematic variables and produces plots and limits. It then performs the same set of analyses to Monte Carlo and compares the background prediction, MC, and potentially the data as well, both as histograms and as limits. When the signal region is blinded, comparing signal to background in this way allows rapid searches for sensitive channels and kinematic variables.

The Crane uses two lists of cuts and kinematic. All parts of the analysis are performed for every cut and for every kinematic variable. Typically the analysis must also be done for data and for every MC mass point. A typical optimization search may involve fifty cuts and fifty kinematic variables considered for three MC mass points in each iteration. This result in over 10,000 automatically generated plots, but a manageable total volume of data less than 2GB and requires only a few hours of computing time. A strict file naming convention is employed to organize and locate plots. Now that nearly every imaginable piece of desirable information has been generated, the task of optimizing and exploring physics becomes the task of browsing a well ordered series of plots on disk. (Finder on Mac OS X is particularly good at this.) Two or three iterations of this, editing the

channel search parameters with each iteration, are typically sufficient to deeply explore and optimize a search strategy.

Some of the features of the Crane analysis framework:

- Encompasses nearly every feature of the analysis:
 - analyzing ntuples,
 - implementing physics object corrections,
 - the developing a search strategy,
 - performing the core analysis,
 - uncertainty analysis,
 - plot production
 - limit setting
- Rapid sensitivity scans over selection criterion and kinematic variables
- Rapid exploration of data once a channel is unblinded.
- Instant turn around time for most plot requests. Simply retrieve the plot from disk.
- Easily performing several analyses in parallel.
- Reliably and rapidly migrate an analysis procedure from one analysis to another.
- Extreme flexibility in computing time, from short targeted exploration runs to more intensive and inclusive scans.
- Ability to easily and rapidly switch between Monte Carlo.
- Automatic generation of publication-quality histograms and limit plots.
- Full suite of handling
 - Produce data cards

- Automatically generate supporting files needed to run limit cards
 - Automatic collection of limit setting output
 - Produces expected limit comparison plots for grids of channel vs. kinematic variable.
 - Produces limit plots
- Virtually all settings are controlled through configuration files rather than hard coded.
 - Can produce data skims
 - Written for root, C++.

Some History:

The Crane analysis framework was developed in the course of searching for stop production. Development and analysis occurred simultaneously starting in August of 2012, 3 weeks after the discovery of the Higgs boson, and continued for seven months. Publication proceedings then took an additional seven months. When the Crane framework was next called upon for the Higgsino analysis, the physics analysis was entirely completed in three days, followed by ten months (and counting) of publication proceedings. This despite the fact that the methodology and formatting had already been fully approved by a previously published analysis. In the mean time, the Crane generated thousands of blinded, largely complete versions of the analysis in order to search for the most sensitive ways to approach our target signals. The results of a select few of these are included in the analysis chapter. Internal to CMS, the Crane was also used to explore a suspicious excess in a colleague's analysis and rapidly determine it to be background-like. (Subsequently additional data drastically reduced the apparent significance of that excess.)

The time required to publish is a major impediment to productivity, consuming 99% of the analyzer's time. Further refinements in the software will certainly increase this percentage. The nearly instantaneous nature of HggX searches suggests a publication strategy where searches for many disparate signals published in a single paper. In particular, natural stops, Higgsino, general di-Higgs production, tth, VBF, heavy Higgs, and various exotic $h(gg)+x$ searches can be performed and published simultaneously about as easily as performing any one of them individually.

The Crane source code can be found on Git Hub here: https://github.com/fiveisgreen/FNAL_Crane.

6.4 SM Higgs Background

The diphoton side band method accounts for all standard model background processes except for the standard model Higgs background. The standard model Higgs is usually singly produced, so selecting Higgs-like events with additional objects typically renders the Higgs background negligible. This is not the case for diphoton + MET and diphoton + light flavored jet searches, where the selection does not suppress the standard model Higgs background.

The standard model Higgs background is analyzed using FullSim Monte Carlo produced and approved by the CMS collaboration. Four production channels are considered, as summarized in Table 6.1. The Higgs boson mass is taken to be $126 \text{ GeV}/c^2$. Cross sections are computed to NNLL for QCD and to NLO for electroweak processes. A 30% uncertainty in the Higgs production cross section is applied due to the field's nascent experimental understanding of the Higgs. This large uncertainty is still typically has no effect on over all limits since the Higgs contribution is thoroughly suppressed by additional object cuts.

Figure 6.2 shows the standard model Higgs contributions to the two-Higgs channel. This is a negligible contribution, which is to be expected since the standard model Higgs is singly produced. However, for the electroweak channel the contribution from the standard model Higgs is of more concern since light flavored jets are fare more common. It contributes ten percent (0.1 events) to the most sensitive E_T^{miss} bin. The background estimates and limit setting procedures for the electroweak channel take the SM Higgs background into account using Fullsim Monte Carlo. The SM Higgs background estimate in the electroweak channel is shown in Figure 6.3.

Table 6.1: The SM Higgs production channels, datasets, and cross sections used in this analysis.

| Production Channel | Dataset | x-sec [pb] |
|---------------------|--|------------|
| Gluon-gluon fusion | /GluGluToHToGG_M-126.8TeV-powheg-pythia6/ Summer12_DR53X-PU_S10_START53_V7A-v1/AODSIM | 19.22 |
| Vector boson fusion | /VBF_HToGG_M-126.8TeV-powheg-pythia6/ Summer12_DR53X-PU_S10_START53_V7A-v1/AODSIM | 1.544 |
| HW^\pm/PHZ | /WH_ZH_HToGG_M-126.8TeV-pythia6/ Summer12_DR53X-PU_S10_START53_V7A-v1/AODSIM | 1.0625 |
| $t\bar{t}h$ | /TTH_HToGG_M-126.8TeV-pythia6/ Summer12_DR53X-PU_S10_START53_V7A-v1/AODSIM | 0.1271 |

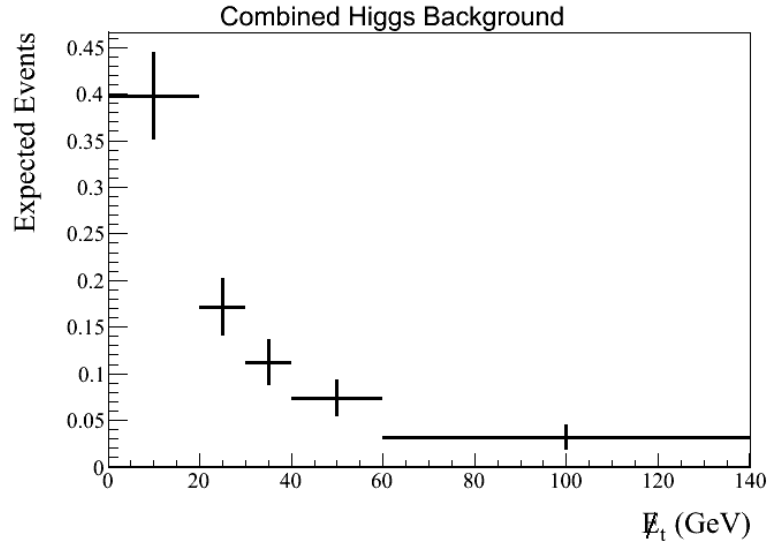


Figure 6.2: Expected standard model Higgs boson background contribution to the two-Higgs channel from FullSim Monte Carlo in combined gluon-gluon fusion, vector boson fusion, and vector boson + Higgs boson production channels. top-top-Higgs is negligible compared to these three production channels. In total, the standard model Higgs production is a negligible background for this channel.

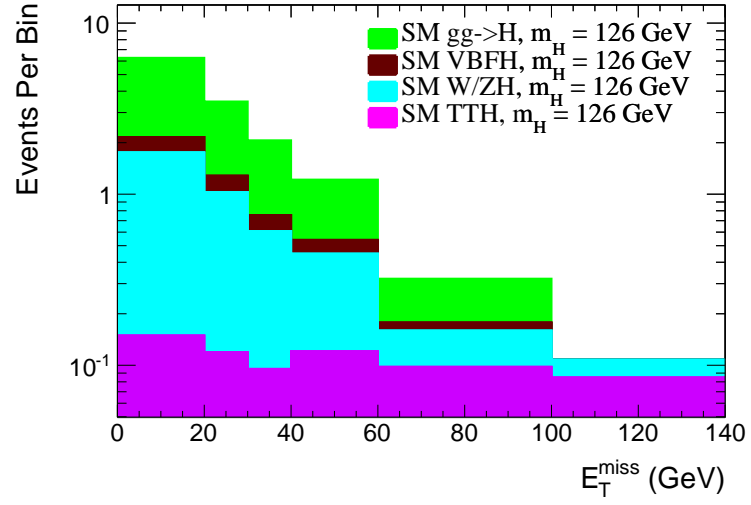


Figure 6.3: Expected standard model Higgs boson background contribution to the electroweak channel from FullSim Monte Carlo in combined gluon-gluon fusion, vector boson fusion, vector boson + Higgs boson production, and top-top-Higgs production channels. In total, the standard model Higgs production is a negligible background for this study.

Chapter 7

Datasets and Trigger

7.1 Data Sets

The amount of data collected by CMS in 2012 is vast and heterogeneous. For this line of analyses, the events of interest are those events containing two isolated photons (in addition to all other objects). These events form the DoublePhoton data sets. For early in 2012 data the single-photon data set is used, that is, sets of data required to contain one isolated photon (in addition to other photons and other objects). The names of these data sets are listed in Table 7.1, although these will only be useful to other members of the CMS collaboration. The data is reformatted CMS Susy group's ntuplizer, which, among other things, computes various derived quantities. It is then skimmed to select events remotely relevant to these analyses to achieve a tractable file size is tractable. These datasets represents $19.7 \text{ fb}^{-1} \pm 4.4 \% (33)$ of proton collision data. Some plots are marked 19.5 fb^{-1} reflecting a different official stance within CMS on how much luminosity the data represents.

Table 7.1: Datasets used in the analysis

| |
|--|
| <i>/Photon/Run2012A – 13Jul2012 – v1/AOD</i> |
| <i>/Photon/Run2012A – recover – 06Aug2012 – v1/AOD</i> |
| <i>/DoublePhoton/Run2012B – 13Jul2012 – v1/AOD</i> |
| <i>/DoublePhoton/Run2012C – PromptReco – v1/AOD</i> |
| <i>/DoublePhoton/Run2012C – PromptReco – v2/AOD</i> |
| <i>/DoublePhoton/Run2012D – PromptReco – v1/AOD</i> |

7.2 Triggers Used

Four high level triggers (HLT) are used. These triggers are listed in Table 7.2. Each trigger was present in CMS online running throughout 2012 data collection. The triggers require events to have

two photons, one of which must have a transverse energy of at least 36 GeV, and the second must have a transverse energy of at least 22 GeV. The calculations energy used by the HLT are crude and is modified later in the analysis, so the energy cut imposed by the triggers is smeared. The energy smearing effects, also known as turn-on-curves, for these triggers can be seen in Figure 7.1. Since only photon pairs with a mass near the Higgs mass are of interest, the turn on effects do not effect this analysis. The triggers require the photons to be slightly isolated. The trigger isolation requirements are strictly looser than the offline photon selection described in Section 4.4.

Table 7.2: Triggers used in the analysis

| |
|--|
| <i>HLT_Photon36_CaloId10_Iso50_Photon22_CaloId10_Iso50</i> |
| <i>HLT_Photon36_CaloId10_Iso50_Photon22_R9Id85</i> |
| <i>HLT_Photon36_R9Id85_Photon22_CaloId10_Iso50</i> |
| <i>HLT_Photon36_R9Id85_Photon22_R9Id85</i> |

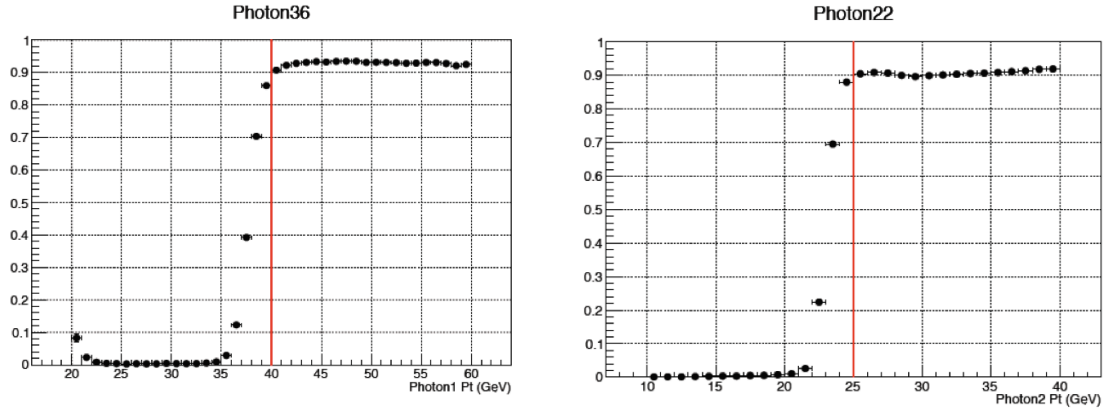


Figure 7.1: Turn-on curves for the leading and sub-leading photon candidates.

The Monte Carlo must accurately model the HLT effects. This is achieved through a cut-based emulation of the triggers. A 0.1% uncertainty is applied to the HLT efficiency to the final limit result to account for systematic uncertainty in this process.

For simulated stop signals, the HLT efficiency was 76 to 78% depending on the stop and Higgsino masses. For simulated Higgsino, the HLT efficiency was between 75 and 80% depending on the Higgsino mass point.

Chapter 8

Analysis Design

8.1 SUSY Partners of the Top Quark (Stops)

8.1.1 Event Selection

For the stop pair production signal described in Section 2.2.3, our signal consists of two Higgs boson decays with two additional b-jets in the event. We restrict our selves to the case where one of the Higgs decays to two photons and use this as a tag. Signal photons will tend to have low rapidity and tend to land in the center of the CMS detector. The other Higgs boson will likely decay to two b-quarks. So we expect at least two b-jets and up to four b-jets in the event and a b-jet resonance. Unfortunately b-tagging is not very reliable so we should expect to miss some of the b-jets. So we will look first at the general case with two $H \rightarrow \gamma\gamma$ like photons and two b-jets. Then further subdivide that case into three channels to gain better sensitivity.

To enforce central photons and reduce background noise, events are required to have at least two photons in the barrel ($|\eta| < 1.4442$). Restricting photons to the barrel sharply increases the signal to background ratio, as can be seen in Figure 8.1. In order to remove HLT trigger turn on effects seen in Figure 7.1, the photons are required to pass $E_T > 40$ GeV and 25 GeV thresholds on the leading and sub-leading photons respectively. The event is then required to have at least one b-jet passing MEDIUM working point selection, and at least one other b-jet passing the LOOSE selection. All combinations of CSV requirements were explored and 1 CSVM + 1 CSVL was selected to balance a high signal to background ratio and signal efficiency.

To tag event as a $H \rightarrow \gamma\gamma$ like, the invariant mass of the two leading photons is required to be between 120 and 131 GeV/ c^2 . Lower and upper sidebands are defined, respectively, as having the

diphoton mass in range 103 to 118 GeV/c^2 and 133 to 163 GeV/c^2 . The diphoton mass distribution and fit for this base selection is shown in Figure 9.1. Figures 8.2 - 8.9 show kinematic distributions for several signal points after the selection requirements and using the fit from Figure 9.1.

We select three signal mass points as working points: $M_{\tilde{t}} = 350 \text{ GeV}/c^2$, $M_{Higgsino} = 135 \text{ GeV}/c^2$ is our most optimistic scenario and has a high cross section. The proximity of the Higgsino mass to the Higgs mass produces significantly different behavior than for other mass points. In particular, it frequently has little E_T^{miss} . $M_{\tilde{t}} = 300 \text{ GeV}/c^2$, $M_{Higgsino} = 290 \text{ GeV}/c^2$ is the case where the \tilde{t} and Higgsino are close in mass. $M_{\tilde{t}} = 400 \text{ GeV}/c^2$, $M_{Higgsino} = 300 \text{ GeV}/c^2$ is typical of higher mass points.

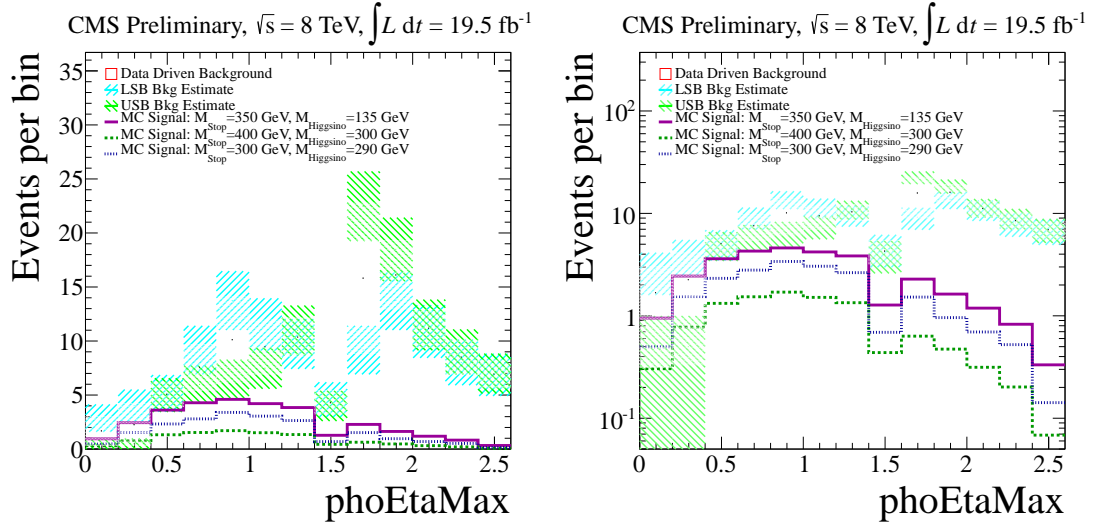


Figure 8.1: Maximum of the absolute values of the two photon's pseudo-rapidities (color points) from expected signal normalized to the integrated luminosity on linear and log scales. The shaded rectangles show the background estimate from the sidebands. For events below 1.4442, both photons are restricted to the barrel. Requiring this dramatically reduces background.

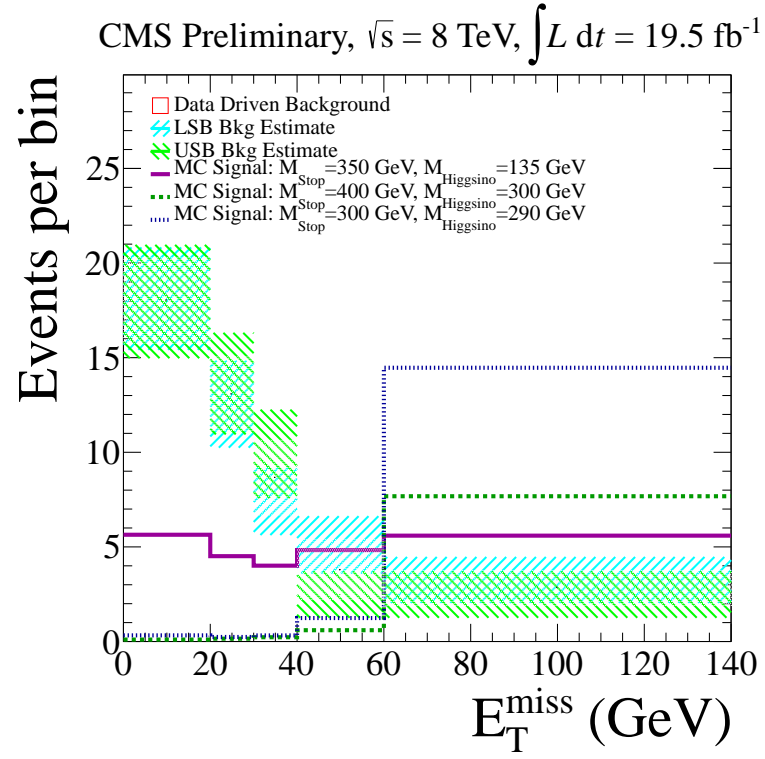


Figure 8.2: E_T^{miss} of expected signal (color points) normalized to the integrated luminosity. The shaded rectangles show the background estimate from the sidebands.

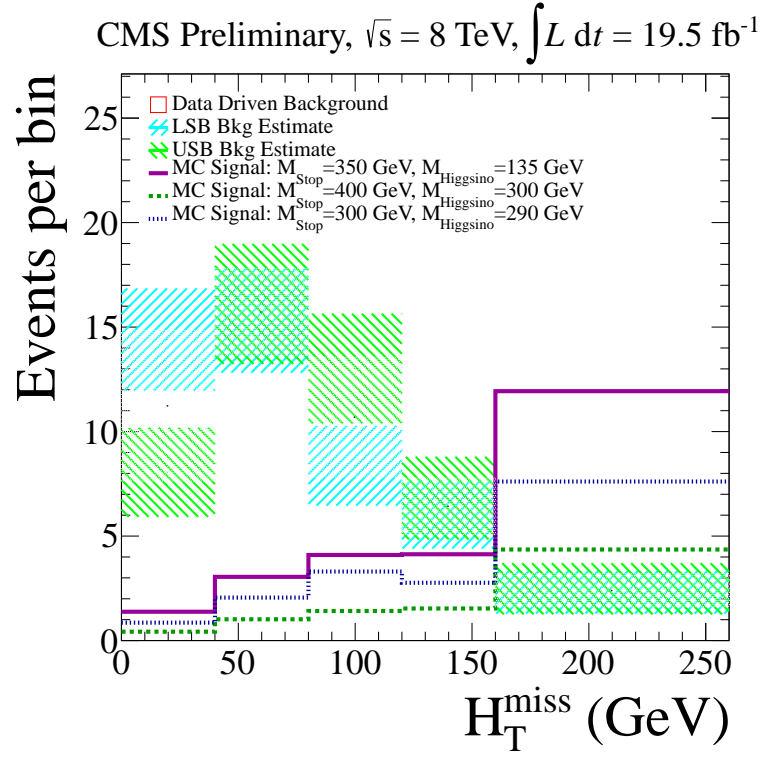


Figure 8.3: MHT of expected signal (color points) normalized to the integrated luminosity. MHT is the transverse momentum the vector sum of all jets with $p_T > 30 \text{ GeV}/c$. The shaded rectangles show the background estimate from the sidebands.

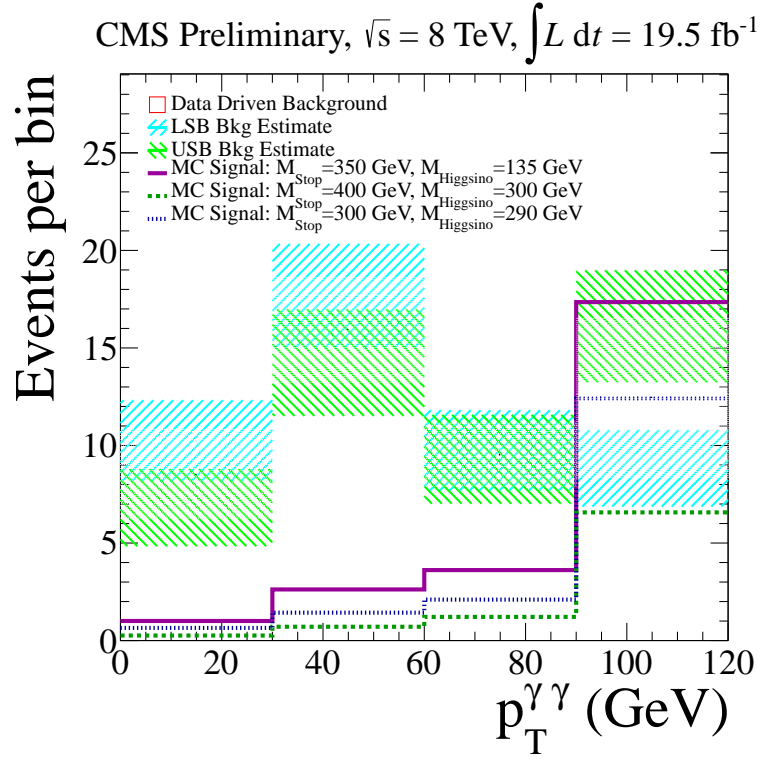


Figure 8.4: Transverse momentum of the diphoton system for expected signal (color points) normalized to the integrated luminosity. The shaded rectangles show the background estimate from the sidebands. Both photons satisfy the photon definition described in Section 4.4.

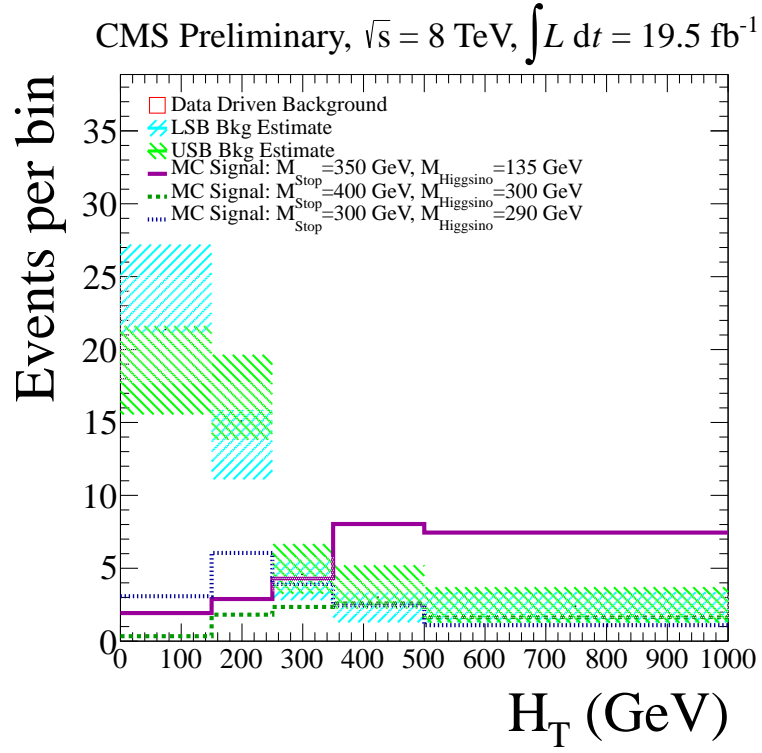


Figure 8.5: H_T of expected signal (color points) normalized to the integrated luminosity. H_T is the scalar sum of the p_T of all jets with $p_T > 30 \text{ GeV}/c$. The shaded rectangles show the background estimate from the sidebands.

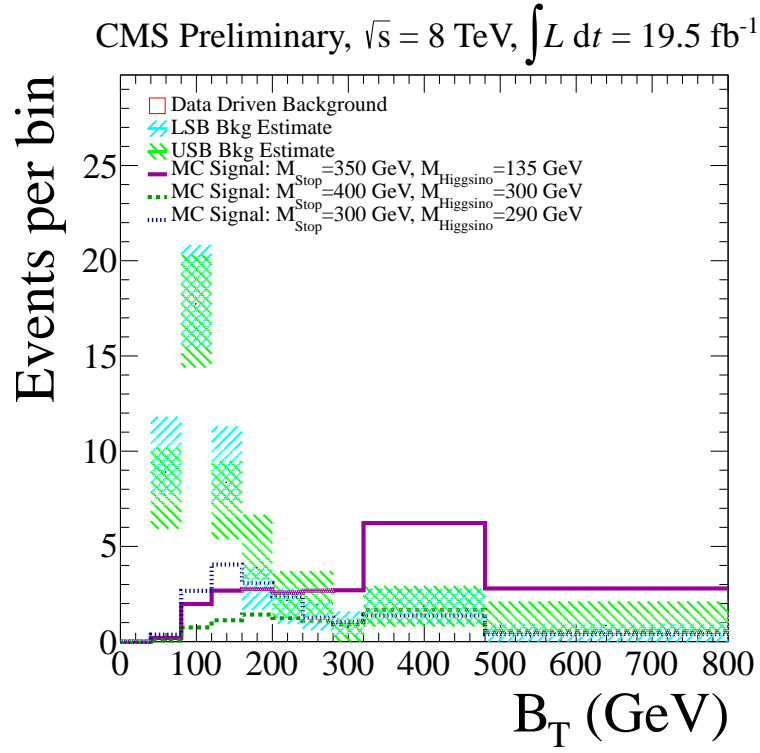


Figure 8.6: Scalar sum of transverse momenta of all b-jets passing the CSV-Loose working point, for expected signal (color points) normalized to the integrated luminosity and the data driven background estimates. The shaded rectangles show the background estimate from the sidebands and the red rectangles are the combined data driven background estimate.

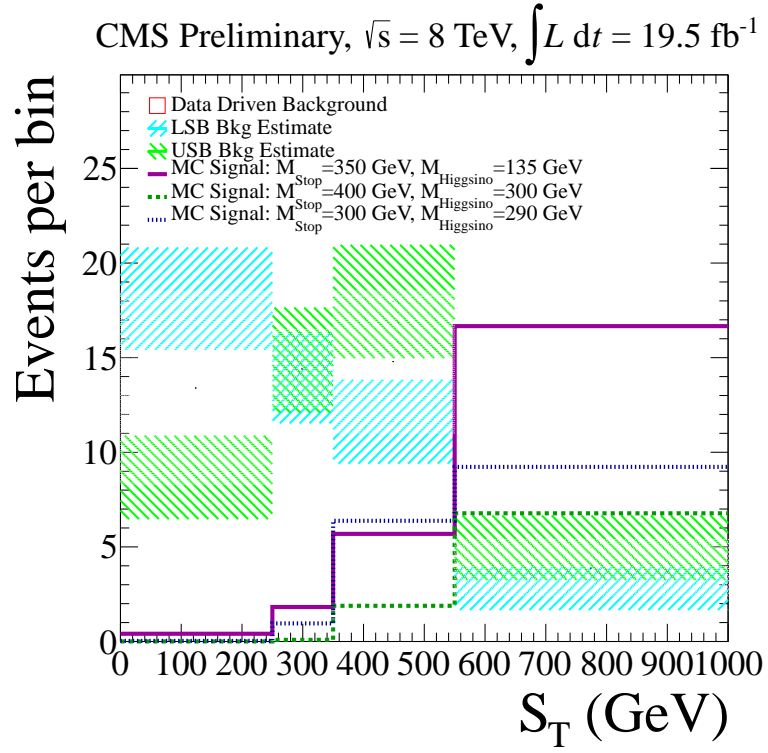


Figure 8.7: S_T for expected signal (color points) normalized to the integrated luminosity. S_T is the scalar sum of the p_T of all the jets in the event with $p_T > 30 \text{ GeV}/c$, photons passing the loose photon definition, and E_T^{miss} . The shaded rectangles show the background estimate from the sidebands.

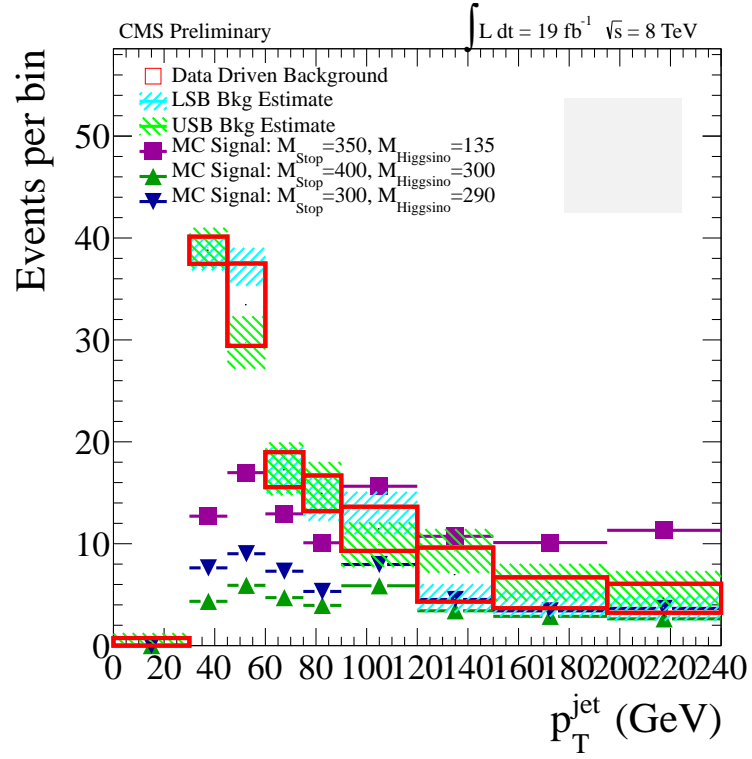


Figure 8.8: Transverse momentum of all jets with $p_T > 30 \text{ GeV}/c$ for expected signal (color points) normalized to the integrated luminosity and the data driven background estimates. The shaded rectangles show the background estimate from each sideband and the red rectangles are the combined data driven background.

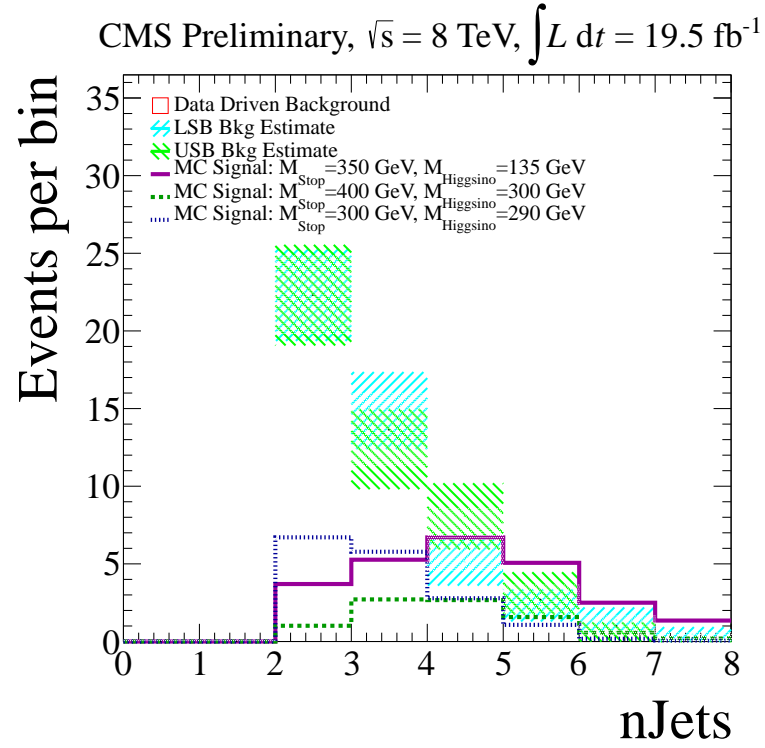


Figure 8.9: Number of jets for expected signal (color points) normalized to the integrated luminosity. The shaded rectangles show the background estimate from the sidebands.

Figures 8.2 - 8.9 show several kinematic variables with some discriminating power between a stop signal and the standard model background. S_T , B_T , H_T and Jet p_T are fairly strong for the lowest mass point but are not as effective for the nearly mass degenerate case. MHT and particularly E_T^{miss} are more versatile, providing good discriminating power against all three working points. For this reason E_T^{miss} was chosen as the main discriminating variable for exploring the stop signal.

$p_T^{\gamma\gamma}$ is not particularly useful for a stop search due to the high background in the last bin. But this will be useful later in the Higgsino search and so is included for comparison. Figure 8.9 shows that the number of jets in the background falls quickly while for the signal 3 to 4 jets are expected. This confirms suspicion that adding a jet cut can substantially increase the signal to background ratio. The signal efficiency for the base selection is displayed in the lower-left plot of Figure 8.12.

To maximize sensitivity, the base selection channel are further partition into three event categories:

1. events with at least one more LOOSE b-jet in addition to the two (i.e. events with three or more b-jets)
2. events for which the invariant mass of the two b-jets is within Higgs mass window, from 95 to 155 GeV/ c^2
3. all other events (two b-jets off the Higgs mass window)

The efficiencies for the selection in each category are shown in Figure 8.12 and E_T^{miss} plots for the signal and background in each category are shown in Figure 8.11. Three diphoton mass distributions are fitted, as shown in Figure 9.2. Each is made with the selection of the corresponding category. The three categories are mutually exclusive so the data and the background prediction for each category is independent of the other two categories.

The width of the $M_{b\bar{b}}$ window is motivated by the Higgs to $b\bar{b}$ mass width seen in Figure 8.10. The invariant mass of the two leading photons is used to isolate the signal and determine the background.

Using E_T^{miss} as the variable of interest and merging the two background estimates as described

in Section 6.1, expected limits can be set using the CLs and LandS tools described in Section 8.6.

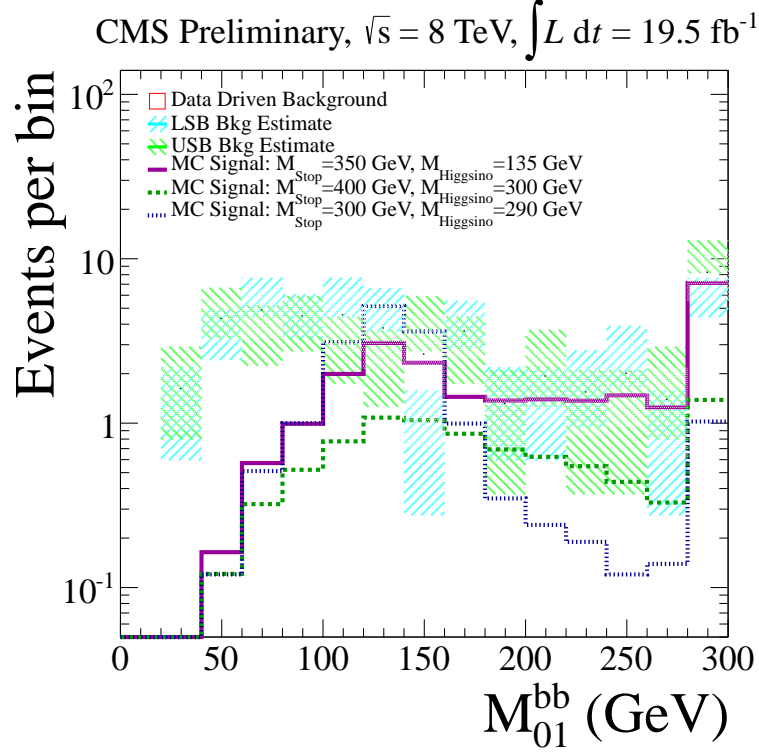


Figure 8.10: Two-body invariant mass of the leading two b-jets for Monte Carlo signal points and background estimates. In the case of four b-jets in the final state there is a six fold combinatoric background hiding the Higgs resonance, resulting in a broad peak. But in cases where the mass difference between the stop and Higgsino is small the leading two b-jets are more likely to be from the Higgs and the Higgs resonance is more pronounced. The vertical gray lines show the boundaries of the $95\text{-}155 \text{ GeV}/c^2 \text{ } M_{bb}$ window.

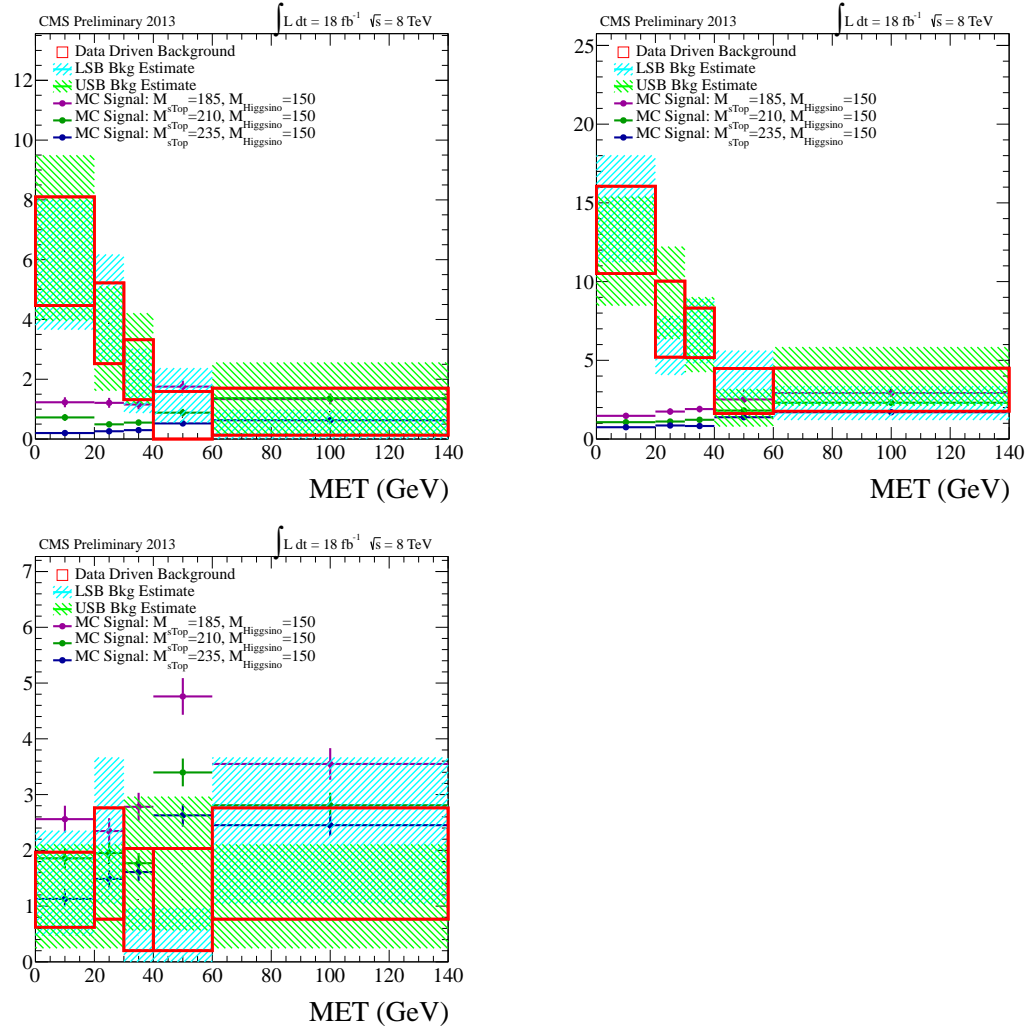


Figure 8.11: Comparison of E_T^{miss} distributions for each of the cut categories for background and Monte Carlo signal. Upper left: the 2 b-jets categories with M_{bb} on the Higgs mass. Upper Right: the 2 b-jets categories with M_{bb} off the Higgs mass. Lower left: the 3 or more b-jets categories.

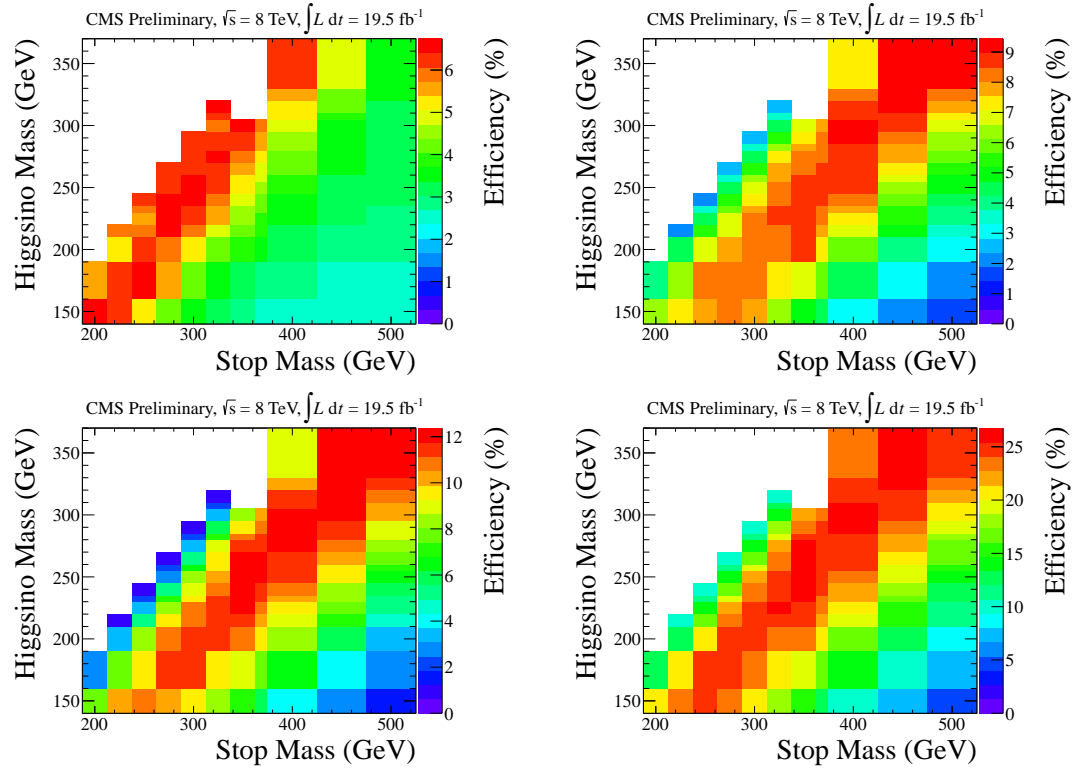


Figure 8.12: Monte Carlo efficiency maps for each of the cut categories. Upper left: the 2 b-jets categories with M_{bb} on the Higgs mass. Upper Right: the 2 b-jets categories with M_{bb} off the Higgs mass. Lower left: the 3 or more b-jets categories. Lower right: the sum of the three categories. In each case both photons be in the barrel with a diphoton mass on the Higgs mass.

8.1.2 Variations on the Fit

The chosen fit function is a potential source of systematic uncertainty. Here the fits are demonstrated using the usual power law, an exponential, a second polynomial and a third order polynomial. The variation in the integral over the signal region from changes in fit function was found to be consistent with the uncertainty in the integral obtained in the fitting procedure. Higher order fit functions have difficulty converging for the low statistics cases. Figure 8.13 shows the fits for each channel and each tested fit function. It is clear in Figure 8.13 that 2^{nd} and 3^{rd} degree polynomial fits are badly behaved at the high mass end.

A power law of the form $A * M_{\gamma\gamma}^{-b}$ is used to describe the diphoton mass distribution. This is a physically sensible choice since the background is dominated by QCD events faking photons.

Table 8.1: Expected Backgrounds using Various Fit Functions

| Fit Function | 3 + b-jets | on h mass | off h mass | total |
|----------------------|---------------|----------------|----------------|----------------|
| Power Law | 6.3 ± 1.5 | 10.8 ± 2.1 | 28.7 ± 3.0 | 46.8 ± 3.8 |
| Exponential | 6.5 ± 1.5 | 11.1 ± 1.9 | 29.4 ± 3.1 | 47.8 ± 3.9 |
| 2nd Order Polynomial | 6.1 ± 1.6 | 12.2 ± 2.2 | 27.9 ± 3.3 | 46.8 ± 4.2 |
| 3rd Order Polynomial | 7.0 ± 1.7 | 6.2 ± 1.7 | 28.4 ± 3.3 | 40.9 ± 4.1 |

Table 8.2: Background estimates made using four fit functions for the three b-jet categories and the combined. Aside from the poor 3rd order polynomial fits, the variation from changing fit functions is well described by the uncertainty on the power law fit. Additional systematic uncertainty from the fit shape is negligible.

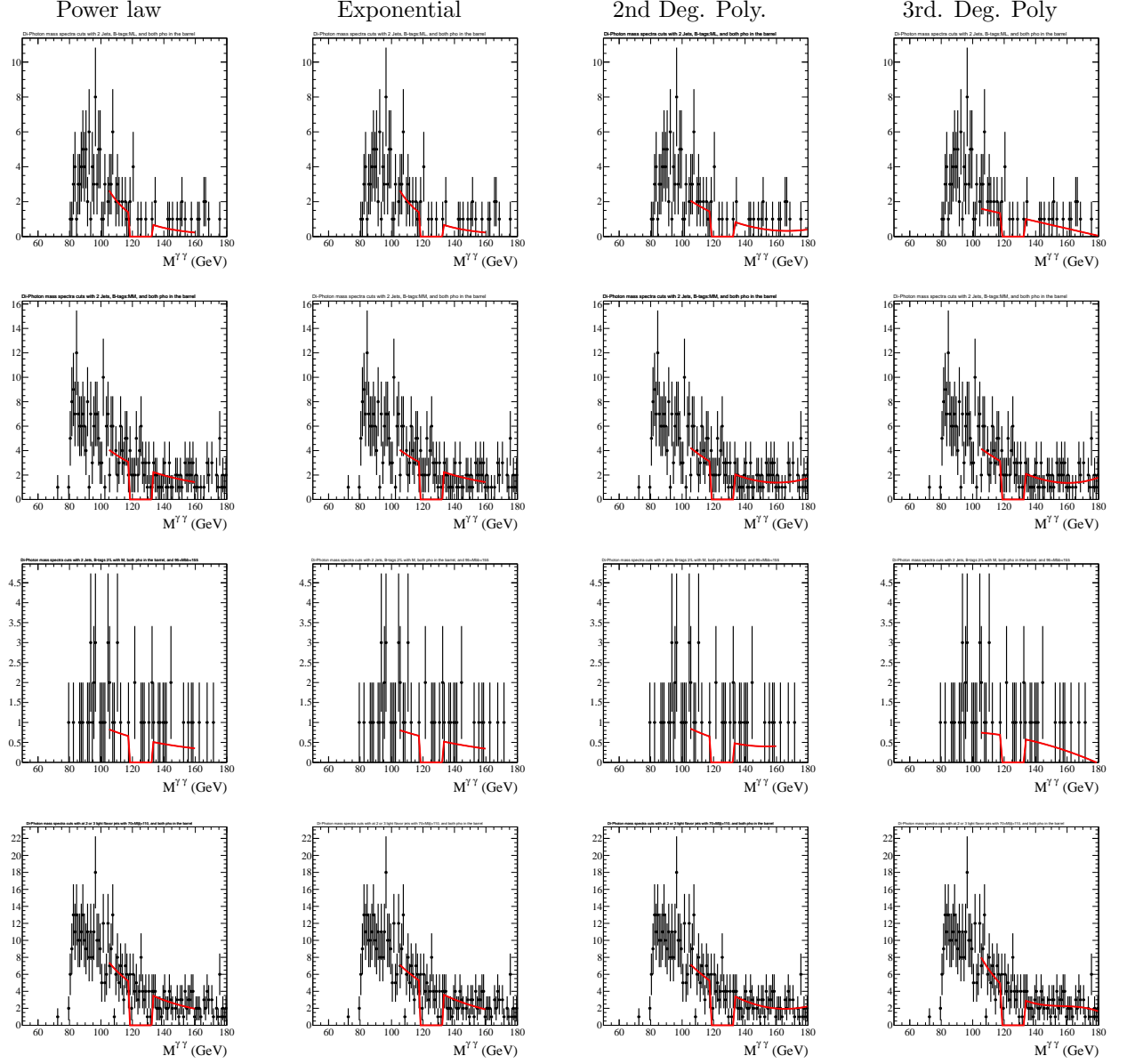


Figure 8.13: A comparison of the fits using different fit functions. First row: The 2 b-jet category with M_{bb} on M_H . Second row: The 2 b-jet category with M_{bb} off of M_H . Third row: The 3 b-jet category. Fourth row: The combination of the three categories. The different columns correspond to different fit functions used. First Columns: two parameter power law fit. Second Columns: an exponential fit Third Columns: A second order polynomial fit. Fourth Columns: A third order polynomial fit.

8.2 Higgsino with b-Jets

Here the design of a search is described for the case where two Higgsinos decaying to two Higgs bosons and gravitinos with one Higgs decaying to diphoton and the other decaying to two b-jets.

The Higgsino with b-jet selection is a part of the stop analysis but the selection re-optimized for Higgsino only production, with adjustments made for the lower cross section and the lack of an extra b-jet. All events passing the selection for this channel are also found within the 2b on M_H channel in the stop analysis.

8.2.1 Pre-selection

Before the primary event selection, event quality is enforced by using a CMS standard E_T^{miss} filter and primary vertex requirement. E_T^{miss} filters are also applied according to the prescription of the CMS JetMET physics object group. The trigger and object selection in this analysis is the same as in CMS AN 13/238.

The filters used are:

- CSC beam halo filter, which vetoes events tagged by the cathode strip chambers as beam halo.
- HBHE noise filter, which vetoes events identified as having high amounts of HCAL noise, which affects E_T^{miss} resolution.
- ECAL dead cell trigger primitive filter, which vetoes events which have a large amount of energy deposited in ECAL cells which are masked out of reconstruction.
- HCAL laser filter, which vetoes events in which the HCAL calibration laser fired during a bunch crossing.
- Tracking failure filter, which vetoes events where large calorimeter deposits have no matched tracks.
- Bad EE supercrystal filter, which vetoes events that have large deposits in the two 5x5 crystal regions of the ECAL endcap which have been seen to produce anomalously high energy readings.

There is also requirement that there be at least one “good” vertex in a given event. A good vertex is defined as one which lies no further from the beam-spot than 24 cm in the z-axis and 2 cm in the x – y plane, and where there are at least 4 degrees of freedom in the vertex fit.

8.2.2 Main Selection

As outlined in the introduction, three selections are employed to search for the two channels of interest—the two-Higgs channel, the lepton channel, and the electroweak channel, as depicted in Figure 1.4. Each channel shares the same photon selection: events are selected which have at least two photons in the barrel ($|\eta| < 1.4442$), $E_T > 40$ GeV and 25 GeV for the leading and sub-leading photons respectively. The invariant mass of the two leading photons is required to be between 120 and 131 GeV/ c^2 . Lower and upper sidebands are defined, respectively, as having the diphoton mass in range 103 to 118 GeV/ c^2 and 133 to 163 GeV/ c^2 . The photon E_T cuts designed to avoid turn on effects seen in Figure 7.1. Restricting photons to the barrel sharply increases the signal to background ratio, as can be seen in Figure 8.1. The diphoton mass distributions and fits for these selections are shown in Figure 9.14 and 9.26.

For the two-Higgs channel we require exactly two b-jets passing MEDIUM working point selection, in addition to the photon selection, and require the di-b-jet mass to be in a 95-155 GeV/ c^2 Higgs mass window. We also veto on leptons in order to keep our selection orthogonal to other analyses. For the electroweak channel, we require two jets (of any flavor), in addition to the photon selection, and require that the dijet mass of the two leading jets be in a 70-110 GeV/ c^2 electroweak mass window. Here again we veto on leptons and also veto on events that enter into two-Higgs selection. Explicitly, we exclude events with two or more jets passing LOOSE working point with one or more also passing the MEDIUM working point where the di-b-jet is in the Higgs window. The difference in b-jet requirements between the two-Higgs selection and the two-Higgs veto ensures that perturbations in the b-jet efficiency estimate will not migrate Monte Carlo events between the two channels.

ZH events may enter into the selection of the two-Higgs channel but their contribution is at most 10% of the total signal in the case of Higgsinos branching 50% of the time to Z bosons. This analysis loses sensitivity when the branching ratio of Higgsinos to Higgs is low enough for this to be of concern, so the HZ contribution has been neglected.

For the two-Higgs channel both Higgs likely carry significant p_T . It is therefore useful to define a quantity called Higgs S_T , which is the scalar p_T sum of the two reconstructed Higgs bosons.

$$Higgs S_T = p_T[P_{\gamma 0}^\mu + P_{\gamma 1}^\mu] + p_T[P_{b0}^\mu + P_{b1}^\mu]$$

It can also be thought of as the scalar sum of transverse energy (S_T) composed only of Higgs bosons. This variable will be used as the sensitive variable for the two-Higgs channel.

Figure 8.14 shows the standard model Higgs contributions to the two-Higgs channel. This is a negligible contribution, which is to be expected since the standard model Higgs is singly produced. However, for the electroweak channel the contribution from the standard model Higgs is of more concern since light flavored jets are far more common. It contributes ten percent (0.1 events) to the most sensitive E_T^{miss} bin. The background estimates and limit setting procedures for the electroweak channel take the SM Higgs background into account using FullSim Monte Carlo. The SM Higgs background estimate in the electroweak channel is shown in Figure 8.15.

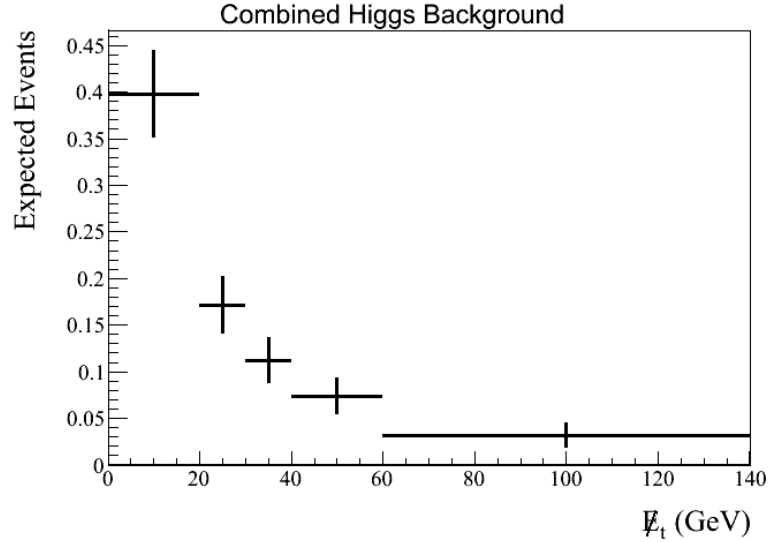


Figure 8.14: Expected standard model Higgs boson background contribution to the two-Higgs channel from FullSim Monte Carlo in combined gluon-gluon fusion, vector boson fusion, and vector boson + Higgs boson production channels. top-top-Higgs is negligible compared to these three production channels. In total, the standard model Higgs production is a negligible background for this channel.

Table 8.3 shows the expected effects of selection cuts on the efficiency of a simulated physics signal.

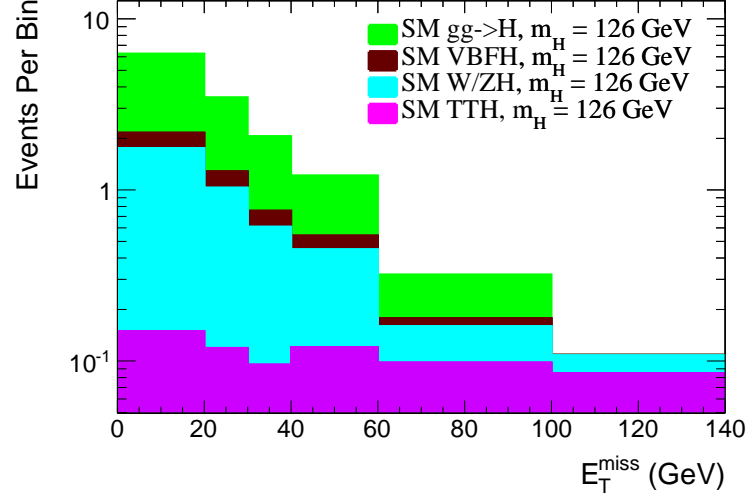


Figure 8.15: Expected standard model Higgs boson background contribution to the electroweak channel from FullSim Monte Carlo in combined gluon-gluon fusion, vector boson fusion, vector boson + Higgs boson production, and top-top-Higgs production channels. In total, the standard model Higgs production is a negligible background for this study.

| Selection | MC Events |
|--|----------------|
| No Selection | 71.5 ± 0.4 |
| Pass HLT | 53.6 ± 0.4 |
| Require 2 Loose Photons | 34.0 ± 0.3 |
| Impose $H(gg)$ mass window requirement | 31.1 ± 0.3 |
| Require both photons be in the barrel | 20.0 ± 0.2 |
| Require 2 CSV-M b-jets | 4.1 ± 0.1 |
| Reject events with leptons | 4.1 ± 0.1 |
| Impose $H(bb)$ mass window requirement | 3.5 ± 0.1 |

Table 8.3: Cutflow for $H(bb)H(\gamma\gamma)$ for $\mu = 130 \text{ GeV}/c^2$. Here the second Higgs is assumed to decay to bb .

8.2.3 Optimization of b-Jet Pair Mass Window

The invariant mass window of the b-jet pair was optimized for signal over sqrt of background efficiency. A baseline invariant mass window of $80\text{-}170 \text{ GeV}/c^2$ was used as a denominator, with selections at $85\text{-}165 \text{ GeV}/c^2$, $90\text{-}160 \text{ GeV}/c^2$, $95\text{-}155 \text{ GeV}/c^2$, and $100\text{-}150 \text{ GeV}/c^2$. Signal efficiencies are obtained by counting events with exactly two b-jets occurring within the $H \rightarrow \gamma\gamma$ signal region of $120\text{-}131 \text{ GeV}/c^2$ for each mass window selection. Background counts are taken in the upper ($133\text{-}163 \text{ GeV}/c^2$) and lower ($103\text{-}118 \text{ GeV}/c^2$) $H \rightarrow \gamma\gamma$ sidebands.

8.2.4 Optimization of b-jet Pair Working Point Combination

The selection of CSV working points for candidate b-jet pairs is also optimized using efficiencies. The following combinations of CSV Loose, Medium, and Tight working points are investigated: Medium-Loose (ML), Medium-Medium (MM), Tight-Loose (TL), Tight-Medium (TM), and Tight-Tight (TT). As a denominator, Loose-Loose (LL) is chosen. Each b-jet pair has invariant mass in the Higgs window of 95-155 GeV/ c^2 . Events for signal efficiencies are chosen in the $h \rightarrow \gamma\gamma$ signal region of 120-131 GeV/ c^2 , and background events are counted in the upper (133-163 GeV/ c^2) and lower (103-118 GeV/ c^2) sidebands.

8.3 Higgsino with Leptons

The Lepton channels are nearly identical to the b-Jet channel except that instead of requiring two b-jet, events with two b-jets are rejected and a lepton is required. A “Lepton” here means an electron or a muon with $E_T > 15$ GeV, as well as the various criteria described in Section 4.4. There are two channels here, a muon channel and an electron channel.

Muon candidates within a $\Delta R < 0.3$ cone around the two leading photons are excluded from consideration to prevent double counting. Then electron candidates within a $\Delta R < 0.3$ cone around the two leading photons and around any identified muons are excluded.

Transverse mass M_T is used as the sensitive variable for both lepton channels. M_T is defined as:

$$M_T = \sqrt{2p_{T,lepton}E_T^{miss} [1 - \cos(\Delta\phi(\vec{p}_{lepton}, E_T^{miss}))]} \quad (8.1)$$

M_T is particularly useful for looking at W decays in cases where one Higgs decays to a W boson. It is also useful for a very different sort of SUSY signal with a HW^\pm final state.

Two sets of scale factors are applied to the muons and electrons in Monte Carlo simulations to correct for otherwise unrealistically lepton identification and isolation efficiencies (42) (49).

A small gap in the b-jet definition is used between the b-jet channel and the lepton channel to prevent Monte Carlo b-jets from migrating between channels when the jet energy corrections are

applied. The lepton channel requires at most 1 CSVL b-jet plus 1 CSVN b-jets, while the b-jet channel requires at least two CSVN b-jets.

8.4 Higgsino with Electroweak Bosons

To target Higgs produced along side electroweak bosons the electroweak channel is introduced. This channel is not very sensitive to new physics but it continues the family of Higgsino channels outlined in Figure 1.4. It also contributes to the combined limit setting statistics. The electroweak channel has the same object definitions, preselection, systematic uncertainties, and so forth as the b-jet and lepton channels. The particulars of the electroweak channel are as follows. First, events with two or more b-jets and events with leptons are rejected to exclude events in the b-jet and lepton channels. Similarly, loose b-jets pairs with a dijet mass in the Higgs mass range used in the b-jet channel are excluded in order to guard against channel overlap. Then two jets are required in pursuit of hadronically decaying electroweak bosons, In addition, a dijet mass between $70 \text{ GeV}/c^2$ and $110 \text{ GeV}/c^2$ is required. This window is designed to admit both W and Z boson decay. A comparison of the signal peaks and the mass window is shown in Figure 8.17.

The electroweak channel uses E_T^{miss} as the sensitive variable. Figure 8.16 shows the E_T^{miss} distribution for this channel under HZ and HW^\pm Monte Carlo. Nearly all the sensitivity comes in the highest E_T^{miss} bin. Since there are no longer two Higgs bosons in the event, Higgs S_T is no longer a sensible variable to consider. Naively it may seem useful to try the analogue version of Higgs S_T : $p_T[P_{\gamma 0}^\mu + P_{\gamma 1}^\mu] + p_T[P_{j 0}^\mu + P_{j 1}^\mu]$ This and its components are explored in Figures 9.29, 9.30, and 9.31, but as can be seen, they are not sensitive observable.

Tables 8.4 and 8.5 show the expected effect of selection cuts on a simulated signal.

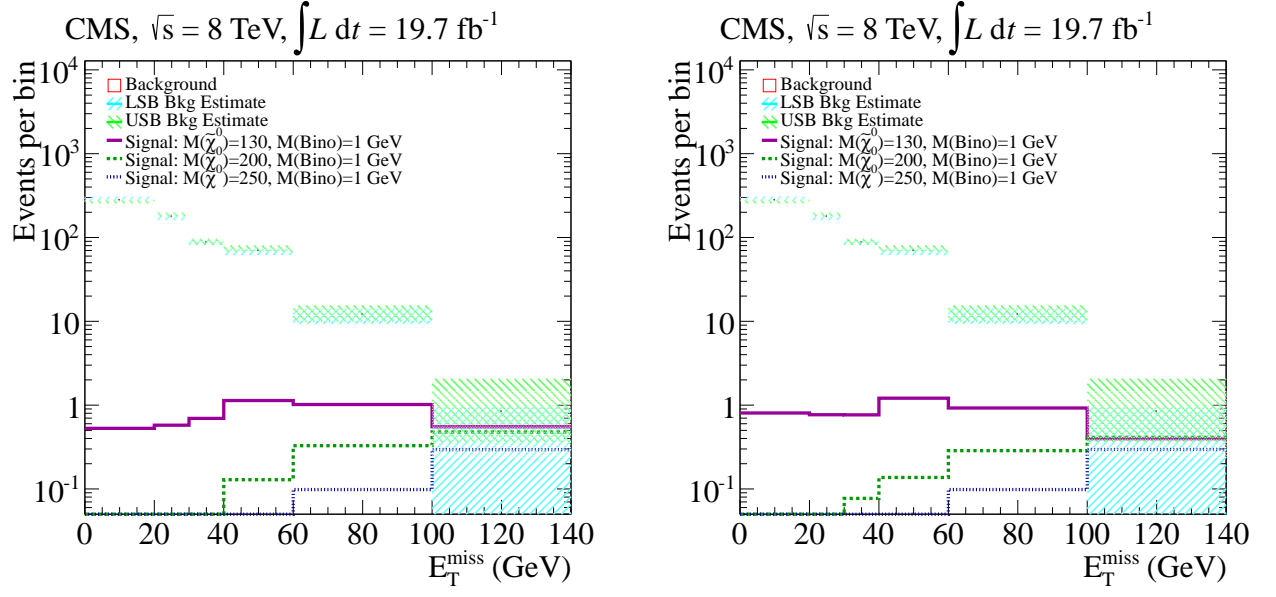


Figure 8.16: E_T^{miss} Distributions for ZH (Left side) and WH (Right side) signals compared to the background.

| Selection | MC Events |
|--|-----------------|
| No Selection | 117.3 ± 0.5 |
| Pass HLT | 89.9 ± 0.4 |
| Require 2 Loose Photons | 57.2 ± 0.4 |
| Impose H(gg) mass window requirement | 51.9 ± 0.3 |
| Require both photons be in the barrel | 32.9 ± 0.3 |
| Pass Lepton Veto | 27.5 ± 0.2 |
| Require 2 Jets exclusive with the bb channel | 13.0 ± 0.2 |
| Impose M(jj) in the mass window | 7.9 ± 0.1 |

Table 8.4: Cutflow for HW^\pm for $\mu = 130 \text{ GeV}/c^2$.

| Selection | MC Events |
|--|----------------|
| No Selection | 63.3 ± 0.3 |
| Pass HLT | 48.3 ± 0.2 |
| Require 2 Loose Photons | 30.9 ± 0.2 |
| Impose H(gg) mass window requirement | 28.0 ± 0.2 |
| Require both photons be in the barrel | 17.9 ± 0.1 |
| Pass Lepton Veto | 16.7 ± 0.1 |
| Require 2 Jets exclusive with the bb channel | 7.7 ± 0.1 |
| Impose M(jj) in the mass window | 4.6 ± 0.1 |

Table 8.5: Cutflow for HZ for $\mu = 130 \text{ GeV}/c^2$.

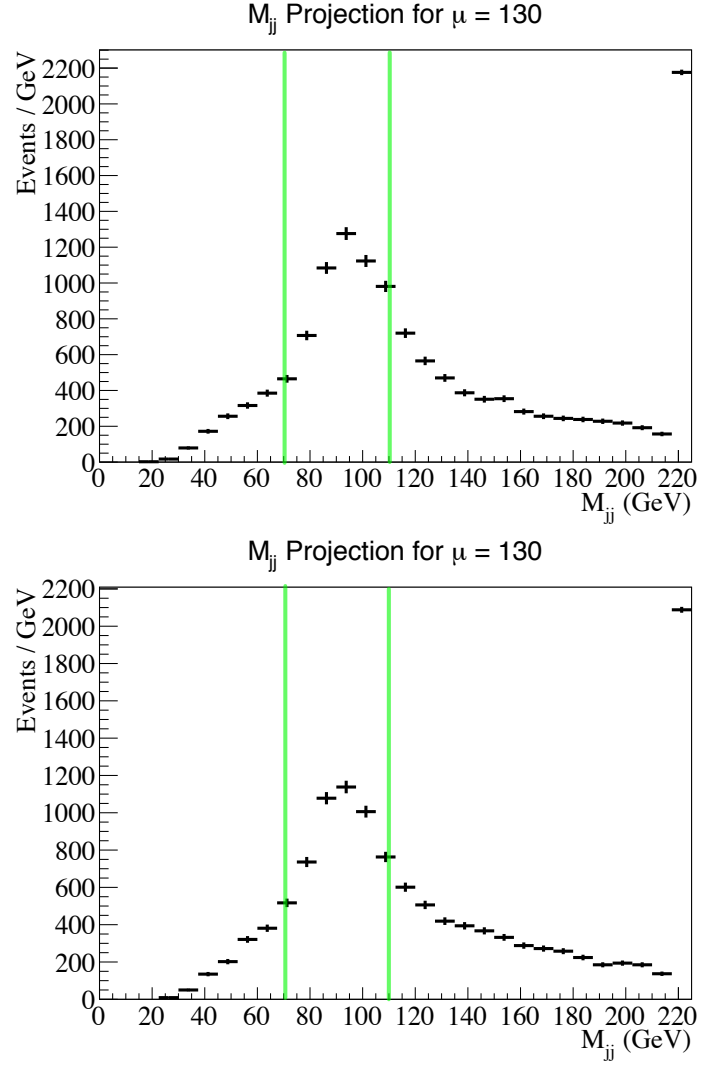


Figure 8.17: Above: M_{jj} distribution for $mu = 130$ ZH production. Below: M_{jj} distribution for $mu = 130$ WH production. The green lines indicate the boundaries of the dijet mass window used. The peaks of both the ZH and WH signal fit comfortably within the window. The last bins include the overflow.

8.5 Systematic Uncertainties

The sources of systematic uncertainties considered are shown in table 8.6. These uncertainties are applied to each of the analyses described in Sections 8.1-8.4. The first six uncertainties apply only to the Monte Carlo. The uncertainty in the theoretical cross section results in the uncertainty in the observed limit contours in Figures 9.12 and 9.13. These systematic uncertainties are used in the limit setting machinery described in Section 8.6. The uncertainty on the signal cross section has been calculated separately for each signal mass point; uncertainties are typically very close to 15%. The analysis is insensitive to the uncertainty on the negligible SM Higgs background uncertainty.

Table 8.6: Sources of systematic uncertainties

| Source of Uncertainty | Value |
|--|------------------------|
| trigger efficiency uncertainty | 0.1% (43) |
| photon efficiency uncertainty | 1% (37) |
| photon resolution uncertainty | 1% (36) |
| b-jet identification uncertainty | shape uncertainty (28) |
| jet energy scale | shape uncertainty (40) |
| luminosity uncertainty | 4.4% (33) |
| signal theoretical cross-section uncertainty | $\sim 15\%$ (32) |
| SM Higgs background uncertainty | 30% (58) |

8.6 Statistical Limit Setting Methods

A LHC-style CLs limit setting procedure is employed to set 95% exclusion limits on supersymmetry models. The CLs limit setting procedure is implemented in a ready-made limit setting tool called LandS, which was developed for the search for the Higgs boson by both the CMS and ATLAS Higgs groups. A proper explanation of the CLs method would double the length of this thesis, so for the detailed of the inner workings of CLs limit setting please refer to references (62), (39) and (12).

Limits can be expressed either as limit cross sections on the signal process, or as r-values. r is the ratio of the limit cross section to the theoretical signal cross section. So an r-values less than 1 indicate a models is excluded at 95% confidence or better.

There are two sets of limits relevant: the expected limits and the observed limits. Expected limits are the where the 95% limit is predicted to fall given the simulated signal behavior and

the background estimate before considering the observed result. The expected limit is a random variable, so this is expressed as the 50th percentile expected limit surrounded by a 1σ band and 2σ band of where that limit may fall. The observed limit is where the actual 95% limit falls once the observed result is unveiled. Observed limits also have some uncertainty as well due to the theoretical uncertainty on the signal cross section.

For those interested in the technical details, frequentist statistics and “Full Toys” are used with the LandS limit setting machinery. The r-value ranges are produced from the 3σ band of “Asymptotic Profile Likelihood” expected limits.

For each channel the limit setting machinery considers a histograms of some sensitive variable of the background estimate, observed events, and simulated signal, as well as systematic uncertainties. So for instance, in the Stop analysis E_T^{miss} is used as the sensitive variable with 5 E_T^{miss} bins. LandS receives three E_T^{miss} histograms: one for the background estimate, one for a signal model with mass parameters under consideration, and one for the observed distribution. If there were no further complications, each E_T^{miss} bin would be treated as a statistically independent counting experiment. But the systematic uncertainties that are shared among all E_T^{miss} bins must be considered. In the language of LandS, these are “parasitic parameters”.

Most systematic uncertainties are modeled as Log-Normal random variables. Jet energy corrections and b-tag efficiencies are modeled as shape uncertainties. That is, their effects are not uniform over the E_T^{miss} distribution so they must be modeled as a characteristic shape in E_T^{miss} that can vary. Table 8.6 shows the systematic uncertainties applied to the Monte Carlo. These systematic uncertainties are the same for all the analyses considered here.

In addition, the uncertainty of the integral of the fit region must be treated as a parasitic parameter since it is the same for each bin of the histogram. In every plot in this document, the background estimate is shown with the uncertainty of the fit integral included in the bin uncertainty of each bin. For limit setting, a different version of these histograms are used where the uncertainty of the integral is excluded from the uncertainty of the bins, and reintroduced as a parasitic parameter.

For the Higgsino analysis, several channels are considered in combination. This includes both the

analyses detailed in this document as well as several other analyses which address other Higgsino signal final states. The LandS CLs machinery is able to combine experimental info from all the channels of these various analyses to produce a grand combined limit. This limit was produced in collaboration with several other analysis groups in CMS and the results are shown in Section 9.5. Several of the systematic uncertainties are shared among different analyses, which necessitated gathering the results from all the contributing analyses and analyzing them all together so that shared systematics varying together.

This grand combination of Higgsino analyses, of which the $\gamma\gamma + X$ analyses here are a part, resulted in the paper in reference (54).

Chapter 9

Results and Limit Setting

9.1 Stops

Figure 9.1 shows the unblinded diphoton mass distribution for the sum of the combined stop channels, along with the power law fit, and signal and sideband regions. Similarly Figure 9.2 shows the unblinded diphoton mass distribution for each of the three stop channels. Table 9.1 presents the total event counts observed and expected for each channel and for the three channels combined. It also shows the event counts that selected signal mass points would produce.

For this section E_T^{miss} is used as the sensitive variable and is used for limit setting. Figure 9.3 shows the E_T^{miss} distribution for the combination of the three channels. Figure 9.4 shows the E_T^{miss} distribution for each of the three channels; these are used for limit setting. Table 9.2 shows the event counts and background estimates for each E_T^{miss} bin of each of the categories. These observations are shared for simulated mass for which a cross section limit is set.

The observed data distributions for other relevant kinematic variables, together with data-driven background and the expectation for signal events are shown in Figures 9.5-9.11.

Table 9.1: Expected and observed event counts

| | on h mass | off h mass | 3 + b-jets | total |
|-----------------------------------|----------------|----------------|---------------|----------------|
| signal 350 / 135 GeV/c^2 | 2.0 | 6.8 | 10.7 | 19.5 |
| signal 300 / 290 GeV/c^2 | 10.1 | 3.9 | 2.1 | 16.2 |
| signal 400 / 300 GeV/c^2 | 1.4 | 2.8 | 4.0 | 8.3 |
| expected BG | 10.8 ± 2.1 | 28.7 ± 3.0 | 6.3 ± 1.5 | 46.5 ± 3.8 |
| observed | 7 | 33 | 6 | 46 |

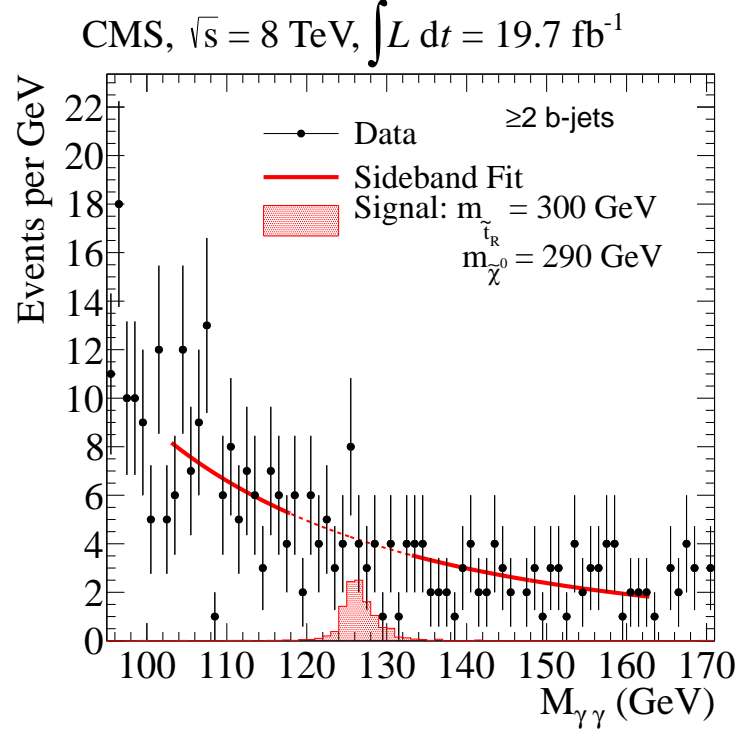


Figure 9.1: Diphoton mass distribution for events with two or more b-jets; detailing the fit to the background (green line) using the Higgs boson mass sidebands. The red lines bound the upper and lower side bands while the blue lines bound the signal region.

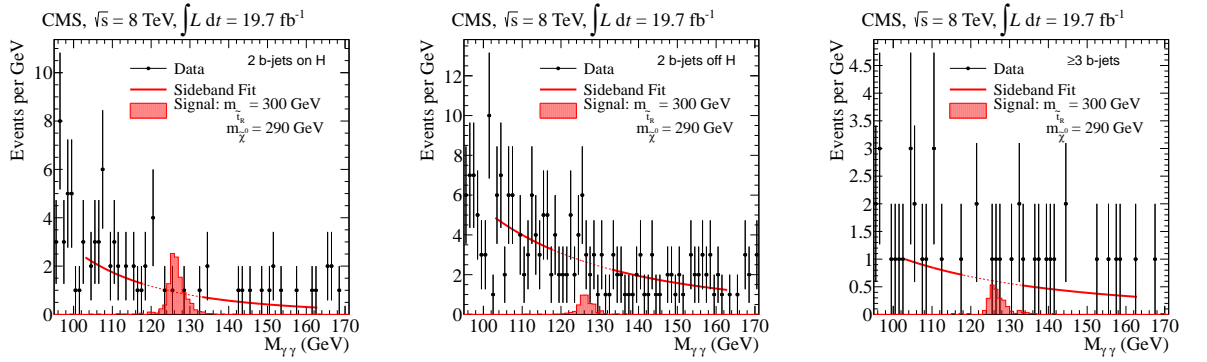


Figure 9.2: Diphoton mass distributions with background fits. From left to right: diphoton mass with exactly two b-jets whose dijet mass is on the Higgs boson mass, exactly two b-jets whose mass is off the Higgs mass, and three or more b-jets.

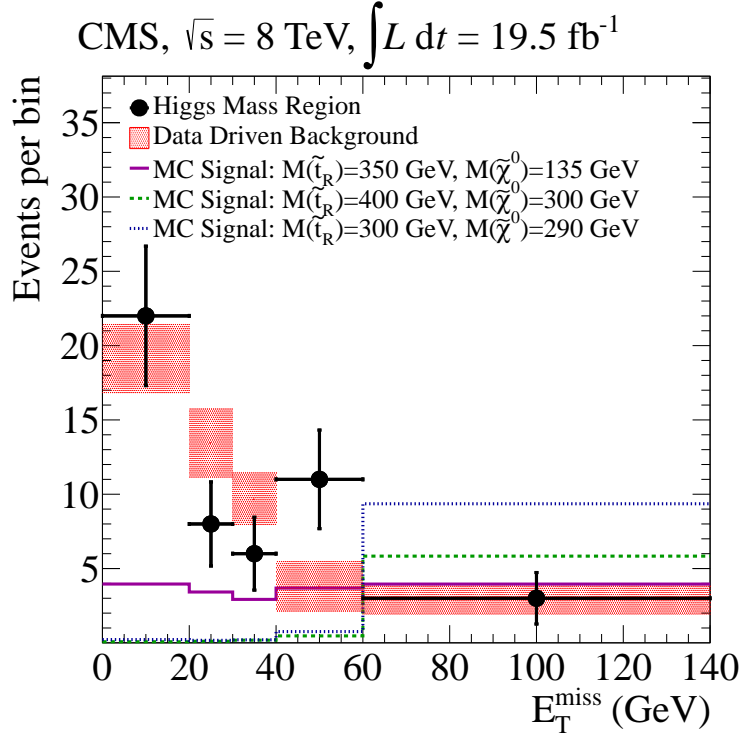
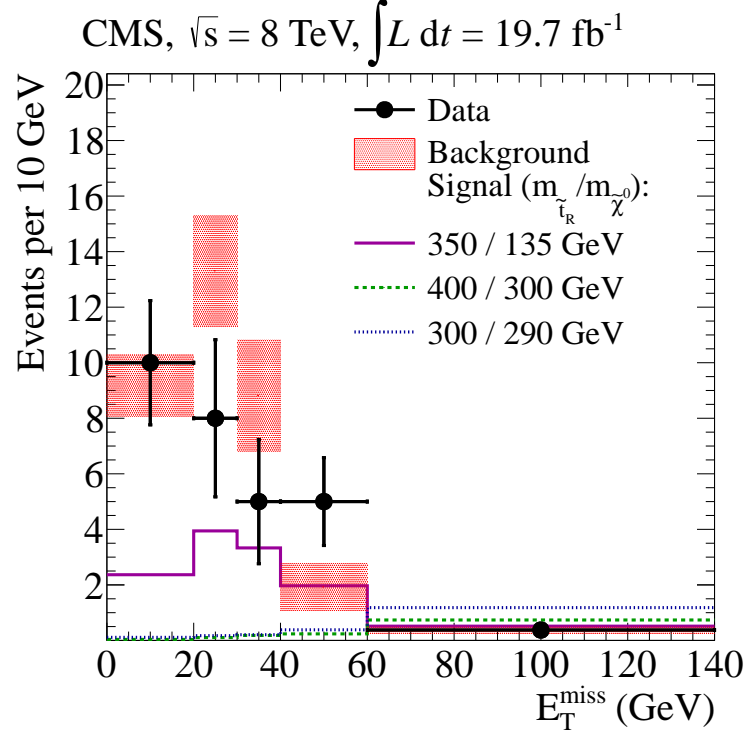


Figure 9.3: Above: E_T^{miss} distributions for diphoton events with two or more b-jets, comparing data, expected background and expected signal (color points) normalized to the integrated luminosity. The shaded rectangles show the background estimate from the sidebands. The last bin includes the overflow. Below: A version of the same histogram using the absolute number of events per bin rather than events per 10 GeV. This shows the behavior at high E_T^{miss} more clearly.

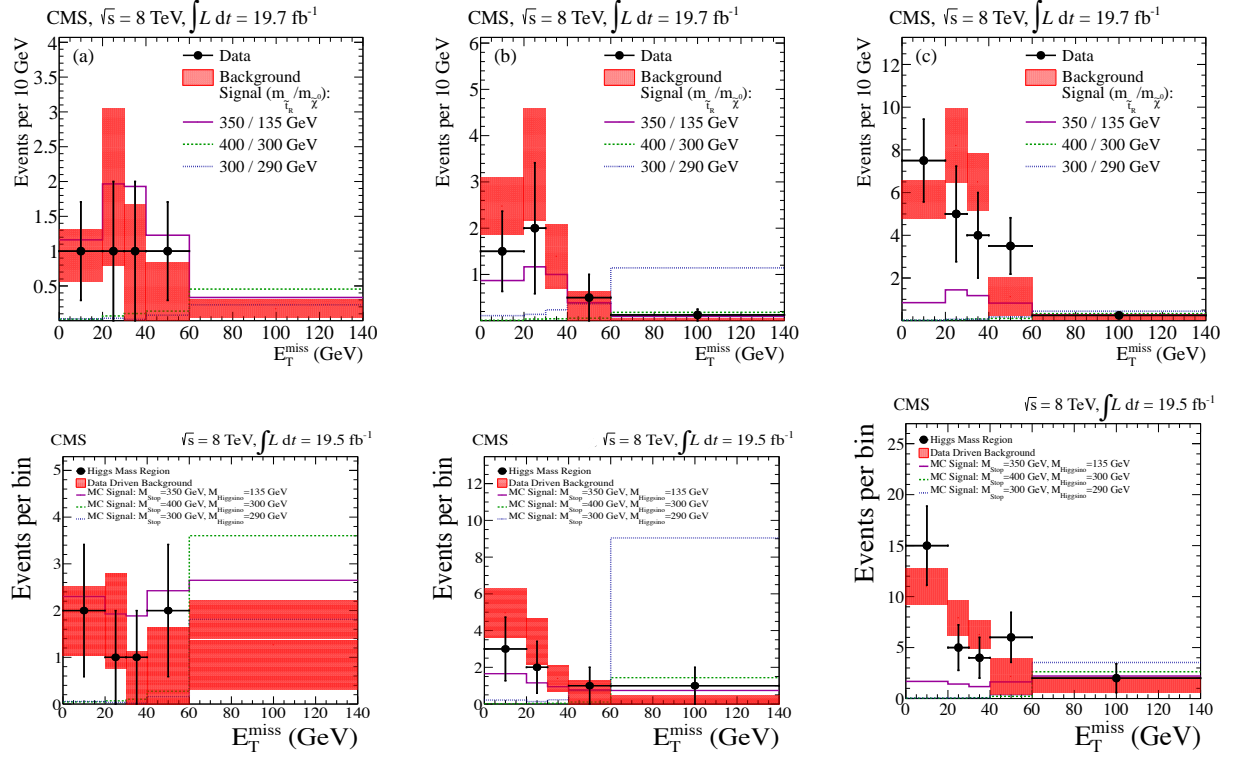


Figure 9.4: E_T^{miss} distributions for the data, background, and selected Monte Carlo points, used for limit setting when subdividing into three categories. Top Row: Besides requiring that the diphoton mass is on the Higgs mass we require (a) three or more b-jets, (b) exactly two b-jets whose dijet mass is on the Higgs boson mass, and (c) exactly two b-jets whose mass is off the Higgs mass. The last bins include the overflow. The E_T^{miss} distribution for the sum of these three channels is shown in Figure 9.3. Bottom Row: The same plots as above with absolute bin content rather than normalized bin content. This makes the behavior more clear at high E_T^{miss} .

Table 9.2: Observations and Background Estimates

| | 2 b-jets on h mass | | 2 b-jets off h mass | | 3+ b-jet | | Total | |
|---------------------------|----------------------|-----------------|-----------------------|-----------------|----------|-----------------|-------|----------------|
| E_T^{miss} (GeV) | Data | Bkg | Data | Bkg | Data | Bkg | Data | Bkg |
| 0-20 | 3 | 5.0 ± 1.3 | 15 | 11.0 ± 1.8 | 2 | 1.77 ± 0.73 | 20 | 18.1 ± 2.3 |
| 20-30 | 2 | 3.4 ± 1.3 | 4 | 7.9 ± 1.7 | 1 | 1.8 ± 1.1 | 7 | 13.1 ± 2.0 |
| 30-40 | 0 | 1.39 ± 0.71 | 5 | 6.3 ± 1.3 | 1 | 0.73 ± 0.84 | 6 | 8.7 ± 2.0 |
| 40-60 | 1 | 0.58 ± 0.68 | 7 | 2.2 ± 1.7 | 2 | 0.73 ± 0.84 | 10 | 3.8 ± 1.6 |
| 60+ | 1 | 0.19 ± 0.28 | 2 | 1.35 ± 0.73 | 0 | 1.3 ± 1.0 | 3 | 2.8 ± 1.0 |

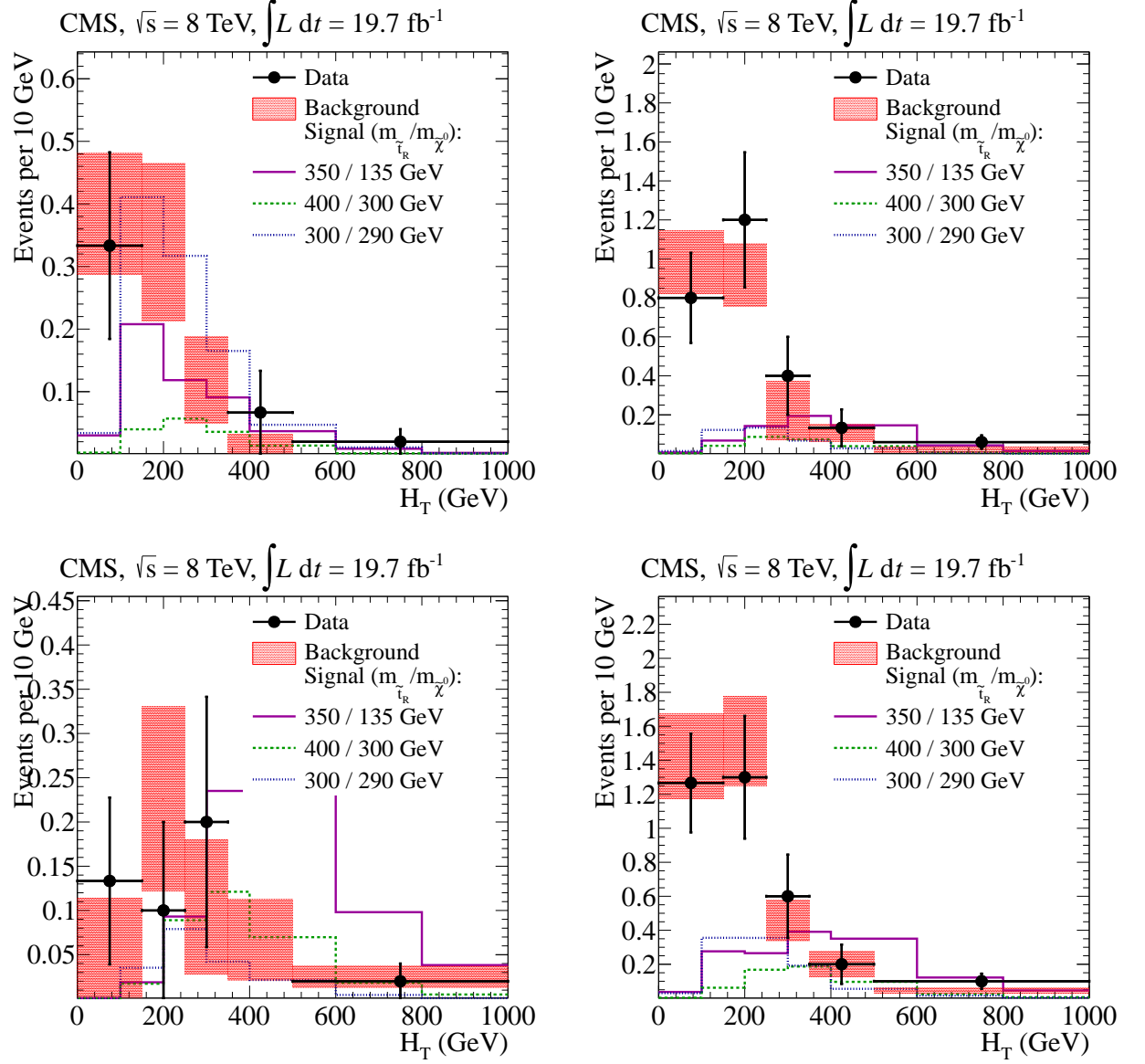


Figure 9.5: H_T for the data, background, and selected Monte Carlo points. H_T is the scalar sum of the p_T of all the jets in the event with $p_T > 30$ GeV/c. Upper left: the 2 b-jets categories with M_{bb} on the Higgs mass. Upper Right: the 2 b-jets categories with M_{bb} off the Higgs mass. Lower left: the 3 or more b-jets categories. Lower right: the sum of the three categories. In each case the two barrel photons are required with diphoton mass on the Higgs mass. The shaded rectangles show the background estimate from the sidebands. The last bin includes the overflow.

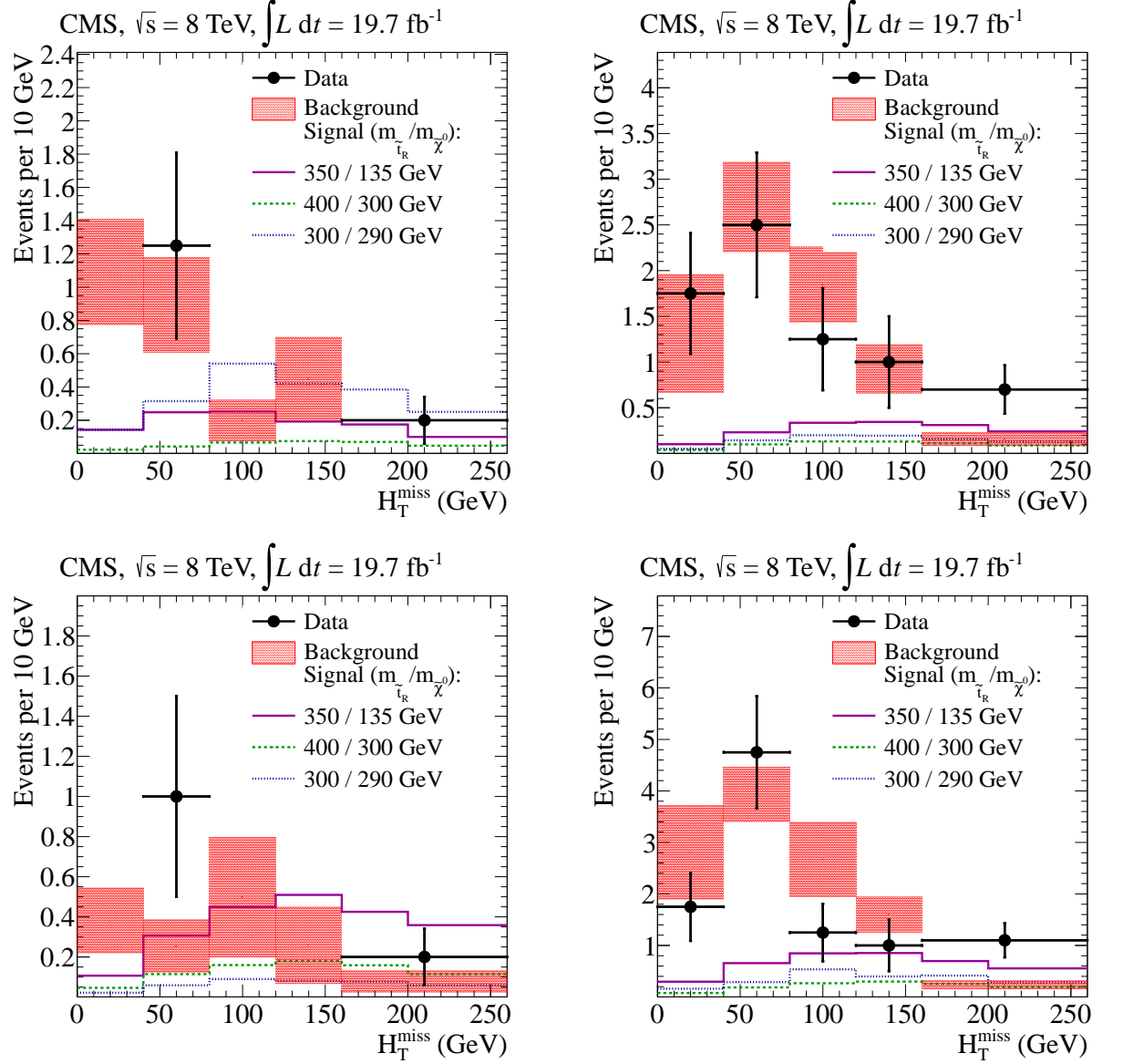


Figure 9.6: M_{HT} for the data, background, and selected Monte Carlo points. M_{HT} is the transverse vector sum of all the jets in the event with $p_T > 30 \text{ GeV}/c$. Upper left: the 2 b-jets categories with M_{bb} on the Higgs mass. Upper Right: the 2 b-jets categories with M_{bb} off the Higgs mass. Lower left: the 3 or more b-jets categories. Lower right: the sum of the three categories. In each case the two barrel photons are required with diphoton mass on the Higgs mass. The last bin includes the overflow.

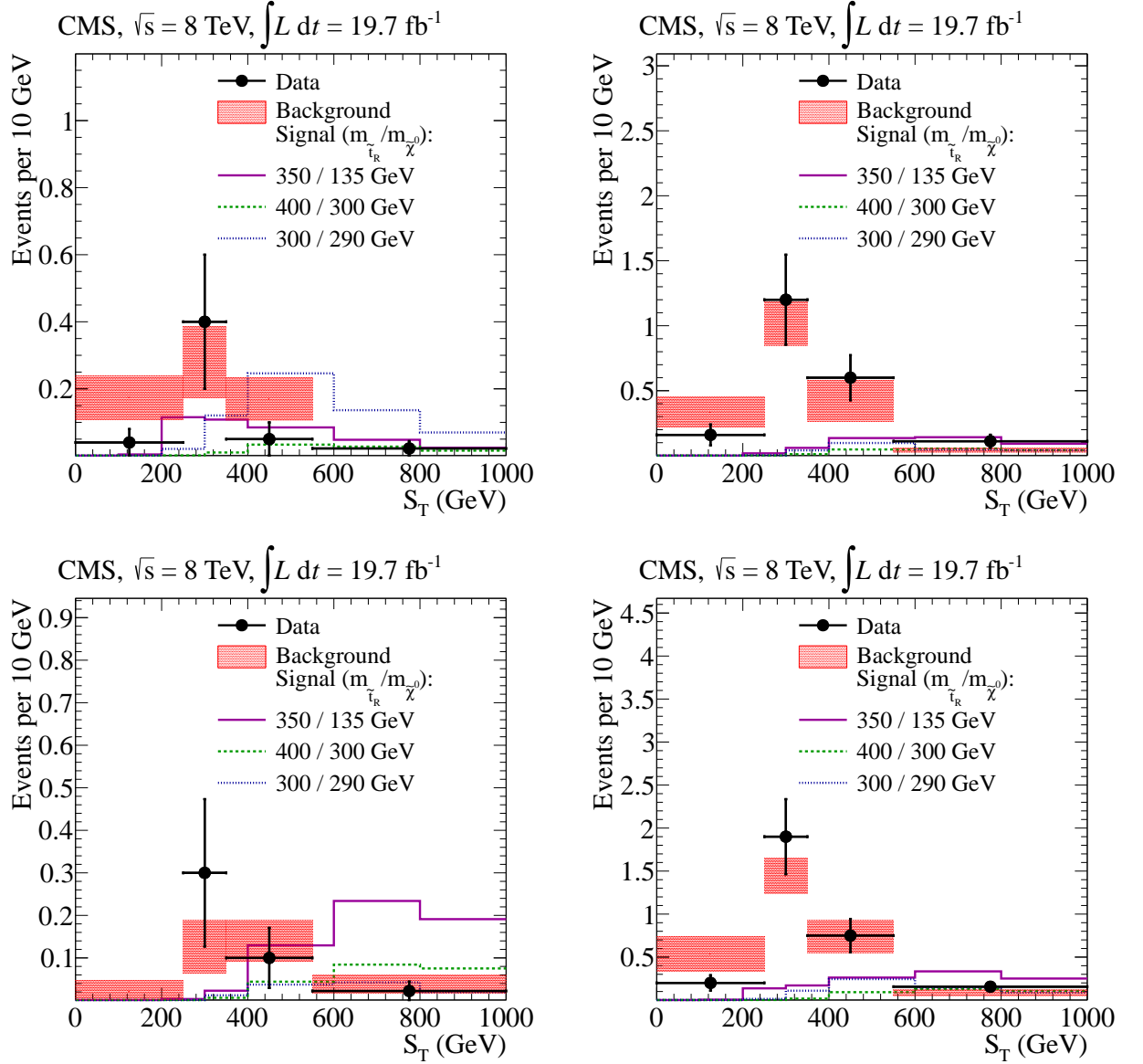


Figure 9.7: S_T for the data, background, and selected Monte Carlo points. S_T is the scalar sum of the p_T of all the jets in the event with $p_T > 30$ GeV/c, photons passing the loose photon definition, and E_T^{miss} . Upper left: the 2 b-jets categories with M_{bb} on the Higgs mass. Upper Right: the 2 b-jets categories with M_{bb} off the Higgs mass. Lower left: the 3 or more b-jets categories. Lower right: the sum of the three categories. In each case the two barrel photons are required with diphoton mass on the Higgs mass. The shaded rectangles show the background estimate from the sidebands, and the colored points are the expected contributions from selected signal points, normalized to the integrated luminosity. The last bin includes the overflow.

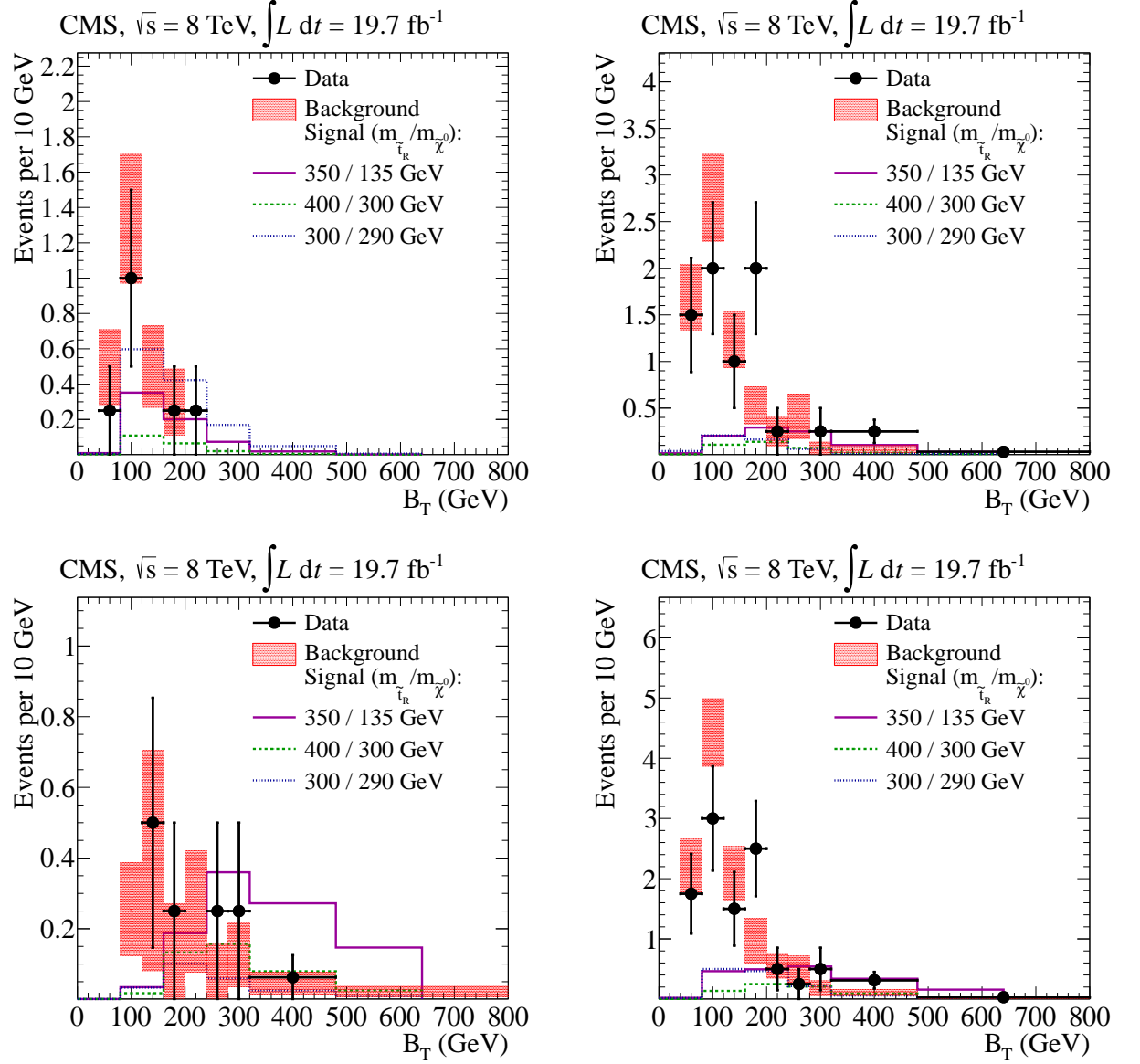


Figure 9.8: B_T for the data, background, and selected Monte Carlo points. B_T is the scalar sum of the p_T of all the b-jets in the event with $p_T > 30$ GeV/c. Upper left: the 2 b-jets categories with M_{bb} on the Higgs mass. Upper Right: the 2 b-jets categories with M_{bb} off the Higgs mass. Lower left: the 3 or more b-jets categories. Lower right: the sum of the three categories. In each case the two barrel photons are required with diphoton mass on the Higgs mass. The shaded rectangles show the background estimate from the sidebands, and the colored points are the expected contributions from selected signal points, normalized to the integrated luminosity. The last bin includes the overflow.

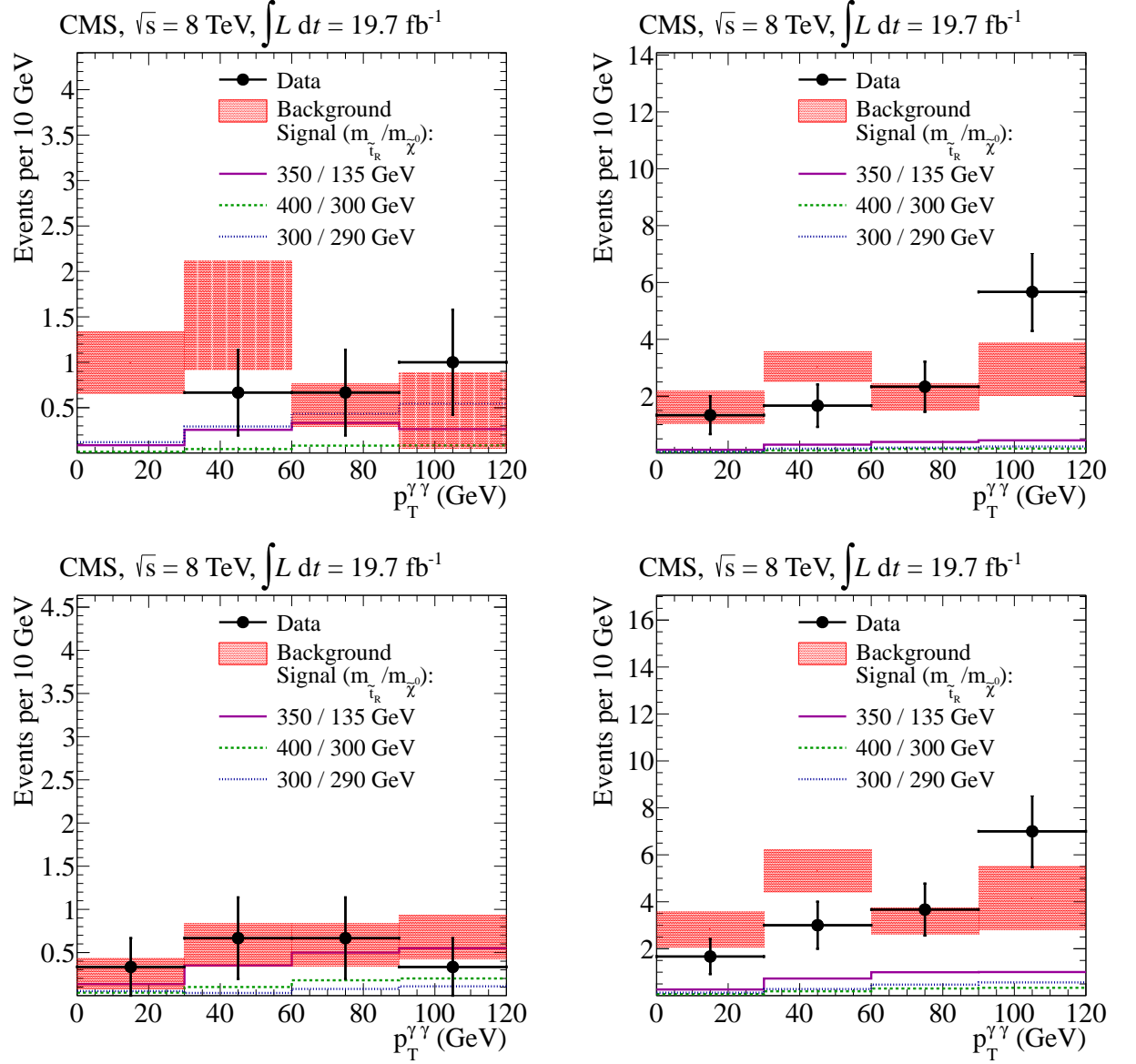


Figure 9.9: Diphoton p_T for the two photons whose mass is on the Higgs mass, for the data, background, and selected Monte Carlo points. Upper left: the 2 b-jets categories with M_{bb} on the Higgs mass. Upper Right: the 2 b-jets categories with M_{bb} off the Higgs mass. Lower left: the 3 or more b-jets categories. Lower right: the sum of the three categories. In each case the two barrel photons are required with diphoton mass on the Higgs mass. The shaded rectangles show the background estimate from the sidebands, and the colored points are the expected contributions from selected signal points, normalized to the integrated luminosity. The last bin includes the overflow.

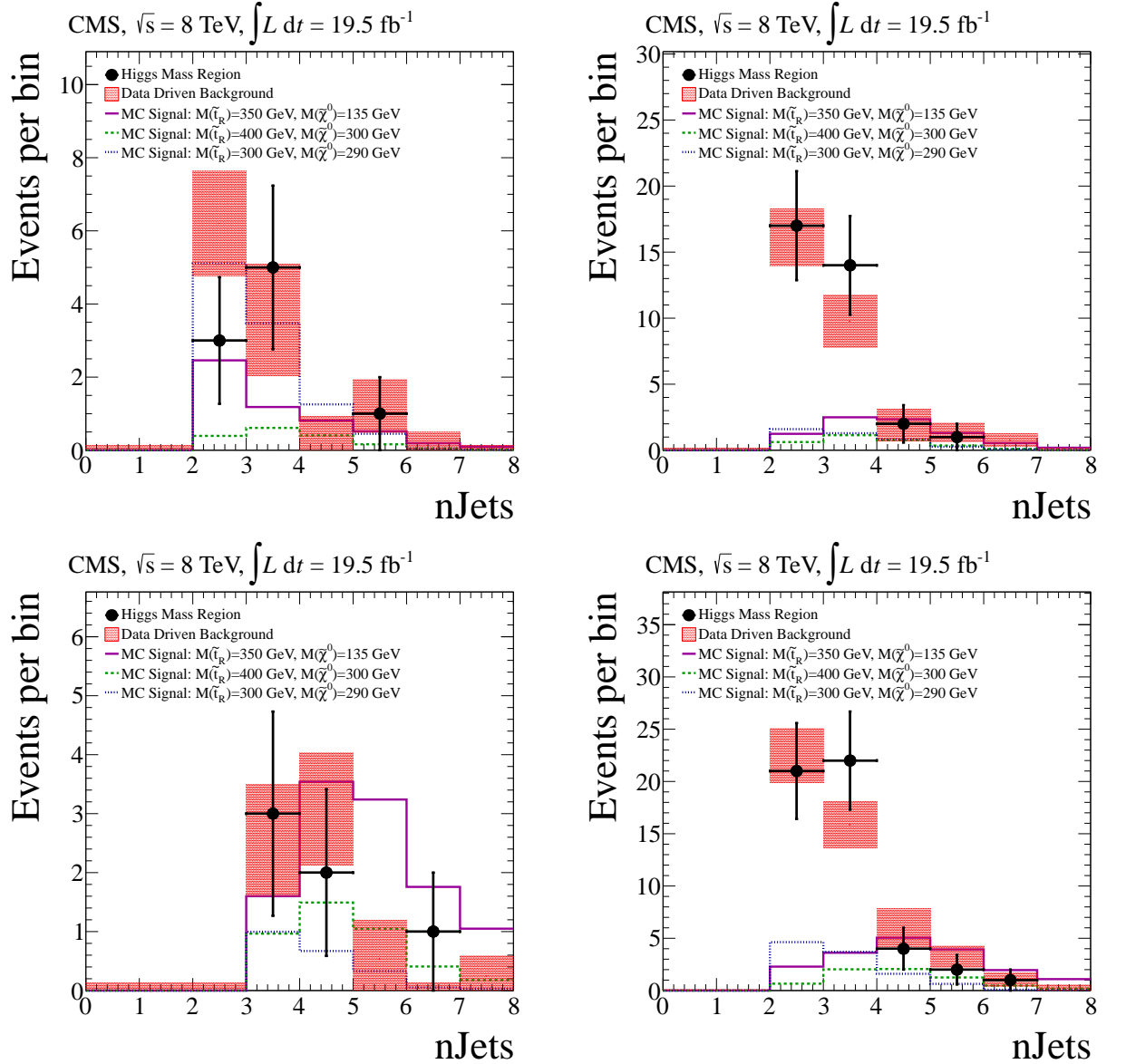


Figure 9.10: Distributions of the number of jets with $p_T > 30 \text{ GeV}/c$ for the data, background, and selected Monte Carlo points. Upper left: the 2 b-jets categories with M_{bb} on the Higgs mass. Upper Right: the 2 b-jets categories with M_{bb} off the Higgs mass. Lower left: the 3 or more b-jets categories. Lower right: the sum of the three categories. In each case the two barrel photons are required with diphoton mass on the Higgs mass. The shaded rectangles show the background estimate from the sidebands, and the colored points are the expected contributions from selected signal points, normalized to the integrated luminosity. The last bin includes events with more than 8 jets.

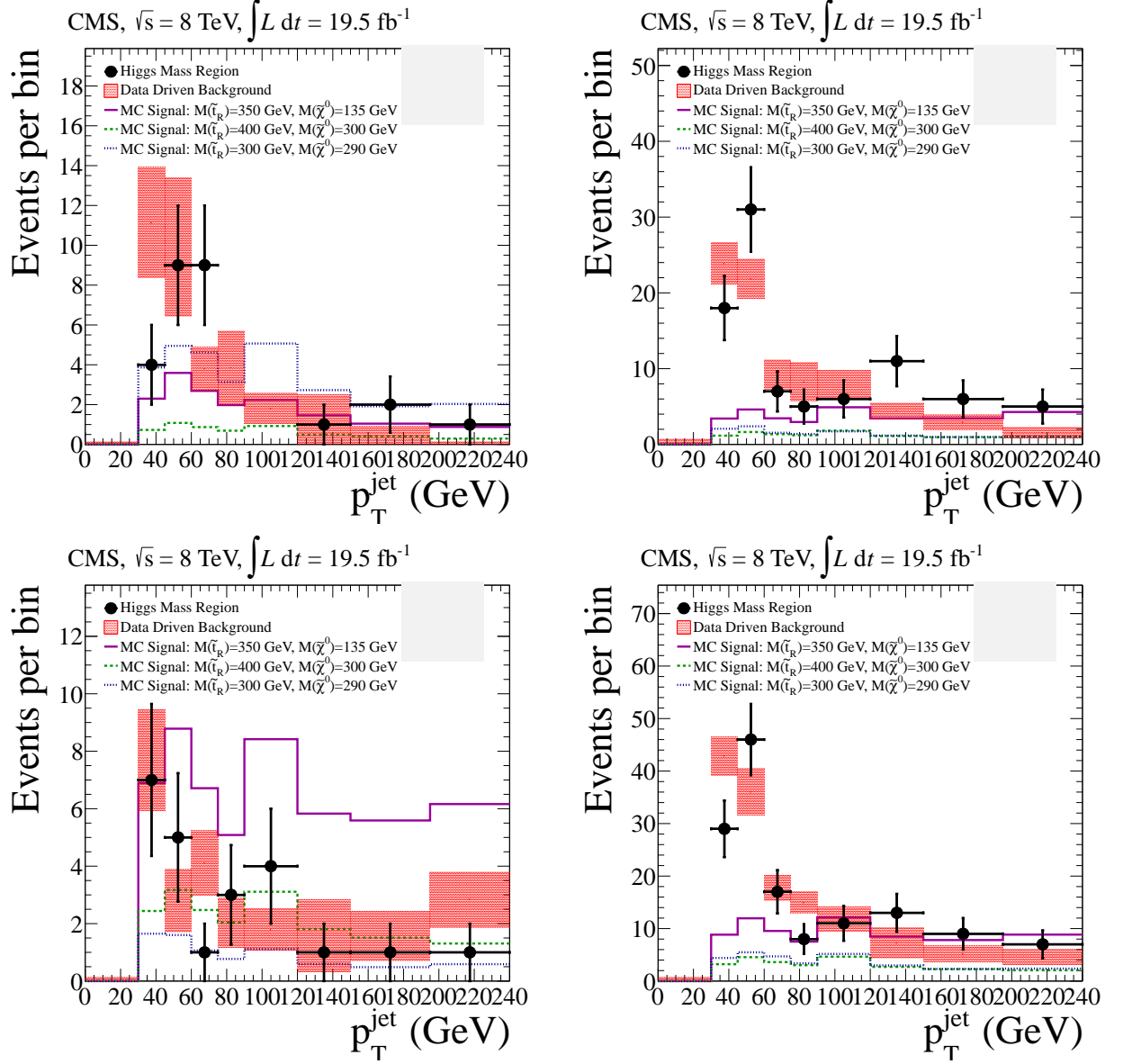


Figure 9.11: Jet p_T for distributions for the data, background, and selected Monte Carlo points. Upper left: the 2 b-jets categories with M_{bb} on the Higgs mass. Upper Right: the 2 b-jets categories with M_{bb} off the Higgs mass. Lower left: the 3 or more b-jets categories. Lower right: the sum of the three categories. In each case the two barrel photons are required with diphoton mass on the Higgs mass. The shaded rectangles show the background estimate from the sidebands, and the colored points are the expected contributions from selected signal points, normalized to the integrated luminosity. The last bin includes the overflow.

9.1.1 Statistical Interpretation

Since the observed data is consistent with the expectation, the Higgs combination, tool described in Section 8.6, is used to set limits on the SUSY production cross sections using the E_T^{miss} distribution as a discriminator.

Figure 9.12 shows the limits on the GMSB model in the stop-Higgsino mass plane with events separated into the three subcategories based on the b-jets. Depending on the Higgsino mass, and conservatively using the minus-one-standard-deviation value for the theoretical cross section, stop masses below 360 to 410 GeV/c^2 are excluded with 95% confidence, corresponding to the region to the left of the thick black line in Figure 9.12.

For comparison, Figure 9.13 shows the limits when events are not separated into the three categories. This demonstrates the modest improvement that event binning delivers, although much of the gain in sensitivity is obscured by the rapidly falling signal cross section.

Table 9.3 lists and compares the results with and without b-jet binning for selected mass points.

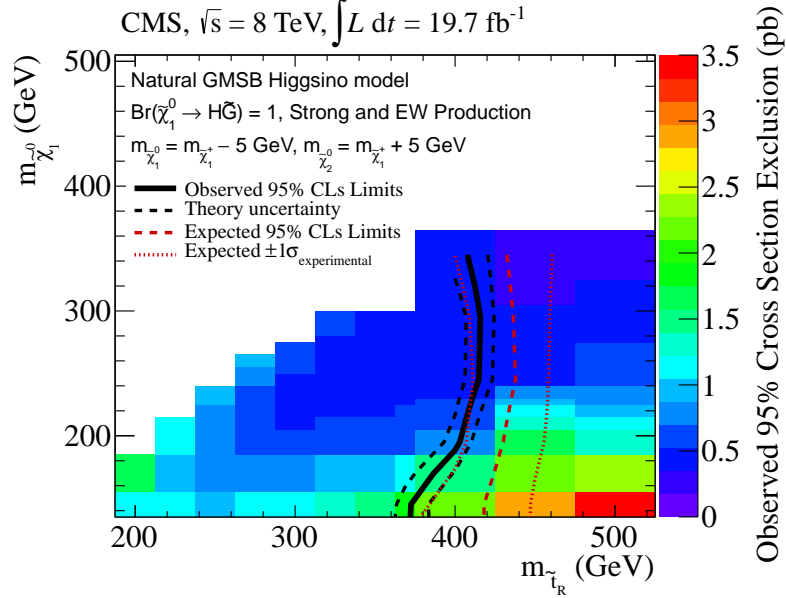


Figure 9.12: Limits on SUSY production cross sections for different stop and Higgsino masses using b-jet categories. The regions to the left of the contours are expected (red) and observed (black) to be excluded with 95% confidence. Black dashed curves reflect the theoretical uncertainty on cross section. Red dotted curves correspond to one standard deviation in expected sensitivity.

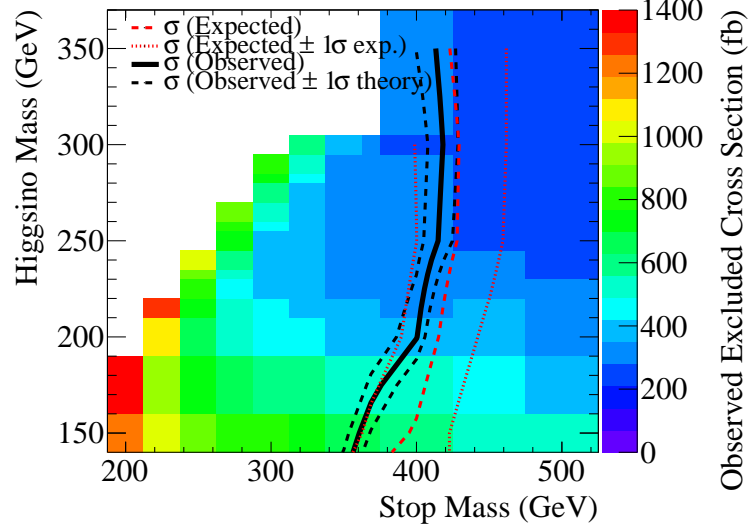


Figure 9.13: Limit on the stop pair production cross section without using categorization.

Table 9.3: Selected Limit Results

| Mass point | | Expected Limit σ (pb) | | Observed Limit σ (pb) | |
|------------|----------------|------------------------------|------------------------|------------------------------|-------------------|
| M_{stop} | $M_{higgsino}$ | binned | unbinned | binned | unbinned |
| 350 | 135 | $1.28^{+0.50}_{-0.33}$ | $1.45^{+0.68}_{-0.45}$ | 1.90 ± 0.27 | 2.02 ± 0.29 |
| 300 | 290 | $0.64^{+0.45}_{-0.25}$ | $0.88^{+0.50}_{-0.30}$ | 1.006 ± 0.148 | 1.048 ± 0.154 |
| 400 | 300 | $1.61^{+0.66}_{-0.43}$ | $1.66^{+0.93}_{-0.57}$ | 2.073 ± 0.296 | 1.918 ± 0.274 |

9.2 Higgsino $b\bar{b}$ Results

The diphoton mass distribution and fits for the two-Higgs channel are shown in in Figures 9.14.

The uncertainty in background estimate from the choice of fit function is negligible compared to the statistical uncertainty in the fit, particularly in low-statistics cases such as the two-Higgs channel.

The fitted function is:

$$N[events/GeV/c^2] = 3.36 * M_{\gamma\gamma}^{-0.55}$$

The integral over the Higgs mass window gives a standard model background estimate of 2.5 ± 1.3 events (53% uncertainty). Table 9.4 presents a simple comparison of the number of observed events in the signal region, the total expected background in the signal region, and expected counts from chosen Higgsino signal mass points.

Figure 9.15 shows the observed distributions of Higgs S_T after the two-Higgs selection requirements and using the fit from Figure 9.14. It includes the data-driven background and the expectation for several signal points. The 2H channel cuts the background sharply enough that low statistics effects obscure the natural shape of the background in Figure 9.15. Figure 9.16 is included to show the natural shape of the background when the b-tag requirement is relaxed to two loose b-jets.

Table 9.6 shows the event counts and background estimates for each Higgs S_T bin of the two Higgs category. Figure 9.17 shows $p_T^{\gamma\gamma}$ and p_T^{bb} for the 2H channel. Higgs S_T is the sum of these two quantities. Figure 9.18 shows the distributions of $M_{\gamma\gamma}$ and M_{bb} .

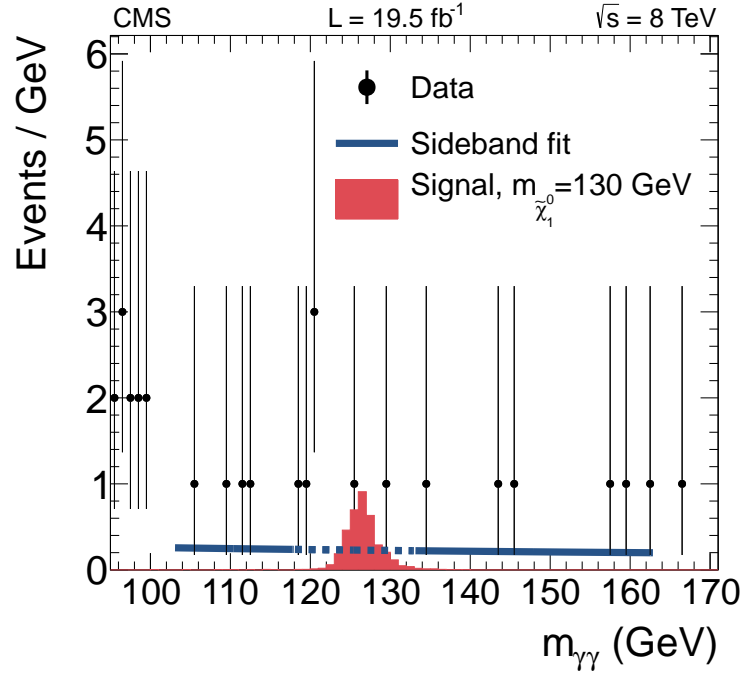
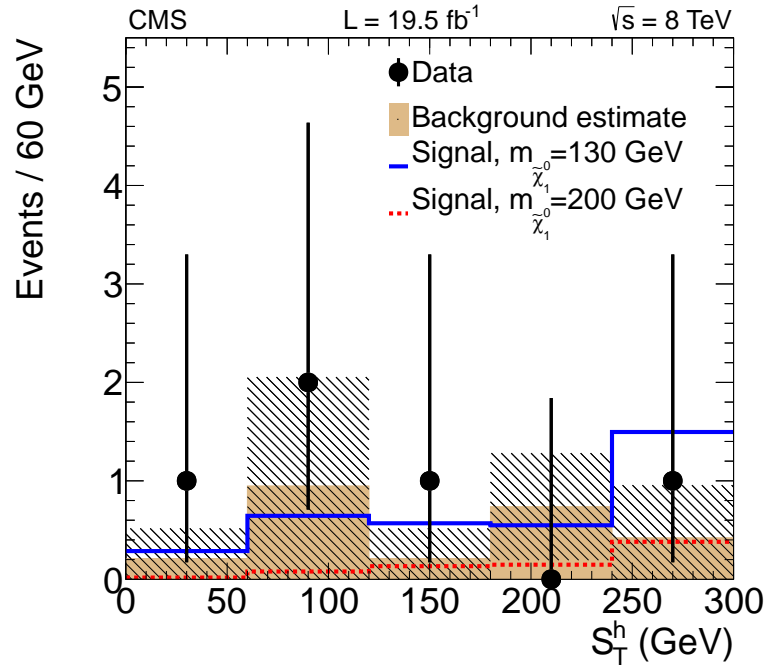


Figure 9.14: Diphoton mass spectrum for the Higgsino two Higgs channel.

Table 9.4: Expected and observed event counts for the Higgsino two Higgs channel

| | 2 B's on h mass |
|-----------------------------|-------------------|
| signal 130 GeV/c^2 | 3.6 |
| signal 200 GeV/c^2 | 0.79 |
| signal 250 GeV/c^2 | 0.31 |
| expected BG | 2.5 ± 1.3 |
| observed | 5 |

Table 9.5: The uncertainties includes the statistical uncertainty and the normalization uncertainty from the fit function.

Figure 9.15: Higgs S_T distributions for the data, background, and selected Monte Carlo points, used for limit setting for the two Higgs channel. The last bins include the overflow. The background estimate uncertainty (black hatching) includes the statistical uncertainty and the normalization uncertainty from the fit function which is the same for all the bins.

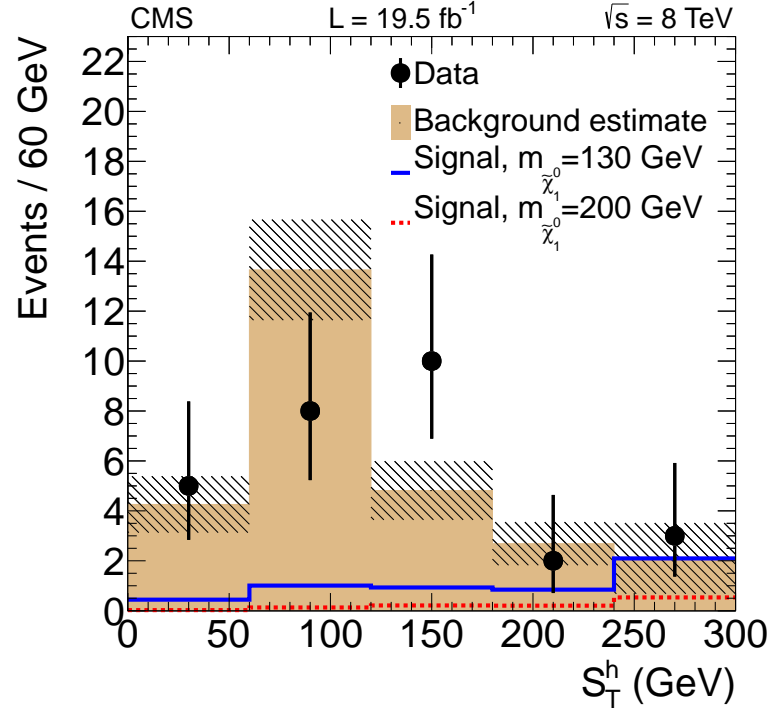


Figure 9.16: Higgs S_T distributions for the data, background, and selected Monte Carlo points when the b-tag requirements of the 2H channel are relaxed. This shows the natural shape of the Higgs S_T background before the effects of low statistics seen in Figure 9.15 become dominant.

Table 9.6: Observations and Background Estimates for the two-Higgs channel

| Higgs S_T bin (GeV) | SM background | Data | HH events, $m_{\tilde{\chi}_1^0} = 130 \text{ GeV}/c^2$ |
|-----------------------|-----------------|------|---|
| 0-60 | 0.21 ± 0.28 | 1 | 0.279 ± 0.027 |
| 60-120 | 0.95 ± 0.99 | 2 | 0.627 ± 0.041 |
| 120-180 | 0.21 ± 0.29 | 1 | 0.553 ± 0.038 |
| 180-240 | 0.74 ± 0.38 | 0 | 0.534 ± 0.037 |
| ≥ 240 | 0.42 ± 0.49 | 1 | 1.455 ± 0.062 |

Table 9.7: The uncertainties includes the statistical uncertainty and the normalization uncertainty from the fit function.

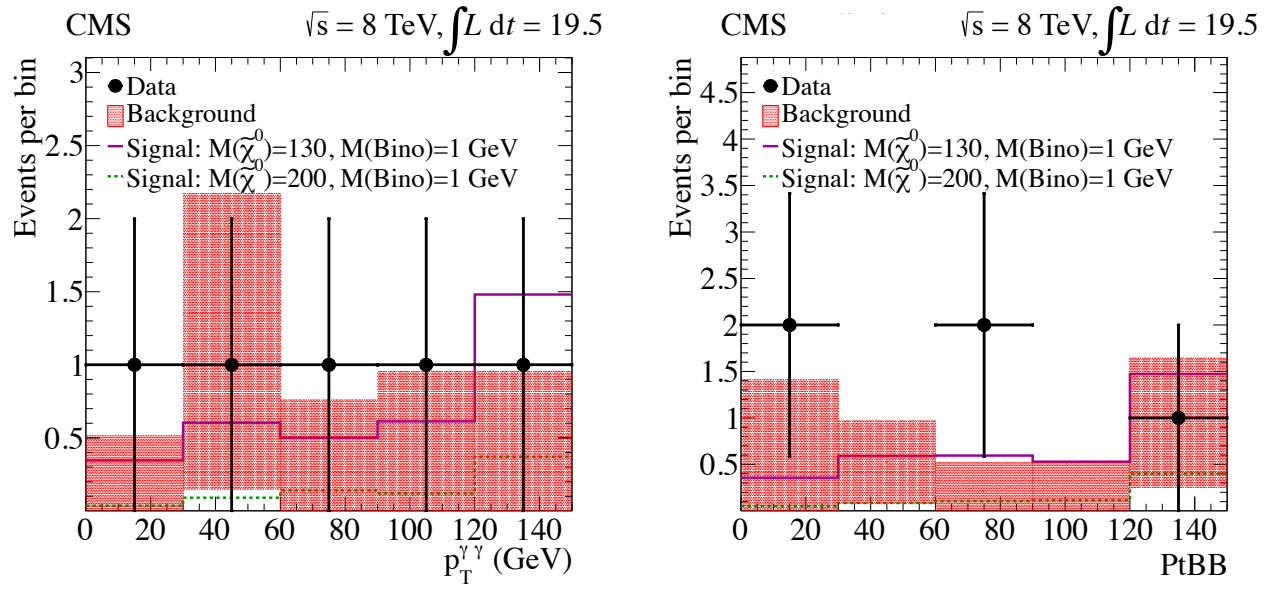


Figure 9.17: $p_T^{\gamma\gamma}$ (left) and p_T^{bb} (right) for the 2H channel. The red indicates the range of background estimates. Signal accumulates at high values in both distributions.

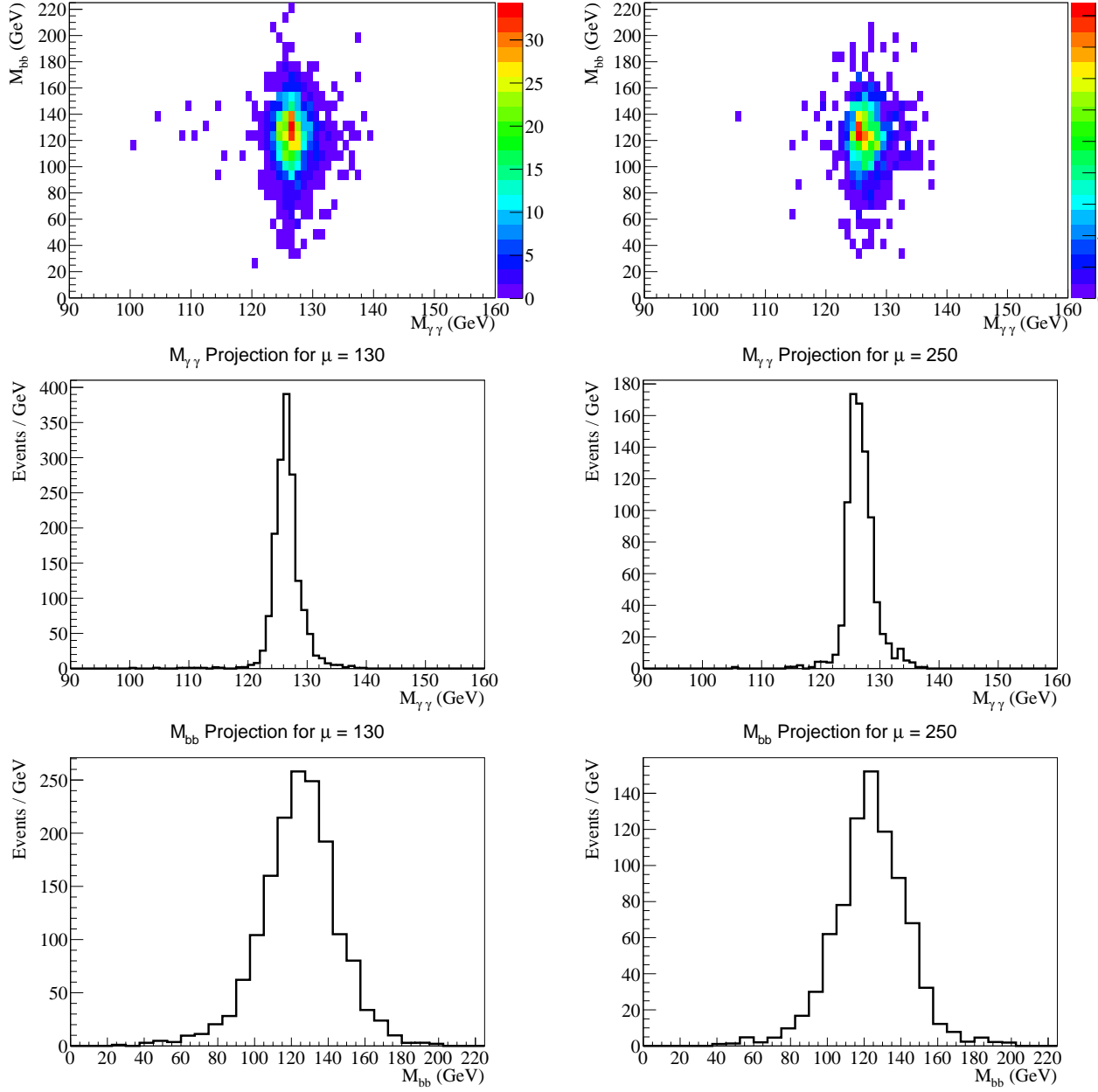


Figure 9.18: Reconstructed Higgs masses decaying through $H(\gamma\gamma) + H$ in the 2H channel. The left column shows the $\mu = 130 \text{ GeV}/c^2$ mass point and the right column shows the $\mu = 250 \text{ GeV}/c^2$ mass point. The top row shows M_{bb} vs. $M_{\gamma\gamma}$. The middle row shows projections onto $M_{\gamma\gamma}$. And the bottom row shows projections onto M_{bb} .

9.2.1 Statistical Interpretation

Figure 9.19 shows the limits obtained for the two-Higgs channel assuming a BR of 100% for $\tilde{\chi}_1^0 \rightarrow H + \tilde{G}$. The limits are expressed both in terms of the limit cross section and the limit r-value. R-values are the ratio between the signal cross section that can be excluded and the theoretical cross section.

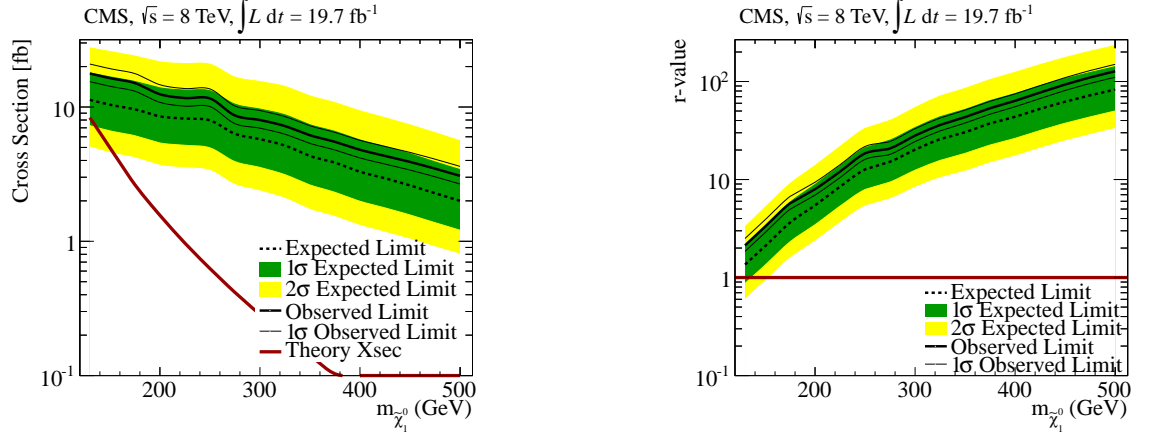


Figure 9.19: Left: Cross section limits for pure HH production and the theory cross section. Right: The corresponding r-values for the limits.

9.3 Higgsino Leptonic Results

The diphoton mass distributions and fits for the lepton channels are shown in in Figures 9.20. The standard model Higgs contribution to these channels are negligible. Table 9.8 presents a simple comparison of the number of observed events in the signal region and the total expected background in the signal region for both lepton channels.

Figures 9.21 and 9.22 present the distributions of M_T , the main sensitive variable, for the muon and electron channels respectively. This information is also represented in Table 9.9 and Table 9.10 which shows the event counts, background estimates, and selected theoretical signal contributions for each M_T bin of the two channels.

Figure 9.23 shows the E_T^{miss} distribution for the two lepton channels for the sake of comparing E_T^{miss} behavior with the other analyses.

The electron channel shows an excess with a p-value of 1.3%. (p-value is the likelihood of seeing that many events or more under the background-only hypothesis.) This should be taken in context with the various other channels considered that do not show excess.

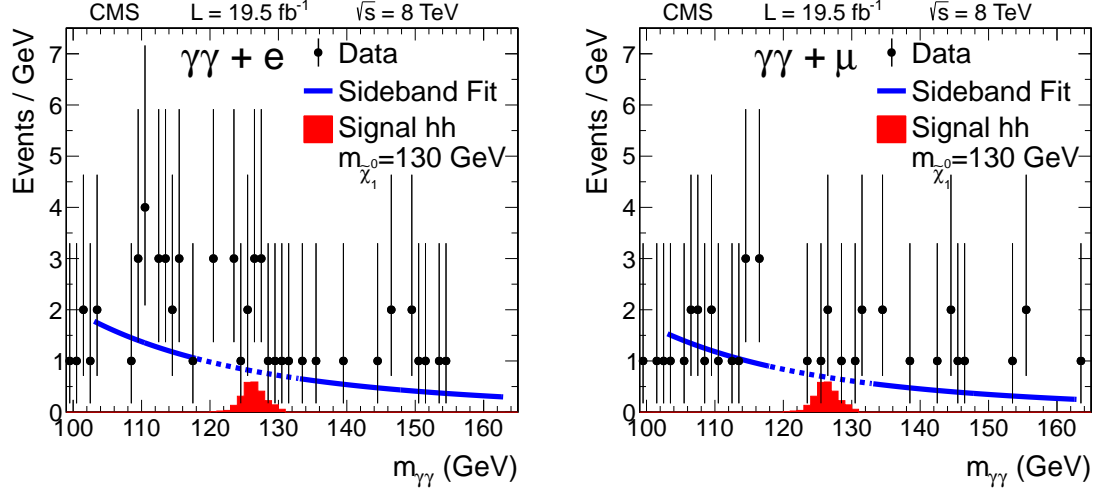


Figure 9.20: The results from fitting a power law in the electron + $h \rightarrow \gamma\gamma$ diphoton invariant mass distribution (left) and same for muons + $h \rightarrow \gamma\gamma$ (right). Also overlaid is the signal yield from addition of all the HH SMS scans with $m_{\tilde{\chi}_1^0} = 130 \text{ GeV}/c^2$, $m_{LSP} = 1 \text{ GeV}/c^2$.

Table 9.8: Comparison of the observed data and background estimates for the lepton channels. The electron channel shows an excess with a 1.3% p-value.

| Channel | Net Background Estimate | Signal Region |
|----------------------|-------------------------|---------------|
| $\gamma\gamma + e$ | 9.11 ± 1.60 | 18 |
| $\gamma\gamma + \mu$ | 7.76 ± 1.48 | 6 |

Table 9.9: Signal region counts and background estimates using M_T variable for the diphoton+electron selection, showing also the signal yields for the signal model with $m_{\tilde{\chi}_1^0} = m_{\tilde{\chi}_2^0} = m_{\tilde{\chi}_1^\pm} = 130 \text{ GeV}/c^2$ and $m_{\tilde{\chi}_1^0} = 1 \text{ GeV}/c^2$. The last three columns show the break-down of the uncertainty in the

| M_T bin [GeV/c^2] | HW $^\pm$ | HH | HZ | Data | Signal Region | Background Estimate |
|--------------------------------|---------------|--------------|--------------|------|---------------|---------------------|
| 0 – 30 | $0.8 \pm .06$ | $.9 \pm .04$ | $.4 \pm .03$ | 4 | | 4.38 ± 1.66 |
| 30 – 60 | $1.0 \pm .07$ | $.9 \pm .04$ | $.4 \pm .03$ | 9 | | 3.21 ± 1.22 |
| 60 – 90 | $1.5 \pm .08$ | $.6 \pm .04$ | $.3 \pm .03$ | 4 | | 1.44 ± 0.85 |
| > 90 | $1.4 \pm .08$ | $.3 \pm .02$ | $.1 \pm .02$ | 1 | | 0.96 ± 0.58 |

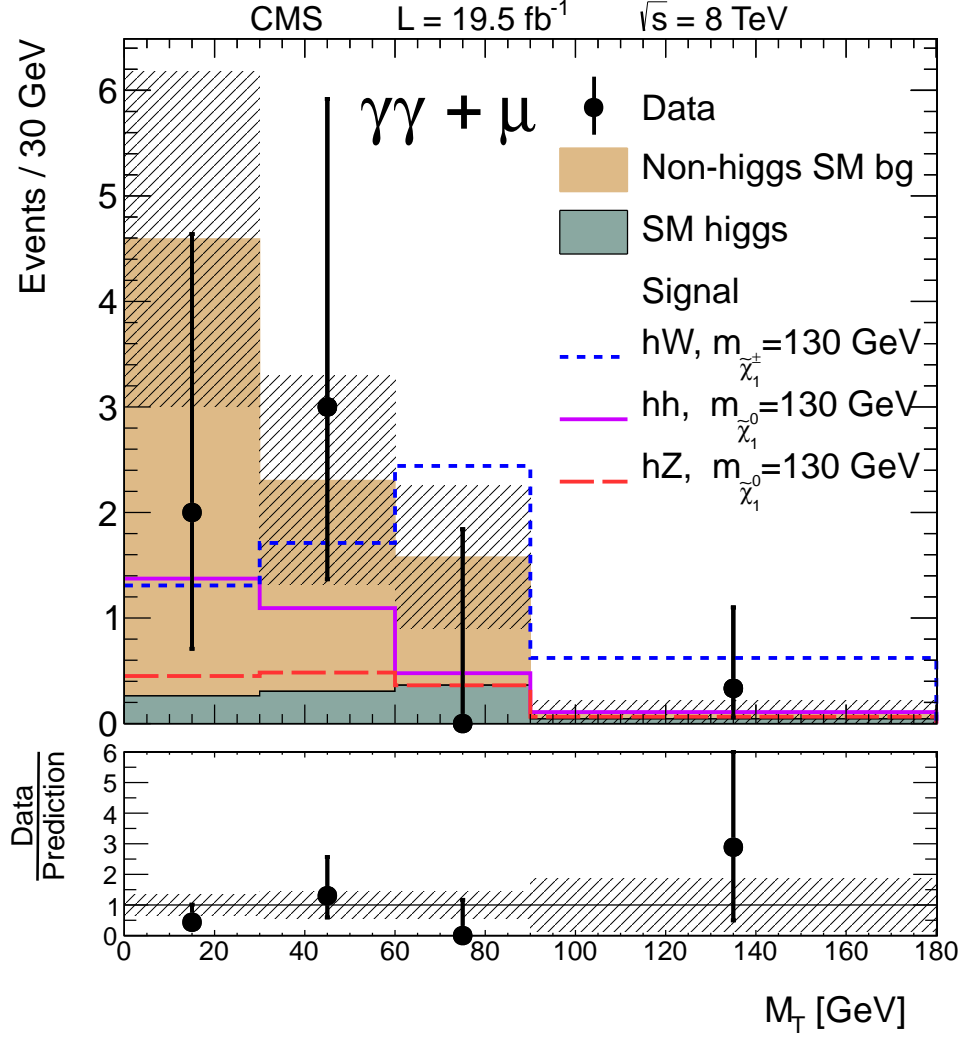


Figure 9.21: The M_T distribution for the muon + Higgs selection. In grey is the sideband estimated non Higgs background, with the statistical and systematic errors from the full background estimate in the red hatching. The SM Higgs background contribution is shown with gray-blue fill. All SM Higgs samples have $m_h = 126 \text{ GeV}/c^2$, and all SMS lines represent the $m_{\tilde{\chi}_2^0} = m_{\tilde{\chi}_1^\pm} = 130 \text{ GeV}/c^2$, $m_{\tilde{\chi}_2^\pm} = 1 \text{ GeV}/c^2$ point.

Table 9.10: Signal region counts and background estimates using M_T variable for the di-photon+muon selection, showing also the the signal yields for the signal model with $m_{\tilde{\chi}_1^0} = m_{\tilde{\chi}_2^0} = m_{\tilde{\chi}_1^\pm} = 130 \text{ GeV}/c^2$ and $m_{\tilde{\chi}_2^\pm} = 1 \text{ GeV}/c^2$.

| $M_T \text{ bin [GeV}/c^2]$ | HW $^\pm$ | HH | HZ | Data | Signal Region | Background Estimate |
|-----------------------------|----------------|----------------|---------------|------|---------------|---------------------|
| 0 – 30 | 1.2 ± 0.07 | 1.2 ± 0.04 | $.5 \pm 0.04$ | 2 | | 4.60 ± 1.59 |
| 30 – 60 | 1.6 ± 0.08 | 1.1 ± 0.05 | $.5 \pm 0.04$ | 3 | | 2.31 ± 0.99 |
| 60 – 90 | 2.3 ± 0.10 | 0.9 ± 0.04 | $.4 \pm 0.03$ | 0 | | 1.59 ± 0.68 |
| > 90 | 1.7 ± 0.09 | 0.2 ± 0.02 | $.2 \pm 0.02$ | 1 | | 0.35 ± 0.30 |

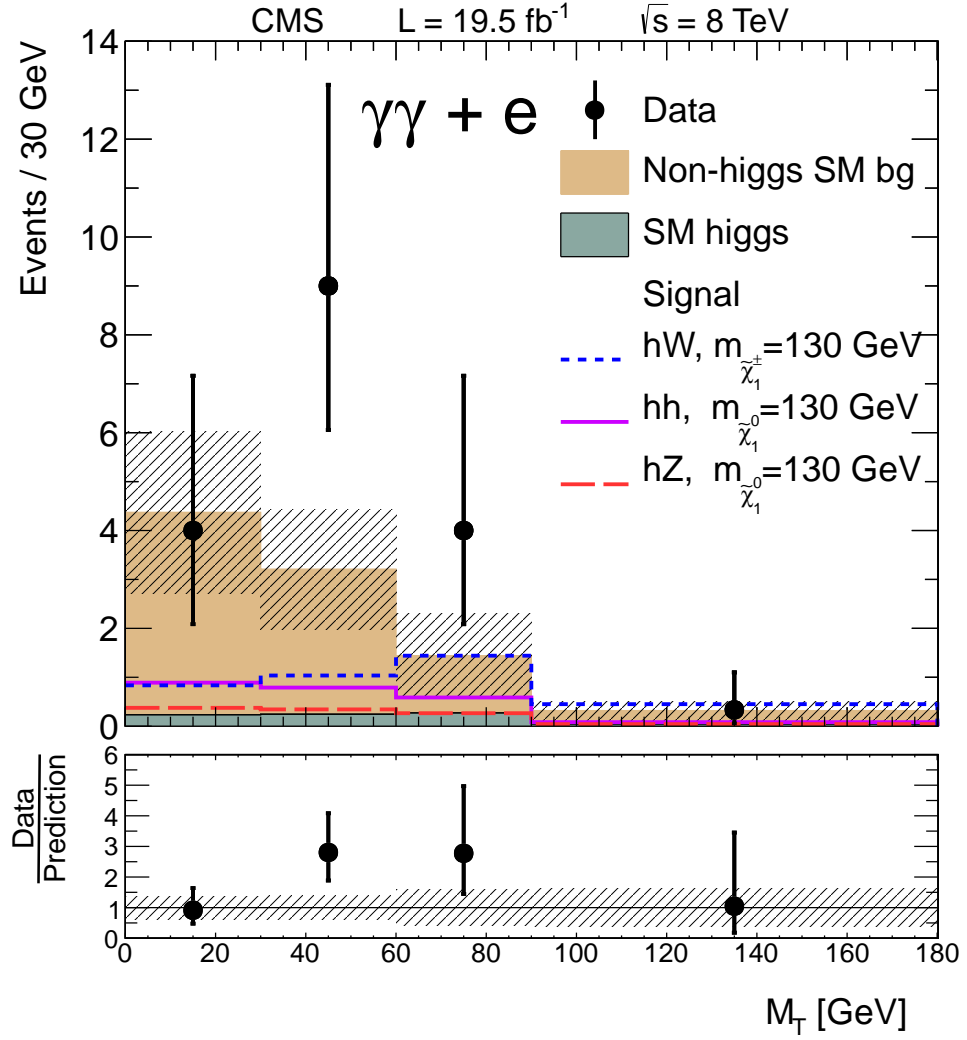


Figure 9.22: The M_T distribution for the electron + Higgs selection. In tan is the sideband estimated non Higgs background, with the statistical and systematic errors from the full background estimate in the red hatching. The SM Higgs background contribution is shown with gray-blue fill. All SM Higgs samples have $m_h = 126 \text{ GeV}/c^2$, and all SMS lines represent the $m_{\tilde{\chi}_2^0} = m_{\tilde{\chi}_1^\pm} = 130 \text{ GeV}/c^2$, $m_{\tilde{\chi}_1^0} = 1 \text{ GeV}/c^2$ point.

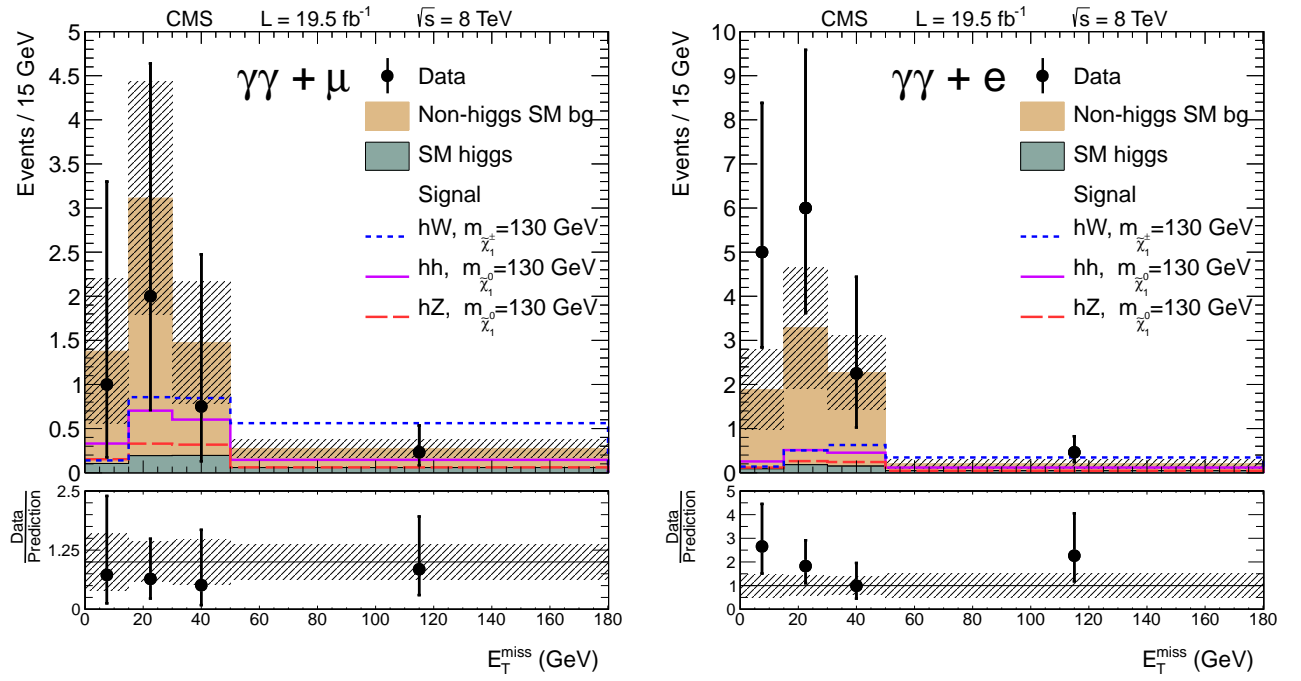


Figure 9.23: E_T^{miss} distributions for the muon channel (left) and electron channel (right).

9.3.1 Statistical Interpretation

Figure 9.24 and 9.25 show the r-values set by attempting to set limits on HH and HZ models from the lepton channels alone. These can also be considered to be the contributions of the lepton channel to the combined Higgsino limit setting. These limits are made using M_T as the sensitive variable. The effects of the electron channel's excess can be seen in the left hand plots where the black observed limits are about 2σ above the expected limits in places, particularly at low masses. The electron channel excess degrades the limit more uniformly for a HH signal than for a HZ signal.

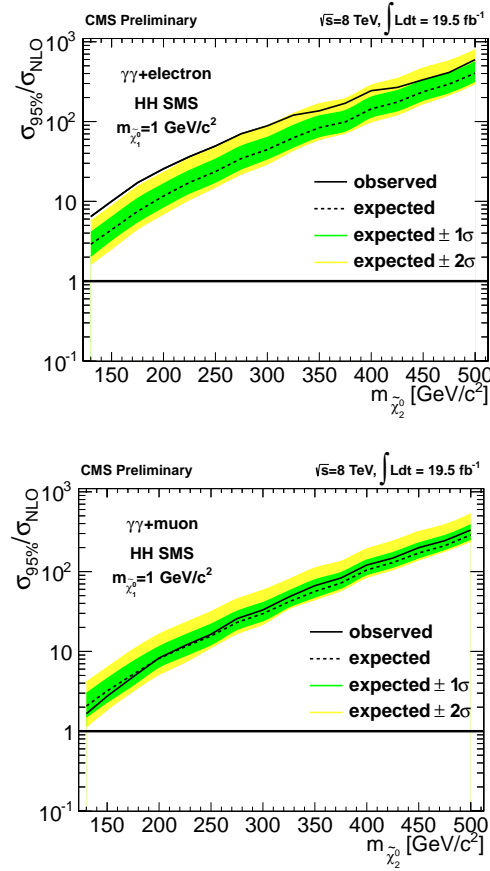


Figure 9.24: r-value limits for the di-photon+electron alone (left) and di-photon+muon alone (right) selections for the HH signal model. Shown are the observed limit (black), expected limit (black dashed), $\pm 1\sigma$ expected limits (green), and $\pm 2\sigma$ expected limits (yellow).

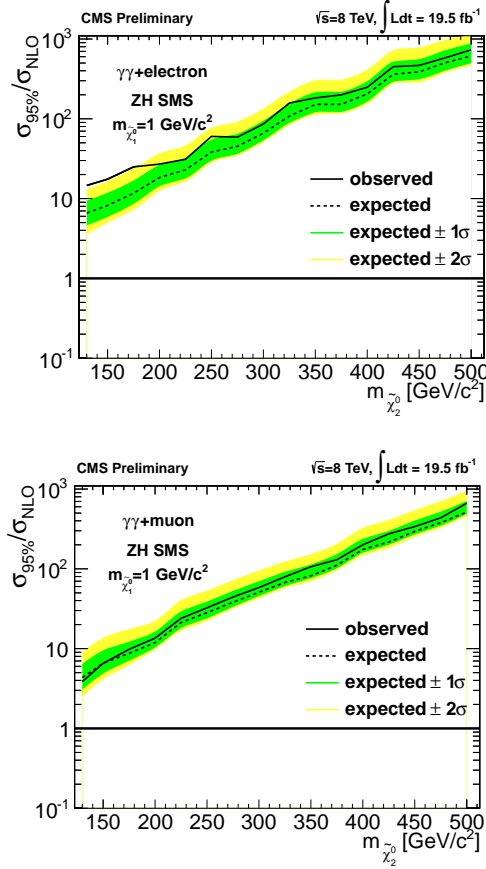


Figure 9.25: r -value limits for the di-photon+electron alone (left) and di-photon+muon alone (right) selections for the HZ signal model. Shown are the observed limit (black), expected limit (black dashed), $\pm 1\sigma$ expected limits (green), and $\pm 2\sigma$ expected limits (yellow).

9.4 Higgsino Electro-Weak Results

The diphoton mass distribution and fits for the electroweak channel are shown in in Figures 9.26.

The uncertainty in background estimate from the choice of fit function is negligible compared to the statistical uncertainty in the fit, particularly in low-statistics cases such as the two-Higgs channel.

The fitted function is:

$$N[\text{events}/\text{GeV}/c^2] = 1.9 * 10^8 * M_{\gamma\gamma}^{-3.1}$$

The integral over the Higgs mass window gives a standard model background estimate of 633 ± 13 events (2% uncertainty). Table 9.11 presents a simple comparison of the number of observed events in the signal region, the total expected background in the signal region, and expected counts from

chosen signal mass points for both HZ and HW^\pm signals.

Figure 9.27 shows the observed distributions of E_T^{miss} after the V+Higgs selection requirements and using the fit from Figure 9.27 and HZ Monte Carlo. Figure 9.28 includes both a version of the plot in Figure 9.27, and compares that to the comparable HW^\pm Monte Carlo and the standard model Higgs background. These include the data-driven background and the expectation for several signal points. This information is represented in Table 9.13 which shows the event counts and background estimates for each E_T^{miss} bin of the electroweak category.

A similar quantity to Higgs S_T can be computed for the electroweak channel by using the p_T of the leading pair of jets for the p_T of the vector boson. This is shown in Figure 9.29 and can be compared to the Higgs S_T in the 2-Higgs channel as seen in Figure 9.15. It should be clear that this is not nearly as sensitive as Higgs S_T is in the 2H channel. The breakdown of $p_T^{\gamma\gamma} + p_T^{jj}$ into $p_T^{\gamma\gamma}$ and p_T^{jj} is shown in Figure 9.30 for HZ and Figure 9.31 for HW^\pm .

Figure 9.32 and Figure 9.33 show comparisons of the diphoton mass and dijet mass for HZ and HW^\pm signals respectively. The upper plots demonstrate that these variables are uncorrelated for the signal models.

Table 9.11: Expected and observed event counts

| | 2 Jets on EWK mass | |
|-----------------------------|--------------------|-----------------|
| | HZ | HW^\pm |
| signal 130 GeV/c^2 | 4.9 | 4.5 |
| signal 200 GeV/c^2 | 0.98 | 1.1 |
| signal 250 GeV/c^2 | 0.47 | 0.46 |
| expected BG | 634.9 ± 13.1 | |
| observed | 694 | |

Table 9.12: The uncertainties includes the statistical uncertainty and the normalization uncertainty from the fit function.

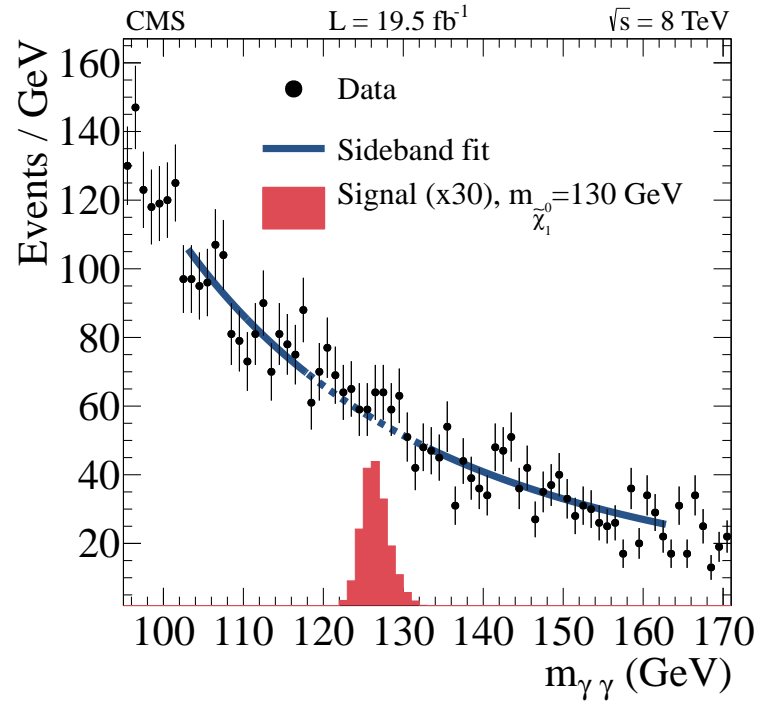


Figure 9.26: Diphoton mass spectrum for the electroweak channel. Here the signal has been scaled up by a factor of 30 to make it visible.

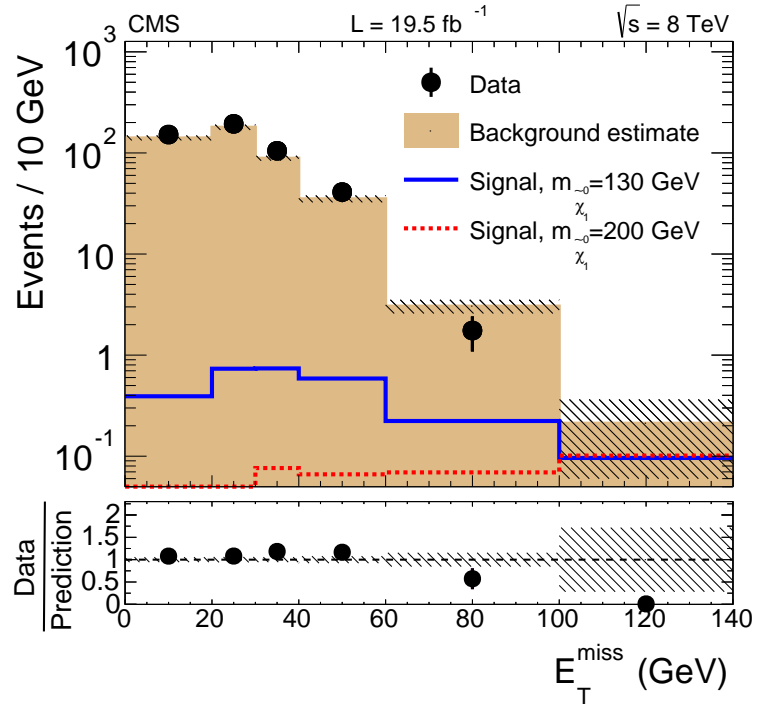


Figure 9.27: Signal and background prediction for the electroweak channel. The last bin includes the overflow. The background estimate (red) uncertainty includes the statistical uncertainty and the normalization uncertainty from the fit function which is the same for all the bins.

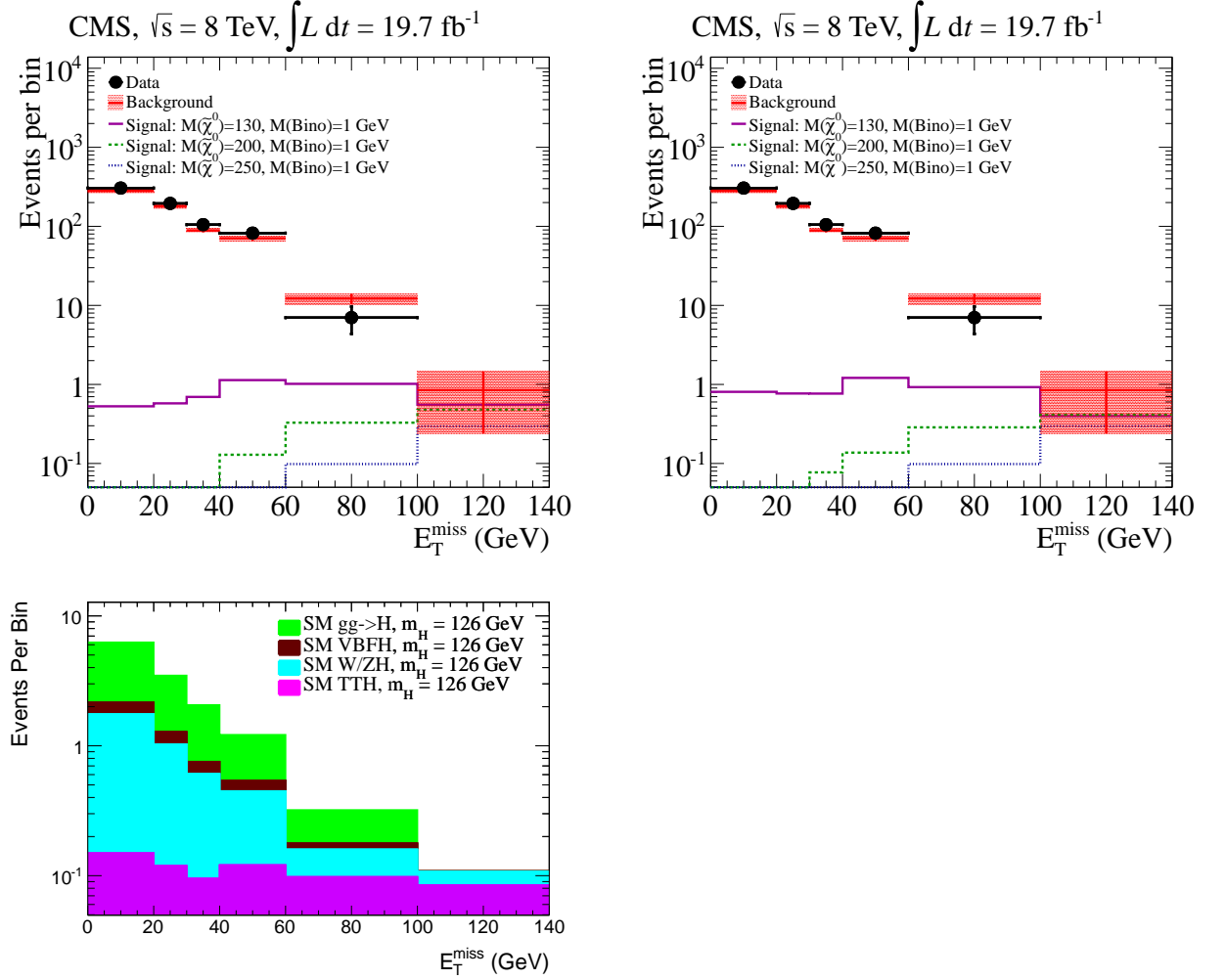
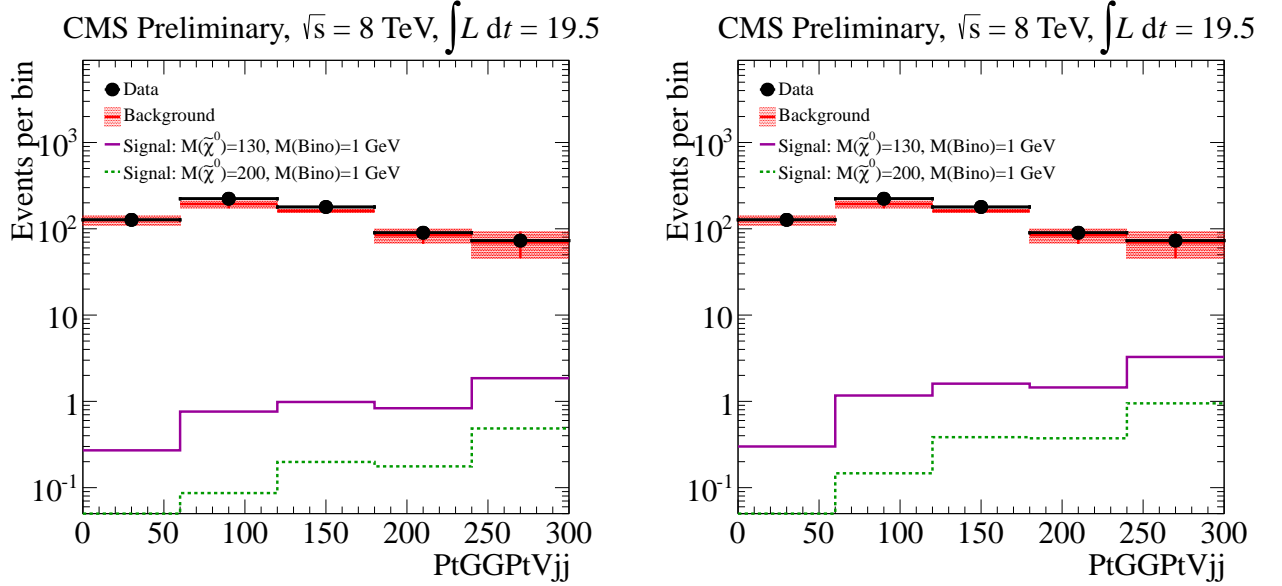


Figure 9.28: Data, background and expected signal comparison for the electroweak channel. Left: E_T^{miss} distributions for the data, data driven background, and selected HW^\pm Monte Carlo points, used for limit setting for the two Higgs channel. Right: The same, but instead using HZ Monte Carlo. Bottom: the expected SM Higgs background contribution. The last bins include the overflow. The background estimate (red) uncertainty includes the statistical uncertainty and the normalization uncertainty from the fit function which is the same for all the bins.

Table 9.13: Observations and Background Estimates for the Electroweak channel

| E_T^{miss} bin (GeV) | SM background | Data | HZ events, $m_{\tilde{\chi}_1^0} = 130 \text{ GeV}/c^2$ |
|-------------------------------|-----------------|------|---|
| 0-20 | 282 ± 15 | 305 | 0.762 ± 0.030 |
| 20-30 | 180 ± 10 | 195 | 0.714 ± 0.029 |
| 30-40 | 89.0 ± 4.7 | 105 | 0.718 ± 0.029 |
| 40-60 | 70.8 ± 5.0 | 82 | 1.142 ± 0.037 |
| 60-100 | 12.2 ± 1.9 | 7 | 0.868 ± 0.032 |
| >100 | 0.85 ± 0.61 | 0 | 0.374 ± 0.021 |

Table 9.14: The uncertainties includes the statistical uncertainty and the normalization uncertainty from the fit function.

Figure 9.29: $p_T^{\gamma\gamma} + p_T^{jj}$ in the electroweak channel for HZ (right) and HW^\pm (left). This is the quantity in the electroweak channel mo st comparable to Higgs S_T in the 2H channel. p_T^{jj} is the p_T of the leading pair of dijets.

9.4.1 Statistical Interpretation

The limits on HZ production considering only the electroweak channel are shown in Figure 9.34.

This is an unphysical situation where Higgsinos always decay to one Higgs boson and one Z, and is meant to illustrate the channels sensitivity and its contribution to the combined result. Clearly a real signal must contain a combination of these three final states with the mixing ration dependent on the Higgsino branching ratios.

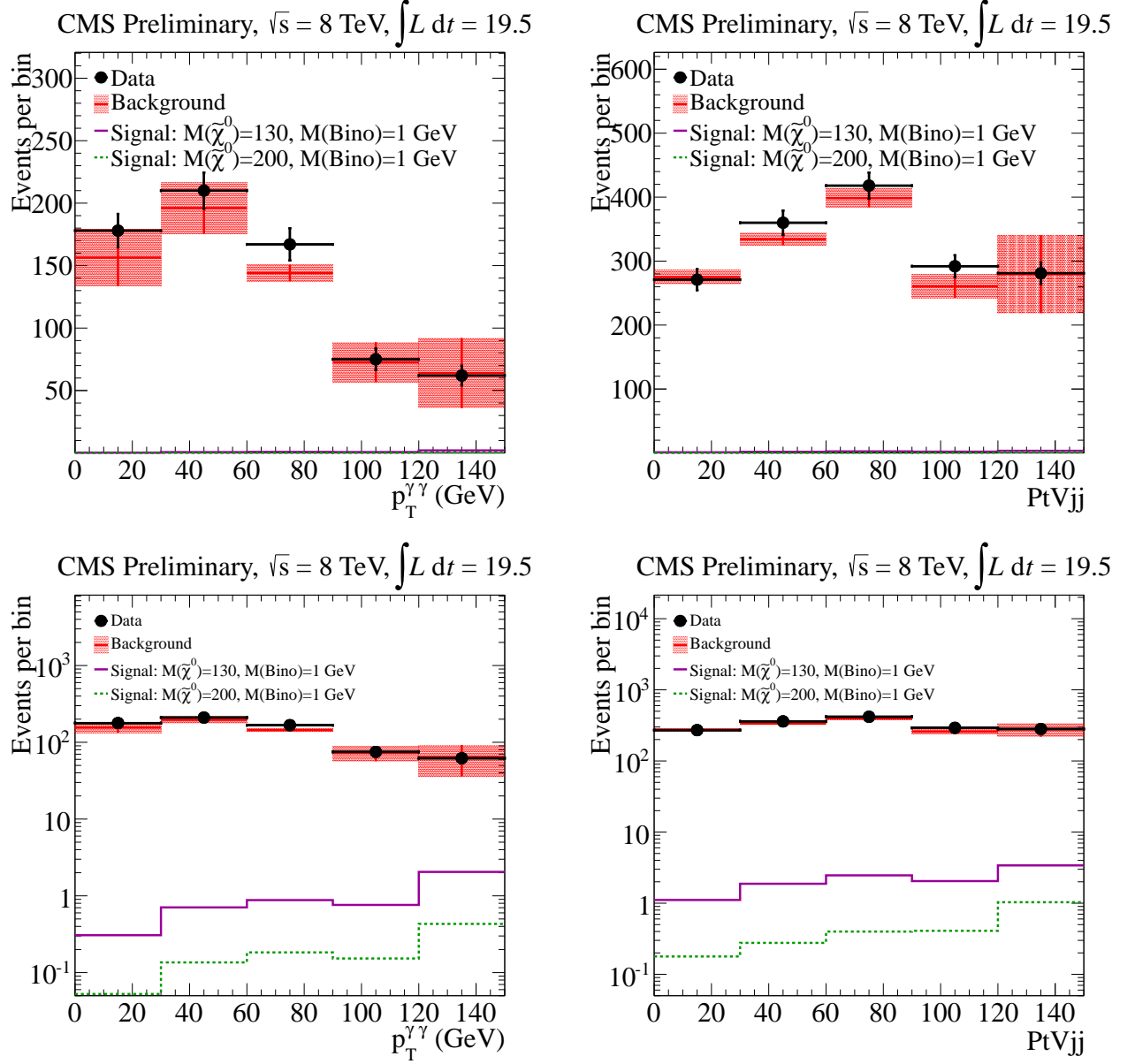


Figure 9.30: $p_T^{\gamma\gamma}$ (left column) and p_T (right column) of the leading pair of jets for the ZH channel. The bottom row shows logarithmic versions of the plots in the top row.

The limits on HW^\pm production are shown in Figure 9.35 from the electroweak channel alone. In this case, the HW^\pm is physically plausible but again is meant to show the contribution of the electroweak channel to a combined limit. R-values are the ratio between the signal cross section that can be excluded and the theoretical cross section.

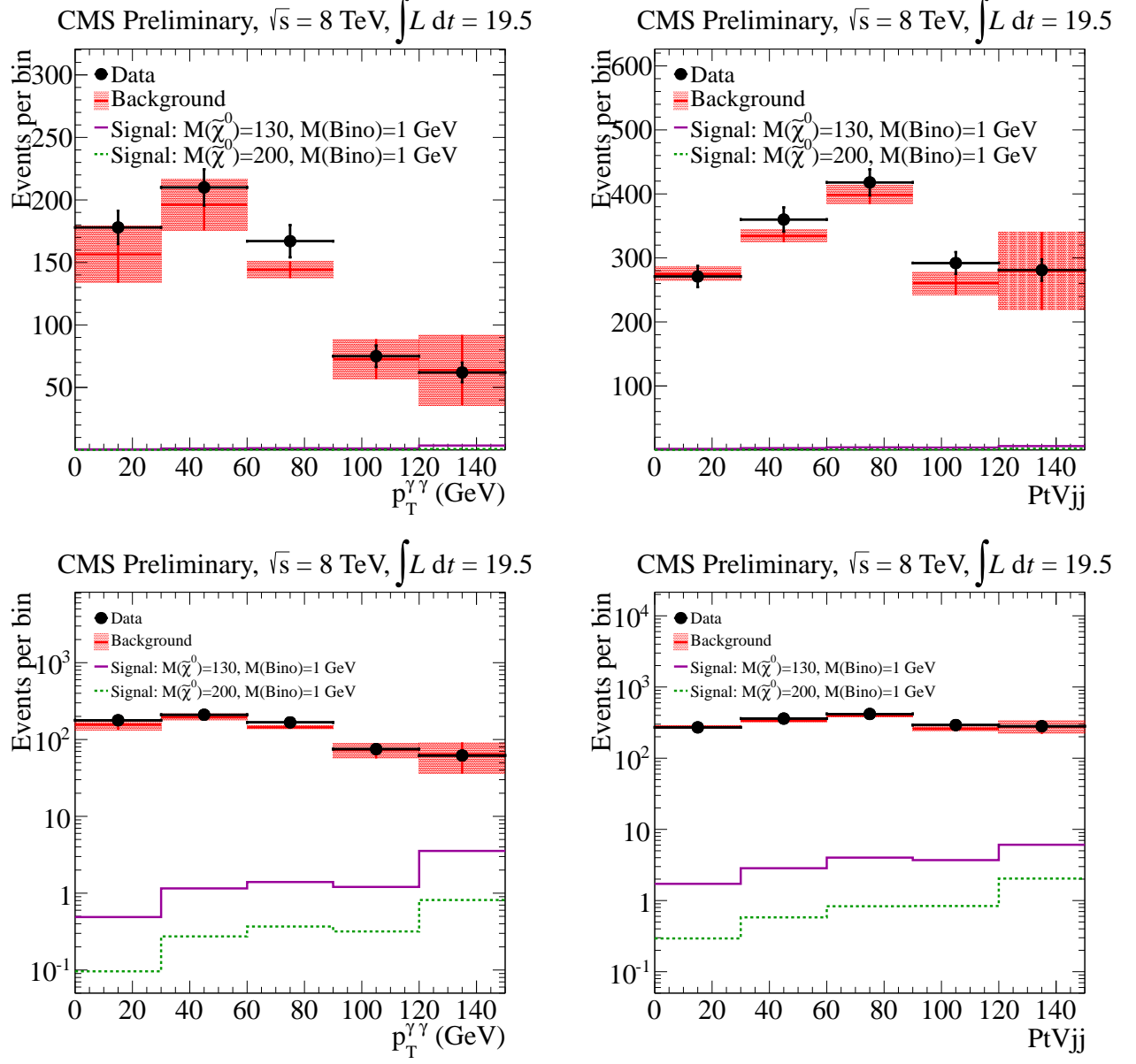


Figure 9.31: $p_T^{\gamma\gamma}$ (left column) and p_T (right column) of the leading pair of jets for the WH channel. The bottom row shows logarithmic versions of the plots in the top row.

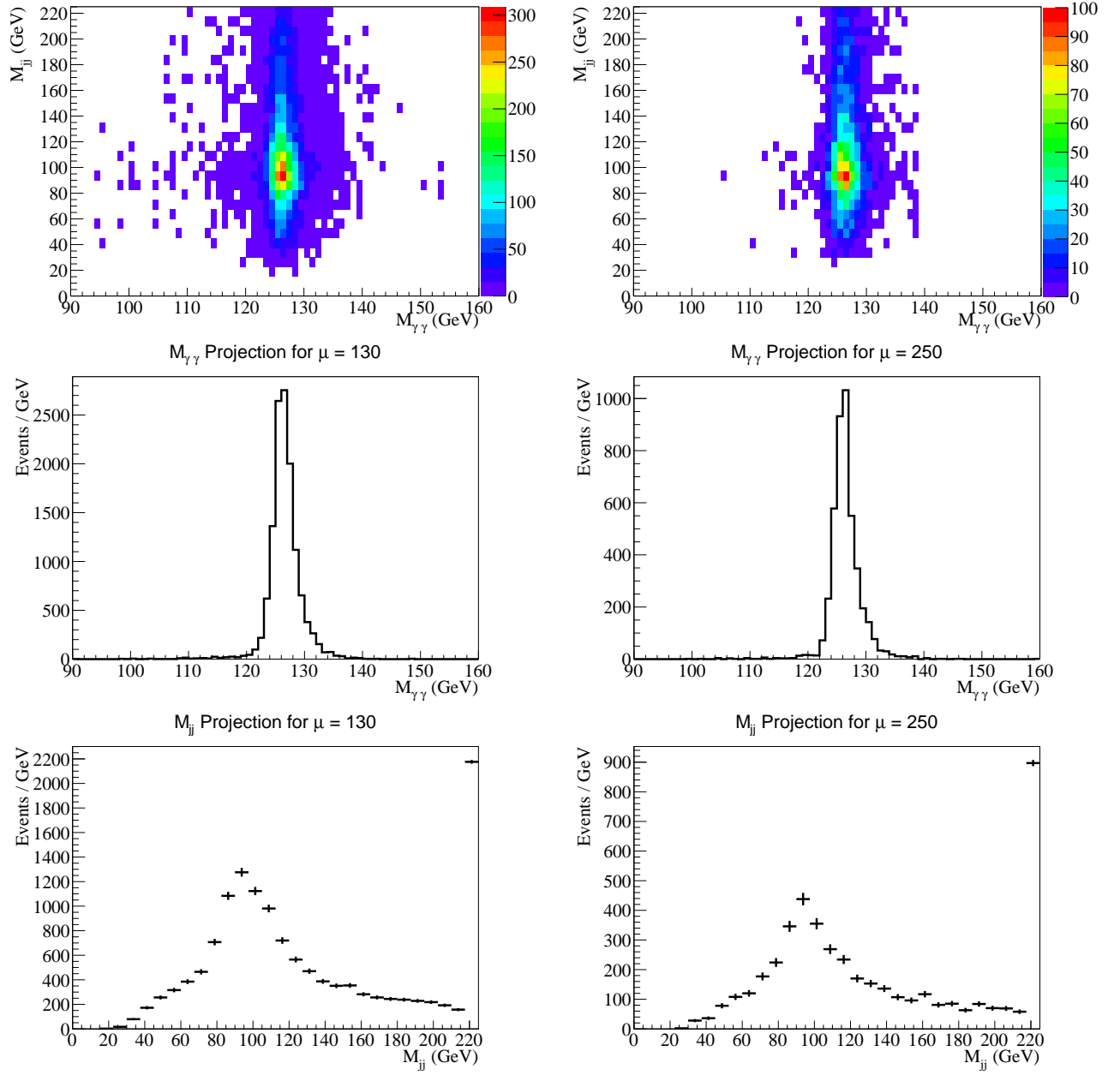


Figure 9.32: Reconstructed boson masses decaying through $H(\gamma\gamma) + Z$ in the electroweak channel. The left column shows the $\mu = 130$ GeV/c^2 mass point and the right column shows the $\mu = 250$ GeV/c^2 mass point. The top row shows M_{jj} vs. $M_{\gamma\gamma}$. M_{jj} is plotted for all pairs of jets passing our jet selection and $H(b\bar{b})$ veto. The middle row shows projections onto $M_{\gamma\gamma}$. And the bottom row shows projections onto M_{jj} .

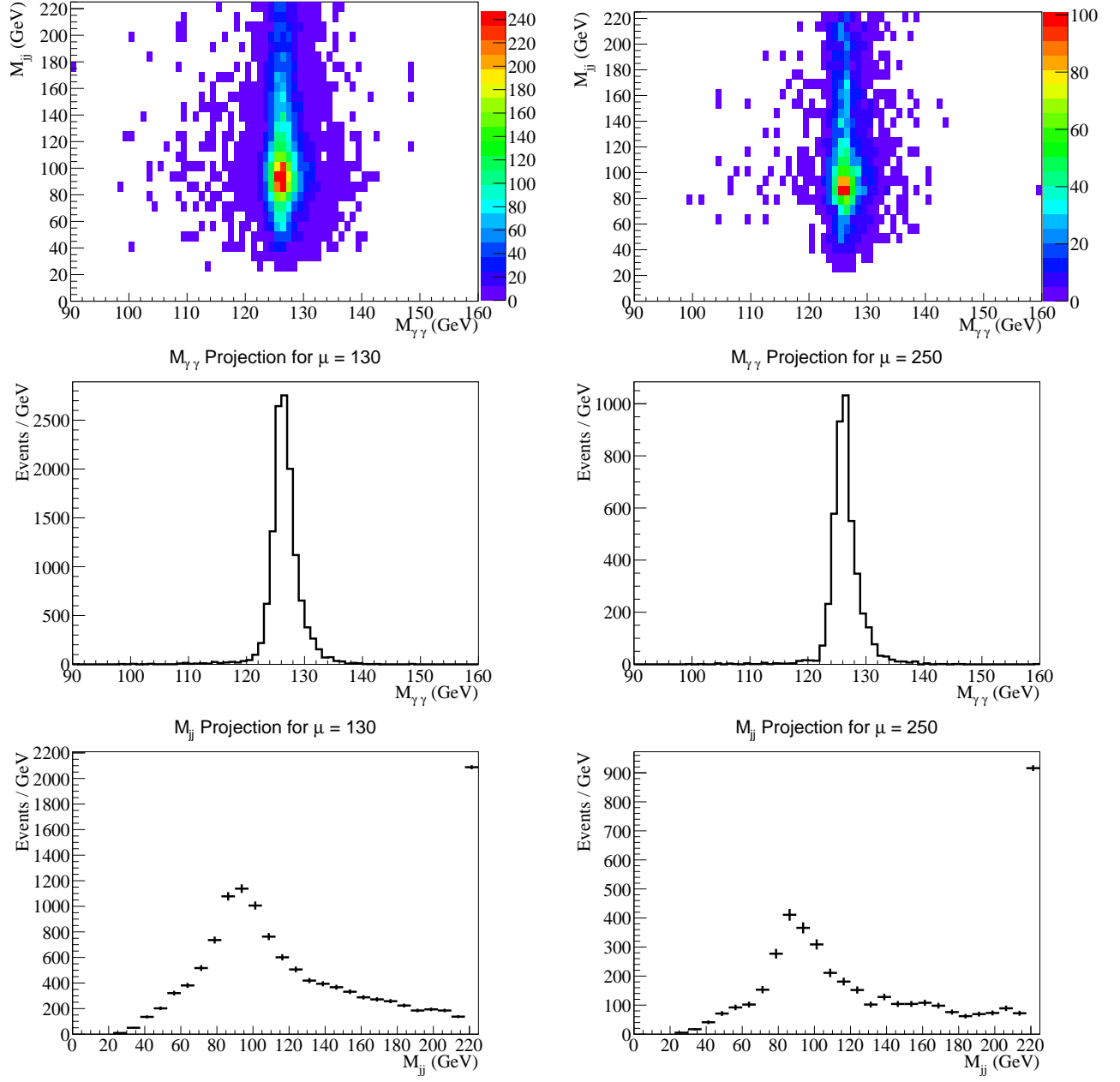


Figure 9.33: Reconstructed boson masses decaying through $H(\gamma\gamma) + W^\pm$ in the electroweak channel. The left column shows the $\mu = 130 \text{ GeV}/c^2$ mass point and the right column shows the $\mu = 250 \text{ GeV}/c^2$ mass point. The top row shows M_{jj} vs. $M_{\gamma\gamma}$. M_{jj} is plotted for all pairs of jets passing our jet selection and $H(b\bar{b})$ veto. The middle row shows projections onto $M_{\gamma\gamma}$. And the bottom row shows projections onto M_{jj} .

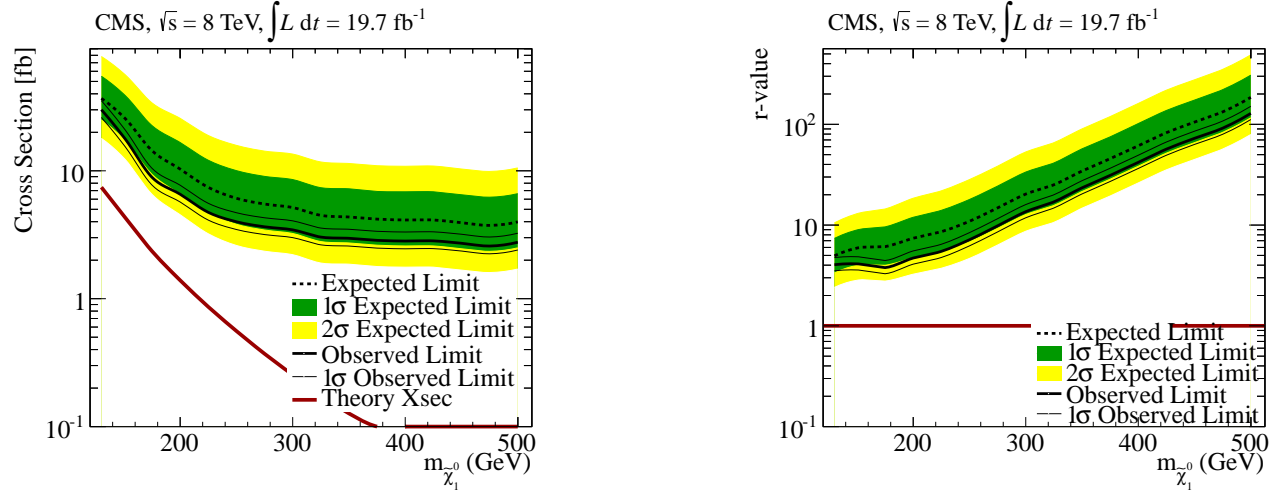


Figure 9.34: Left: Cross section limits for pure HZ production and the theory cross section. Right: The corresponding r-values for the limits.

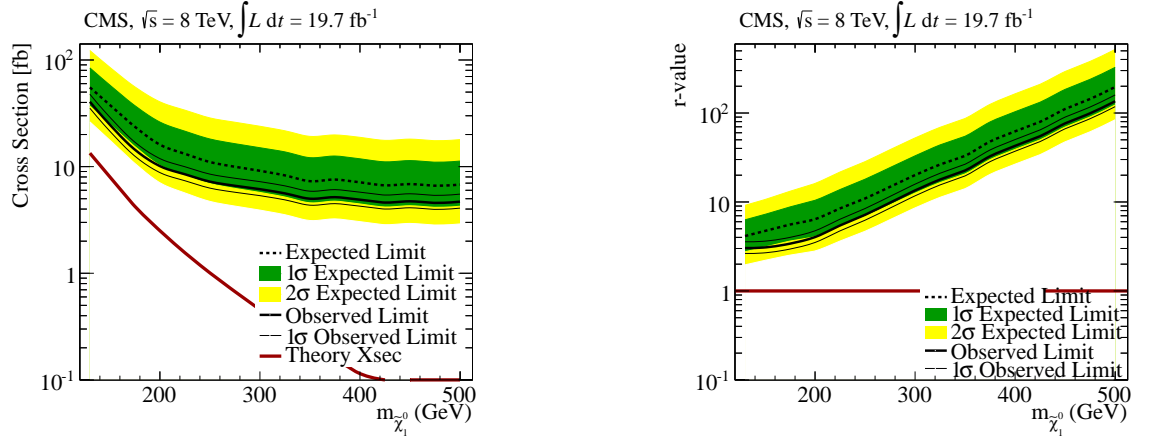


Figure 9.35: Left: Cross section limits for pure HW^\pm production and the theory cross section. Right: The corresponding r-values for the limits (see (10)).

9.5 Higgsino Combination Interpretation

As discussed earlier, a Higgsino signal decays to several channels necessitating that the results of several analyses be combined to maximize sensitivity. The Higgsino bb , Higgsino Lepton, and Higgsino Electroweak analysis channels were conceived as components of this combination. Here the limits from these channels are combined with results from four other analyses to give the combined limit. The other analyses are the CMS Multi-lepton analysis (26; 55), the CMS 4b analysis (4), the CMS $2b2\ell$ (22), and the CMS $2j2\ell$ analysis (21). Further details of the combination process and combined results can be found in reference (54).

For simplicity, these analyses consider one of three pure Higgsino intermediate decay topologies: HH , HZ , or ZZ . Then sliding Higgsino branching ratios were created by weighting the efficiencies in data cards from each analysis according to the topology:

$$HH : BR^2$$

$$HZ : 2 * BR * (1 - BR)$$

$$ZZ : (1 - BR)^2$$

A frequentist LHC-style profiled likelihood test statistics (39) is applied, using the Combine statistical tool described in Section 8.6.

Figure 9.36 shows the main Higgsino limit result. The region to the lower left of thick black line is excluded. This result is further explored in Figures 9.37 and Figure 9.38. Figures 9.37 shows the main Higgsino limit result along with three 1D slices of this plot corresponding to selected branching ratios. In particular, the upper plot shows the limits under the assumption of a 100% Higgsino to Higgs branching ratio. Here several excesses have stacked to produce a 3σ excess at low Higgsino mass. Also included in this figure are some explanations of which regions of the expected limit are dominated by each analysis. As indicated here, the diphoton analyses presented in this document bring the expected limit to turn up and reach the 100% branching ratio at low masses. Without this excess the diphoton analyses would have enabled the Higgsinos models to be fully exclude below $135 \text{ GeV}/c^2$ regardless of branching ratio.

Figure 9.38 further examines these 1D slices, overlaying the expected limits obtained from individual analysis. This is useful for examining which parts of the limit receive significant contributions from each analysis.

The legend here needs some explanation:

- $\gamma\gamma b\bar{b}$ refers to the sum of the Higgsino with $b\bar{b}$ analysis and the Higgsino with electro-weak bosons analysis presented here.
- $\gamma\gamma\ell$ refers to both the Higgsino with leptons analysis presented here.
- $\geq 3\ell$ refers to the CMS multi-lepton analysis (which has a well studied excess) (26; 55).
- $b\bar{b}b\bar{b}$ refers to the CMS $4b$ analysis (4).
- $2b2\ell$ refers to the CMS $H(2b)Z(2\ell)$ analysis (22).
- $2j2\ell$ refers to the CMS $Z(2j)Z(2\ell)$ analysis (21).

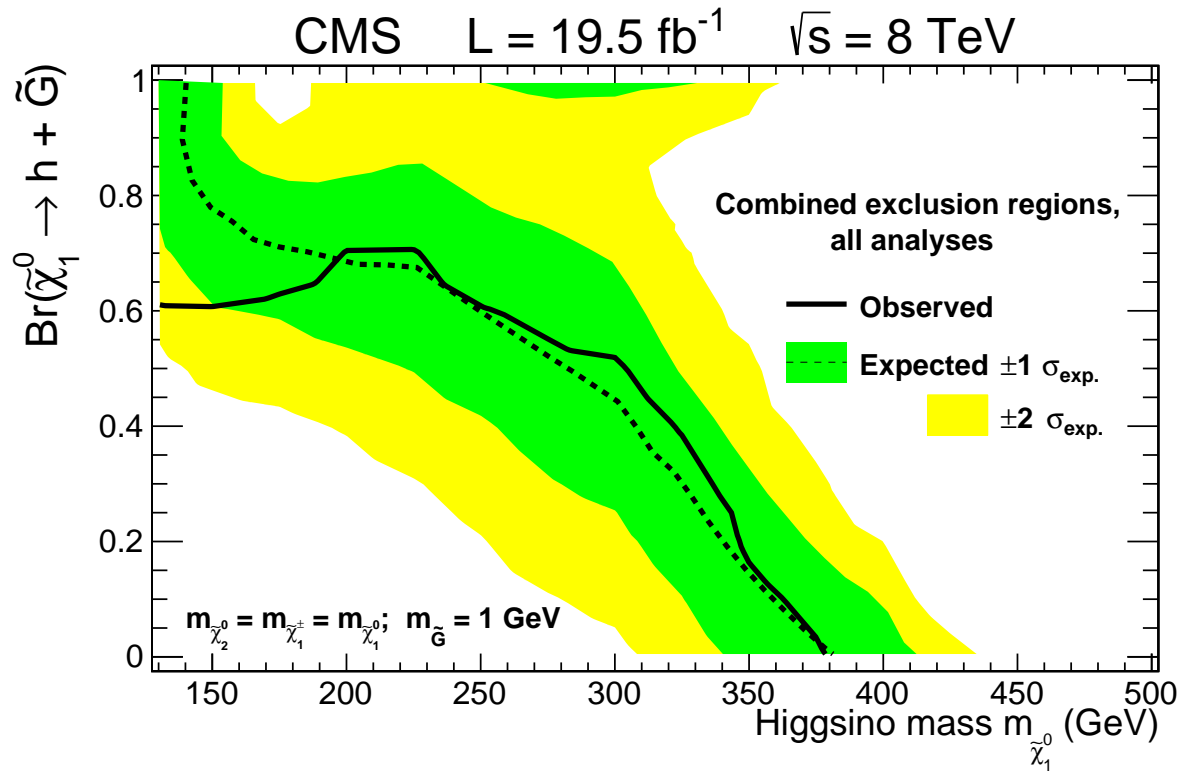


Figure 9.36: Combined Higgsino limit, employing information from the $2\gamma 2b$, $2\gamma + \ell$, Multi-lepton, $4b$, $2b2\ell$, and $2j2\ell$ analyses. On the vertical axis is the branching ratio of Higgsino to Higgs bosons, as opposed to decays to Z bosons.

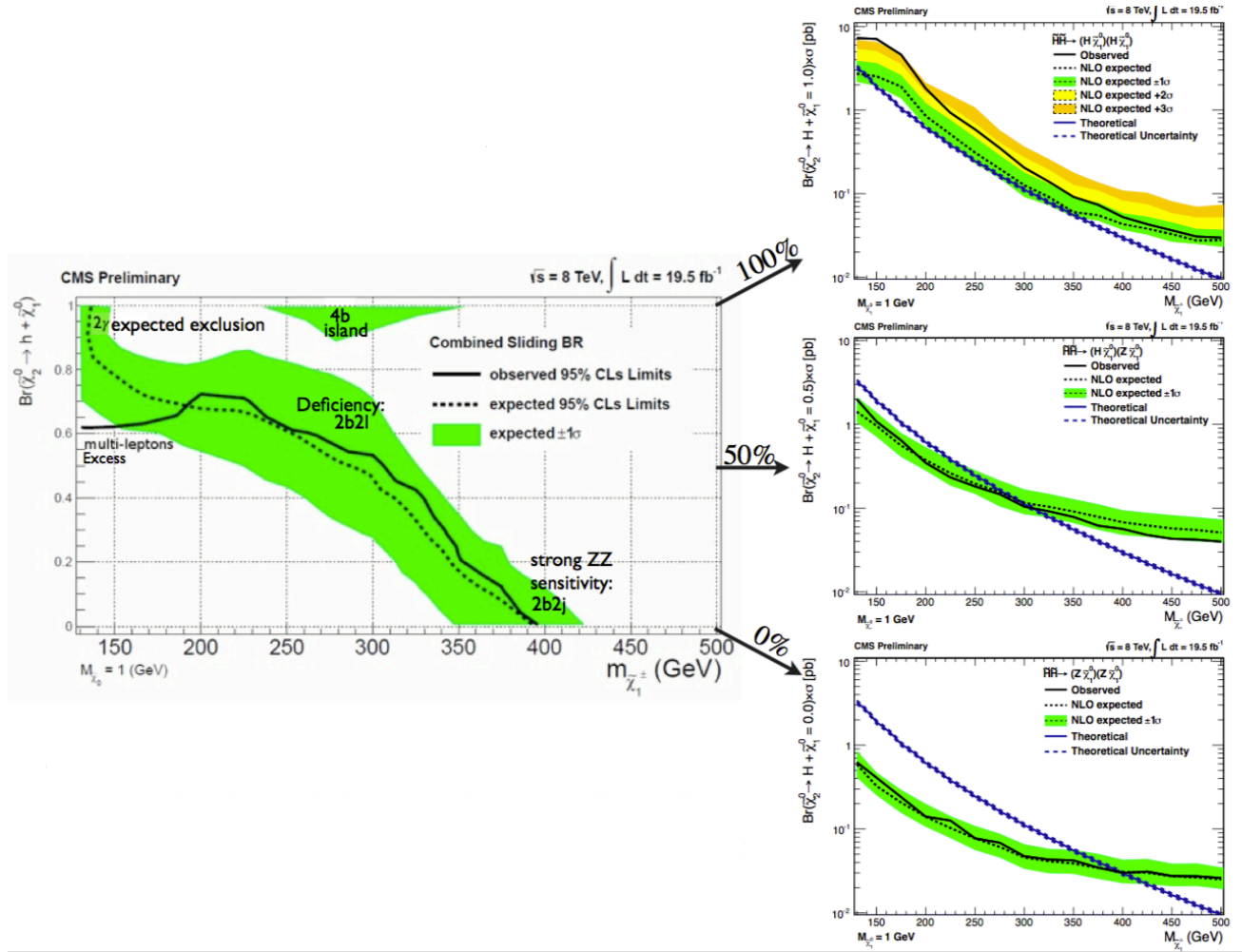


Figure 9.37: Left: the combined limit plot from Figure 9.36 with salient features of the limit labeled by their primary influence. Right: 1D slices of the limit plot for the 100%, 50%, and 0% Higgs branching fractions.

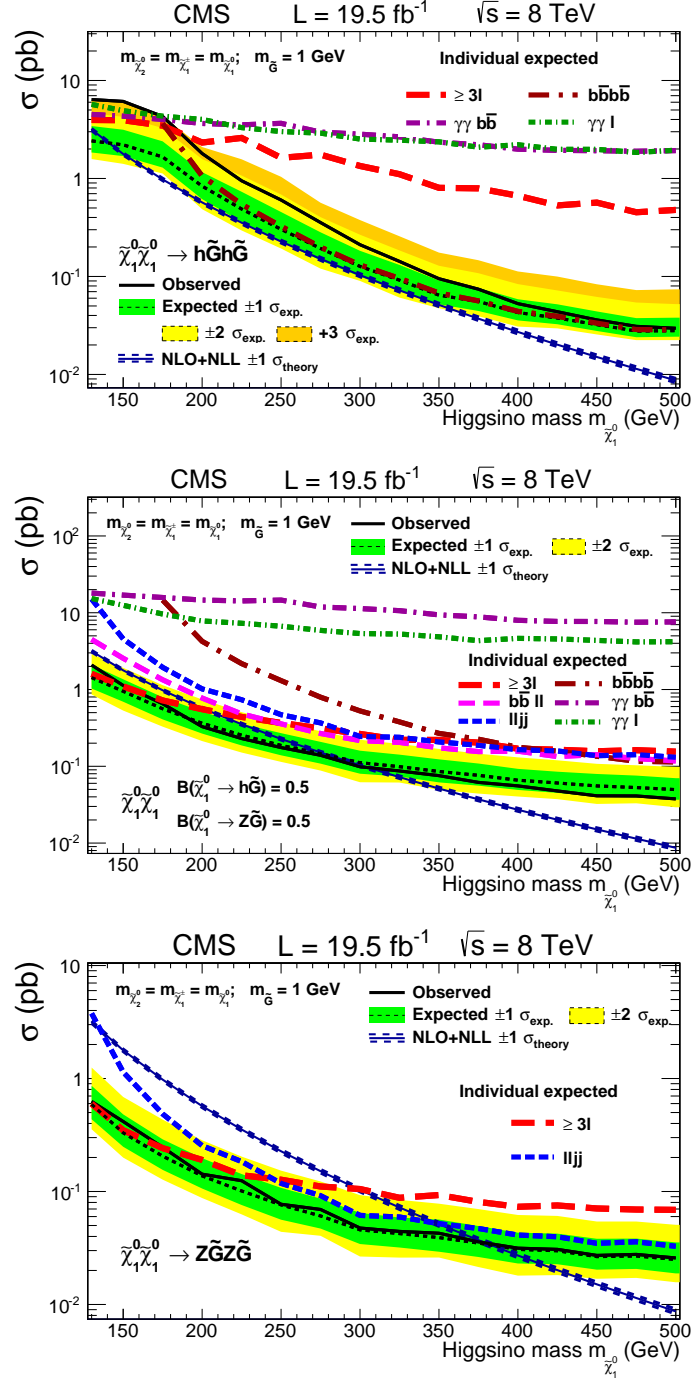


Figure 9.38: One dimensional slices of the limit from Figure 9.36 overlaid with the limits from individual contributing analyses. These are the same three plots as on the right side of Figure 9.37. Top: 100% Higgs branching fraction (pure HH), Middle: 50%, Bottom: 0% Higgs branching fraction (pure ZZ). $2\gamma + X$ analyses contribute significantly at low Higgsino mass and high branching fraction. The electroweak channel is included in $\gamma\gamma + b\bar{b}$.

Chapter 10

Conclusion

10.1 Summary

Two searches are presented for two production mechanisms for a “natural” SUSY model in which stops (\tilde{t}_R) and Higgsinos ($\tilde{\chi}_1^0$) are pair produced in proton-proton collisions in the CMS detector at $\sqrt{s} = 8\text{ TeV}$. These searches endeavor to tag a $H \rightarrow \gamma\gamma$ decay and use an innovative and versatile diphoton sideband method to set backgrounds.

In the first, stops are pair produced along with a secondary Higgsino pair production process. Stops then decay to Higgsinos and a third generation quark. Higgsinos are assumed to decay entirely to Higgs bosons and a Goldstino (\tilde{G}) which escapes the detector. This search is approached using $H \rightarrow \gamma\gamma$ tagging of one Higgs boson and searching for two or more b-jets, and is not combined with other search channels. Interesting 95% confidence limits are set, excluding a significant portion of stop-Higgsino mass plane up to top squark masses of 410 GeV (see Figure 9.12).

In the second search, a related natural SUSY model is pursued where Higgsinos are pair produced in the absence of other SUSY particles such as stops. The Higgsinos are allowed to decay to a Goldstino and either a Higgs boson (H) or a Z boson. Four diphoton channels are described here, which are combined with other analyses (54) to produce combined 95% confidence limits on Higgsino production as a function of Higgsino mass and branching fraction (Figure 9.36). The diphoton channels contribute sensitivity precisely where the multi-lepton analysis ((26; 55)) shows an intriguing excess. If this excess were absent, the diphoton channels would allow Higgsinos below 130 GeV to be excluded for all branchings (see Figure 9.37). This indicates that diphoton channels will be an important part of future Higgsino searches at the LHC.

In both searches, no significant evidence for a signal was observed.

These searches impose constraints on di-Higgs boson and Higgs plus vector boson production that can be extended beyond these two specific SUSY models. In particular, reinterpretations of the Higgsino search are considered for a different model where Wino-like neutralino + charginos are produced resulting in a Higgs boson and a W boson (3; 10).

The diphoton sideband method is developed here and is shown to be a robust and versatile tool for investigating physics signals that involve a Higgs boson.

10.2 Outlook

Associated Higgs is and will continue to be an exciting direction of study for Higgs sector physics and the diphoton channel will be an important part of this. While the diphoton method can yield interesting limits on its own, the most stringent limits will always come from combining analyses which address multiple Higgs decay channels. The diphoton channel is perhaps the most versatile among the possible means for searching for studying Higgs decay, enabling the rapid data-driven evaluation of any $\gamma\gamma + X$ final state with any kinematic variable.

Several avenues of improvement to the diphoton channel are apparent. The narrow natural width of the $H \rightarrow \gamma\gamma$ decay (a few MeV); while the observed width is dominated by detector effects. In the diphoton sideband method, the background is linearly dependent on the width of the Higgs mass window. Therefore, significant advances can be made by improving the diphoton mass resolution. In these analyses, a multivariate analyzer was used to correct photon energies and improve the photon resolution. Unfortunately, the version of the MVA that was available to CMS SUSY group did not produce as great of an improvement in resolution as the version used by the CMS Higgs group. Improving the photon resolution MVA used for associated Higgs production analyses should be a central topic of interest for future analyses.

The analyses presented here, and likely all diphoton analyses thus far, have focused on a simple cut based analysis and a single kinematic variable. Appendix A explores the prospects of using the full kinematic information available in the event with the diphoton sideband method. This would

give a general, powerful, and re-interpretable tool for detecting Higgs sector physics.

Several extensions of this work are immediately apparent. First and foremost is to revisit these channels with $\sqrt{s} = 13$ TeV proton collision data in Run 2 of the LHC. This will extend the limits seen here and enhance or destroy the curious excesses seen in the Higgsino analyses and those described in Appendix B. Also, a $\gamma\gamma + \tau$ channel would nicely compliment the other lepton channels. Also, a combination of searches could be applied to the stop analysis in the same way that was done for the Higgsino analysis.

The neutralino-chargino compressed spectrum can support cases where a significant fraction of neutralinos decay to photons, motivating a $H + \text{high } p_T \gamma$ search (see Appendix B).

Diphoton channel associated Higgs production studies should also find uses in heavy Higgs to 2 Higgs searches, and standard model associated Higgs production studies: VBF, ttH. Perhaps, in some future high energy collider, it may be used to standard model HH.

Bibliography

- [1] The fast simulation of the CMS detector at the LHC. In *International Conference on Computing in High Energy and Nuclear Physics (CHEP 2010)*. *J. Phys.: Conference Series* 331 (2011) 032049.
- [2] Particle-flow event reconstruction in CMS and performance for jets, taus, and MET. Technical Report CMS-PAS-PFT-09-001, CERN, 2009. Geneva, Apr 2009.
- [3] Search for electroweak production of charginos and neutralinos in final states with a Higgs boson in pp collisions at 8 TeV. Technical Report CMS-PAS-SUS-13-017, CERN, Geneva, 2013.
- [4] Search for electroweak production of higgsinos in channels with two Higgs bosons decaying to b quarks in pp collisions at 8 TeV. Technical Report CMS-PAS-SUS-13-022, CERN, Geneva, 2014.
- [5] Search for supersymmetry in final states with missing transverse energy and 0, 1, 2, 3, or at least 4 b-quark jets in 8 TeV pp collisions using the variable AlphaT. 2012.
- [6] J. Abdallah et al. A study of the b-quark fragmentation function with the delphi detector at LEP I and an averaged distribution obtained at the Z pole. *Eur.Phys.J.*, C71:1557, 2011.
- [7] Wolfgang Adam, R Frhwirth, Are Strandlie, and T Todor. Reconstruction of electrons with the gaussian-sum filter in the CMS tracker at the LHC. Technical Report CMS-NOTE-2005-001, CERN, Geneva, Jan 2005.
- [8] Johan Alwall, Michel Herquet, Fabio Maltoni, Olivier Mattelaer, and Tim Stelzer. MadGraph 5: going beyond. *JHEP*, 06:128, 2011.
- [9] S. Ambrosanio, Gordon L. Kane, Graham D. Kribs, Stephen P. Martin, and S. Mrenna. Search for supersymmetry with a light gravitino at the Fermilab Tevatron and CERN LEP colliders. *Phys.Rev.*, D54:5395–5411, 1996.
- [10] S. Arora, Anthony Barker, K. Burt, C. Contreras-Campana, E. Contreras-Campana, D. Feld, F. Golf, J. Gran, Y. Gershtein, R. Gray, G. Hanson, M. Hildreth, B. Hooberman, A. Lath, D. Mason, K. Mei, D. Morse, D. Olivito, S. Panwalkar, M. Park, R. Patel, S. Randall, S. Somalwar, S. Thomas, P. Thomassen, M. Walker, and P. Zywicki. Shared note for the susy with higgs search. CMS Note 2013/226, 2013.
- [11] S. Ask, M.A. Parker, T. Sandoval, M.E. Shea, and W.J. Stirling. Using gamma+jets production to calibrate the Standard Model Z(nunu)+jets background to new physics processes at the LHC. *JHEP*, 1110:058, 2011.
- [12] ATLAS Collaboration. Procedure for the LHC Higgs boson search combination in summer 2011. 2011.
- [13] Riccardo Barbieri and G.F. Giudice. Upper bounds on supersymmetric particle masses. *Nucl.Phys.*, B306:63, 1988.
- [14] Florian Beaudette. The CMS particle flow algorithm. pages 295–304, 2014.
- [15] W. Beenakker, S. Brensing, M.n Krämer, A. Kulesza, E. Laenen, Leszek Motyka, and Irene Niessen. Squark and gluino hadroproduction. *Int. J. Mod. Phys. A*, 26:2637, 2011.

- [16] W. Beenakker, R. Hopker, and M. Spira. PROSPINO: A program for the production of super-symmetric particles in next-to-leading order QCD. 1996.
- [17] W. Beenakker, R. Hopker, M. Spira, and P. M. Zerwas. Squark and gluino production at hadron colliders. *Nucl. Phys. B*, 492:51, 1997.
- [18] W. Beenakker, M. Klasen, M. Krämer, T. Plehn, M. Spira, and P. M. Zerwas. Production of charginos, neutralinos, and sleptons at hadron colliders. *Phys. Rev. Lett.*, 83:3780–3783, Nov 1999.
- [19] Wim Beenakker, Silja Brensing, Michael Krämer, Anna Kulesza, Eric Laenen, and Irene Niessen. Soft-gluon resummation for squark and gluino hadroproduction. *JHEP*, 12:041, 2009.
- [20] Zvi Bern, Lance J. Dixon, and Carl Schmidt. The diphoton background to a light Higgs boson at the LHC. *Nucl.Phys.Proc.Suppl.*, 116:178–182, 2003.
- [21] S. Bhattacharya, T. Speer, M. Luk, A. Avetisyan, Malik S., U. Heintz, and M. Narain. Inclusive search for heavy vector-like top quarks in multiple-lepton final states at $\sqrt{s} = 8$ TeV. CMS Note 2013/006.
- [22] Campagnari C. et al. Search for beyond-the-standard model physics in events with a Z boson, a Higgs boson, and missing transverse energy. CMS Note 2013/217, 2013.
- [23] S. Chatrchyan et al. The CMS experiment at the CERN LHC. *JINST*, 3:S08004, 2008.
- [24] Serguei Chatrchyan et al. Search for anomalous production of multilepton events in pp collisions at $\sqrt{s} = 7$ TeV. *JHEP*, 1206:169, 2012.
- [25] Serguei Chatrchyan et al. Energy calibration and resolution of the CMS electromagnetic calorimeter in pp collisions at $\sqrt{s} = 7$ TeV. *JINST*, 8:P09009, 2013.
- [26] Serguei Chatrchyan et al. Search for anomalous production of events with three or more leptons in pp collisions at $\sqrt{s} = 8$ TeV. *Phys. Rev. D*, 90:032006, 2014.
- [27] CMS BTag POG. B-tagging operating points for 53X Summer13 studies at 8 TeV. Available at <https://twiki.cern.ch/twiki/bin/viewauth/CMS/BTagPerformanceOP>, 2010.
- [28] CMS BTag POG. Re-weighting of events to account B-tag efficiency and mistag scale factors. Available at <https://twiki.cern.ch/twiki/bin/viewauth/CMS/BTagWeight>, 2010.
- [29] CMS BTag POG. Recommendation for operating points. Available at https://twiki.cern.ch/twiki/bin/viewauth/CMS/BtagPOG#Recommendation_for_Operating_Poi, 2010.
- [30] CMS Collaboration. Natural SUSY Higgsino NLSP Scenario. Available at <https://twiki.cern.ch/twiki/bin/view/CMS/NaturalSUSYHiggsinoNLSP>, 2010.
- [31] CMS Collaboration. Photon reconstruction and identification at $\sqrt{s} = 7$ TeV. CMS Physics Analysis Summary CMS-PAS-EGM-10-005, 2010.
- [32] CMS Collaboration. SUSY Cross Sections for 8 TeV Stops and Sbottoms. Available at <https://twiki.cern.ch/twiki/bin/view/LHCPhysics/SUSYCrossSections8TeVstopsbottom>, 2010.
- [33] CMS Collaboration. Cms luminosity based on pixel cluster counting - summer 2012 update. Technical Report CDS Record 1482193, 2012.
- [34] CMS Collaboration. Photon ID performance with 19.6fb^{-1} of data collected at $\sqrt{s} = 8$ TeV with the CMS detector. CMS Detector Performance Note CMS-DP-2013-010, 2013.
- [35] CMS Collaboration. Shared note for the SUSY with Higgs search. CMS Analysis Note CMS-AN-13-226, 2013.

- [36] CMS Collaboration. Updated measurements of the new Higgs-like boson at 125 GeV in the two photon decay channel. CMS Analysis Note CMS-AN-13-008, 2013.
- [37] CMS EGamma POG. Tag and probe efficiency scale factors using Zee candidates for 8 TeV (2012A+2012B). Available at https://twiki.cern.ch/twiki/bin/viewauth/CMS/CutBasedPhotonID2012#Tag_Probe_efficiency_scale_facto, 2010.
- [38] CMS EGamma POG. Electron identification twiki for simple cut based photon ID 2012 (EgammaCutBasedIdentification). Available at <https://twiki.cern.ch/twiki/bin/view/CMS/EgammaCutBasedIdentification>, 2012.
- [39] CMS Higgs PAG. Documentation of the RooStats-based statistics tools for Higgs PAG. Available at <https://twiki.cern.ch/twiki/bin/view/CMS/SWGuideHiggsAnalysisCombinedLimit>, February 2014.
- [40] CMS JetMET POG. Jet energy corrections for CMS users. Available at https://twiki.cern.ch/twiki/bin/view/CMS/JetEnergyScale#Jet_Energy_Corrections_for_CMS_u, 2010.
- [41] CMS Muon POG. Baseline muon selections. Available at https://twiki.cern.ch/twiki/bin/view/CMSPublic/SWGuideMuonId#Muon_Isolation, 2010.
- [42] CMS Muon POG. Reference muon ID and isolation efficiencies. Available at https://twiki.cern.ch/twiki/bin/viewauth/CMS/MuonReferenceEfs#Samples_reconstructed_before_22, 2013.
- [43] CMS SUSY PAG. Susy object experts. Available at <https://twiki.cern.ch/twiki/bin/viewauth/CMS/SusyObjectExperts>, 2012.
- [44] CMS Collaboration. Higgs to gamma gamma, fermiophobic. 2012.
- [45] CMS Collaboration. Search for supersymmetry in events with same-sign dileptons. 2012.
- [46] W. Cottingham, D. Greenwood, and J. Shiflett. *An Introduction to the Standard Model of Particle Physics*. Cambridge University Press, Cambridge, 2007.
- [47] Nathaniel Craig, John Killick, and Jared Evans. Exclusive Higgs Decayer tool. Private communication.
- [48] Savas Dimopoulos, Michael Dine, Stuart Raby, and Scott D. Thomas. Experimental signatures of low-energy gauge mediated supersymmetry breaking. *Phys.Rev.Lett.*, 76:3494–3497, 1996.
- [49] EGamma POG. Electron efficiency using tag and probe. Available at <http://lovedeep.web.cern.ch/lovedeep/work12/Dec7TnP2012dataID/intro.html>, 2013.
- [50] Benjamin Fuks, Michael Klasen, David R. Lamprea, and Marcel Rothering. Gaugino production in proton-proton collisions at a center-of-mass energy of 8 TeV. *JHEP*, 1210:081, 2012.
- [51] Benjamin Fuks, Michael Klasen, David R. Lamprea, and Marcel Rothering. Precision predictions for electroweak superpartner production at hadron colliders with Resummino. *Eur.Phys.J.*, C73:2480, 2013.
- [52] Kiel Howe and Prashant Saraswat. Excess Higgs production in neutralino decays. *JHEP*, 1210:065, 2012.
- [53] Rudolph Emil Kalman. A new approach to linear filtering and prediction problems. *Transactions of the ASME–Journal of Basic Engineering*, 82(Series D):35–45, 1960.
- [54] Vardan Khachatryan et al. Searches for electroweak neutralino and chargino production in channels with Higgs, Z, and W bosons in pp collisions at 8 TeV. 2014.

- [55] Vardan Khachatryan et al. Searches for electroweak production of charginos, neutralinos, and sleptons decaying to leptons and W, Z, and Higgs bosons in pp collisions at 8 TeV. *Eur. Phys. J. C*, 74:3036, 2014.
- [56] Michael Krämer, Anna Kulesza, Robin van der Leeuw, Michelangelo Mangano, Sanjay Padhi, Tilman Plehn, and Xavier Portell. Supersymmetry production cross sections in pp collisions at $\sqrt{s} = 7$ TeV. 2012.
- [57] A. Kulesza and L. Motyka. Threshold resummation for squark-antisquark and gluino-pair production at the LHC. *Phys. Rev. Lett.*, 102:111802, 2009.
- [58] LHC Higgs Cross Section Working Group. SM Higgs production cross sections at $\sqrt{s} = 8$ TeV. Available at <https://twiki.cern.ch/twiki/bin/view/LHCPhysics/CERNYellowReportPageAt8TeV>, 2010.
- [59] Stephen P. Martin. A Supersymmetry primer. *Adv.Ser.Direct.High Energy Phys.*, 21:1–153, 2010.
- [60] Konstantin T. Matchev and Scott D. Thomas. Higgs and Z boson signatures of supersymmetry. *Phys.Rev.*, D62:077702, 2000.
- [61] Patrick Meade, Matthew Reece, and David Shih. Prompt decays of general neutralino NLSPs at the Tevatron. *JHEP*, 1005:105, 2010.
- [62] Bernhard Mistlberger and Falko Dulat. Limit setting procedures and theoretical uncertainties in Higgs boson searches. 2012.
- [63] K.A. Olive et al. Review of particle physics. *Chin.Phys.*, C38:090001, 2014. Supersymmetry Theory review available at <http://pdg.lbl.gov/2014/reviews/rpp2014-rev-susy-1-theory.pdf>.
- [64] Michele Papucci, Joshua T. Ruderman, and Andreas Weiler. Natural SUSY endures. *JHEP*, 1209:035, 2012.
- [65] A. S. Perloff. Pileup measurement and mitigation techniques in CMS. Presented at CALOR 2012: 15th International Conference on Calorimetry in High Energy Physics, 2012. https://cms-mgt-conferences.web.cern.ch/cms-mgt-conferences/conferences/pres_display.aspx?cid=757&pid=5564.
- [66] Torbjörn Sjöstrand, Stephen Mrenna, and Peter Z. Skands. PYTHIA 6.4 physics and manual. *JHEP*, 05:026, 2006.
- [67] William R. Spearman. *Measurement of the mass and natural width of the Higgs boson in the H to ZZ to 4l decay channel with the ATLAS detector*. Phd, Harvard University, 2014.

Appendix A

Non-parametric Multivariate Methods

The diphoton side band background method is extremely general and can provide us the background distributions for every kinematic variable we can imagine except the diphoton mass. So far we have used the most sensitive single variable available and discard large amounts of additional information. This strongly suggests the use of multivariate techniques.

Typically multivariate techniques are over specialized towards one particular signal model and are too complex for theorists to rapidly adapt to other signals. Therefore we are interested in constructing a non-parametric multivariate function that describes how background-like an event is. The univariate output of this function can then be analyzed with the diphoton side band method in the same manner as the other single variable discriminants explored in this thesis. We may then use this as a model independent search tool that theorists can also easily employ for reinterpretations.

We would like to be alerted to events with unusually extreme combinations of kinematic variables under the background distribution, even when the individual measurements are not so rare when compared with 1D projections of the background distribution. In particular, we are interested in:

- E_T^{miss}
- p_T sum of b-jets
- p_T sum of light flavored jets
- The number of b-jets present
- Higgs S_t
- The number of additional leptons present

- p_{Tt} sum of additional leptons
- How tight in CSV the b-jets are
- How tight the two photons are
- How well reconstructed the photons are in terms of their R9
- Whether there is a pair of jets (especially the b-jets) with di-jet mass compatible with the decay of a W^\pm , Z, or Higgs boson.
- The presence of a third photon, particularly if that extra photon is higher in p_T than the two photons composing the Higgs.
- p_T sum of all photons

Combining this information would be a straightforward process using a Fisher Discriminant if the variables of interest were uncorrelated, however we cannot reasonably assume this. H-matrix method can be used to remove linear correlations and develop a single χ^2 variable describing how well an event matches the background distribution. Process the data in three passes. First determine the means $\langle x_i \rangle$ of each of the variable of interest x_i . Second, determine the covariance matrix M .

$$M_{ij} = \frac{1}{N} \sum_{n=1}^N (x_{i,n} - \langle x_i \rangle)(x_{j,n} - \langle x_j \rangle)$$

where the sum is over N training events. Invert the correlation matrix to get $H = M^{-1}$. Next on the third pass over the data compute the χ^2 .

$$\chi_k^2 = \sum_{i,j} (x_{i,k} - \langle x_i \rangle) H_{ij} (x_{j,k} - \langle x_j \rangle)$$

There are several options for how to train the means and H-matrix. First, Monte Carlo may be used. Any differences between the Monte Carlo behavior and that of data will appear as a decrease in sensitivity. It may be trained on a data sideband, such as events with one photon in the barrel and one in the endcap. Unfortunately this produces unacceptable loss of sensitivity if other photon variables are considered. There is also the prospect of training the background sample. This ensures that the correlations being canceled are kinematically accurate, although it introduces an additional small systematic uncertainty.

We are more interested in $1 - CDF(MET)$, which may be interpreted as the probability that an training event has a this much MET or more. Several such probabilities will later be combined by Fisher's method, so it will be convenient to take the negative natural log of this. $L_{MET} = -\ln(1 - CDF(MET))$. This is simply a function on which the diphoton side band methods can be applied, now using the main data where both photons are in the barrel. We have no expectations that the background the main sidebands will be exactly modeled by that in the training sample although we expect it to be close enough to not degrade sensitivity too much. In any case, we only want this variable as an auspicious backdrop on which to compare the signal and background. We expect the background to behave like a decaying exponential $\exp(-L_{MET})$ from $L=0$ to infinity. We can then search for excesses of signal events with large L . So far this is not significantly different than the searches using MET described in Section 8.1.

We can now add additional information by considering additional variables. We construct similar L 's for many other variable that show some lesser ability to distinguish between signal and background, and have the property that larger values are more signal-like. It is easy enough to transform kinematic variables so to meet this last condition. (Ex: $\eta \rightarrow 5 - |\eta|$) Since they are all probabilities, they are on an equal footing and can be directly combined. We sum the L 's to create a combined log likelihood variable L^* . We can use L -modules for coarsely binned histograms, discrete variables (like the number of b-jets), and booleans (like the presence or absence of a M_{jj} consistent with a Z). Events that score highly on L^* are those that have surprising extreme combination of values. Thus we have a modular approach that can consider much more of the available information about the event to aid in separating background from signals. Signal should be unusual in multiple respects, and collect at high values of L^* .

This allows the discriminating power of all available variables to be used without tuning the search to a particular model and largely circumventing the curse of dimensionality. The resulting L -variables should be easy to reinterpret and easy for theorists to use. Using multiple variables incurs some look-elsewhere effect but consistently account for it.

Appendix B

Anomalies

In the course of investigating with little new physics observed in 2012 data and the promise of Run 2 data on the way, several informal yet moderately careful unblinded studies were performed. Some surprising excesses were seen in the course of these studies that should be carefully followed up on when more LHC data arrives using blinded studies. Quite a few channels were informally explored besides those theoretically motivated. While efforts were taken to reduce bias, the look-elsewhere effect may be significant. Therefore, the significance of the following observations cannot be evaluated further in 2012 data and must be returned to in Run 2 of the LHC.

When investigating diphoton + dilepton events, with the two photons consistent with a Higgs boson decay, four events are observed in the signal window with zero side band events. Informal studies of these events were performed and it was concluded that nothing definitive could be concluded without additional data. All dilepton pairs were opposite side di-electron events. The absence of muons may be due to a difference in lepton efficiency between electrons and muons. These events are contained within the electron channel presented in Tables 9.8 and 9.22. The event numbers of interest are:

| Run | Lumisection | Event |
|--------|-------------|------------|
| 207920 | 500 | 748865301 |
| 203987 | 39 | 50527407 |
| 206446 | 784 | 1072391444 |
| 207231 | 524 | 792766566 |

When investigating three-photon events with the sub-leading and sub-sub leading events consistent with a Higgs boson decay, an excess with approximately 1.5 sigma significance was observed.

This search is motivated by neutralino pair production with one branch decaying through a photon to a Gravitino, and the other branch decaying through a Higgs boson to a gravitino.

Also, excess is observed immediately upon the use of the MVA methods described in the Appendix refsec:mva of approximately 2 sigma significance.